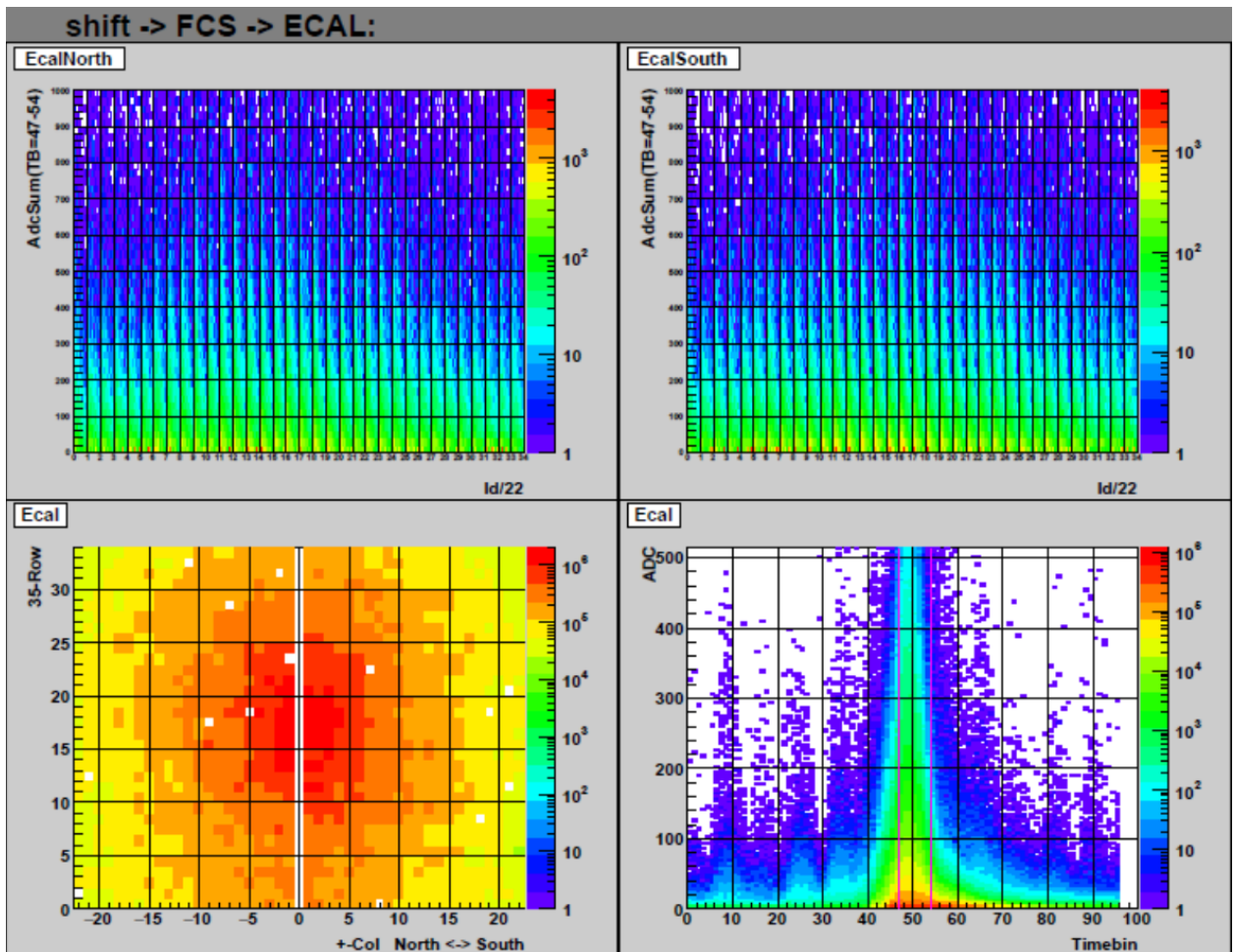


# The STAR Beam Use Request for Run-22 and data taking in 2023-25

The STAR Collaboration



FCS EMCAL plots from online monitoring during Run-21.

Bottom left: distribution of hits across all the EMCAL modules.

Bottom right: energy deposition as a function of time bin in the electronics readout.

Top: Energy deposition vs module ID.

# 1 Executive Summary

2 This Beam Use Request outlines the strong physics programs proposed by STAR collabora-  
3 tion for data taking during Run-22 and 2023-2025.

4 STAR's **highest scientific priority** is to initiate the "must-do" Cold QCD forward  
5 physics program enabled by the newly completed suite of forward detectors via the collection  
6 of transversely polarized  $pp$  data at 510 GeV in Run-22. A combination of soft and hard  
7 probes collected during 2023-25 will be used to probe the QGP's microstructure and continue  
8 our unique forward physics program via the collection of high statistics Au+Au,  $p$ +Au, and  
9  $pp$  data at  $\sqrt{s_{NN}} = 200$  GeV.

10 Run-22 takes full advantage of STAR's new forward detection capabilities, consisting of a  
11 Forward Calorimeter System (FCS) and a Forward Tracking System (FTS) located between  
12  $2.5 < \eta < 4$ , while also capitalizing on the recent BES-II detector upgrades. As shown  
13 in Table 1, we propose **a dedicated 20 cryo-week transversely polarized  $pp$  run**  
14 **at  $\sqrt{s} = 510$  GeV**. We note that an 18 cryo-week run would very detrimental to STAR  
15 achieving all our physics goals. Due to the need to commission the new detectors in the the  
16 first weeks of running, a reduction of two weeks will result in more than a  $\sim 15\%$  reduction  
17 in our sampled luminosity estimates; the loss will occur once the detectors and RHIC will  
18 be operating at their most efficient.

**Table 1: Proposed Run-22** assuming 20 cryo-weeks, including an initial one week of cool-down and a two weeks set-up time.

$\sqrt{s}$ (GeV)	Species	Polarization	Run Time	Sampled Luminosity	Priority
510	$pp$	Transverse	16 weeks	400 pb <sup>-1</sup>	1

19 These data will enable STAR to explore, with unprecedented precision, forward jet  
20 physics that probe both the high-x (largely valence quark) and low-x (primarily gluon)  
21 partonic regimes.

22 The STAR collaboration has also identified a number of topics that together make a  
23 compelling case to take data during Runs 23-25 alongside sPHENIX, and successfully com-  
24 plete RHIC's scientific mission. This scientific program is enabled by the first opportunity  
25 to capitalize on the combination of the BES-II and Forward Upgrades in the data collected  
26 from Au+Au,  $p$ +Au, and  $pp$  collisions at  $\sqrt{s_{NN}} = 200$  GeV as outlined in Table 2.

27 Significantly increased luminosities, the extended acceptance at mid-rapidity due to the  
28 iTPC, improved event plane and triggering capabilities of the EPD, and the ability to probe  
29 the previously inaccessible forward region are all exploited in our Hot QCD program, that  
30 informs on the microstructure of the QGP, and our Cold QCD program that will utilize  
31 transverse polarization setting the stage for related future measurements at the EIC.

32 By combining the data collected via Au+Au collisions at 200 GeV in Run-23 and Run-  
33 25 we will be able to address important questions about the inner workings of the QGP,

34 including the temperature dependence of the shear and bulk viscosities, the 3-D nature of  
 35 the initial state, how global vorticity is transferred to the spin angular momentum of particles  
 36 on such short time scales and the chiral properties of the medium.

37 In Run-24 STAR considers it critical that we collect approximately equal nucleon-nucleon  
 38 luminosities for  $pp$  and  $p+Au$  at 200 GeV. In this way we can optimize the statistical precision  
 39 of several critical observables that require comparisons between results in both  $pp$  and  $p+Au$ .  
 40 We request transversely polarized protons for both datasets. Assuming 28 cryo-weeks in Run-  
 41 24 we expect to record samples that represent a factor 4.5 times the luminosity that STAR  
 42 sampled during transversely polarized  $pp$  collisions in Run-15 and 3 times the luminosity  
 43 sampled during transversely polarized  $p+Au$  collisions in Run-15.

**Table 2: Proposed Run-23 - Run-25** assuming 28 cryo-weeks of running every year, and 6 weeks set-up time to switch species in 2024. Sampled luminosities assume a "take all" triggers.

$\sqrt{s_{NN}}$ (GeV)	Species	Number Events/ Sampled Luminosity	Year
200	Au+Au	10B / 31 nb <sup>-1</sup>	2023
200	$pp$	235 pb <sup>-1</sup>	2024
200	$p+Au$	1.3 pb <sup>-1</sup>	2024
200	Au+Au	10B / 31 nb <sup>-1</sup>	2025

44 This text still needs to be finalized after agreement within the collaboration:

45 As requested, we also considered the scenario that each run is reduced to only 20 cryo-  
 46 weeks in 2023-25. The dramatic decrease in sampled luminosity resulting from this scenario  
 47 will have a serious negative impact on us achieving all of our physics goals outlined in this  
 48 BUR.

49 If such a negative scenario unfolds, the STAR collaboration would continue to request  
 50 Au+Au,  $p+Au$ , and  $pp$  running as outlined in Table 3. The ordering of this running could  
 51 be optimized to minimize time lost to moving the magnets for  $p+Au$  running. This scenario  
 52 would result in a significant increase in both the statistical and systematic uncertainties of  
 53 all the data. The hard probe, thermal di-lepton, and photon-induced di-lepton and  $J/\psi$   
 54 programs most significantly hit from the Au+Au program, while in the  $pp$  and  $p+Au$  goals  
 55 of XXX will be most significantly impacted.

56 Finally in Section 5 we propose the collection of two datasets as the opportunity arises.  
 57 One proposal enables the determination of nuclear deformation parameters of heavy-ion  
 58 nuclei which are important to improve our modeling and subsequent understanding of the  
 59 hydrodynamical response of the medium. Information on these deformation parameters are  
 60 of significant interest to the nuclear structure physics community, and heavy ion collisions  
 61 have very different sensitivity on and might probe different aspects of these parameters.

62 The other proposal expands our fixed-target program to include other light beam and  
 63 target combinations. These data will help clarify the role and mechanisms of nucleon stop-  
 64 ping. In addition, light nucleus cross sections in the target/projectile regions using beams

**Table 3: Proposed Run-23 - Run-25** assuming 20 cryo-weeks of running every year, and 6 weeks set-up time to switch species in 2024. Sampled luminosities assume a "take all" triggers.

$\sqrt{s_{\text{NN}}}$ (GeV)	Species	Number Events/ Sampled Luminosity
200	Au+Au	10B / 32 nb <sup>-1</sup>
200	<i>pp</i>	214 pb <sup>-1</sup>
200	<i>p</i> +Au	1.2 pb <sup>-1</sup>

65 of 3-50 GeV/n are of great interest to the NASA Space Radiation community.

# 66 Contents

67	<b>1 Highlights from the STAR Program</b>	<b>1</b>
68	1.1 Highlights from the Heavy Ion Program . . . . .	1
69	1.1.1 Bulk Correlations . . . . .	1
70	1.1.2 pp and Heavy-Ion Jet Measurements . . . . .	9
71	1.1.3 Heavy-flavor . . . . .	14
72	1.1.4 Light Flavor and Ultra-peripheral Collisions . . . . .	16
73	1.2 CME Search and Isobar Run . . . . .	20
74	1.2.1 Introduction . . . . .	20
75	1.2.2 Modality of Isobar Running at RHIC . . . . .	20
76	1.2.3 Blinding of Data Sets and Preparation for Analyses . . . . .	21
77	1.2.4 Methods for the Isobar Blind Analyses . . . . .	22
78	1.2.5 Observables for Isobar Blind Analyses . . . . .	23
79	1.2.6 Benchmarking CME Observables Against EBE-AVFD Model . . . . .	27
80	1.2.7 Prospect of CME Search Beyond the Isobar-era . . . . .	31
81	1.3 Cold QCD Highlights . . . . .	34
82	1.3.1 Introduction . . . . .	34
83	1.3.2 Longitudinal Program . . . . .	34
84	1.3.3 Transverse Program . . . . .	35
85	1.3.4 Unpolarized Program . . . . .	41
86	1.4 Run-21 Performance . . . . .	44
87	1.4.1 Performance to Date . . . . .	44
88	1.4.2 Projections to Complete the Run-21 Physics Priorities . . . . .	46
89	1.5 Physics Opportunity for Run-21 . . . . .	49
90	<b>2 Cold QCD Physics with <math>p^\uparrow p^\uparrow</math> and <math>p^\uparrow + A</math> Collisions at 510 and 200 GeV</b>	<b>51</b>
91	2.1 Run-22 Request for $p^\uparrow p^\uparrow$ Collisions at 510 GeV . . . . .	53
92	2.1.1 Inclusive Transverse Spin Asymmetries at Forward Rapidities . . . . .	53
93	2.1.2 Sivers and Efremov-Teryaev-Qiu-Sterman Functions . . . . .	55
94	2.1.3 Transversity, Collins Function and Interference Fragmentation Function	60
95	2.1.4 Probing Unpolarized Distributions in the Proton . . . . .	67
96	2.1.5 Spatial Imaging of the Nucleon . . . . .	67
97	2.2 Run-24 Request for Polarized $pp$ and $p+A$ Collisions at 200 GeV . . . . .	70
98	2.2.1 Spin Physics with Polarized $pp$ and $p+A$ Collisions at 200 GeV . . . . .	71
99	2.2.2 Physics Opportunities with Unpolarized proton-Nucleus Collisions . . . . .	76
100	<b>3 Exploring the Microstructure of the QGP (Run-23 and Run-25 Au+Au)</b>	<b>90</b>
101	3.1 Correlation Measurements Utilizing Extended Acceptance . . . . .	92
102	3.2 Correlation Measurements Utilizing the Enhanced Statistics . . . . .	100
103	3.3 Hard Probes: Jets and Heavy Flavor . . . . .	105
104	3.3.1 Precision Jet Measurements to Study the QGP Micro-Structure . . . . .	106
105	3.3.2 Deconfinement and Thermalization With Charmonia Measurements . . . . .	109

106	3.4	Electromagnetic Probes and Ultra-peripheral collisions . . . . .	112
107	3.4.1	Probing the degrees of freedom of the medium and its transport prop- erties: . . . . .	112
108	3.4.2	Studying the Photon Wigner Function and Final-state Magnetic Fields in the QGP . . . . .	113
109	3.4.3	Ultra-peripheral Au+Au Collisions: Probe Gluon Distribution Inside the Nucleus . . . . .	115
110			
111			
112			
113	<b>4</b>	<b>Forward Upgrade</b>	<b>117</b>
114	4.1	Status . . . . .	118
115	4.2	Forward Calorimeter System . . . . .	118
116	4.3	Forward Silicon Tracker . . . . .	119
117	4.4	Forward sTGC Tracker . . . . .	120
118	4.5	Software . . . . .	121
119	<b>5</b>	<b>Future Opportunities</b>	<b>124</b>
120	5.1	Shape Tomography of Atomic Nuclei Using Collective Flow Measurements . .	124
121	5.2	Fixed-target Measurements Using Light Beam and Target Combinations . .	128
122	<b>6</b>	<b>Charge for 2021 NPP PAC</b>	<b>130</b>

# 1 Highlights from the STAR Program

## 1.1 Highlights from the Heavy Ion Program

### 1.1.1 Bulk Correlations

Over the past years, the STAR collaboration has performed a series of correlation measurements directed towards a comprehensive understanding of the QCD phase diagram and the bulk properties of the QGP phase. Here we highlight the most recent STAR results on bulk correlations, which are expected to shed light on the QCD phase diagram as well as on the transport properties of the QGP.

#### Net-proton number fluctuations and a crossover search

One of the main goals in heavy-ion collision experiments is to understand a phase diagram of QCD matter with respect to temperature ( $T$ ) and baryon chemical potential ( $\mu_B$ ). In the Beam Energy Scan program (BES-I), heavy-ion collisions experiments were carried out by varying the collision energy in order to scan wide region of the baryon chemical potential of  $30 < \mu_B$  (MeV)  $< 400$ . The STAR experiment has measured higher-order fluctuations up to the fourth-order of net-proton multiplicity distributions from the BES-I. The fourth-order fluctuations were found to have a non-monotonic beam energy dependence within  $3.0\sigma$  significance [43], which could indicate a critical point exists at  $\sqrt{s_{NN}} \approx 7.7$  GeV. More precise measurements with enhanced statistics at low collision energies of  $3.0 < \sqrt{s_{NN}}$  (GeV)  $< 19.6$  will be performed in the Beam Energy Scan program phase II (BES-II) and the Fixed-Target program (FXT).

On the other hand, it is also important to establish a nature of the phase transition experimentally at small  $\mu_B$  region. A smooth crossover is predicted at  $\mu_B$  by first principle lattice QCD calculations [80]. However, there is not direct experimental evidence of the smooth crossover. Theoretically, the sixth-order fluctuations of baryon numbers are expected to be negative near the phase transition temperature [91,97,148]. The STAR experiment has measured the sixth-order fluctuations,  $C_6/C_2$ , of net-proton distributions using high statistics data sets at  $\sqrt{s_{NN}}=27, 54.4, \text{ and } 200$  GeV. Figure 1 shows net-proton  $C_6/C_2$  as a function of collision centrality. Most of the data points for 27 and 54.4 GeV are consistent with statistical baseline ( $C_6/C_2 = 1$ ) except for central collisions at 27 GeV. On the other hand, the  $C_6/C_2$  values at 200 GeV are negative systematically from peripheral to central collisions. The experimental results are compared with lattice QCD and UrQMD calculations. Results for 27 and 54.4 GeV are consistent with UrQMD calculations, while for 200 GeV results are below the UrQMD calculations. The negative values observed in central collisions at 27 and 200 GeV are qualitatively consistent with QCD-based model and lattice QCD calculations within large uncertainties. The current results are dominated by large statistical uncertainties, which makes it difficult to extract definitive physics messages. The statistical accuracy for 200 GeV will be significantly improved by Au+Au collisions in Run-23 and Run-25.

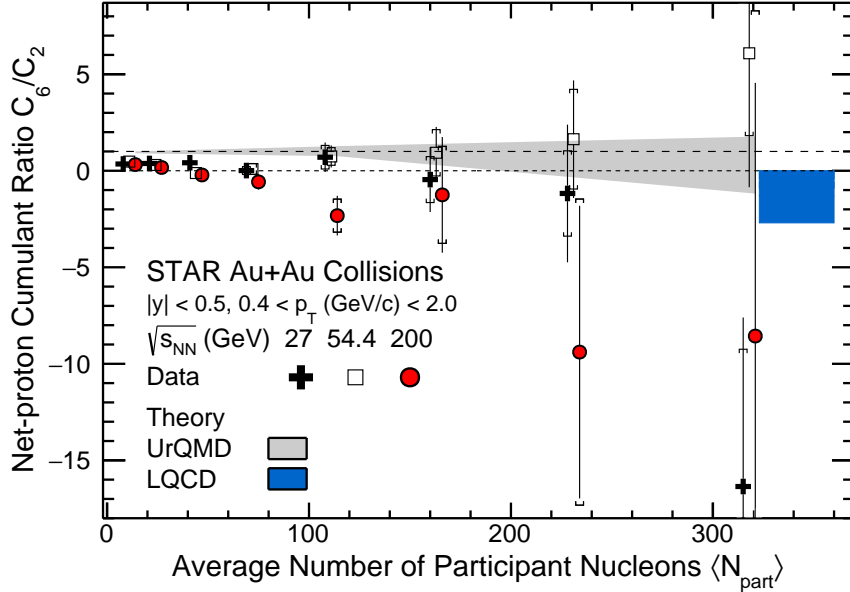


**Figure 1:** Collision centrality dependence of net-proton  $C_6/C_2$  in Au+Au collisions for  $\sqrt{s_{NN}} = 27, 54.4,$  and  $200$  GeV within  $|y| < 0.5$  and  $0.4 < p_T$  (GeV/c)  $< 2.0$ . Points for different beam energies are staggered horizontally to improve clarity. A shaded band show the results from UrQMD model calculations. The lattice QCD calculations for  $T = 160$  MeV and  $\mu_B < 110$  MeV are shown as a blue band at  $\langle N_{part} \rangle \approx 340$ .

### 160 Global polarization of $\Xi$ and $\Omega$ hyperons in Au+Au collisions at 200 GeV:

161 The phenomenon of global polarization in heavy-ion collisions results from the partial  
 162 transformation of the orbital angular momentum of colliding nuclei into the spin angular  
 163 momentum of the particles produced in the collision [223,312]. Consequently, these particles  
 164 display globally polarized along the direction of the initial orbital momentum of the nuclei.  
 165 Global polarization was first measured by the STAR Collaboration in the beam energy scan  
 166 Au+Au collisions [24].

167 Although the energy dependence of the  $\Lambda$  polarization can be to a good degree described  
 168 by theoretical models [172, 300, 310, 317], several questions remain open, and the detailed  
 169 modeling of the global polarization and dynamical approach of spin is under development.  
 170 Therefore, further experimental inputs are crucial for understanding the vorticity and polar-  
 171 ization phenomena in heavy-ion collisions. Recently STAR collaboration reported the first  
 172 measurements of the global polarization of spin  $s = 1/2$   $\Xi^-$  and  $\Xi^+$  hyperons, as well as  
 173 spin  $s = 3/2$   $\Omega$  hyperons in Au+Au collisions at 200 GeV.

174 Figure 2 shows the collision energy dependence of the  $\Lambda$  hyperon global polarization  
 175 previously measured [20, 24] along with the new  $\Xi$  and  $\Omega$  global polarizations measurements  
 176 at  $\sqrt{s_{NN}} = 200$  GeV. For  $\Xi$  and  $\Omega$  polarizations and to reduce the statistical uncertainty  
 177 we averaged over particle and antiparticle, 20%-80% centrality range, transverse momentum  
 178  $p_T > 0.5$  GeV/c, and rapidity  $|y| < 1$ . Global polarization of  $\Xi^-$  and  $\Xi^+$  measurements via  
 179 daughter  $\Lambda$  polarization show positive values, with no significant difference between  $\Xi^-$  and

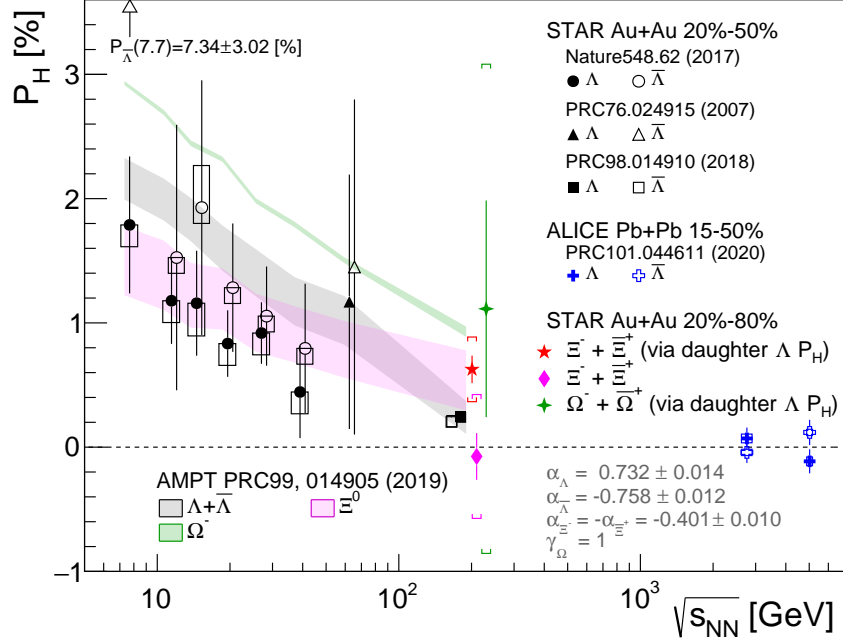


**Figure 2:** The energy dependence of the hyperon global polarization measurements. The points corresponding to  $\Lambda$  and  $\bar{\Lambda}$  polarizations, as well as  $\Xi$  and  $\Omega$  points in Au+Au collisions at  $\sqrt{s_{NN}} = 200$  GeV are slightly shifted for clarity. Previous results from the STAR [16, 24] and ALICE [20] experiments compared here are rescaled by new decay parameter indicated inside the figure. The data point for  $\bar{\Lambda}$  at 7.7 GeV is out of the axis range and indicated by an arrow with the value. The results of the AMPT model calculations [315] for 20-50% centrality are shown by shaded bands where the band width corresponds to the uncertainty of the calculations.

180  $\bar{\Xi}^+$  ( $P_{\bar{\Xi}} (\%) = 0.77 \pm 0.16$  (stat.)  $\pm 0.49$  (syst.) and  $P_{\Xi^-} (\%) = 0.49 \pm 0.16$  (stat.)  $\pm 0.20$  (syst.)).  
181 The average polarization value obtained by this method is  $\langle P_{\bar{\Xi}} \rangle (\%) = 0.63 \pm 0.11$  (stat.)  $\pm$   
182  $0.26$  (syst.). The  $\Xi + \bar{\Xi}$  polarization was also measured via analysis of the angular distribution  
183 of daughter  $\Lambda$  in  $\Xi$  rest frame. This result,  $\langle P_{\Xi} \rangle (\%) = -0.07 \pm 0.19$  (stat.)  $\pm 0.50$  (syst.),  
184 has larger uncertainty in part due to a smaller value of  $\alpha_{\Xi}$  compared to  $\alpha_{\Lambda}$ , which leads  
185 to smaller sensitivity of the measurement. The weighted average of the two measurements  
186 is  $\langle P_{\Xi} \rangle (\%) = 0.47 \pm 0.10$  (stat.)  $\pm 0.23$  (syst.), which is larger than the polarization of  
187 inclusive  $\Lambda + \bar{\Lambda}$  measured at the same energy for 20%-80% centrality,  $\langle P_{\Lambda} \rangle (\%) = 0.24 \pm$   
188  $0.03 \pm 0.03$  [24], although the difference is still not significant considering the statistical and  
189 systematic uncertainties of both measurements. Also the  $\Omega^-$  Global polarization is presented  
190 in Fig. 2. The result show large uncertainty,  $\langle P_{\Omega} \rangle (\%) = 1.11 \pm 0.87$  (stat.)  $\pm 1.97$  (syst.)  
191 for 20%-80% centrality and more precise measurements will be needed to make a definitive  
192 statement. Future measurements with higher precision will shed light on the uncertainty of  
193 the decay parameter  $\gamma_{\Omega}$ , as well as experimental results on the global polarization of spin-3/2  
194 particles, providing critical information about spin dynamics in heavy-ion collisions.

195 **Nuclear deformation measurements:**

196 Deformation is a fundamental property of atomic nuclei that reflects the correlated nature  
 197 of the dynamics of nucleons within the quantum many-body system. The majority of atomic  
 198 nuclei possess an intrinsic deformation, most of which is an axial quadrupole, or ellipsoidal,  
 199 deformation.

200 Prior relativistic heavy-ion collision measurements from STAR reported strong signatures  
 201 of nuclear deformation using detailed comparisons between Au+Au collisions and U+U col-  
 202 lisions [48]. These measurements suggest that U+U collisions being much more deformed  
 203 in their ground state. Consequently, we can say that these detailed comparisons between  
 204 Au+Au and U+U collisions enabled us to examine the geometry of the colliding nuclei.

205 Recently it has been suggested to examine the geometry of the colliding nuclei using the  
 206 correlation coefficient,  $\rho(v_n^2, [p_T])$  [98, 101, 154, 159, 224, 274];

$$\rho(v_n^2, [p_T]) = \frac{\text{cov}(v_n^2, [p_T])}{\sqrt{\text{Var}(v_n^2)}\sqrt{\text{Var}([p_T])}}, \quad (1)$$

207 which might be more sensitive to the initial-state geometry, because it leverages the correla-  
 208 tion between the eccentricity-driven flow harmonics  $v_n$  and the average transverse momentum  
 209 of particles in an event  $[p_T]$ . The latter is related to the transverse size of the overlap region,  
 210 so events that have similar energy-density but smaller initial-state transverse size should  
 211 have a larger radial expansion and consequently larger mean transverse momentum [99]. It  
 212 has also been proposed that the  $\rho(v_n^2, [p_T])$  correlator is sensitive to the correlations between  
 213 the initial size and the initial-state deformation of colliding nuclei [152, 153].

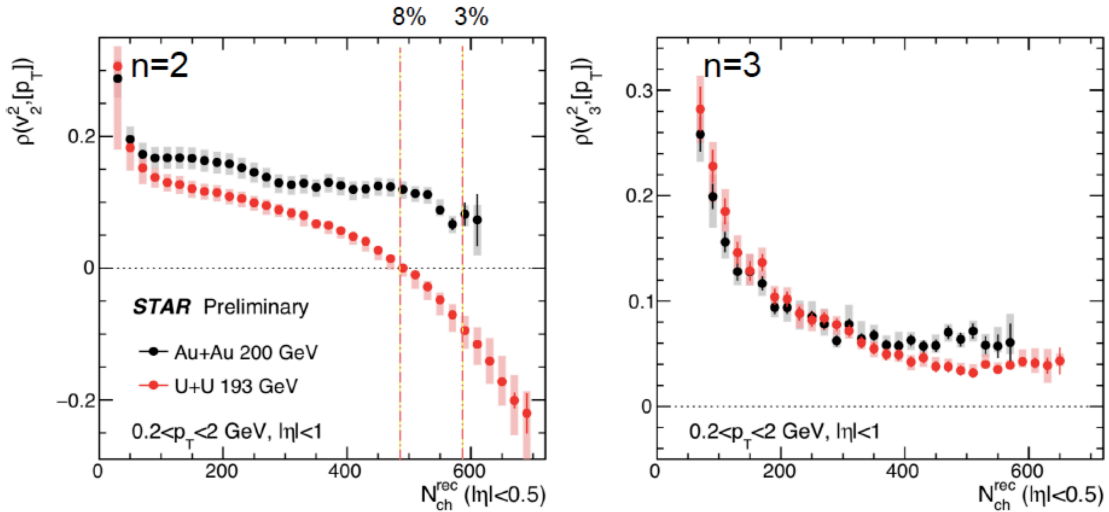


**Figure 3:** The  $N_{ch}$  dependence of the  $\rho(v_2^2, [p_T])$  correlator panel (a) and  $\rho(v_3^2, [p_T])$  correlator panel (b) for U–U at 193 GeV and Au–Au at 200 GeV.

214 Figure 3 presents the  $N_{ch}$  dependence of the  $\rho(v_2^2, [p_T])$  correlator panel (a) and  $\rho(v_3^2, [p_T])$   
 215 correlator panel (b) for U–U at 193 GeV and Au–Au at 200 GeV. Data are shown for

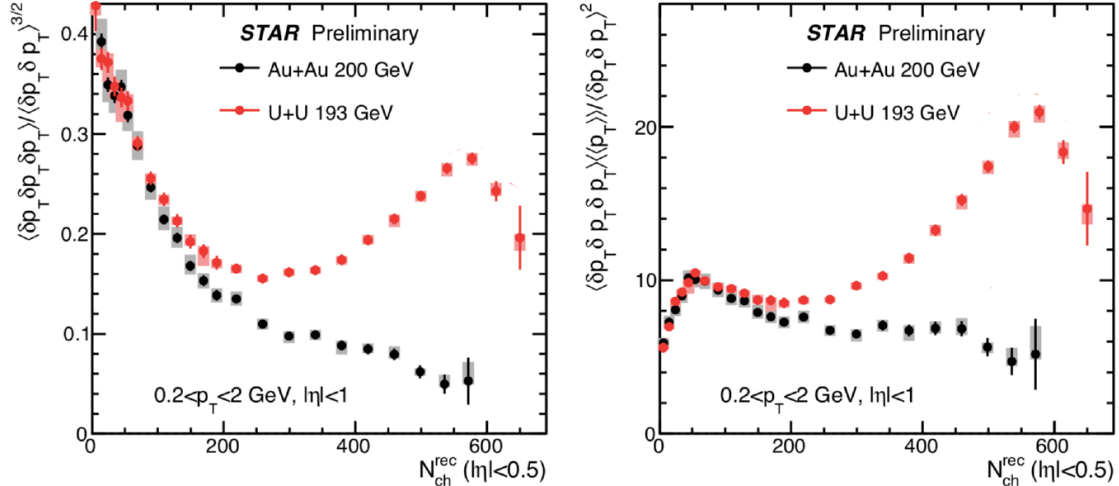


**Figure 4:** The  $N_{ch}$  dependence of the standard skewness panel (a) and intensive skewness panel (b) for U–U at 193 GeV and Au–Au at 200 GeV.

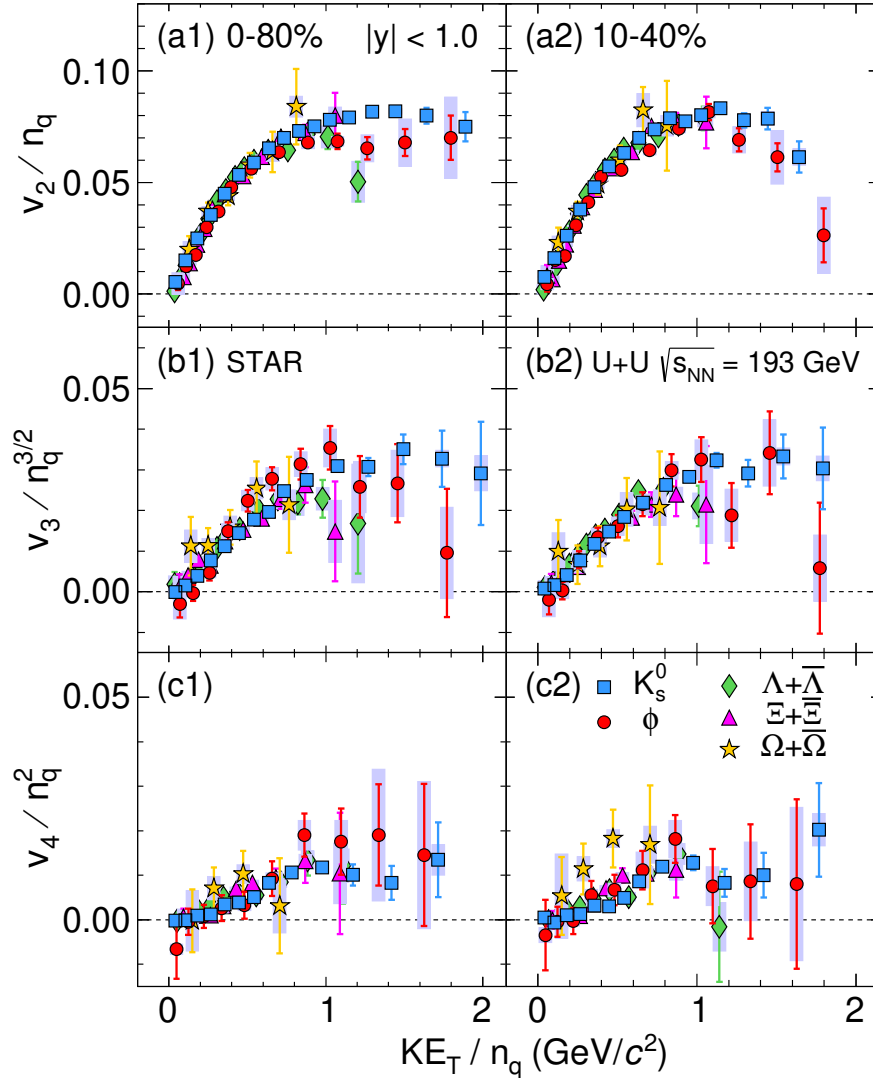
216  $0.2 < p_T < 2.0$  GeV/ $c$  and  $|\eta| < 1.0$ . The presented  $\rho(v_2^2, [p_T])$  measurement is shown to  
 217 be negative in central U+U collisions, while it is positive in central Au+Au collisions. Such  
 218 an effect is compatible with the theoretical expectations [152], and is caused by the prolate  
 219 deformation of  $^{238}\text{U}$  nuclei. Also the  $\rho(v_2^2, [p_T])$  in U+U collisions is lower than in Au+Au  
 220 collisions across essentially the full  $N_{ch}$  range. In panel (b) we present the  $\rho(v_3^2, [p_T])$  that  
 221 shows minor difference between Au+Au and U+U collisions.

222 Also, it had been argued that the  $p_T$  dimensionless skewness depends on the system size  
 223 and shape [155]. The standardized and *intensive* skewness are shown in Fig. 4 for U–U at  
 224 193 GeV and Au–Au at 200 GeV. The presented dimensionless skewness measurement shows  
 225 a nonmonotonic trend for U–U at central collisions. This large difference between U–U and  
 226 Au–Au could be attributed to the deformation of  $^{238}\text{U}$  nuclei.

### 227 Azimuthal anisotropy measurements of strange and multi-strange hadrons in U– 228 U collisions at 193 GeV:

229 Stronger constraints on transport and hydrodynamic model simulations can be achieved  
 230 via investigating the azimuthal anisotropy of identified particles as a function of transverse  
 231 momentum and collision centrality. Also, one can understand the initial conditions in heavy-  
 232 ion collisions via varying the collision system size. This could be achieved by performing  
 233 collisions of Uranium nuclei which have a deformed shape. Uranium nuclei possess a prolate  
 234 shape [266], consequently, there are collision configurations (body-body collisions) in which  
 235 the initial overlap region is not spherical even in central collisions. Moreover, depending  
 236 on the angles of the two colliding Uranium nuclei relative to the reaction plane, several  
 237 other collision configurations of U+U collisions are possible [86, 164, 249]. Studying these  
 238 various collision shapes will provide an additional constrain for the initial conditions in  
 239 models [165, 212, 213].

Recently we reported the results on flow coefficients  $v_n$  ( $n = 2, 3, \text{ and } 4$ ) of  $K_s^0$ ,  $\phi$ ,  $\Lambda$ ,  $\Xi$ , and  $\Omega$  at mid-rapidity ( $|y| < 1.0$ ) in U+U collisions at  $\sqrt{s_{NN}} = 193$  GeV.



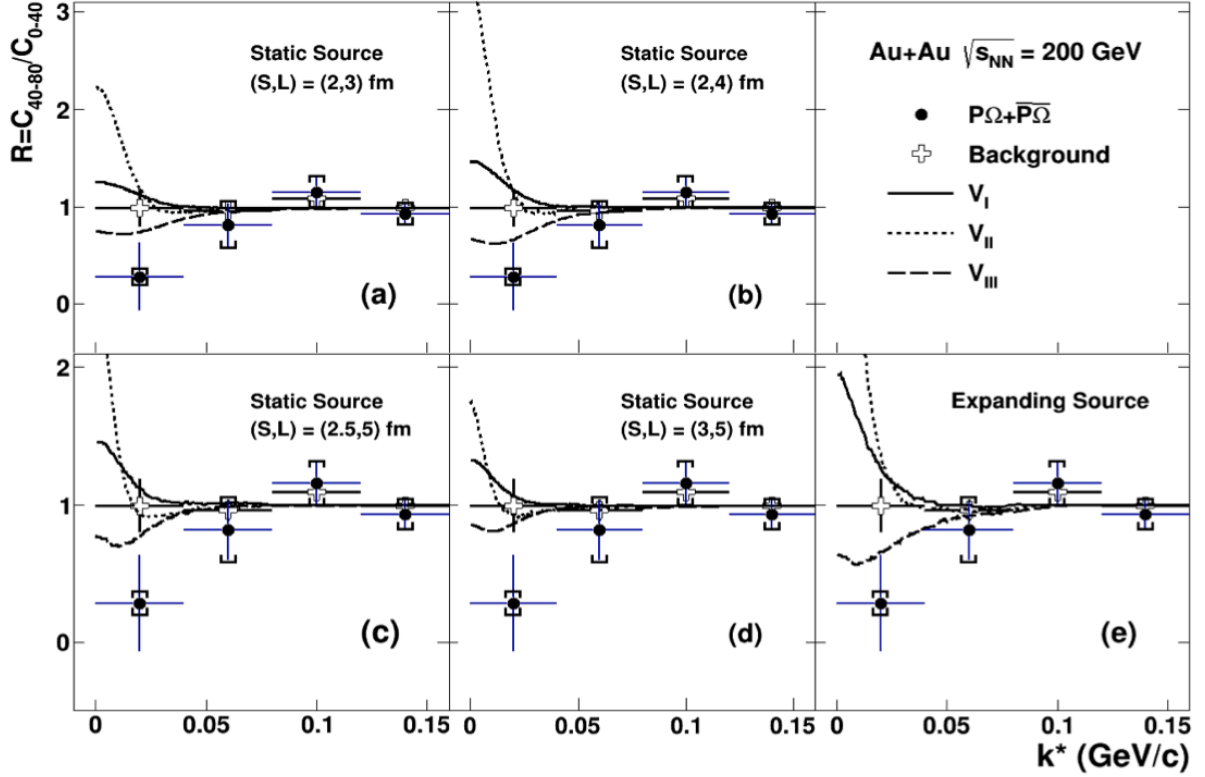
**Figure 5:** Flow coefficients  $v_2$ ,  $v_3$ , and  $v_4$  as a function of transverse kinetic energy  $KE_T/n_q$  for various particles at mid-rapidity ( $|y| < 1$ ) in U+U collisions at  $\sqrt{s_{NN}} = 193$  GeV, scaled by the number of constituent quarks ( $n_q$ ) to the power  $n/2$ . Left panels represent results for minimum bias (0-80%) and right panels for centrality class (10-40%). The error bars represent statistical uncertainties. The bands represent point-by-point systematic uncertainties.

Figure 5 presents the measurements of  $v_n$  coefficients scaled by  $n_q^{n/2}$  as a function of  $KE_T/n_q$ , for strange and multi-strange hadrons in U+U collisions at  $\sqrt{s_{NN}} = 193$  GeV. Our measurements show that the NCQ scaling holds within experimental uncertainties for each harmonic order  $n = 2, 3$  and 4. The  $v_n/n_q^{n/2}$  vs.  $KE_T/n_q$  values lie on a single curve for all the particle species within a  $\pm 15\%$ . The measured NCQ scaling of  $v_n$  coefficients indicates

247 the evolution of partonic collectivity during the QGP phase in heavy-ion collisions. This  
 248 observed scaling also suggests the formation of hadrons through quark coalescence in the  
 249 intermediate  $p_T$  range ( $2.0 \text{ GeV}/c < p_T < 4.0 \text{ GeV}/c$ ) [147, 240]. Although there are consid-  
 250 erable differences between U+U and Au+Au in the collision geometry, the hydrodynamical  
 251 evolution and the coalescence mechanism for hadron formation persist-key features of QGP  
 252 drops formed in nucleus-nucleus collisions.

### 253 **Studies of strong interactions:**

254 The study of nucleon-nucleon ( $NN$ ), nucleon-hyperon ( $NY$ ), and hyperon-hyperon ( $YY$ )  
 255 interactions are fundamental to understand the physics of relativistic heavy-ion collisions,  
 256 neutron stars the existence of various exotic hadrons. A significant amount of  $NN$  scattering  
 257 data allows us to construct precise  $NN$  potential models. However, the limited availability  
 258 of  $NY$  scattering data and no scattering data for the  $YY$  systems creates understanding  
 259 the  $NY$  and  $YY$  potentials complicated and challenging. It has become possible to study  
 260 with Lattice QCD constraints of the strong interactions [301]. Commonly, the experimental  
 261 information on the bound states of strange baryons and nucleons (hypernuclei) is used to  
 262 provide information on  $YY$  interactions [13]. However, the extraction of strong interactions'  
 263 parameters becomes difficult due to, e.g., contaminated by many-body effects. High-energy  
 264 heavy-ion collisions provide a significant number of hyperons in each collision, which provides  
 265 an excellent opportunity to study strong interactions. Measurement of two-particle correla-  
 266 tions at low relative momentum, with the femtoscopy method, has been used to study the  
 267 space-time dynamics of the source created in heavy-ion collisions [50], [21]. In addition to  
 268 this, the measurement of two-particle correlations at low relative momentum can also be used  
 269 to measure final state interactions (FSI) between nucleons and hyperons. A recent study of  
 270 lattice QCD calculations for heavy quark masses shows that the  $N\Omega$  interaction is attractive  
 271 at all distances [302]. Using this  $N\Omega$  interaction, the shape of the two-particle correlation  
 272 function at low relative momentum changes significantly with the strength of the  $N\Omega$  at-  
 273 traction [196]. However, the Coulomb interaction in the  $p\Omega$  channel makes it challenging to  
 274 access the strong interaction parameters directly from the measured two-particle correlation  
 275 function. Therefore, a new measure, namely the ratio of the correlation functions between  
 276 the peripheral (small) and central (large) collision systems, is proposed in [196]. This ratio  
 277 provides direct access to the strong interaction between proton and omega, independent of  
 278 the model used for the emission source. The attractive nature of an  $N\Omega$  interaction leads to  
 279 the possible existence of the  $N\Omega$  dibaryon. Such an  $N\Omega$  dibaryon is the most interesting can-  
 280 didate after the H-dibaryon [173]. Several attempts have been made to estimate the binding  
 281 energy of the  $N\Omega$  state in different QCD-motivated models [302]. The  $N\Omega$  dibaryon can be  
 282 produced in high-energy heavy-ion collisions through the coalescence mechanism [277]. The  
 283 measurement of the  $p\Omega$  correlation function for peripheral and central  $Au-Au$  collisions at  
 284  $\sqrt{s_{NN}} = 200 \text{ GeV}$ , presented in Fig.6, provides insight into the existence of an  $N\Omega$  dibaryon.



**Figure 6:** The solid circle represents the ratio ( $R$ ) of the small system (40-80% collisions) to the large system (0-40% collisions) for proton-omega and  $\bar{p}\Omega$ . The error bars correspond to the statistical errors, and caps correspond to systematic errors. The open crosses represent the ratio for background candidates from the side-band of omega invariant mass. Predictions for the ratio of the small system to the large system for  $p\Omega$  interaction potentials  $V_I$ ,  $V_{II}$  and  $V_{III}$  for static source with different source sizes  $(S, L) = (2,3)$ ,  $(2,4)$ ,  $(2.5, 5)$  and  $(3,5)$  fm, where  $S$  and  $L$  are corresponding to small and large systems, are shown in (a), (b), (c) and (d) respectively. In addition, the prediction for the expanding source is shown in (e) [31].

### 285 1.1.2 pp and Heavy-Ion Jet Measurements

286 The STAR jet program has recently focused on a new generation of measurements that  
 287 are aimed at differentially studying jet production and fragmentation mechanisms in proton-  
 288 proton and heavy-ion collisions. In this section, we highlight recent results on jet substructure  
 289 in p+p collisions along with a measurement of correlations between jet production and the  
 290 underlying event (UE) in proton-Gold (p+Au) collisions. These measurements serve a dual  
 291 purpose in that they help us studying fundamental QCD in comparison with Monte Carlo  
 292 (MC) models and theoretical calculations and as a reference for hot/cold nuclear matter  
 293 effects in heavy ion collisions.

294 **Differential measurements of jet substructure in  $p+p$  collisions:** As jets are compos-  
 295 ite objects built from a parton shower and its fragmentation, they contain rich substructure  
 296 information that can be exploited via jet finding algorithms [233]. These algorithms typically  
 297 employ an iterative clustering procedure that generates a tree-like structure, which upon an  
 298 inversion, gives access to a jet’s substructure at different steps along the cluster tree. The  
 299 most common toolkit for such measurements is SoftDrop grooming [219] which employs a  
 300 Cambridge/Aachen re-clustering of a jet’s constituents and imposes a criterion at each step  
 301 as we walk backwards in the de-clustered tree

$$z_g = \frac{\min(p_{T,1}, p_{T,2})}{p_{T,1} + p_{T,2}} > z_{cut} \left( \frac{R_g}{R_{jet}} \right)^\beta ; R_g = \Delta R(1, 2) \quad (2)$$

302 where  $z_{cut} = 0.1$  is a momentum fraction threshold and  $\beta$  is the angular exponent which in  
 303 our analysis is set to zero [220]. These default values for the parameters make the SoftDrop  
 304 observable comparable to theoretical calculations and at the infinite momentum limit, they  
 305 converge to the DGLAP splitting functions.

306 STAR has recently published jet substructure measurements at the first split [9, 33] for  
 307 jets of varying transverse momenta ( $p_T$ ) and jet radius in p+p collisions at  $\sqrt{s} = 200$  GeV.  
 308 A compilation of the different observables are shown in Figure 7 for  $R = 0.6$  jets with  
 309  $30 < p_{T,jet} < 40$  GeV/c where the data are shown in the filled red star markers and are  
 310 compared to theoretical calculations [188] shown in the shaded gray bands. The red band  
 311 represents the total systematic uncertainty resulting from the variation of the tracking effi-  
 312 ciency, tower energy scale, hadronic correction due to tracks matched with towers and the  
 313 unfolding procedure. The top panels show the SoftDrop observable groomed momentum  
 314 fraction ( $z_g$ , top left) and the groomed jet radius ( $R_g$ , top right) where we see a relatively  
 315 good comparison with the theory prediction which do not include any non-perturbative cor-  
 316 rections. The calculations reproduce the  $z_g$  distribution in data for high  $p_t$ , large-radius jets  
 317 (the publication [33] includes jets of various momenta and radii, and the calculations do not  
 318 reproduce the distributions at lower jet momenta and smaller jet radii) whereas the  $R_g$  have  
 319 significant quantitative differences with the data which can be characterized as a shape func-  
 320 tion due to non-perturbative corrections. The bottom two panels of Figure 7 shows the first  
 321 measurements of the invariant and groomed jet mass for the same jet selections as the top  
 322 panels. The jet mass is sensitive to the virtuality of the jet [231] and is related to both the

323 momentum and the angular scales [189]. The same theoretical calculation severely under-  
 324 predicts the jet mass distributions primarily due to the lack of hadronization corrections and  
 325 the overall small jet scales which lead to large theoretical uncertainties. The grooming pro-  
 326 cedure overall helps in reducing these non-perturbative effects and as a result, the groomed  
 327 jet mass data exhibits a similar level of disagreement as to the groomed jet radius.

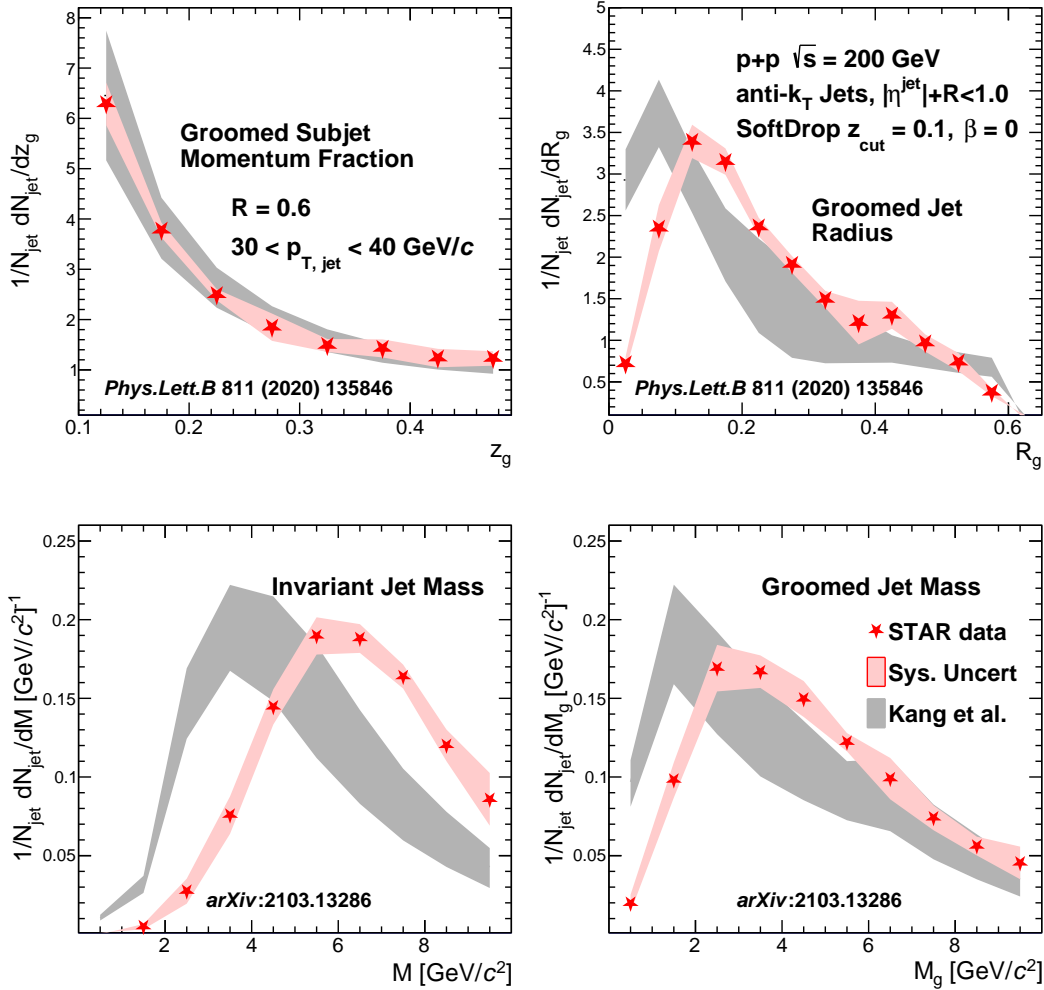


**Figure 7:** Comparisons of the first split SoftDrop groomed subjet momentum fraction  $z_g$  (top left), groomed jet radius  $R_g$  (top right), invariant jet mass  $M$  (bottom left) and the groomed jet mass  $M_g$  (bottom right) shown in the red markers to theoretical calculations in the shaded back regions.

328 These double differential measurements were corrected in both jet  $p_T$  and  $z_g/R_g$  simul-  
 329 taneously and show quite a significant variation in substructure for jets of a particular  $p_T$ .  
 330 STAR has recently measured the correlations between the momentum and angular scales of  
 331 jet substructure at the first split as shown in Figure 8. The jet  $p_T$  increases from the top  
 332 left to the bottom right with each panel containing three sets of data markers represent-  
 333 ing a selection on the groomed jet radius,  $0 < R_g < 0.15$  (blue),  $0.15 < R_g < 0.3$  (red),

334  $0.3 < R_g < 0.4$  (black). The correlations between  $z_g - R_g$  are unfolded via an 2-D iterative  
 335 Bayesian procedure as implemented in the RooUnfold package [64] and followed by a boot-  
 336 strap correction for the jet energy scale. The final results are a first in jet substructure that  
 337 are corrected and presented in 3-D i.e.,  $z_g$  vs  $R_g$  vs  $p_{\text{jet},T}$ .

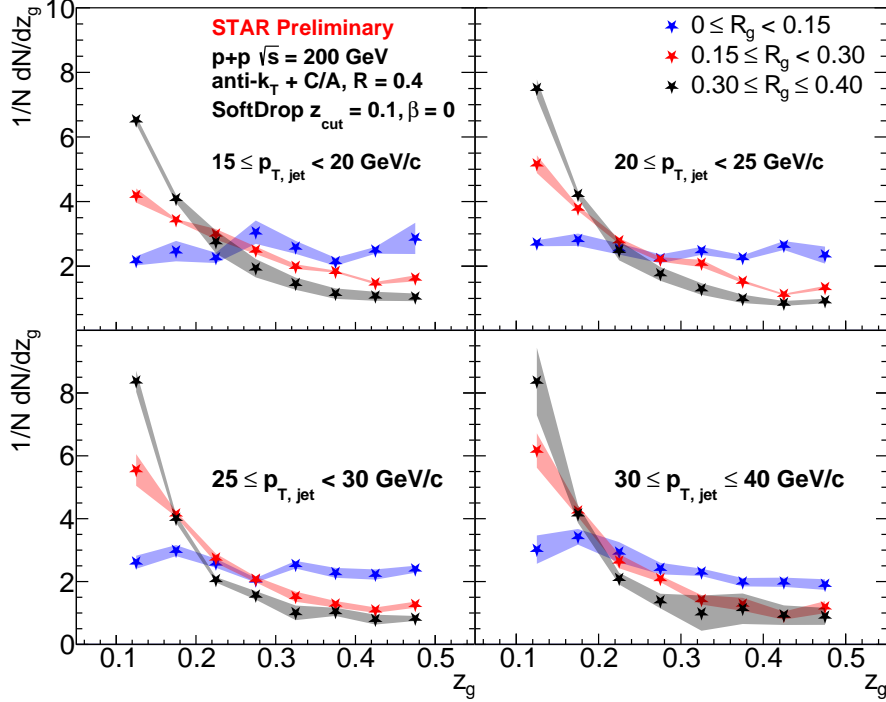


**Figure 8:** Differential measurements of the first split SoftDrop groomed subjet momentum fraction for jets of varying opening angle ( $0 < R_g < 0.15$ ,  $0.15 < R_g < 0.3$ ,  $0.3 < R_g < 0.4$  in the blue, red and black markers) and transverse momenta ( $15 < p_T < 20$  GeV/ $c$  in the top left to  $30 < p_T < 40$  GeV/ $c$  in the bottom right).

338 The data shows a stark modification in the shape of the splitting  $z_g$  as the  $R_g$  is varied  
 339 from small the large angle. Narrow or collinear splits are found to have a symmetric distri-  
 340 bution implying a near equal probability for soft or hard splittings. Wide angle splits on the  
 341 contrary are strongly peaked at small values of  $z_g$  resulting in those splits containing softer  
 342 emissions. The dependence on the jet  $p_T$  is observed to be weak compared to the  $R_g$  which  
 343 essentially drives the  $z_g$  distribution for jets in our kinematics. These measurements signify  
 344 the need of all three observables towards the goal of tagging jets with a unique substructure.

345 Since the jet cluster tree extends beyond a first split, one can iteratively apply the Soft-  
 346 Drop procedure on the hardest surviving branch and measure the jet substructure at each  
 347 split along the de-clustered tree [137]. Such measurements enable a study of the parton  
 348 shower and evolution of both the momentum and angular scales within a jet. Upon applying  
 349 the iterative SoftDrop procedure to the jets studied in this measurements, we reconstruct a  
 350 collection of observables corresponding to the total number of splittings  $n$  and  $z_g^n$  and  $R_g^n$  at

351 each split. We limit our measurement to the first three surviving splits within the jets and  
 352 present the results fully corrected in 3-D corresponding to the jet  $p_T$ ,  $z_g/R_g$ , and the split  
 353 number  $n$ . The detector smearing effects on the  $z_g/R_g, p_T^{\text{jet}}$  are corrected via a 2-D Bayesian  
 354 iterative unfolding via RooUnfold and the splitting hierarchy is corrected by matching the  
 355 splits based on the prong that initiates that particular split at both the particle and detector  
 356 level  $\Delta R_{\text{initiator}} < 0.1$ .

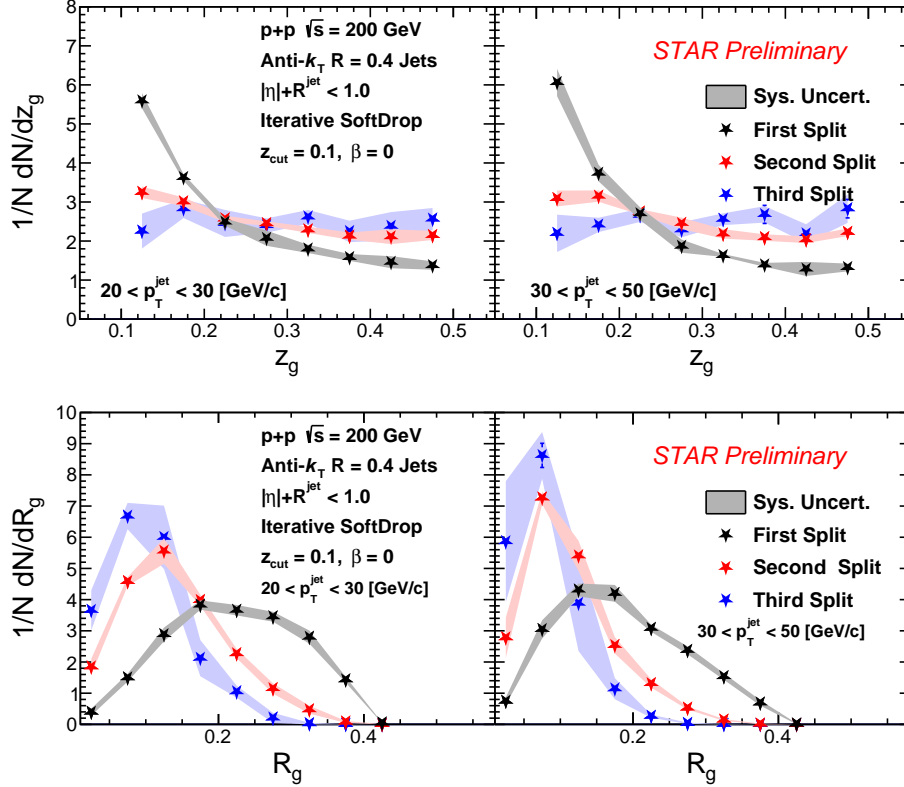


**Figure 9:** Measurements of the iterative SoftDrop splitting observable for the first (black markers), second (red markers) and third (blue markers) splits shown for the  $z_g$  (top panels) and  $R_g$  (bottom panels) observables for two jet momenta selections (left -  $20 < p_T^{\text{jet}} < 30$  and right -  $30 < p_T^{\text{jet}} < 50$  GeV/c).

357 The data are shown in Figure 9 for the first, second and third splits in the black, red and  
 358 blue colored markers, respectively. The corresponding colored shaded regions behind the  
 359 data markers represent total systematic uncertainty resulting from variations in the similar  
 360 sources as shown in Figure 7 with the addition of an extra systematic to the corrected data  
 361 shape based on the split matching criterion varied by  $0.1 \pm 0.025$ . These first measurements  
 362 detail a remarkable feature of substructure evolution along the jet shower where we observe  
 363 a gradual variation in moving from the first to the third splits. The  $R_g$  at a split can also be  
 364 interpreted as the available phase space for subsequent emissions/splits and is also related to  
 365 the virtuality at the split. As the  $R_g$  gets progressively narrower with increasing the split  $n$ ,

366 the shape of the  $z_g$  also changes from being peaked at smaller values i.e asymmetric splitting,  
 367 to a flatter distribution with increased probability for symmetric splits. In comparing the left  
 368 and right panels of Figure 9, a weak dependence on the jet  $p_T$  is observed whilst the phase  
 369 space restrictions, via selecting a split, significantly impacting the substructure observables.

370 These novel multi-dimensional measurements of jet substructure enable a critical compar-  
 371 ison with MC event generators and quantitatively assess the impact of perturbative (parton  
 372 showers) and non-perturbative (hadronization, multi-parton interactions) models and theo-  
 373 retical calculations with small jet and subjet scales that are close to  $\Lambda_{\text{QCD}}$ . With a corrected  
 374 split hierarchy, we now have a measurement separated in the split formation time along a jet  
 375 shower. This technique will be utilized in an upcoming heavy ion measurements in Au+Au  
 376 collisions resulting in a space-time tomography of jet quenching and parton energy loss by  
 377 tagging on jets of a specific substructure.

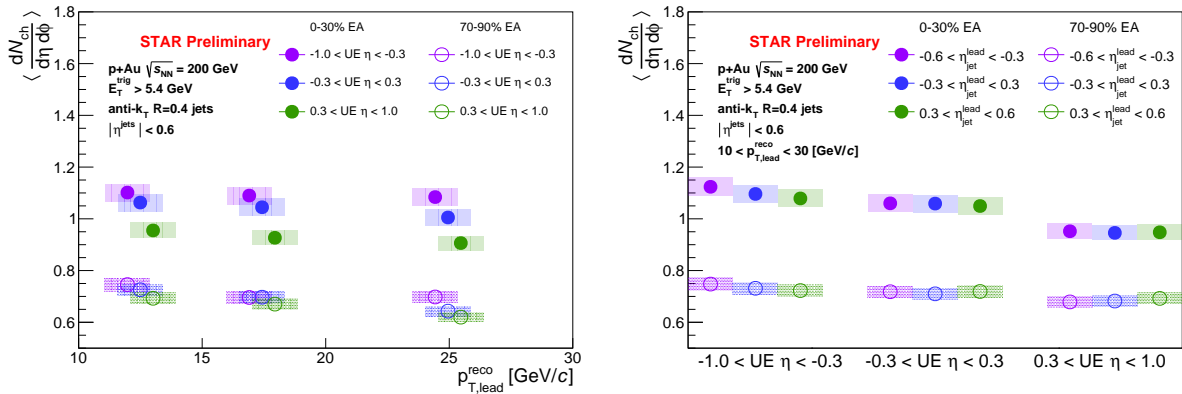


**Figure 10:** Average corrected charged particle multiplicity in the UE in low/high (open/filled symbols) activity p+Au collisions measured differentially as a function of the reconstructed jet momenta (left panel) and the forward, mid and backward rapidity (right panel).

378 **Correlations of the UE and jet production in p+Au collisions:** Jets are originated  
 379 from high- $Q^2$  parton scattering at very early in hadronic collisions. Beside this high- $Q^2$   
 380 process, particles are also produced from the elastic and inelastic scatterings of multiple  
 381 partons from each of the colliding beams. These processes are often described as the non-  
 382 perturbative and non-factorizable in comparison with the jet production and a recent STAR  
 383 measurement [39] of the canonical underlying event vs the jet momenta in p+p collisions  
 384 shows an anti-correlation where the particle multiplicity in the off-axis region [**Nihar: De-**  
 385 **fine off-axis region**] away from the jet decreases as the jet momenta increases. This slight  
 386 negative correlation is understood to be consistent with energy conservation restricting par-  
 387 ticle production in the transverse region as the leading jet becomes more energetic.

388 Asymmetric p+Au collisions offer a natural extension of such measurements where one  
 389 can study the dependence of this anti-correlation on the event activity and the jet rapidity,  
 390 i.e. if the jet is perceived to have come from the Au or p beam. The event activity (EA)  
 391 is defined as the sum of ADC hits in the Au-going inner Beam Beam Counter (east iBBC)

392 located at  $\eta \in [-5, -2]$ . The EA deciles are defined from the EA distribution in minimum  
 393 bias events and high/low EA events are selected as 0–30%/70–90%. The preliminary results  
 394 are shown in Figure 10 where the UE average charged particle multiplicity  $\langle dN_{ch}/d\eta d\phi \rangle$  for  
 395 high/low EA events (filled/open markers) are measured as a function of the leading jet  $p_T$   
 396 (left panel) and the UE  $\eta$  (right panel). The multiplicity is corrected for detector effects  
 397 and the shaded regions represent the systematic uncertainty on the tracking efficiency. Each  
 398 panel also has three different colored markers corresponding to UE  $\eta$  in the left and jet  $\eta$   
 399 in the right panel. These results are not corrected for the jet energy scale and resolution  
 400 which will be included in the final published results. The UE mean multiplicity in p+Au  
 401 collisions have a significant dependence on the EA as expected, with high EA events having  
 402 large multiplicity. We also observe a slight anti-correlation on the jet momenta for the  
 403 proton going direction ( $0.3 < \eta < 1.0$ ), similar to p+p collisions, along with a significant  
 404 dependence on the UE  $\eta$ , especially in high EA events. The Au-going side has relatively  
 405 similar  $\langle dN_{ch}/d\eta d\phi \rangle$  within uncertainties and meaning the UE multiplicity is independent  
 406 on the leading jet  $\eta$ .

407 These results, along with recent STAR preliminary measurements on semi-inclusive jet  
 408 yield in high/low EA p+Au collisions, point to an early time correlation between the high  $Q^2$   
 409 scattering leading to jet production and the low energy processes which result in the forward  
 410 activity. The UE multiplicity shows very little anti-correlation with the jet momenta and is  
 411 currently explored as a selection of event EA for future measurements to reduce the early  
 412 time or long range effects which nominally result from selecting on forward activity.

413 **Isobar Collisions:** The isobar data collected by STAR during Run18 is a high statistics  
 414 minimum bias dataset where the primary goal was to study differences in chiral magnetic  
 415 effects between the colliding species Ru and Zr 1.2. The jet working group in STAR is  
 416 involved in ongoing measurements of energy loss via inclusive charged hadrons suppression  
 417 and semi-inclusive hadron-jet measurements exploiting these high statistics and low pile-  
 418 up data. Isobar data provides a motivation to study energy loss for various system sizes  
 419 in comparisons with Au+Au collisions and also enables an opportunistic study of system  
 420 geometry dependence.

### 421 1.1.3 Heavy-flavor

422 Heavy-flavor (HF) quarks are produced predominately via hard scatterings of partons in  
 423 p(A)+p(A) collisions. Kinematic distributions and hadronization probabilities of HF quarks  
 424 in  $\bar{A}A$  collisions can be different than those in  $pp$  collisions due to interactions of HF quarks  
 425 with the QGP medium. Understanding these differences allows us to determine properties  
 426 of the QGP. STAR has recently published two papers on heavy flavor production: 1) the  
 427 measurement of inclusive  $J/\psi$  polarization in  $pp$  collisions at  $\sqrt{s_{NN}}=200$  GeV [35] and 2)  
 428 observation of  $D_s/D^0$  enhancement in Au+Au collisions at  $\sqrt{s_{NN}} = 200$  GeV [44]. The former  
 429 measures the  $J/\psi$  polarization in  $pp$  collisions with improved precision and over a wider  
 430  $p_T$  range, and thus provides a stricter constraint on quarkonium production mechanisms.  
 431 The latter reveals that the strange-charm meson ( $D_s$ ) yield is significantly enhanced in

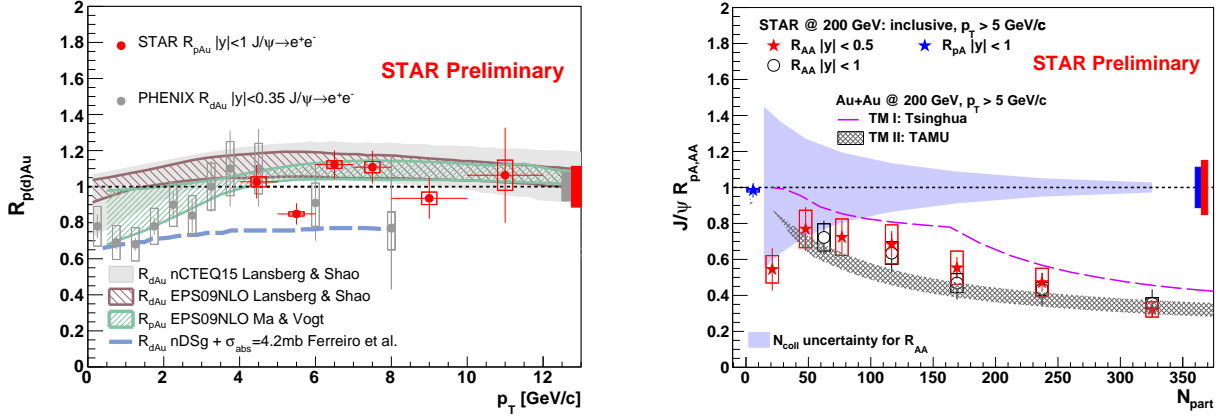


**Figure 11:** Left:  $R_{p(d)Au}$  vs.  $p_T$  for inclusive  $J/\psi$  in p(d)+Au collisions at  $\sqrt{s_{NN}} = 200$  GeV. Red circle: this analysis; grey circle: PHENIX  $R_{dAu}$  in  $|y| < 0.35$  [59]; grey band:  $R_{dAu}$  from nCTEQ15 nuclear PDF sets [218]; brown shadowed:  $R_{dAu}$  from EPS09 NLO nuclear PDF sets [218]; green shadowed:  $R_{pAu}$  from EPS09 NLO nuclear PDF sets [229]; blue dashed line:  $R_{dAu}$  nDSg +  $\sigma_{abs} = 4.2$  mb [145]. Right:  $R_{pAu}$  and  $R_{AA}$  vs.  $N_{part}$ . Blue star: this analysis; red star: STAR  $R_{AA}$   $|y| < 0.5$  [29]; violet dashed line: Tsinghua model [331]; black shadowed: TAMU model [330].

432 Au+Au collisions with respect to that in elementary  $ppe+p/e+e$  collisions and confirms that  
 433 coalescence is an important hadronization mechanism also for charm quarks in heavy-ion  
 434 collisions. Below we describe new results from STAR on inclusive  $J/\psi$  production in p+Au  
 435 collisions at  $\sqrt{s_{NN}} = 200$  GeV and in Au+Au collisions at  $\sqrt{s_{NN}} = 54.4$  GeV.

436  $J/\psi$  production has been found to be suppressed in Au+Au collisions at RHIC top  
 437 energies [29, 52]. Such a suppression can be produced from color screening of the  $c\bar{c}$  potential  
 438 by the QGP medium, and by cold nuclear matter (CNM) effects from e.g., nuclear parton  
 439 distribution functions, energy loss or absorption in the nucleus, and interaction with co-  
 440 moving hadrons. Moreover, in heavy-ion collisions  $J/\psi$  can be produced from recombination  
 441 of uncorrelated  $c$  and  $\bar{c}$  in the QGP. Therefore, in order to precisely determine the suppression  
 442 due to the color screening effect alone, it is important to quantify the CNM effects, and be  
 443 able to disentangle the color-screening and recombination effects.

444 STAR has reported a preliminary result on the nuclear modification factor  $R_{pA}$  for in-  
 445 clusive  $J/\psi$  with  $p_T > 4$  GeV/c and  $|y| < 1$ , as shown in Fig. 11. The result is extracted  
 446 in the dielectron channel from the data collected from  $pp$  and p+Au collisions at  $\sqrt{s_{NN}} =$   
 447 200 GeV in 2015. Compared to previous measurements, this result presents a more precise  
 448 determination of the CNM effects for high- $p_T$  inclusive  $J/\psi$  at the RHIC top energy. The  
 449 measured  $R_{pAu}$  is consistent with unity, suggesting little suppression in this kinematic region  
 450 due to the CNM effects. The result confirms that the color-screen effect is the main cause  
 451 of the large suppression of high- $p_T$  inclusive  $J/\psi$  observed in Au+Au collisions at  $\sqrt{s_{NN}} =$   
 452 200 GeV. These data points provide a stronger constraint on theoretical calculations for  $J/\psi$   
 453 suppression due to the CNM effects and  $J/\psi$  production mechanisms in heavy-ion collisions.

454 STAR has also released at the 2021 Strangeness in Quark Matter conference a new pre-

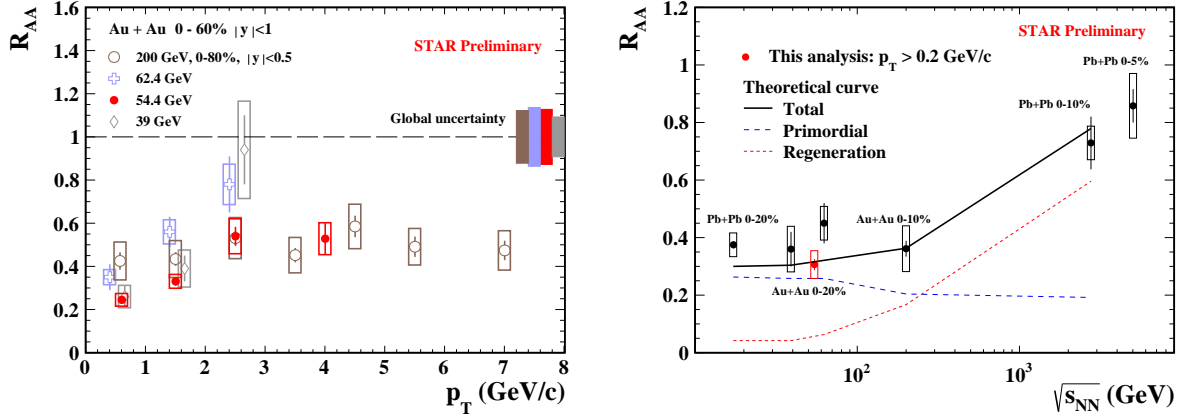


**Figure 12:** Left:  $R_{AA}$  vs.  $p_T$  for inclusive  $J/\psi$  in Au+Au collisions at  $\sqrt{s_{NN}} = 54.4$  GeV (this analysis) and at 39, 62.4 and 200 GeV [52]. Right:  $R_{AA}$  vs.  $\sqrt{s_{NN}}$  for inclusive  $J/\psi$  in Pb+Pb collisions at  $\sqrt{s_{NN}} = 17.2$  GeV [17, 205], 2.76 [15] and 5.02 TeV [85], and in Au+Au collisions at 39, 62.4 and 200 GeV [29, 52].

455 liminary result on the nuclear modification factor  $R_{AA}$  for inclusive  $J/\psi$  in Au+Au collisions  
 456 at  $\sqrt{s_{NN}} = 54.4$  GeV. The result is extracted in the dielectron channel from BES-II data  
 457 collected in 2017. As can be seen in Fig. 12, the measured  $R_{AA}$  at  $\sqrt{s_{NN}} = 54.4$  GeV is  
 458 consistent with those measured at  $\sqrt{s_{NN}} = 39, 62.4$  and 200 GeV [52], suggesting a partial  
 459 cancellation of  $J/\psi$  suppression due to the color-screen effect by  $J/\psi$  produced from recom-  
 460 bination. Indeed, the  $J/\psi$  yields in heavy-ion collisions from SPS [17, 205], RHIC [29, 52] and  
 461 LHC experiments [15, 85] at  $\sqrt{s_{NN}}$  ranging from 17.2 GeV to 5.02 TeV can be described by  
 462 model calculations that incorporate both the color-screening and recombination effects [330].

#### 463 1.1.4 Light Flavor and Ultra-peripheral Collisions

464 The Light Flavor Spectra and Ultra-peripheral Collisions (LFSUPC) physics working group  
 465 is responsible for the measurements of calibrated production yields and spectra in inclusive  
 466 ion-ion collisions, ultra-peripheral collisions, and exclusive p+p collisions.

467 Elastic scattering plays an important role in proton-proton scattering at high energies.  
 468 At the the LHC, for example, it makes up 20% of the total cross section. The  $pp$  elastic and  
 469 total cross sections have been measured at  $pp$  colliders, however there exists a large energy  
 470 gap between the measurements at the ISR and the LHC. The are proton-antiproton data  
 471 from the Tevatron, however these are expected to have differences to the  $pp$  cross sections.  
 472 It is important to fill the gap between the ISR and LHC to constrain the phenomenological  
 473 models and to better understand the differences to the proton-antiproton data. The STAR  
 474 detector was upgrades to include far-forward Roman Pots which were previously used by the  
 475 PP2PP experiment. Figure 13 Shows the STAR results for the elastic, inelastic, and total  
 476 cross sections compared to the world data for both proton-proton and proton-antiproton  
 477 collisions. The STAR results are 200 GeV are in good agreement with the trends of the  
 478 world data and with the COMPETE predictions [38]

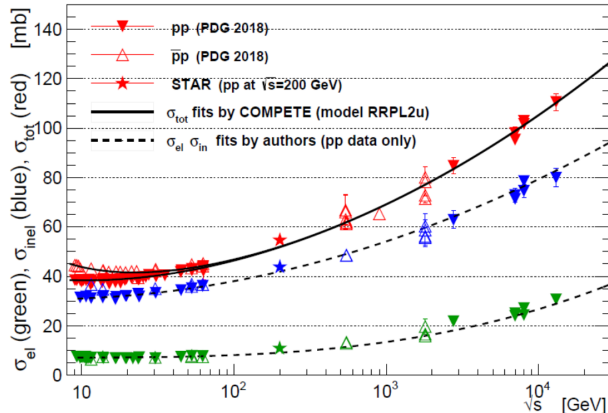


**Figure 13:** Comparison of STAR results on  $\sigma_{tot}$ ,  $\sigma_{inel}$ , and  $\sigma_{el}$  with the world data for data below 1.8 TeV, the Tevatron and the LHC experiments. The COMPETE prediction for  $\sigma_{tot}$  is also shown (solid curve). The dashed curves represent STAR fits to  $\sigma_{inel}$  and  $\sigma_{el}$  using the same function at COMPETE. STAR data were not used in the fit.

479 The first results from the STAR fixed-target program for Au+Au collisions at  $\sqrt{s_{NN}}$   
480 = 3.0 GeV are now becoming available. Figures 14 shows the most advanced analyses  
481 from these data. The left panel of fig. 14 shows the  $\phi/K^-$  ratio as a function of collision  
482 energy. What is striking about this plot is the significant enhancement of the  $\phi$  yield  
483 as compared to that of the charge kaons. The Grand Canonical Ensemble, which assumes  
484 a system of infinite extent, predicts significantly lower relative yields for the  $\phi$  due to its  
485 heavier mass. However in the finite and ephemeral systems created in heavy-ion collisions  
486 near the production threshold, there is a strong tendency for the strange quarks and anti-  
487 quarks to coalesce into a  $\phi$ . This tendency had been previously noted in experiments at  
488 GSI. The recent STAR results provide data for three different centrality ranges, which allows  
489 comparison to the lighter beam-target combinations from GSI, to better constrain the strange  
490 quark coalescence radius. The transport models, UrQMD and SMASH, which include both  
491 resonance decays and the finite size effects, can reasonably describe the  $\phi/K^-$  ratio at this  
492 energy. These results suggest a significant change in the strangeness production mechanisms  
493 at  $\sqrt{s_{NN}} = 3.0$  GeV as compared to that in higher energy collisions. This could shed new  
494 light on the understanding of the QCD Equation of State in the high baryon density regime.

495 The STAR fixed-target program covers the collision energy range where the yields of  
496 hyper-nuclei are expected to be maximized. The hyper-nuclei are understood to be created  
497 via the coalescence of hyperons with neutrons and protons. Although the hyperon yields in-  
498 crease approximately linearly with  $\ln(\sqrt{s_{NN}})$ , due to the stopping of the participant baryons,  
499 the density of neutrons and protons is significantly higher at these lower energies. Thus, the  
500 hyper-nucleus production is expected to be maximized at at  $\sqrt{s_{NN}} = 5$  GeV. The accep-  
501 tance to hyper-nucleus detection is maximized at the lowest fixed-target energies making  
502 this lowest energy fixed-target data set an ideal laboratory for the study of hyper-nuclei.  
503 Even with only a few hundred million Au+Au collisions at  $\sqrt{s_{NN}} = 3$  GeV, as compared to

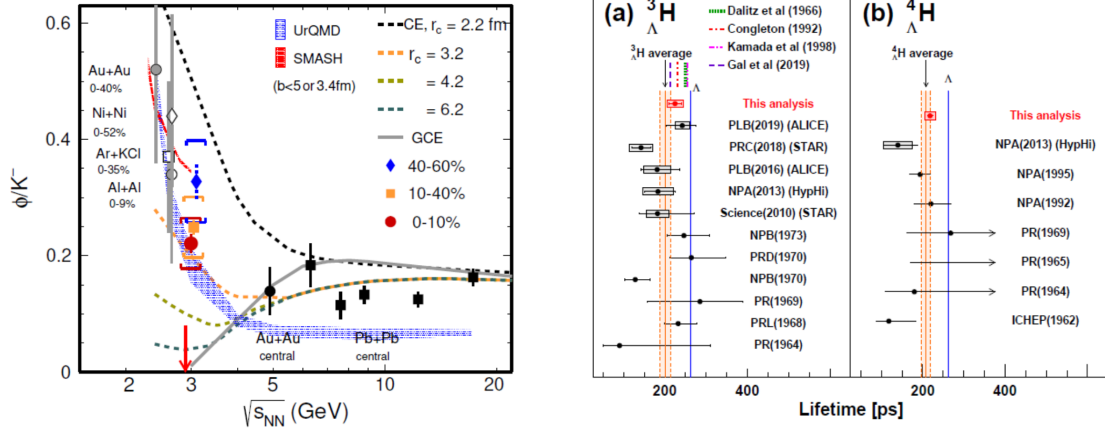


**Figure 14:** (Left)  $\phi/K^-$  ratio as a function of collisions energy  $\sqrt{s_{NN}}$ . The colored data points show the recent STAR measurements in the centrality bins. The red arrow depicts the  $\phi$ -meson production threshold in proton-proton collisions. The grey solid line represents a thermal model based on the Grand Canonical Ensemble (GCE) while the dashed lines represent calculations based on the Canonical Ensemble (CE) with four different parameters of strangeness correlation radius ( $r_c$ ). The blue and red bands show transport model calculations using UrQMD and SMASH respectively. (Right)  ${}^3_{\Lambda}\text{H}$  (a) and  ${}^4_{\Lambda}\text{H}$  (b) measured lifetime compared to previous measurements, model calculations and the free  $\Lambda$  lifetime. The experimental average lifetimes and the corresponding uncertainties of  ${}^3_{\Lambda}\text{H}$  (a) and  ${}^4_{\Lambda}\text{H}$  are also shown as orange bands.

504 the few billion at 200 GeV, we are able to achieve far more significant yields of hyper-nuclei  
505 and reduce the uncertainty on the measurements of their properties. One of the first proper-  
506 ties of interest is the lifetimes of the hyper-nuclei. The question being addressed is whether  
507 incorporating a hyperon within a nucleus stabilizes or de-stabilizes the hyperon, one notes  
508 that neutrons are stabilized when bound within a nucleus. This question has been addressed  
509 both theoretically and experimentally for several decades, as seen in the right panel of fig.  
510 14. The preliminary results from the STAR fixed-target data for the lifetimes of  ${}^3_{\Lambda}\text{H}$  (a) and  
511  ${}^4_{\Lambda}\text{H}$  have the highest precision of any measurement to date conclusively demonstrating the  
512 the lifetimes are significantly smaller than the free  $\Lambda$  lifetime. The  ${}^3_{\Lambda}\text{H}$  lifetime is consistent  
513 with theoretical calculations assuming the  ${}^3_{\Lambda}\text{H}$  is weakly bound state and including pion final  
514 state interactions.

## 515 1.2 CME Search and Isobar Run

### 516 1.2.1 Introduction

517 A decisive experimental test of the Chiral Magnetic Effect (CME) has become one of the  
 518 major scientific goals of the heavy-ion physics program at RHIC. The existence of CME  
 519 will be a leap towards an understanding of the QCD vacuum, establishing a picture of the  
 520 formation of a deconfined medium where chiral symmetry is restored, and will also provide  
 521 unique evidence of the strongest known electromagnetic fields created in relativistic heavy-  
 522 ion collisions [200, 201]. The impact of such a discovery goes beyond the community of  
 523 heavy-ion collisions and will possibly be a milestone in physics. The remaining few years  
 524 of RHIC running and analyses of already collected data probably provide the only chance  
 525 for dedicated CME searches in heavy-ion collisions in the foreseeable future. Significant  
 526 efforts from STAR, as well as other collaborations, have been dedicated towards developing  
 527 methods and observables to isolate possible CME-driven signals from non-CME background  
 528 contributions in measurements of charge separation across the reaction plane. Many clever  
 529 ideas have been proposed and applied to existing data. However, a general consensus is that  
 530 measurements from isobar collisions, Ruthenium+Ruthenium (Ru+Ru) that has 5 – 9%  
 531 higher B-field than Zirconium+Zirconium (Zr+Zr), thus a 10 – 18% larger CME correlation  
 532 signal because of its  $B^2$  dependence, provide the best solution. At the time of writing this  
 533 BUR document, STAR has already produced all the data for the final step of the analysis,  
 534 the two species are separated and the analyzers are running their codes to produce the final  
 535 results. We discuss the steps of blind analysis at length in the following sections.

### 536 1.2.2 Modality of Isobar Running at RHIC

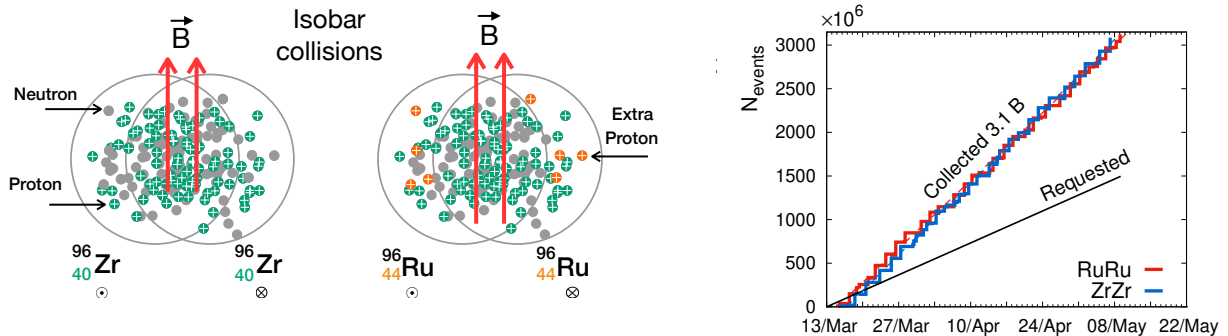


**Figure 15:** Left: Cartoon of the isobar collisions, about 10 – 18% stronger B-field squared is expected in Ru+Ru collisions as compared to Zr+Zr. Right: Summary of the Isobar data collected during Run-18.

537 Colliding isobars, particularly Ru+Ru and Zr+Zr, to make a decisive test of CME was  
 538 proposed by Voloshin in Ref [313], the same paper also proposed to use Uranium collisions

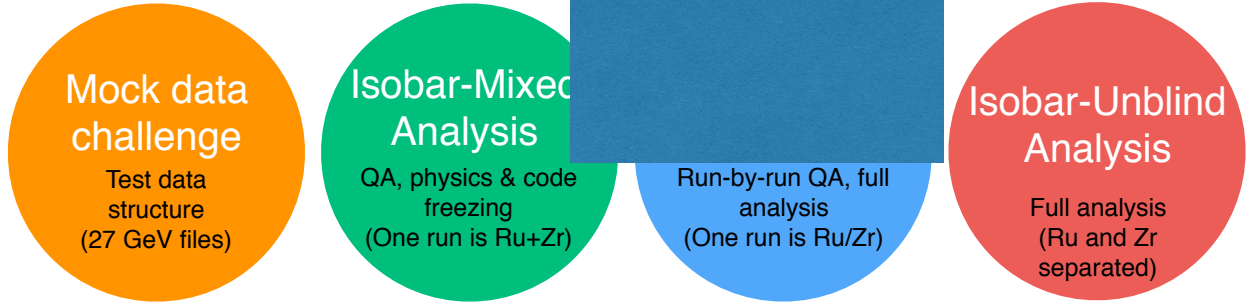


**Figure 16:** Cartoon showing steps of analysis consisting of the mock-data challenge and the three-step isobar blind analysis. This cartoon is based on the procedure for the blind analysis of isobar data that have been outlined in Ref [30]. At the time of writing of this document the two species are separated and analyzers in STAR are running their codes as a part of the last step (shown in red).

539 to disentangle signal and background of CME. The possible difference in the signals relies on  
 540 the 10–18% higher B-field squared in Ru+Ru compared to Zr+Zr, due to four extra protons  
 541 in each Ru nucleus [132], in contrast to about 4% difference in flow driven background [275].  
 542 Such estimates are sensitive to details of the shape, charge distribution and neutron skin  
 543 thickness of the two isobar nuclei [132, 163, 320].

544 In the 2017-18 RHIC BUR [296] STAR proposed to collect data for two 3.5 week periods  
 545 in Run-18. The projection was based on the prospect of achieving five-sigma significance in  
 546 a scenario where the measurement of  $\Delta\gamma$  has 80% non-CME background. This, however,  
 547 relies on the assumption that the systematic uncertainties of the measurements are only a  
 548 few percent, and much smaller than the statistical uncertainty. This started a large scale  
 549 collaboration wide effort in synergy with the RHIC collider accelerator department to plan  
 550 for the isobar running in 2018. Based on the studies of previous years of data from Au+Au  
 551 and U+U collisions several major sources of systematics in the measurement of  $\Delta\gamma$  were  
 552 identified. The major sources include: run-to-run variation of detector response due to loss  
 553 of acceptance, change in efficiency and variation in luminosity that affects the number of  
 554 reconstructed tracks in the TPC. This eventually leads to uncorrectable systematic uncer-  
 555 tainties in  $\Delta\gamma$ , the main observable to measure charge separation across the event plane. In  
 556 order to minimize such systematics a running proposal was developed to: 1) switch species  
 557 between each store and, 2) keep long stores with a level luminosity; aiming for specific rates  
 558 in the coincidence measurements of beam fragments via zero-degree calorimeters. The aim  
 559 was to maintain exact balance of run and detector conditions for the two species so that  
 560 observations in the two systems are equally affected and can later on be largely eliminated  
 561 in the ratios of observables.

### 562 1.2.3 Blinding of Data Sets and Preparation for Analyses

563 The procedure to blind the isobar data was already in place well ahead of the actual data  
 564 taking to limit the access of the data to the analysts to eliminate possible unconscious biases.

565 At the successful conclusion of the isobar run in 2018 STAR had collected more than 3 billion  
566 minimum-bias events for each isobar species. A total of five institutional groups agreed to  
567 perform blind analyses on the data. The analysts from each group will focus on a specific  
568 analysis described in the following section. The substantial overlap of some analyses will  
569 help cross check the results.

570 The details of the blinding procedure and data structure were decided by an analysis  
571 blinding committee (ABC) who are not part of the team of analysts but work in close  
572 collaboration with STAR experts who are part of the production team. The idea is to provide  
573 the analysts access to data where species-specific information are disguised or removed prior  
574 to the final step, shown in red in Fig. 16. Careful consideration is taken by the ABC to make  
575 sure only the essential information to do the analysis-specific quality assurance of the data  
576 is available to the analysts, to ensure the integrity of the CME Isobar analyses. The quality  
577 assurance, calibration and centrality determination work, that require species information,  
578 are done only by STAR experts who are not a part of the blind analysis team.

#### 579 1.2.4 Methods for the Isobar Blind Analyses

580 The detailed procedure for the blind analyses of isobar data have been outlined in Ref [30].  
581 Figure 16 is a cartoon that summarizes the mock-data challenge and three steps of the blind  
582 analysis.

583 The zeroth step shown, in the extreme left of Fig. 16 (orange circle), was the mock-  
584 data challenge; a crucial step to familiarize the analysts with the technicalities of the data  
585 structures that have been specifically designed for blind analysis, and ensure the blinding  
586 worked.

587 The first step shown in Fig. 16 (green circle) as the “isobar-mixed analysis” was truly the  
588 first step of the blind analysis. This was also the most challenging step from the point of  
589 view of the analysts. In this step they were provided with a data sample where each “run”  
590 comprised of events that were a mixed sample of the two species. In this step the analysts  
591 performed the full quality assurance (QA) and physics analysis of the data, documented every  
592 detail of their procedures and froze the codes. After the completion of this step, no changes  
593 to the analysis code or procedures are permissible. The only permissible change in the  
594 following step is to reject bad runs or pile-up events. However, in order to avoid unconscious  
595 bias, such rejections could not be done arbitrarily. Instead, an automated algorithm for bad  
596 run rejection was developed and corresponding codes frozen. The stability of the automated  
597 QA algorithm was tested on existing Au+Au and U+U data.

598 The second step shown in Fig. 16 (blue circle) is referred to as the “isobar-blind analysis”.  
599 For this the analysts were provided with files each of which contained data from a single,  
600 but blinded, species. From this step on-wards, the analysts were only allowed to run their  
601 previously frozen codes. The main purpose of this step was to perform run-by-run QA of  
602 the data. The files each contained a limited number of events that could not lead to any  
603 statistically significant result. Although a pseudo-run-number was used for each file, the  
604 time ordering was preserved with a unique mapping that was unknown to the analysts. It  
605 was important to maintain the time ordering to identify time-dependent changes in detectors

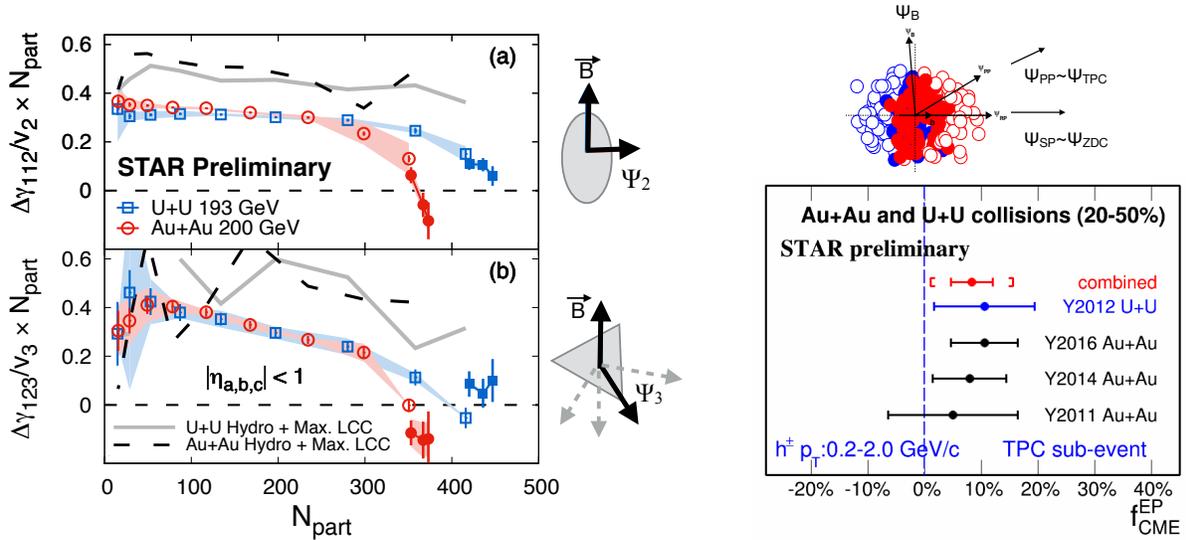


**Figure 17:** (Left) Measurement of charge separation along second and third order event planes in Au+Au and U+U collisions. (Right) Fraction of possible CME signal in the measurement of  $\Delta\gamma$  with respect to spectator and participant planes [328].

606 and run conditions as a part of the run-by-run QA. A similar automated algorithm was also  
 607 used for identifying and rejecting bad runs. After this step no more changes are allowed in  
 608 terms of QA.

609 The final step of isobar blind analysis shown by red circle in Fig. 16 is referred to as  
 610 “isobar-unblind” analysis. In this step, the species information will be revealed and the  
 611 physics results will be produced by the analysts using the previously frozen codes. The  
 612 findings from this step will be directly submitted for publication without alteration. If a  
 613 mistake is found in the analysis code, the erroneous results will also accompany the corrected  
 614 results.

### 615 1.2.5 Observables for Isobar Blind Analyses

616 Isobar blind analysis will specifically focus on the following observables. The general strategy  
 617 is to compare two isobar species to search for a significant difference in whatever observable  
 618 used. The following sections describe these procedures in brief with comments on the out-  
 619 look for isobar blind analysis: 1) measurement of higher order harmonics of  $\gamma$ -correlator, 2)  
 620 exploiting the relative charge separation across participant and spectator planes, 3) differ-  
 621 ential measurements of  $\Delta\gamma$  to identify and quantify backgrounds, 4) the use of R-observable  
 622 to measure charge separation. The first three approaches are based on the aforementioned  
 623 three-particle correlator and the last employs slightly different approaches to quantify charge  
 624 separation. There is also another analysis which will be performed using the signed balance  
 625 function, but this is not part of the blind analyses.

626 **Mixed harmonics measurements with second and third order event planes:**

627 In order to proceed in this section, it is better to rewrite the conventional  $\gamma$ -correlator  
 628 by a more general notation as  $\gamma_{112} = \langle \cos(\phi_a^\alpha + \phi_b^\beta - 2\Psi_2) \rangle$ . The idea is to measure  
 629 charge separations across the third harmonic event plane by constructing a new correla-  
 630 tor  $\Delta\gamma_{123} = \gamma_{123}(OS) - \gamma_{123}(SS)$ , where  $\gamma_{123} = \langle \cos(\phi_a^\alpha + 2\phi_b^\beta - 3\Psi_3) \rangle$  was introduced  
 631 by CMS collaboration in Ref [287]. Since the  $\Psi_3$  plane is random and not correlated to  
 632 B-field direction (see Fig. 17),  $\gamma_{123}$  is purely driven by non-CME background, the contri-  
 633 bution of which should go as  $v_3/N$ . This is very useful to contrast signal and background  
 634 scenarios by comparing measurements in the two isobaric collision systems. Since Ru+Ru  
 635 has larger B-field than Zr+Zr but comparable background, the case for CME would be  
 636 as follows:  $(\Delta\gamma_{112}/v_2)^{\text{Ru+Ru}}/(\Delta\gamma_{112}/v_2)^{\text{Zr+Zr}} > 1$  and  $(\Delta\gamma_{112}/v_2)^{\text{Ru+Ru}}/(\Delta\gamma_{112}/v_2)^{\text{Zr+Zr}} >$   
 637  $(\Delta\gamma_{123}/v_3)^{\text{Ru+Ru}}/(\Delta\gamma_{123}/v_3)^{\text{Zr+Zr}}$ . Fig. 17 (left) shows the measurement of these observables  
 638 in U+U and Au+Au collisions. Within the uncertainties of the measurements, no significant  
 639 difference in the trend of  $\Delta\gamma_{112}/v_2$  and  $\Delta\gamma_{123}/v_3$  is observed for the two collision systems  
 640 except for the very central events. Predictions from hydrodynamic model calculations with  
 641 maximum possible strength of local charge conservation [275] is shown on the same plot.  
 642 Overall observation indicates the backgrounds dominate the measurements and a similar  
 643 analysis of the isobar data is highly anticipated.

644 **Charge separation along participant and spectator planes:** This analysis makes use  
 645 of the fact that the B-field driven signal is more correlated to the spectator plane, in contrast  
 646 to flow-driven backgrounds which are maximal along the participant plane. The idea was  
 647 first introduced in Ref. [321] and later on followed up in Ref. [314]. It requires measurement  
 648 of  $\Delta\gamma$  with respect to the plane of produced particles, a proxy for the participant plane, as  
 649 well as with respect to the plane of spectators. In STAR, the two measurements can be done  
 650 by using  $\Psi_2$  from the TPC and  $\Psi_1$  from the ZDCs, respectively. The approach is based on  
 651 three main assumptions: 1) the measured  $\Delta\gamma$  has contributions from signal and background,  
 652 which can be decomposed as  $\Delta\gamma = \Delta\gamma^{\text{bkg}} + \Delta\gamma^{\text{sig}}$ , 2) the background contribution to  $\Delta\gamma$   
 653 should follow the scaling  $\Delta\gamma^{\text{bkg}}(\text{TPC})/\Delta\gamma^{\text{bkg}}(\text{ZDC}) = v_2(\text{TPC})/v_2(\text{ZDC})$  and, 3) the signal  
 654 contribution to  $\Delta\gamma$  should follow the scaling  $\Delta\gamma^{\text{sig}}(\text{TPC})/\Delta\gamma^{\text{sig}}(\text{ZDC}) = v_2(\text{ZDC})/v_2(\text{TPC})$ .  
 655 The first two have been known to be working assumptions, widely used for a long time and  
 656 can be used to test the case of CME [314] if  $(\Delta\gamma/v_2)(\text{ZDC})/(\Delta\gamma/v_2)(\text{TPC}) > 1$ . The validity  
 657 of the last one was studied and demonstrated in Ref. [321]. Using all three equations one  
 658 can extract [328] the fraction of possible CME signal  $f_{\text{CME}} = \Delta\gamma^{\text{sig}}/\Delta\gamma$  in a fully data-driven  
 659 way as shown in Fig. 17(right). This analysis will be done with the isobar data and the case  
 660 for CME will be  $f_{\text{CME}}^{\text{Ru+Ru}} > f_{\text{CME}}^{\text{Zr+Zr}} > 0$ .

661 **Differential measurements of  $\Delta\gamma$  to identify and quantify background:** *Invariant*  
 662 *mass dependence of charge separation:* Differential measurements of  $\Delta\gamma$  with invariant mass  
 663 and relative pseudorapidity provide interesting prospects to identify and quantify the sources  
 664 of flow and non-flow driven backgrounds. The idea to use invariant mass is simple and was  
 665 first introduced in Ref. [329]. Resonances are widely identified by observing structures in

666 the invariant mass spectra of the decay daughters. Consider a pair of opposite sign pions for  
 667 example, it is known that a large fraction of them come from the neutral resonances that  
 668 show up in the invariant mass spectrum of  $m_{inv}(\pi^+ + \pi^-)$ . If we restrict the analysis to  
 669 pairs of pions, differential measurements of  $\Delta\gamma$  with  $m_{inv}(\pi^+ + \pi^-)$  should also show similar  
 670 peak like structures if background from neutral resonances dominate the charge separation.  
 671 Indeed similar peak structures are observed and an analysis has been performed to extract  
 672 the possible fraction of CME signals from the current measurements [37]. This analysis relies  
 673 on the assumption that CME signals do not show peak like structures in  $m_{inv}(\pi^+ + \pi^-)$  and  
 674 also requires an assumption of  $m_{inv}$  dependence of the CME signal, therefore calls for more  
 675 theoretical insight in this direction have been made.

676 *Relative pseudorapidity dependence:* The relative pseudorapidity dependence of azimuthal  
 677 correlations are widely studied to identify sources of long-range components that are domi-  
 678 nated by early time dynamics as compared to late time correlations that are prevented by  
 679 causality to appear as short-range correlations. The same can be extended to charge depen-  
 680 dent correlations which provide the impetus to explore the dependence of  $\Delta\gamma$  on the pseudo-  
 681 rapidity gap between the charge carrying particles  $\Delta\eta_{ab} = |\eta_a - \eta_b|$  in  $\langle \cos(\phi_a^\alpha + \phi_b^\beta - 2\Psi_{RP}) \rangle$ .  
 682 Such measurements have been performed in STAR with Au+Au and U+U data. It turns  
 683 out that the possible sources of short-range correlations due to photon conversion to  $e^+ - e^-$ ,  
 684 HBT and Coulomb effects can be identified and described as Gaussian peaks at small  $\Delta\eta_{ab}$ ,  
 685 the width and magnitude of which strongly depend on centrality and system size. Going to  
 686 more peripheral centrality bins, it becomes harder and harder to identify such components  
 687 as they overlap with sources of di-jets fragmentation that dominates both same-sign and  
 688 opposite sign correlations. An effort to decompose different components of  $\Delta\gamma$  via study of  
 689  $\Delta\eta_{ab}$  can be challenging although a clear sign of different sources of correlations are visible in  
 690 change of shape of individual same-sign and opposite sign measurements of  $\gamma$ -correlator [307].

691 In any case, these differential measurements of  $\Delta\gamma$  in isobar collisions provide the prospect  
 692 to extract the  $m_{inv}(\pi^+ + \pi^-)$  and  $\Delta\eta$  dependence of CME signals that will provide much  
 693 deeper insights on the origin of the effect. Comparing the differential measurements in  
 694 Ru+Ru and Zr+Zr it will be possible to extract the invariant mass and the relative pseu-  
 695 dorapidity distribution of the CME signal that will provide deeper insight into the origin of  
 696 the phenomenon.

697 **Alternate measure: The novel R-observable:** The  $R$ -observable is actually a dis-  
 698 tribution, introduced in Ref. [230], and defined as the ratio of two distribution functions  
 699 of the quantity  $\Delta S$  parallel and perpendicular to B-field direction defined as  $R_{\Psi_m}(\Delta S) =$   
 700  $C_{\Psi_m}(\Delta S)/C_{\Psi_m}^\perp(\Delta S)$ . Here  $\Delta S$  measures the difference in the dipole moment of the positive  
 701 and negative charge in an event (see Ref. [230] for details). The shape of  $R_{\Psi_2}(\Delta S)$  will  
 702 be sensitive to CME as well as non-CME background. Model calculations have established  
 703 several unique features of this observable: 1) presence of CME signal will lead to a concave  
 704 shape of the  $R_{\Psi_2}(\Delta S)$ , 2) increasing strength of CME signal will increase the concavity of  
 705  $R_{\Psi_2}(\Delta S)$ . In the original paper [230] a second correlator  $R_{\Psi_3}(\Delta S)$  was proposed which  
 706 will measure charge separation purely driven by non-CME background and may serves as

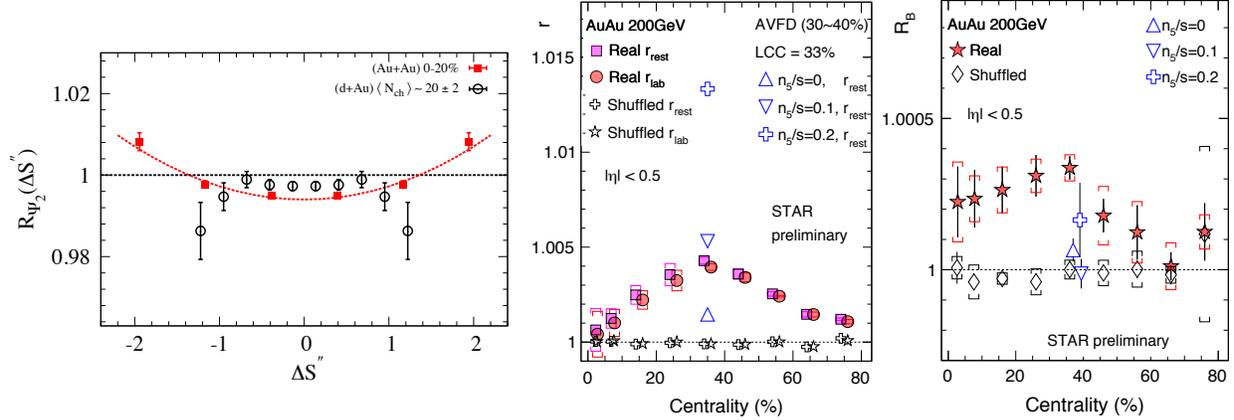


**Figure 18:** (Left) The R-observable shown for different collision systems, a concave shape is consistent with CME expectation [32]. (Right) The two main quantities  $r$  and  $R_B$  derived from the signed balance function, deviation from unity is consistent with CME expectations [225].

707 a baseline. However, recent investigation has shown that due to symmetry properties of  
 708 harmonics in R-variable, the results for  $R_{\Psi_3}(\Delta S)$  correlator may be difficult to interpret and  
 709 require further studies. Therefore, ongoing and future experimental studies from STAR will  
 710 focus only on  $R_{\Psi_2}$

711 The measurement of  $R_{\Psi_2}$  is shown in Fig.18. The quantity  $\Delta S''$  shown is a slight variant of  
 712 ( $\Delta S$ ) that incorporates correction for particle number fluctuations and event plane resolution.  
 713 The observation of Fig.18 indicates more concave shape for  $R_{\Psi_2}$  in Au+Au whereas flat or  
 714 convex shapes for  $p/d$ +Au indicates that the measurements are consistent with expectations  
 715 of CME [32]. For isobar collisions, the case of CME will be confirmed if: a concave shape is  
 716 observed for the ratio of the observables  $R_{\Psi_2}(\Delta S)^{Ru+Ru}/R_{\Psi_2}(\Delta S)^{Zr+Zr}$ .

717 **Alternate measure: The signed Balance function:** A very recently proposed ob-  
 718 servable to search for CME via the signed balance function (SBF) [303]. The idea is to  
 719 account for the ordering of the momentum of charged pairs measured by the width of SBF  
 720 that is expected to be different for out-of-plane as compared to in-plane measurement cap-  
 721 tured in the ratio  $r_{lab}$ . In addition, one can also account for the boost due to collective  
 722 expansion of the system that forces all pairs to move in the same direction and measure the  
 723 ratio in pair rest frame  $r_{rest}$ . In the presence of CME, the individual ratios, as well as the  
 724 double ratio  $R_B = r_{rest}/r_{lab}$ , are expected to be greater than unity. Preliminary measure-  
 725 ments, shown in Fig. 18 (right), from STAR in Au+Au 200 GeV data seem to be consistent  
 726 with CME expectation. This observable will be studied with the isobar data but not as a  
 727 part of the blind analysis. The CME expectation is: 1)  $r(Ru + Ru) > r(Zr + Zr)$ , and 2)  
 728  $R_B(Ru + Ru) > R_B(Zr + Zr)$ .

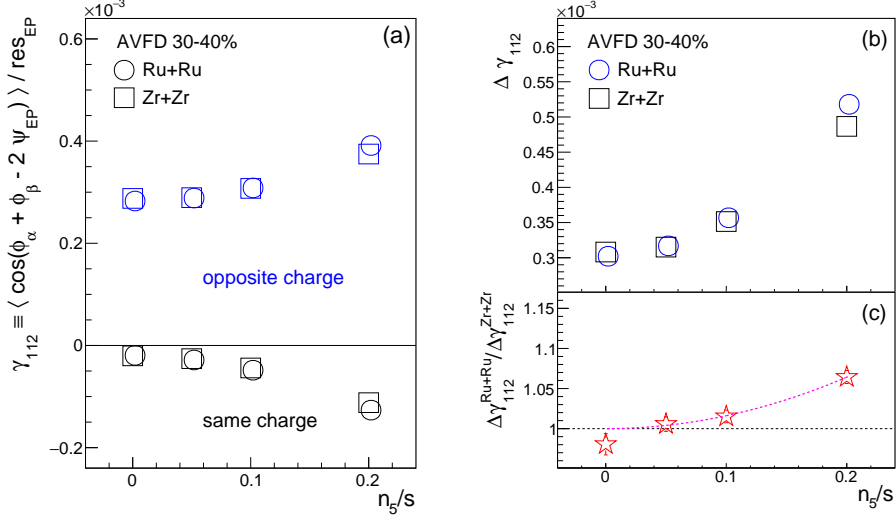
### 1.2.6 Benchmarking CME Observables Against EBE-AVFD Model

As the STAR Collaboration is analyzing the data from isobaric collisions with multiple CME observables, it is desirable to have a controlled study on observables so that their relative performance can be understood and calibrated. This will serve as an important reference point when interpreting isobaric data. In this section, we present a benchmark study for three CME observables, namely, the inclusive  $\gamma$  correlator [311], the  $R$  correlator [72, 230] and the signed balance functions [303]. The first two observables are included in STAR's blind-analysis, for which the study was conducted with frozen code that was checked into STAR official repository as part of blinding procedure. The last one is not part of blind-analysis, but it has intrinsic connections [118] with the other two thus it is also presented here for completeness. For a full version of this study, please refer to [118].

The model used in this study is event-by-event anomalous-viscous fluid dynamics (EBE-AVFD) model [184, 281, 282]. It implements the anomalous transport current from CME into fluid dynamics framework to simulate the evolution of fermion currents on an event-by-event basis and to evaluate the resulting charge separation in QGP, on top of the neutral bulk background described by the VISH2+1 hydrodynamic simulations [295] with Monte-Carlo Glauber initial conditions, followed by a URQMD hadron cascade stage [89, 95]. This new tool allows one to quantitatively and systematically investigate the CME signal and account for the resonance contributions.

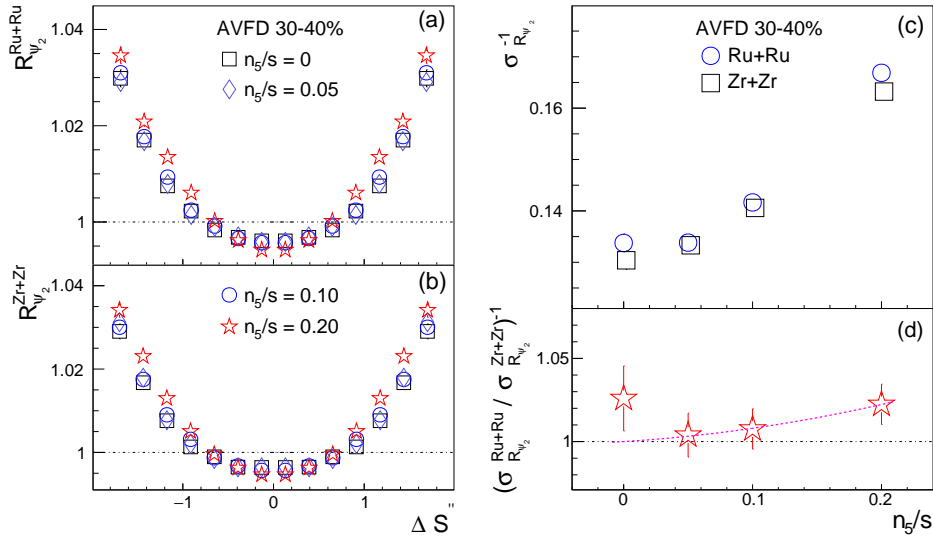
For each of the two isobaric collision systems, Ru+Ru and Zr+Zr at  $\sqrt{s_{NN}} = 200$  GeV, four cases of the EBE-AVFD events have been generated, with  $n_5/s = 0, 0.05, 0.1, \text{ and } 0.2$ , respectively. Here  $n_5$  is the initial axial charge density and  $s$  is the entropy density. A strong CME effect is expected when  $n_5/s$  is large. The centrality selection for all the cases focuses on 30-40% central collisions, where the potential CME signal is relatively easy to detect owing to good event plane resolutions. 200 million events are produced for each case of  $n_5/s = 0$  and  $n_5/s = 0.2$ , and 400 million events for each of the rest two cases. To mimic the detection performance of the STAR Time Projection Chamber, the simulated particles in the EBE-AVFD events are randomly rejected according to a transverse-momentum dependent tracking efficiency.

Figure 19 presents the EBE-AVFD calculations of  $\gamma_{112}^{\text{OS(SS)}}$  (a) and  $\Delta\gamma_{112}$  (b) as functions of  $n_5/s$  for 30-40% isobaric collisions at  $\sqrt{s_{NN}}=200$  GeV. The ratios of  $\Delta\gamma_{112}$  between Ru+Ru and Zr+Zr is delineated in panels (c). At each  $n_5/s$  value,  $\gamma_{112}^{\text{OS}}$  remains positive and  $\gamma_{112}^{\text{SS}}$  stays negative, both with larger magnitudes at higher  $n_5/s$ . Although the CME expects  $\gamma_{112}^{\text{OS}}$  and  $\gamma_{112}^{\text{SS}}$  to be symmetric around zero, there exist some charge-independent backgrounds such as momentum conservation and elliptic flow that shift both  $\gamma_{112}^{\text{OS}}$  and  $\gamma_{112}^{\text{SS}}$  up or down. Therefore, we shall focus on  $\Delta\gamma_{112}$ , which shows a finite background contribution at  $n_5/s = 0$  and increases with the CME signal. The difference between Ru+Ru and Zr+Zr is better viewed with the ratio of  $\Delta\gamma_{112}^{\text{Ru+Ru}}/\Delta\gamma_{112}^{\text{Zr+Zr}}$ . This ratio is consistent with unity at  $n_5/s = 0$ , and increases quadratically with  $n_5/s$  as demonstrated by the 2<sup>nd</sup>-order-polynomial fit function that passes (0, 1) (dashed line). The quadratically-increasing trend is expected, because this ratio is a linear function of the CME signal fraction in  $\Delta\gamma_{112}$  in a two-component perturbative framework [131], and the latter is proportional to  $(n_5/s)^2$  or  $a_1^2$ . The significance values of



**Figure 19:** EBE-AVFD calculations of  $\gamma_{112}^{\text{OS(SS)}}$  (a) and  $\Delta\gamma_{112}$  (b) as functions of  $n_5/s$  for 30-40% isobaric collisions at  $\sqrt{s_{\text{NN}}} = 200$  GeV, together with the ratio of  $\Delta\gamma_{112}$  (c) between Ru+Ru and Zr+Zr. In panel (c), the 2<sup>nd</sup>-order-polynomial fit function illustrates the rising trend starting from (0, 1).

771 the  $\Delta\gamma_{112}^{\text{Ru+Ru}}/\Delta\gamma_{112}^{\text{Zr+Zr}}$  ratio, along with other ratios to be discussed, are stored in Table 4.



**Figure 20:** Distributions of  $R(\Delta S''_2)$  from EBE-AVFD events of 30-40% Ru+Ru (a) and Zr+Zr (b) at 200 GeV with different  $n_5/s$  inputs. Panel (c) depicts  $\sigma_{R2}^{-1}$  vs  $n_5/s$ , extracted from panels (a) and (b), and the  $\sigma_{R2}^{-1}$  ratios between Ru+Ru and Zr+Zr are shown in panel (d), where the 2<sup>nd</sup>-order-polynomial fit function shows the rising trend starting from (0, 1).

772

**Table 4:** The statistical significance of  $(O^{\text{Ru+Ru}}/O^{\text{Zr+Zr}} - 1)$  for different experimental observables.  $N_{\text{event}}$  is the number of events used for each isobaric system of 30-40% centrality in the simulation. See [118] for discussions on observables that are listed but not discussed in this document.

$n_5/s$	$N_{\text{event}}$	$\Delta\gamma_{112}$	$\Delta\delta$	$\kappa_{112}$	$r_{\text{lab}}$	$\sigma_{R2}^{-1}$
0	$2 \times 10^8$	-1.50	-2.89	-1.21	-0.77	1.33
0.05	$4 \times 10^8$	0.62	-6.16	1.37	0.47	0.29
0.10	$4 \times 10^8$	1.91	-16.81	3.43	3.11	0.62
0.20	$2 \times 10^8$	7.73	-42.96	14.07	5.96	1.84

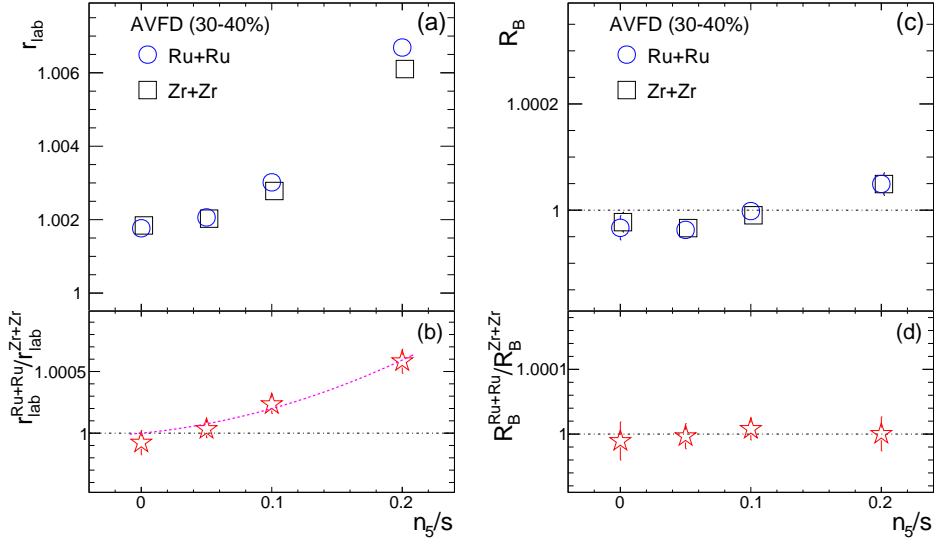


**Figure 21:**  $r_{\text{lab}}$  (a) and  $R_B$  (c) as function of  $n_5/s$  from the EBE-AVFD model for 30-40% Ru+Ru and Zr+Zr collisions at  $\sqrt{s_{\text{NN}}} = 200$  GeV, with their ratios between Ru+Ru and Zr+Zr in panels (b) and (d), respectively. In panel (b), the 2<sup>nd</sup>-order-polynomial fit function demonstrates the rising trend starting from (0, 1).

773 A similar frozen-code analysis is performed for the  $R(\Delta S_2)$  correlator, and the results  
774 are presented in Figure 20. Panels (a) and (b) show the  $R(\Delta S_2'')$  [230] distributions from  
775 EBE-AVFD events of 30-40% Ru+Ru and Zr+Zr collisions, respectively, at  $\sqrt{s_{\text{NN}}} = 200$   
776 GeV with different  $n_5/s$  inputs. As  $n_5/s$  increases, the  $R(\Delta S_2'')$  distribution becomes more  
777 concave, qualitatively representing more CME contributions. To quantify the distribution  
778 shape, the Gaussian width ( $\sigma_{R2}$ ) is obtained by fitting each  $R(\Delta S_2'')$  distribution with an  
779 inverse Gaussian function, and the resultant  $\sigma_{R2}^{-1}$  values are depicted in panel (c), increasing  
780 with  $n_5/s$ . The  $\sigma_{R2}^{-1}$  ratios between Ru+Ru and Zr+Zr are shown in panel (d). We fit the  
781  $\sigma_{R2}^{-1}$  ratios with a 2<sup>nd</sup>-order polynomial function starting from (0, 1).

782 Figure 21 presents the sensitivity study for the signed balance functions. This approach  
783 is not part of the STAR blind analysis, but follows the same procedure as used in the Quark  
784 Matter 2019 Conference proceedings [225]. The observables  $r_{\text{lab}}$  and  $R_B$  [303] are exhibited  
785 in panels (a) and (c) as function of  $n_5/s$  from the EBE-AVFD model for 30-40% Ru+Ru

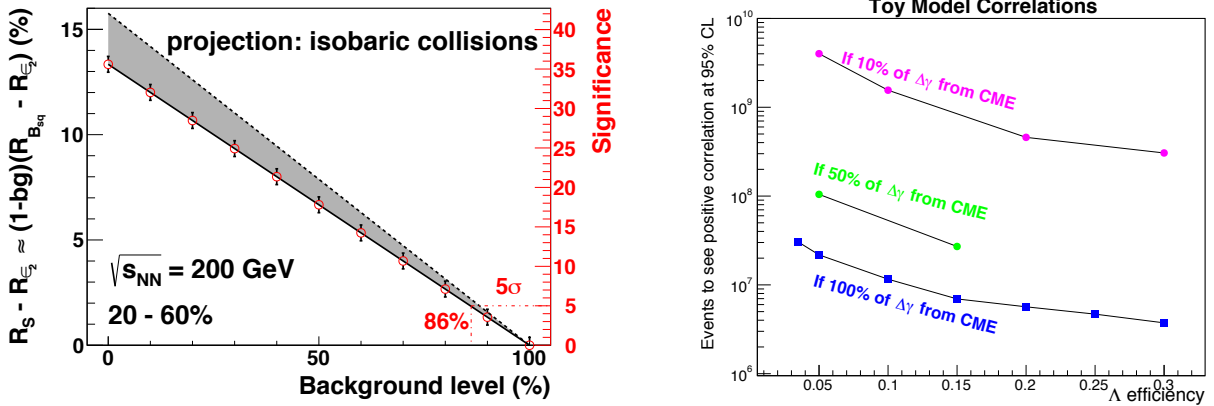


**Figure 22:** (Left) Projection plot taken from a previous beam user request document [296] indicating the anticipated significance in the measurement of charge separation as a function of the CME signal fraction prepared using 2.5 B simulated events. (Right) Estimation of the number of events required to see positive correlation between net  $\Lambda$  helicity with out-of-plane charge separation sensitive to local parity violation at 95% confidence level, plotted against the efficiency of  $\Lambda(\bar{\Lambda})$  reconstruction (see [146] for details).

786 and Zr+Zr collisions at  $\sqrt{s_{NN}} = 200$  GeV. The corresponding ratios between Ru+Ru and  
 787 Zr+Zr are shown in panels (b) and (d), respectively.  $r_{lab}$  increases with the CME signal  
 788 in each isobaric collision. The  $r_{lab}$  ratio between the two systems should roughly obey a  
 789 2<sup>nd</sup>-order polynomial function that starts from (0, 1). This relation is demonstrated with  
 790 the corresponding fit in Fig. 21(b). Panel (d) does not show a clear trend for the ratio of  
 791  $R_B^{Ru+Ru}/R_B^{Zr+Zr}$ , which is not a complete surprise:  $R_B$  looks for a higher-order effect in the  
 792 difference between  $r_{lab}$  and  $r_{rest}$ , and thus requires much more statistics than  $r_{lab}$ .

793 To summarize for this section, in this study [118], we have established the relation between  
 794 these methods via analytical derivation, and employed both simple Monte Carlo simulations  
 795 and the EBE-AVFD model to verify the equivalence between the kernel components of these  
 796 observables (not shown in this document). Our study supports the assumption that the CME  
 797 signal and the background contributions can be linearly added up in such kernel components.  
 798 We have extracted their sensitivities to the difference between Ru+Ru and Zr+Zr collisions  
 799 at  $\sqrt{s_{NN}} = 200$  GeV from 30-40% central events generated by EBE-AVFD.  $\Delta\delta$  and  $\kappa_{112}$   
 800 may render better sensitivities than other observables, which could be a model-dependent  
 801 feature instead of a universal truth, and needs to be further scrutinized by data. The same  
 802 significance level has been corroborated for  $\Delta\gamma_{112}$ ,  $r_{lab}$  and  $\sigma_{R2}^{-1}$ , if put on an equal footing. In  
 803 the implementation of the STAR frozen codes, slight differences in the kinematic cuts cause  
 804 the apparently worse sensitivity of  $\sigma_{R2}^{-1}$  than the other observables. This study provides a  
 805 reference point to gauge the STAR isobaric-collision data.

### 1.2.7 Prospect of CME Search Beyond the Isobar-era

It is important to discuss the strategy for CME search beyond the isobar-era. While it is true that such a strategy needs to be finalized based on the outcome of the isobar program, we would like to get started by considering two possible scenarios at top RHIC energy: 1) isobar program results in a significance of  $3\sigma$  and below, 2) isobar program results in a significance of  $3\sigma$  and above.

In the first scenario one can infer from the projection plot of Fig. 22 that the upper limit of the fraction of CME signal should be less than or equal to 8%. Under such a scenario can STAR perform a follow up measurement to achieve a decisive  $5\sigma$  significance and establish a conclusive evidence of CME? It turns out such a measurement is possible even with a single Au+Au 200 GeV data set during the year 2023 running of STAR concurrently with sPHENIX. Current CME related analyses of the aforementioned Au+Au 200 GeV extraction using elliptic flow and charge separation with respect to spectator and participant planes yields 4% statistical uncertainty with 2.4 B events ( $2 - 3\sigma$  significance). In order to get  $5\sigma$  significance with the same analysis one needs to have a statistical uncertainty of order 1.6% which would require about  $(4/1.6)^2 \times 2.4 = 15$  Billion events. Therefore, as per the previous estimates of anticipated 10 Billion events that can be collected by STAR during Run-23, one can achieve about  $4\sigma$  significance on the upper limit of a possible CME signal fraction in the measurement of charge separation. This estimate does not account for two important facts that can lead to higher significance and a decisive measurement. The first is that the magnitude of the projected B-field on the reaction plane is higher in Au+Au collisions as compared to isobar collisions. The second one is that the iTPC upgrade enhances the charge particle multiplicity by 50% and therefore triplet ( $\sim dN/d\eta^3$ ) (pair  $\sim dN/d\eta^2$ ) statistics by a factor of 3.4 (2.3). So the final conclusion is that even if isobar program results in a  $3\sigma$  measurement running STAR in 2023 will result in a  $> 4\sigma$  measurement. This conclusion assumes that the systematic uncertainty can be controlled to be smaller than the statistical uncertainty, i.e. below 2%.

For the second scenario ( $> 3\sigma$  measurement from isobar program) we will also be able to establish an upper limit of the fraction of CME signal. For example, in Fig. 22 we see that a  $5\sigma$  significance will establish 13% CME signal and a discovery of the CME phenomenon in heavy-ion collisions. The impact of such a discovery will be a significant milestone. Running STAR in 2023 concurrently with sPHENIX would be essential to perform dedicated precision measurements to further investigate and characterize the phenomenon.

A topic that may be addressed with future data is event-by-event correlations between CME charge separation and other parity-odd features of the event. One such analysis is motivated by the idea that the local parity violation (characterized in each event by a net topological charge  $Q$ ) that is expected to work with the spectator-produced magnetic field to give the CME should also cause a net helicity of  $\Lambda(\bar{\Lambda})$  with the same handedness in each event as the charge separation relative to the B-field.

We are looking for evidence of an event-by-event correlation between these two parity-odd effects as suggested in [146]. To do this, we first need to measure the charge separation with respect to the first-order reaction plane in each event which we can characterize by the

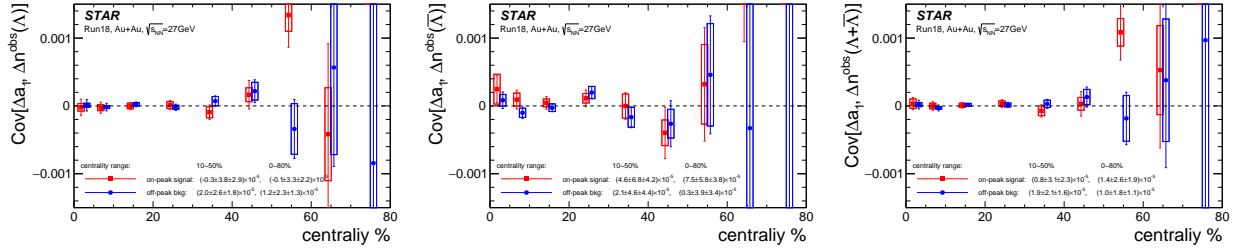


**Figure 23:** The covariance between  $\Delta a_1$  and measured  $\Delta n$  for  $\Lambda$  (Left),  $\bar{\Lambda}$  (Middle), and the sum of them (Right) as functions of centrality. The red markers come from the  $\Lambda(\bar{\Lambda})$  mass peak region with purity correction and blue markers come from the side bands for pure background.

848 azimuthal correlator ( $\Delta a_1 \equiv \langle \sin(\phi^+ - \Psi_{RP}) \rangle - \langle \sin(\phi^- - \Psi_{RP}) \rangle$ ). We next need to determine  
 849 the imbalance in the handedness of  $\Lambda(\bar{\Lambda})$ ,  $\Delta N = N_L - N_R$ . A measured correlation between  
 850  $\Delta a_1$  and  $\Delta N$  would be strong evidence for the CME and underlying local parity violation,  
 851 and would extend the measurement into other parity-odd effects. Note also that the flow-  
 852 related backgrounds that plague charge-separation measurements are not expected to affect  
 853  $\Delta N$  or this correlation measurement. We use a similar toy model to that used in [146] to  
 854 estimate the number of events required to see non-zero correlations between  $\Delta a_1$  and  $\Delta N$   
 855 at the 95% confidence level as a function of the efficiency of  $\Lambda(\bar{\Lambda})$  reconstruction for various  
 856 cases with different CME signal fraction in the  $\Delta\gamma$  measurement (see Fig. 22(right)). The  
 857 chief unknown in this estimate is the extent to which strange quarks may be counted as light  
 858 quarks and so will have a net handedness imparted by the parity-odd domain.

859 Although Fig. 22(right) suggests that this will be a topic that may require the large data  
 860 sets of future runs, these event number estimates have a large uncertainty, making it very  
 861 useful to perform such an analysis with existing data both to search for a correlation signal  
 862 and as an exercise of the analysis method.

863 To explore this correlation, we have analyzed the Run-18 Au+Au collision data at  
 864  $\sqrt{s_{NN}} = 27$  GeV. The  $\Lambda(\bar{\Lambda})$  baryons are reconstructed by their decay daughter tracks and  
 865 identified by topological cuts. Each  $\Lambda$  handedness is estimated by decay kinematics. After  
 866 a purity correction,  $N_L$  and  $N_R$  are calculated for both  $\Lambda$  and  $\bar{\Lambda}$  in each event, and then  
 867  $\Delta n$  (normalized  $\Delta N$ ,  $\Delta n = \frac{N_L - N_R}{(N_L + N_R)}$ ) is calculated. The observable  $\Delta a_1$  can be calculated  
 868 from primordial particles' azimuthal angles w.r.t. the first-order EP measured by the Event  
 869 Plane Detector (EPD). The covariance between  $\Delta n$  and  $\Delta a_1$  is then calculated for the event  
 870 sample. In this exploratory measurement, the covariance is consistent with zero, and so no  
 871 correlations have been observed beyond statistical fluctuations (see Fig. 23).

872 Regardless of the outcome of the measurements with the isobar program, that will be  
 873 performed at the top RHIC energy, one question will remain. What happens at lower collision  
 874 energy? In this context a new idea has emerged. The newly installed event-plane detector  
 875 (EPD) upgrade provides a new capability at STAR towards CME search at lower collision  
 876 energy and for the Beam Energy Scan phase-II program [57]. The idea is simple, at lower  
 877 energies EPD acceptance ( $2.1 < |\eta| < 5.1$ ) falls in the region of beam rapidity ( $Y_{beam}$ ) and

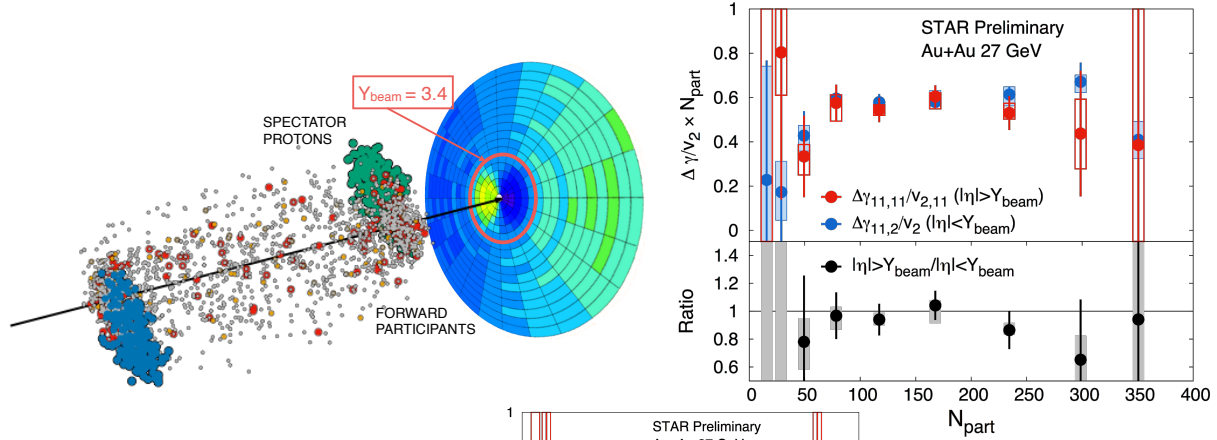


**Figure 24:** Prospect of CME search with the BES-II data. (Left) Single simulated UrQMD event and EPD detector acceptance that covers beam rapidity and detects both forward participants and spectators in 27 GeV Au+Au collisions that have large directed flow which changes sign at  $\eta = Y_{\text{beam}} = 3.4$ . (Right)  $\gamma$ -correlators scaled by  $v_2$  across different event-planes and double ratio of spectator/participant event plane results which would be above unity for finite CME scenario.

878 can measure the plane of strong directed flow ( $\Psi_1$ ) of spectator protons, beam fragments  
 879 and stopped protons, therefore strongly correlated to the B-field direction (See Fig. 24). The  
 880 next step is to measure  $\Delta\gamma$  with respect to  $\Psi_1$  and compare it with the measurement of  $\Delta\gamma$   
 881 along  $\Psi_2$  planes from outer regions of EPD and TPC at mid-rapidity that are relatively more  
 882 weakly correlated to the B-field directions. A test of CME scenario will be to see if large  
 883 difference is observed in the measurements. First preliminary measurements from STAR as  
 884 shown in Fig, 24 are dominated by uncertainty but seem to show good prospects for the  
 885 CME search at lower energies. With the higher statistics data from the BES-II (7.7-19.6  
 886 GeV) and fixed target programs more precise measurements are possible.

## 887 1.3 Cold QCD Highlights

### 888 1.3.1 Introduction

889 The goal of the STAR Cold QCD program is to probe the spin and flavor structure of the  
890 proton and understand the role of spin in Quantum Chromodynamics, exploiting the unique  
891 capability of RHIC to provide longitudinally and transversely polarized  $pp$  collisions at mul-  
892 tiple energies. Measurements with longitudinal beam polarizations have given new insights  
893 into the helicity structure of the proton, while measurements with transverse polarizations  
894 have provided new ways to probe polarized parton distribution functions in the collinear and  
895 transverse momentum dependent frameworks. This program is complemented by studies  
896 of polarized p+p elastic scattering and central exclusive production, in which a far-forward  
897 proton is detected intact.

898 Since 2009, RHIC STAR has completed several highly successful polarized  $pp$  runs both  
899 at  $\sqrt{s} = 200$  GeV and  $\sqrt{s} = 500/510$  GeV. Moreover,  $p$ +Au and  $p$ +Al datasets with a  
900 transversely polarized proton beam have been recorded in 2015 at  $\sqrt{s} = 200$  GeV to address  
901 important physics problems, including the underlying non-perturbative mechanism respon-  
902 sible for large forward transverse single spin asymmetries, the ridge phenomenon and the  
903 possible onset of gluon saturation effects. Table 5 summarizes the STAR sampled luminos-  
904 ity and the luminosity averaged beam polarization as measured by the hydrogen jet (H-jet)  
905 polarimeter.

906 Since the last PAC meeting, there have been four publications in Phys. Rev. D and nine  
907 new preliminary releases that are highlighted in the following section. Additionally, STAR  
908 has one analysis, Run-13 inclusive jet and dijet  $A_{LL}$  at mid-rapidity, that just formed its  
909 God Parent Committee.

### 910 1.3.2 Longitudinal Program

911 STAR has recently completed and published in PRD Letters its results for the high precision  
912 inclusive jet and dijet longitudinal double-spin asymmetries,  $A_{LL}$ , from Run-15  $pp$  collisions  
913 at  $\sqrt{s} = 200$  GeV [10], which was selected for an *Editors' Suggestion*. These results are  
914 sensitive to the gluon helicity distribution in the proton, especially for the medium gluon  
915 momentum fractions in the range from  $x \simeq 0.05$  to  $x \simeq 0.5$ . Figure 25 shows the new  
916 results of dijet  $A_{LL}$  together with the Run-9 results of Ref. [54] and the expected  $A_{LL}$   
917 values for the DSSV14 [129] and NNPDFpol1.1 [252] parton distributions. The results are  
918 in good agreement with previous measurements at  $\sqrt{s} = 200$  GeV and with the theoretical  
919 evaluations of prior world data. They have better precision and thus provide further evidence  
920 that  $\Delta G(x, Q^2)$  is positive for  $x > 0.05$ .

921 Dijet measurements at larger pseudorapidity and higher center-of-mass energy probe  
922 lower values of partonic momentum fraction  $x$ , a region where the gluon helicity distribution  
923 is still poorly constrained. The first measurement of  $A_{LL}$  for intermediate pseudorapidity  
924 dijets [26] used Run-9 data at  $\sqrt{s} = 200$  GeV. Figure 26 shows preliminary results for  
925 intermediate pseudorapidity dijet  $A_{LL}$  using Run-12 STAR  $pp$  data at  $\sqrt{s} = 510$  GeV. The  
926 higher collision energy of the Run-12 preliminary results will provide lower kinematic reach

**Table 5:** Summary of polarized  $pp$  and p-A running periods at RHIC since 2009, including center-of-mass energy, STAR’s integrated luminosity and the average beam polarization for blue (B) and yellow (Y) beams from the H-jet polarimeter.

Year	System	$\sqrt{s}$ (GeV)	Recorded Lumi. ( $\text{pb}^{-1}$ )	Polarization Orientation	B/Y $\langle P \rangle$ (%)
2009	$pp$	200	25	Longitudinal	55/55
2009	$pp$	500	10	Longitudinal	39/39
2011	$pp$	500	12	Longitudinal	48/48
2011	$pp$	500	25	Transverse	48/48
2012	$pp$	200	22	Transverse	61/56
2012	$pp$	510	82	Longitudinal	50/53
2013	$pp$	510	300	Longitudinal	51/52
2015	$pp$	200	52	Transverse	53/57
2015	$pp$	200	52	Longitudinal	53/57
2015	$p\text{Au}$	200	0.45	Transverse	60/–
2015	$p\text{Al}$	200	1	Transverse	54/–
2017	$pp$	510	320	Transverse	55/55

927 in partonic momentum fraction  $x$  relative to the Run-9 results, and further constrain the  
 928 low- $x$  behavior of  $\Delta G(x, Q^2)$ .

929 The longitudinal spin transfer,  $D_{LL}$ , of  $\Lambda$  and  $\bar{\Lambda}$  are expected to be sensitive to the  
 930 helicity distributions of the strange quark and anti-quark and the longitudinal polarized  
 931 fragmentation functions. Figure 27 shows new  $D_{LL}$  preliminary results based on the Run-  
 932 15 dataset at 200 GeV [323], which have about two times larger statistics than previously  
 933 published results from the Run-9 dataset [25]. The new results cover transverse momenta  
 934 up to 8.0 GeV/ $c$ , and are consistent with zero within uncertainty.

### 935 1.3.3 Transverse Program

936 There have been three new preliminary results released and two publications from the trans-  
 937 verse spin program since the last PAC meeting. The highlights include new preliminary  
 938 results for the Collins asymmetries for a charge hadron in a jet [259], interference fragmenta-  
 939 tion function (IFF) asymmetries for di-pion [260], and hyperon transverse spin transfer [323]  
 940 in  $\sqrt{s} = 200$  GeV  $pp$  collisions. Moreover, the A-dependence of transverse single spin asym-  
 941 metries (TSSA) for  $\pi^0$  at forward rapidity in  $pp$   $p+\text{Au}$  and  $p+\text{Al}$  at 200 GeV, and isolated  
 942  $\pi^0$  & EM-jet TSSA in  $pp$  collisions at 200 GeV and 500 GeV are now both published in Phys.  
 943 Rev. D [36, 40].

944 In the soft-collinear-effective theory framework, the Collins asymmetry combines the  
 945 collinear quark transversity in the proton with the transverse momentum dependent Collins  
 946 fragmentation function [122, 191, 192], and thus provides a cleaner probe of the Collins frag-  
 947 mentation function than that in semi-inclusive deep inelastic scattering (SIDIS). This also

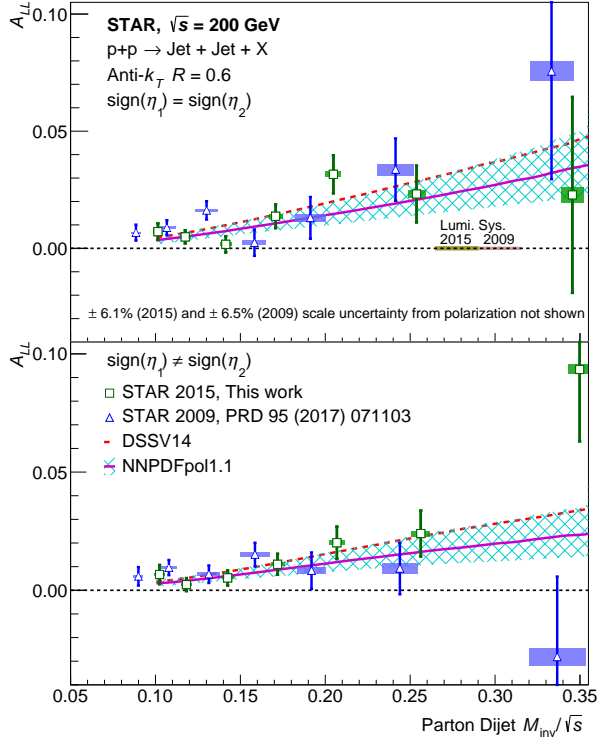


**Figure 25:**  $A_{LL}$  versus  $M_{inv}/\sqrt{s}$  for dijets with the  $\text{sign}(\eta_1) = \text{sign}(\eta_2)$  (top) and  $\text{sign}(\eta_1) \neq \text{sign}(\eta_2)$  (bottom) event topologies [10]. The square markers show the present data, whereas the triangle markers show the data of Ref. [54]. The results are compared to theoretical predictions for dijets from DSSV14 [129] and NNPDF-pol1.1 [252] with its uncertainty.

948 enables tests of evolution, universality and factorization breaking in the TMD formalism.  
 949 Figure 28 shows the combined Run-12 and Run-15 preliminary Collins asymmetries for  
 950 charged pions within jets with jet  $p_T$  dependence. The measured asymmetries at positive  $x_F$   
 951 are larger than theoretical predictions [122] which are based on the transversity and Collins  
 952 fragmentation function from SIDIS and  $e^+e^-$  processes with TMD approach.

953 In transversely polarized proton collisions, di-hadron production is also sensitive to  
 954 transversity. The coupling of transversity to the di-hadron fragmentation function creates  
 955 azimuthal modulations which leads to observed asymmetries. STAR has released new pre-  
 956 liminary results on di-pion ( $\pi^+\pi^-$ ) correlation asymmetry [260] based on the Run-15  $\sqrt{s} =$   
 957 200 GeV dataset, as shown in Fig. 29. Figure 29 shows  $A_{UT}^{\sin(\phi_{RS})}$  versus the di-pion invariant  
 958 mass,  $M_{inv}^{\pi^+\pi^-}$ , in the forward pseudorapidity region ( $\eta^{\pi^+\pi^-} > 0$ ). The asymmetry signal is  
 959 enhanced near the  $\rho$  mass ( $M_{inv}^{\pi^+\pi^-} \approx 0.78 \text{ GeV}/c^2$ ), consistent with the theory prediction.  
 960 The statistical precision of the 2015 result is significantly improved compared to the previous  
 961 Run-6 measurement.

962 Transverse Spin transfer,  $D_{TT}$ , of hyperons in  $pp$  collisions can provide a connection to  
 963 the transversity distribution of the  $s(\bar{s})$  quark in the proton and the polarized fragmentation  
 964 functions. STAR has published its first measurement of the transverse spin transfer of  $\Lambda$  and  
 965  $\bar{\Lambda}$  hyperons at  $\sqrt{s} = 200$  GeV based on the Run-12  $pp$  data set [28]. A new  $D_{TT}$  preliminary  
 966 result using the Run-15  $pp$  dataset has been released [323]. The Run-15 dataset is about  
 967 twice as large as the Run-12 dataset, allowing for better statistical precision. Figure 30 shows  
 968 the preliminary Run-15 results for  $D_{TT}$  versus  $\Lambda(\bar{\Lambda}) p_T$ . The new results are consistent with

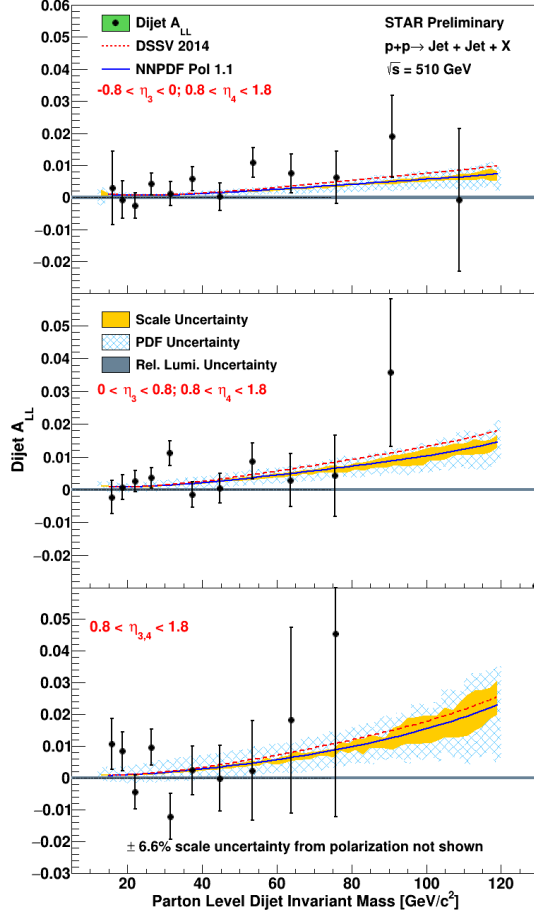


**Figure 26:** Preliminary results of  $A_{LL}$  as a function of parton-level invariant mass for dijets from Run-12 data at 510 GeV with the East Barrel-Endcap (top), West Barrel-Endcap (middle) and Endcap-Endcap (bottom) event topologies [215]. The curves represent theoretical predictions of  $A_{LL}$  for the DSSV14 [129] and NNPDFpol1.1 [252] parton distributions.

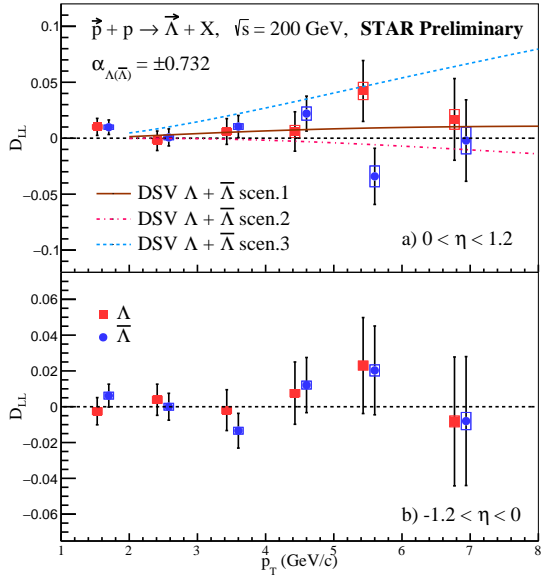


**Figure 27:** Preliminary results of longitudinal spin transfer,  $D_{LL}$ , of  $\Lambda$ (red) and  $\bar{\Lambda}$ (blue) from Run-15  $pp$  data set [323]. The top and bottom panels are for the positive and negative  $\eta$  with respect to the polarized beam, respectively. The results for the  $\bar{\Lambda}$  have been shifted to larger  $p_T$  slightly for clarity.

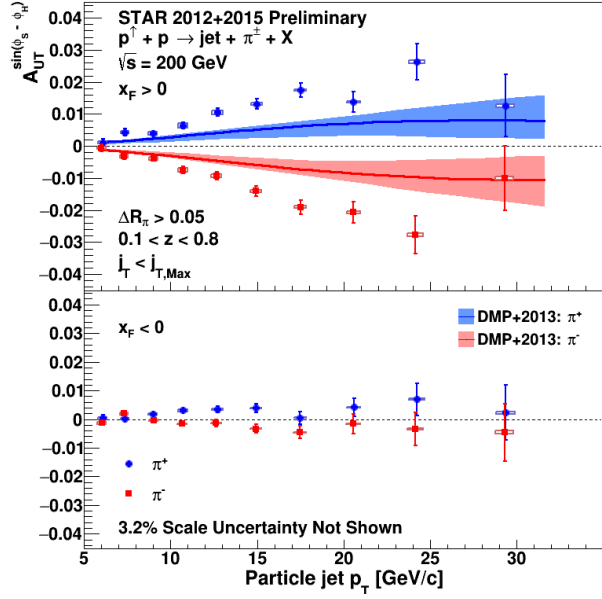


**Figure 28:** Preliminary results for the the combined Run-12 and Run-15 Collins asymmetry plotted for identified  $\pi^+$  (blue) and  $\pi^-$  (red) particles as a function of jet  $p_T$  for jets that scatter forward relative to the polarized beam ( $x_F > 0$ ) on top panel and those scatter backward ( $x_F < 0$ ) on lower panel [259]. The full range of both  $z$  and  $j_T$  are integrated over. Theoretical evaluations from [123] with their uncertainties are presented for  $\pi^+$  (blue) and  $\pi^-$  (red).

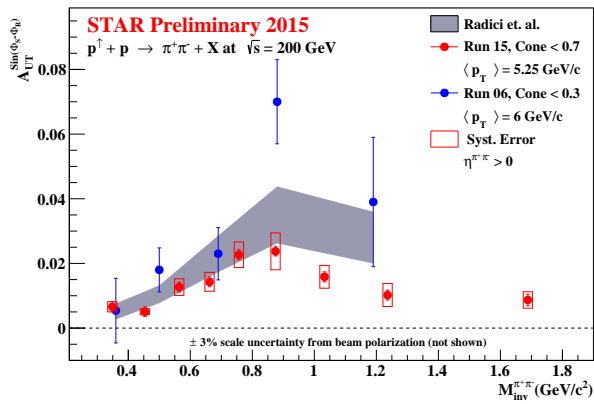


**Figure 29:** Preliminary results of di-hadron asymmetry  $A_{UT}^{sin(\phi_{RS})}$  as a function of  $M_{inv}^{\pi^+\pi^-}$ , integrated over  $p_T^{\pi^+\pi^-}$  in forward pseudo-rapidity region ( $\eta^{\pi^+\pi^-} > 0$ ) at  $\sqrt{s} = 200$  GeV from Run-15 together with previously published Run-6 data. The error bars represent the statistical uncertainty, while the boxes represent the systematic uncertainty.

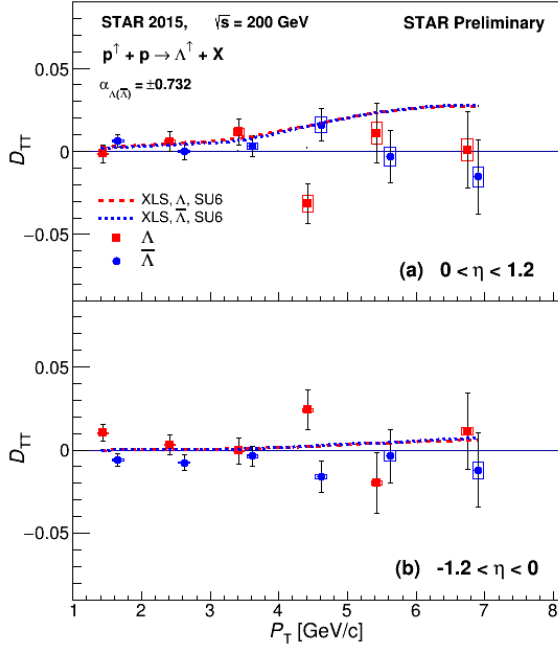


**Figure 30:** Preliminary results of  $D_{TT}$  versus  $\Lambda(\bar{\Lambda}) p_T$  from STAR Run-15  $pp$  dataset at  $\sqrt{s} = 200$  GeV [323]. The upper panel is for positive  $\eta$  with respect to the polarized beam and the lower panel is for negative  $\eta$ . The results are compared with a model calculation [322]. The  $\Lambda$  results have been offset to slightly smaller  $p_T$  values for clarity.

969 zero within uncertainties, and also are consistent with model predictions.

970 A new STAR publication reports on the transverse single spin asymmetry (TSSA) for  
 971 forward neutral pions produced in polarized proton collisions with protons ( $pp$ ), aluminum  
 972 nuclei ( $p+Al$ ) and gold nuclei ( $p+Au$ ) at  $\sqrt{s} = 200$  GeV are measured with the FMS in Run-  
 973 15 [40]. The measured asymmetries, presented in Fig. 31, are found to rise with transverse  
 974 momentum at  $x_F < 0.5$ , while they flatten or fall at larger  $x_F$ . The results are consistent  
 975 with a weak nuclear  $A$  dependence. Moreover, a further observation is that the TSSA is  
 976 significantly larger for isolated  $\pi^0$ s than for non-isolated  $\pi^0$ s, which are accompanied by  
 977 additional jet-like fragments.

978 The TSSA of neutral pions in  $pp$  collisions at both  $\sqrt{s} = 200$  GeV and 500 GeV from FMS  
 979 data are shown in Fig. 32. The 200 GeV data are from Run-15, while the 500 GeV data are  
 980 from the Run-11. The results have been accepted for publication [36]. A continuous increase  
 981 of the TSSA with Feynman- $x$  indicates a weak dependence on the center-of-mass energy.  
 982 Pions with no nearby particles ("isolated"), which may not arise from conventional parton  
 983 fragmentation, tend to have a higher TSSA than non-isolated pions, which suggests that a  
 984 different mechanism (i.e., diffractive) other than the Sivers or Collins effects is required to  
 985 explain these results. The theoretical calculations presented in the plot are based on the  
 986 TMD and collinear twist-3 functions from a recent global analysis [110], which also includes  
 987 previous forward  $\pi^0$  and charged hadron TSSA data from RHIC in the fit. The theoretical  
 988 calculation differs from our measurement and only provides a reasonable description of the  
 989 non-isolated  $\pi^0$  in the low- $x_F$  region.

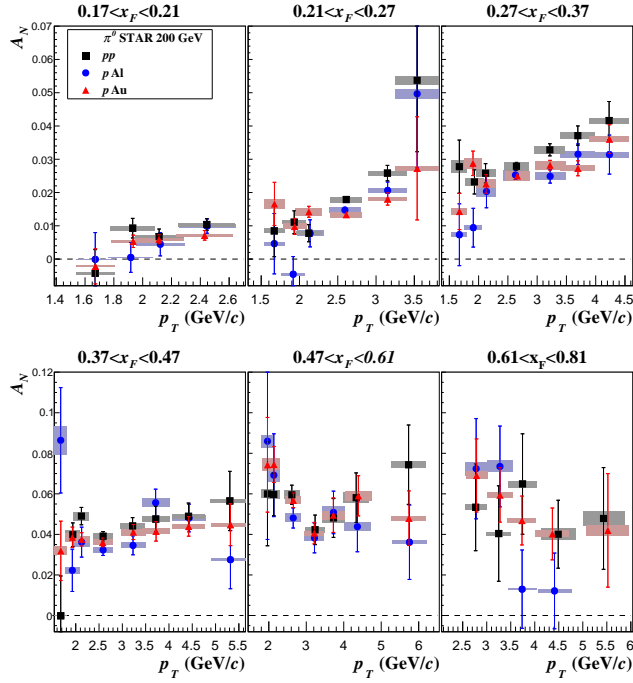


**Figure 31:** Transverse single spin asymmetry for forward  $\pi^0$  production as a function of transverse momentum for six Feynman  $x_T$  regions [40]. The results for three collisions systems are shown, the black squares are for  $pp$  blue circles for  $p$ +Al and red triangles for  $p$ +Au collisions. The statistical uncertainties are shown with vertical error bars and the filled boxes indicate the horizontal and vertical systematic uncertainties.

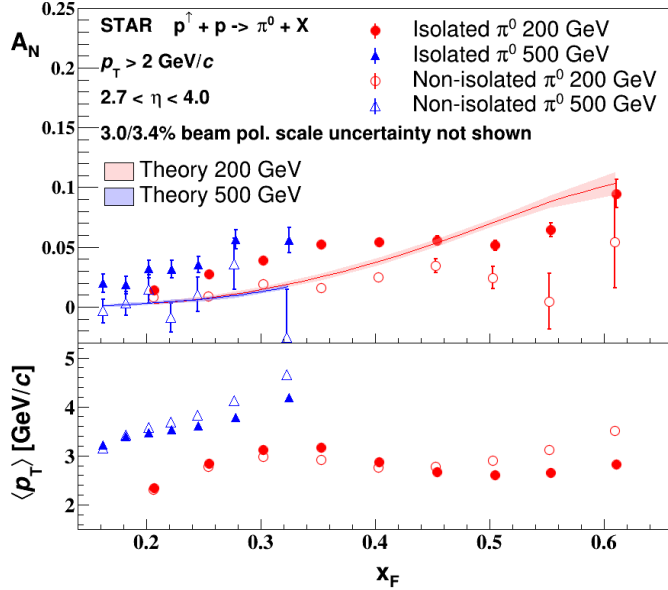


**Figure 32:** Results for the transverse single-spin asymmetry as function of Feynman- $x$  for the isolated and non-isolated  $\pi^0$  in transversely polarized  $pp$  collisions at  $\sqrt{s} = 200$  and 500 GeV [36]. Theory curves based on a recent global fit [110] are also shown. The average transverse momentum of the  $\pi^0$  for each  $x_F$  bin is shown in the lower panel.

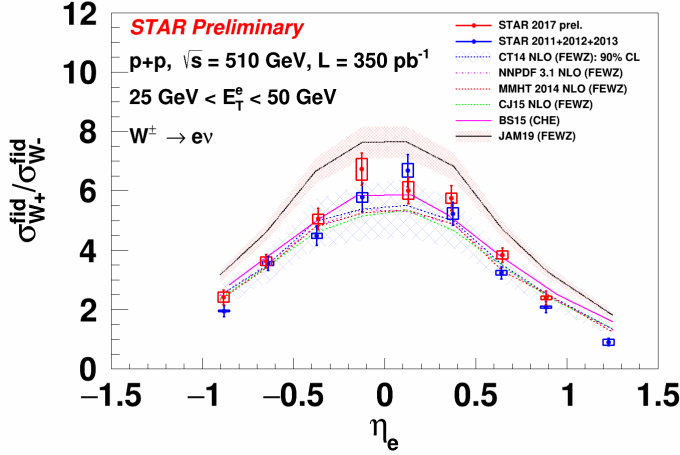


**Figure 33:** Comparison of  $W^+$  and  $W^-$  cross-section ratio as a function of lepton pseudorapidity for the Run-17 dataset to the recently published combined Runs-11, 12 and 13 datasets [42]. The central values correspond to the mean value of  $\eta_e$  distribution for that bin. The error bars represent the statistical uncertainty, whereas the rectangular boxes represent the systematic uncertainty for the respective data point. These measurements are compared to various theory frameworks, which use several different PDF inputs.

### 1.3.4 Unpolarized Program

Since the last PAC meeting STAR has published one paper on the  $W$  and  $Z$  cross sections and their ratios for the combined Run-11, Run-12, and Run-13  $\sqrt{s} = 500/510$  GeV  $pp$  datasets [42]. The  $W^+/W^-$  cross-section ratio is a unique measurement that is sensitive to the unpolarized  $\bar{d}/\bar{u}$  quark distribution and will provide insight and constraints to its  $x$  dependent distribution. This STAR measurement is complementary to the Drell-Yan results from NuSea [306] and SeaQuest [136], covering the overlapping  $x$  region of about  $0.1 - 0.35$  at higher  $Q^2 (= M_W^2)$ . The  $W^+/W^-$  cross-section ratio measured with Run-17 dataset at  $\sqrt{s} = 510$  GeV has been released as preliminary [248]. Figure 33 shows the ratio plotted as a function of lepton pseudorapidity for the combined Run-11,12 and 13 published results and the Run-17 preliminary result.

Measurements of the differential inclusive jet cross section in  $pp$  collisions can be incorporated into global fits to provide constraints on the unpolarized gluon PDFs. Differential inclusive jet cross section results at  $\sqrt{s} = 200$  GeV and 510 GeV from STAR's Run-12 dataset have been released as preliminary [185, 186]. The measurement at  $\sqrt{s} = 200$  GeV, as seen in Fig. 34, corresponds to a range of  $x_T \equiv \frac{2p_T^{\text{jet}}}{\sqrt{s}}$  from 0.067 up to 0.5, allowing for the possibility of constraining the unpolarized gluon PDF at high- $x$ . The measurement at  $\sqrt{s} = 510$  GeV, shown in Fig. 35, is sensitive to lower  $x$  values of the gluon PDF compared to the 200 GeV measurement.

The azimuthal correlation of forward di-hadrons produced in  $pp$  and  $p$ -A collisions provides an essential tool to access the underlying gluon dynamics in the nonlinear evolution region. STAR has released preliminary results for the measurement of azimuthal correlations of di- $\pi^0$  produced in the forward direction ( $2.6 < \eta < 4.0$ ) in  $pp$ ,  $p$ +Al and  $p$ +Au collisions at  $\sqrt{s} = 200$  GeV from the Run-15 data set [119]. A clear suppression of the correlated yields of back-to-back pairs is observed in  $p$ +Al and  $p$ +Au compared with the reference  $pp$  collisions. The larger suppression found in  $p$ +Au than  $p$ +Al collisions exhibits the saturation scale,

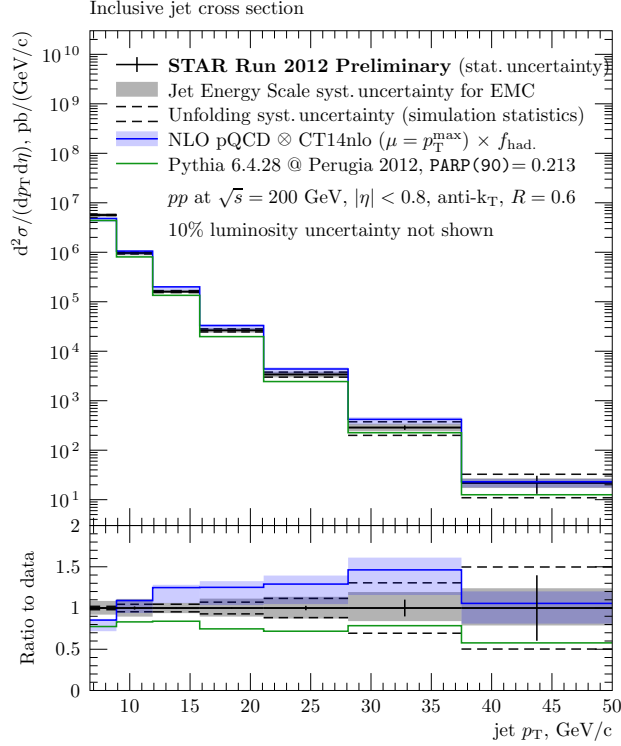


**Figure 34:** Differential inclusive jet cross section for  $pp$  collisions at  $\sqrt{s} = 200$  GeV as a function of jet  $p_T$  corrected for underlying event. The measurement is compared to a prediction from the PYTHIA Monte Carlo generator. Another comparison is to a prediction of the NLO pQCD theory with a bin-by-bin correction for effects of the hadronization estimated using the same PYTHIA generator.

1016  $Q_s^2$ , dependence on  $A$ . The observed suppression of back-to-back pairs as a function of event  
 1017 activity and  $p_T$  from Fig. 36 points to the non-linear gluon dynamics arising at high parton  
 1018 densities.

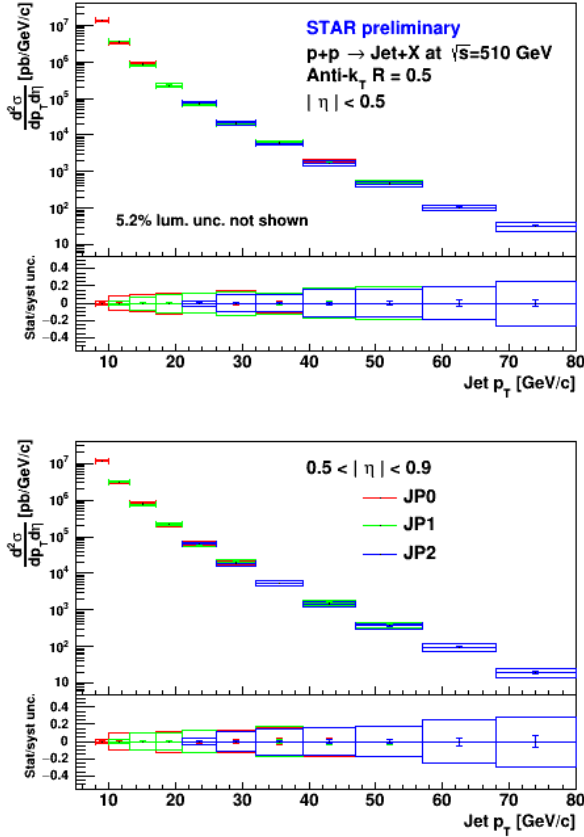


**Figure 35:** Differential inclusive jet cross section,  $\frac{d^2\sigma}{dp_T d\eta}$ , as a function of particle jet transverse momentum  $p_T$  for JP0, JP1 and JP2 triggered samples within two  $\eta$  regions,  $|\eta| < 0.5$  and  $0.5 < |\eta| < 0.9$ . The result show excellent agreement between triggers, which indicates an accurate simulation of the trigger efficiency used in detector effect unfolding.

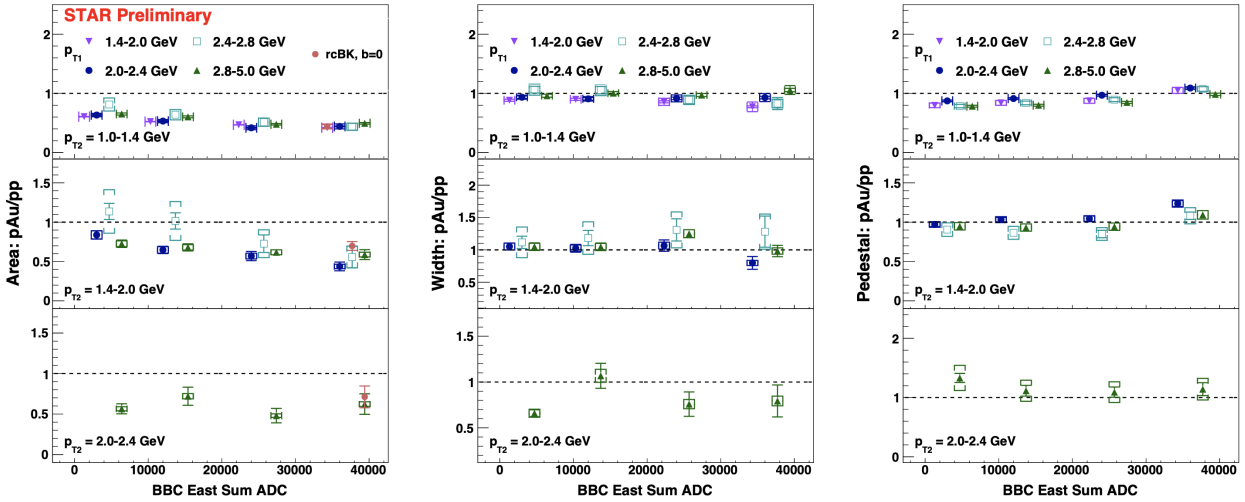


**Figure 36:** Comparison of back-to-back di- $\pi^0$  pair yields ratio the width and the level of pedestal in  $p$ +Au and minBias  $pp$  collisions as a function of di- $\pi^0$ 's  $p_T$  and event activity. Energy deposited at east Beam-Beam Counter (BBC) quantifies the “event activity”. The measured area ratio is compared with theory predictions based on rcBK model [73].

1019 **1.4 Run-21 Performance**

1020 In this section, we will review the BES-II collider and fixed-target performance to date  
 1021 detailing which of the Run-21 physics priorities have been completed. Careful study of these  
 1022 performance metrics will be used to make projections about the required time to complete  
 1023 the remaining Run-21 physics priorities. As our projections indicate that we are highly  
 1024 likely to complete the Run-21 priorities within the allotted run-time, we also propose an  
 1025 additional physics topic which could be addressed if time is available toward the end of  
 1026 Run-21 operations.

1027 The highest priority for Run-21 was to complete the BES-II physics program. Most of  
 1028 the BES-II collider and fixed-target systems had been completed in RHIC years 2018-2020.  
 1029 The only remaining system to be completed was the 7.7 GeV collider system. This had been  
 1030 chosen to be run last as it was expected to be the most difficult from an operations point of  
 1031 view. Tests of the 7.7 GeV collider program had been performed in 2019 (without electron  
 1032 cooling) and in 2020 (with electron cooling), and projections using the best performance  
 1033 from 2020 suggested that, conservatively, it would require 28 weeks to complete the 7.7 GeV  
 1034 collider system. STAR optimistically projected that the 7.7 GeV collider system would be  
 1035 completed in 11-20 weeks, and proposed a prioritized physics program that could make use  
 1036 of beam-time if available (see tabel 6).

**Table 6:** Physics Priorities for Run-21

Priority	Beam Energy	$\sqrt{s_{NN}}$	System	Events	Weeks	Goals
1	3.85	7.7	Au+Au	100 M	11-20	Complete BES-II
2a	3.85	3.0	Au+Au	300 M	3 days	Fluctuations
2b	44.5	9.1	Au+Au	50 M	1 day	Stopping
2b	70	11.5	Au+Au	50 M	1 day	Stopping
2b	100	13.7	Au+Au	50 M	1 day	Stopping
3a	100	200	O+O	400 M	4 days	Small systems (min bias)
3a	100	200	O+O	200 M	4 days	Small Systems (central)
3b	8.65	17.3	Au+Au	250 M	2.5	Additional BES-II energy
3c	3.85	3.0	Au+Au	2 B	3	Double hyper-nucleus search

1037 **1.4.1 Performance to Date**

1038 Priority 1:  
 1039 STAR started taking physics data for the 7.7 GeV collider program on January 31st, and  
 1040 completed the event statistics goals on May 1st. This was a total of 90 days (or 12.8 weeks)  
 1041 of data taking. The 7.7 GeV run did prove to be very technically challenging. At the start  
 1042 of data taking in early February, the good event rates were only half of those that had been  
 1043 achieved the year before. Optimizations and improvements included: using the Tandem (as  
 1044 opposed to EBIS) to achieve the maximum intensity at injection, including a beta-squeeze

1045 ten minutes into the fill (made possible by the reduction of the beam emittance due to the  
 1046 electron cooling), optimizing the longitudinal matching for injection from the AGS to RHIC,  
 1047 developing a new "low tune" for RHIC, and implementing dampers. After this month of  
 1048 optimizations, the store-average good event rate reached 30 Hz, which was a factor of five  
 1049 better than was achieved in 2010, and a factor of two better than the best rates achieved  
 1050 in the 2020 tests. The key run-averaged performance metrics are detailed in table 7, and  
 1051 compared to those achieved for the other BES-II collider energies. Although the store-average  
 1052 good event rate reached 30 Hz in the later half of the run, the run-averaged value was 22 Hz,  
 1053 which was close to the most optimistic projection. The second most significant performance  
 1054 metric is the average hours of data taking per day. This metric is influenced by the store  
 1055 length, the up-time of the collider, the up-time of the experiment, and the fraction of time  
 1056 dedicated to other programs (CeC and APEX) and maintenance. STAR had estimated 12-15  
 1057 hours per day of data taking. Over the course of the run, an average of 13 hours per day  
 1058 was achieved, however, it should be noted that an average of 1.5 hours per day had been  
 1059 dedicated to CeC and APEX during the 90 days of 7.7 GeV running; therefore the average  
 1060 hours per day was also close to the most optimistic projection. Data quality assurance is  
 1061 performed on a run-by-run basis by the shift crews, on a daily basis by remote QA shifters  
 1062 using fast offline production, and on a weekly basis by the physics working groups.

**Table 7:** Achieved and projected experiment performance criteria for the BES-II Au+Au collider program.

Collision Energy (GeV)	7.7	9.2	11.5	14.6	17.1	19.6	27
Performance in BES-I	2010	NA	2010	2014	NA	2011	2011
Good Events (M)	4.3	NA	11.7	12.6	NA	36	70
Days running	19	NA	10	21	NA	9	8
Data Hours per day	11	NA	12	10	NA	9	10
Fill Length (min)	10	NA	20	60	NA	30	60
Good Event Rate (Hz)	7	NA	30	23	NA	100	190
Max DAQ Rate (Hz)	80	NA	140	1000	NA	500	1200
Performance in BES-II ( <b>achieved</b> )	2021	2020	2020	2019	2021	2019	2018
Required Number of Events	100	160	230	300	250	400	NA
<b>Achieved Number of Events</b>	<b>101</b>	<b>162</b>	<b>235</b>	<b>324</b>	TBD	<b>582</b>	<b>560</b>
fill length (min)	<b>30</b>	<b>45</b>	<b>25</b>	<b>45</b>	50	<b>60</b>	<b>120</b>
Good Event Rate (Hz)	<b>22</b>	<b>33</b>	<b>80</b>	<b>170</b>	265	<b>400</b>	<b>620</b>
Max DAQ rate (Hz)	<b>600</b>	<b>700</b>	<b>550</b>	<b>800</b>	1300	<b>1800</b>	<b>2200</b>
Data Hours per day	<b>13</b>	<b>13</b>	<b>13</b>	<b>9</b>	15	<b>10</b>	<b>9</b>
Projected number of weeks	11-20	8.5-14	7.6-10	5.5	2.5	4.5	NA
weeks to reach goals	<b>12.8</b>	<b>14.6</b>	<b>8.9</b>	<b>8.6</b>	TBD	<b>5.1</b>	<b>4.0</b>

1063 Priority 2:

1064 The second priority really breaks down in two distinct fixed-target physics programs. The  
 1065 first (indicated as Priority 2a in Table 6) required 300 M minimum bias events from fixed-  
 1066 target collisions using the 3.85 GeV Au beam. This study used the same beam energy as  
 1067 the 7.7 GeV collider program, therefore it was efficient to run immediately after the 7.7 GeV  
 1068 program was completed as the reconfiguration of the collider was minimal. The fixed-target  
 1069 program did need a long beta star lattice and used only twelve bunches in the yellow ring,  
 1070 and STAR needed to reconfigure its trigger. All of these changes were completed efficiently,  
 1071 and within three hours of the completion of the 7.7 GeV collider run, STAR was taking  
 1072 physics data for the 3.85 GeV fixed-target run. The physics goals for this 3.85 are fluctuation  
 1073 measurements, therefore, strict requirements were placed in consistency of operations and  
 1074 minimization of pile-up. These operational requirements limited the store length to two  
 1075 hours, which was shorter than the expected four hours this resulted in the 3.3 days instead  
 1076 of the expected 3.0 days. On a positive note, the eTOF detector system, which is critical for  
 1077 this energy, was live for 99.6% of all events recorded.

1078 The second part of the priority 2 fixed-target program (indicated as Priority 2b in Table  
 1079 6) required 50 M events at three higher energies (44.5, 70, and 100 GeV). Changing the col-  
 1080 lider from low-energy to high-energy operations required reconfiguring the injection kickers,  
 1081 the abort kickers, conditioning the RHIC magnets to run at full current, and developing  
 1082 three new energies with 5 m beta star lattices. Developing the high rigidity 100 GeV beam  
 1083 for fixed-target operations proved especially challenging as the 1.8 mm vertical shift in the  
 1084 beam necessary to graze the target was at the limit of the capabilities of the collider and  
 1085 maintaining the optimal luminosity required maximum use of the BBQ kicker, injection mis-  
 1086 match, and IBS scattering to produce the largest emittance 100 GeV Au beam ever seen. In  
 1087 total, the reconfiguration, beam development, and data taking took a little over three days  
 1088 (with data taking times of 12,12, and 10 hours for each of the three beams). Each of these  
 1089 three energies completed data taking with a single store. Overall performance was exactly as  
 1090 expected. A summary of the Run-21 fixed-target performance is compared to the expected  
 1091 metrics and to previous years runs in Table 8.

#### 1092 1.4.2 Projections to Complete the Run-21 Physics Priorities

1093 Priority 3a:

1094 The O+O system at  $\sqrt{s_{NN}} = 200$  GeV provides a small system for flow and correlation  
 1095 studies. The events request is divided in a 400 M events request for minimum bias data and  
 1096 a 200 M event request for central collisions (top 5%). There is ample luminosity for O+O  
 1097 collisions at full energy to fill the STAR DAQ bandwidth, therefore a few operational choices  
 1098 have been made to increase the quality of the recorded data. First, the beams are being  
 1099 collided with a 1.65 mrad angle, which helps by limiting the vertex distribution to  $\pm 30$  cm  
 1100 in  $z$ . Second, the luminosity is being limited by slightly adjusting the offsets the beams in  $y$   
 1101 to limit the minimum bias trigger rate to 4 kHz to minimize the pile-up. This program was  
 1102 started on May 8th. For the minimum bias part of the program achieved an average of 14  
 1103 hours per day of data taking, and good events rates of 7.5 M events per hour as expected for  
 1104 a program that efficiently filled the STAR DAQ bandwidth. We finished the minimum bias

**Table 8:** Achieved and projected experiment performance criteria for the BES-II Au+Au fixed-target program.

Beam Energy	$\sqrt{s_{NN}}$ (GeV)	Expected Duration	Actual Duration	Proposed Events	Recorded Events	Year
3.85	3.0	4 days	3.5 days	100 M	258 M	2018
3.85	3.0	3 days	3.3 days	300 M	307 M	<b>2021</b>
3.85	3.0	3 weeks	TBD	2 B	TBD	<b>2021</b>
4.59	3.2	2 days	46 hours	200 M	200.6 M	2019
5.75	3.5	1 day	23 hours	100 M	115.6 M	2020
7.3	3.9	0.5 days	12 hours	50 M	52.7 M	2019
7.3	3.9	1 day	29 hours	100 M	117 M	2020
9.8	4.5	1 day	31 hours	100 M	108 M	2020
13.5	5.2	1 days	21 hours	100 M	103 M	2020
19.5	6.2	1 days	22 hours	100 M	118 M	2020
26.5	7.2	parasitic	2 days	none	155 M	2018
26.5	7.2	parasitic	3.5 days	none	317 M	2020
26.5	7.2	parasitic	TBD	none	TBD	2021
31.2	7.7	0.5 days	11.5 hours	50 M	50.6 M	2019
31.2	7.7	1 day	26 hours	100 M	112 M	2020
44.5	9.1	0.5 days	12 hours	50 M	53.9 M	<b>2021</b>
70	11.5	0.5 days	12 hours	50 M	51.7 M	<b>2021</b>
100	13.7	0.5 days	10 hours	50 M	50.7 M	<b>2021</b>

1105 event statistics requirements on Sunday May 16th with 404 M good events. For the central  
1106 collisions, the luminosity was increased by a factor of five by reducing the vertical offset of  
1107 the beams. There was still sufficient luminosity to fill the STAR DAQ bandwidth. As it was  
1108 important the hardware trigger did not bias the top 5% of centrality events, which will be  
1109 selected in offline analysis, the trigger efficiency was only 45%. We completed the central  
1110 collision data set on May 21st (5 days) with 212 M good events. It had been expected to  
1111 take 4-5 days to complete the central collisions goals. Upon completion of the physics goals  
1112 for the O+O system, the field for the STAR solenoid has been flipped and another three  
1113 days (shared with CeC) of minimum bias will be taken. These data are needed to carefully  
1114 study the alignment, calibrations, and corrections needed to maximize the tracking accuracy  
1115 of the STAR TPC. It is projected that data taking for O+O will be completed on May 24th.

1116 Priority 3b:

1117 The Au+Au system at  $\sqrt{s_{NN}} = 17.3$  GeV adds an energy to the BES-II collider program  
1118 where there is a larger than average gap between adjacent energies and where there is hint  
1119 of a change in the ratios of the light nuclei which could suggest an increase in neutron  
1120 fluctuations. The projections for the key merits are interpolated from those achieved to the  
1121 14.6 and 19.6 GeV collider systems (see Table 7). RHIC will need one day to reconsider  
1122 the injection and abort kickers and to tune the 17.3 GeV collisions. Data taking is expected

1123 to take 21-27 days depending on how rapidly RHIC reaches optimal performance. Two and  
1124 a half days of CeC, APEX, and maintenance have been included in the data taking time  
1125 estimates. It is projected that data for the 17.3 GeV Au+Au system will be completed by  
1126 June 14-20th.

1127 Priority 3c:

1128 STAR will return to 3.85 GeV fixed target running toward the end of Run-21. The physics  
1129 goals for this period are the search for the doubly-strange hyper-nucleus. As this is a rare  
1130 particle search and not a fluctuations measurement, the conduct of operations will be opti-  
1131 mized for the total number of recorded events and not for reduction of pile-up. Data taking  
1132 is expected to take 23-28 days (mostly depending on weather in June). Two and a half days  
1133 of CeC, APEX, and maintenance have been included in the data taking time estimate. It is  
1134 projected that data for this 3.85 GeV fixed-target system will be completed by July 7-10th  
1135 (July 10th would be a hard stop in preparation for warm-up).

1136 Priority X:

1137 In previous years, STAR has recorded 26.5 GeV fixed-target data parasitically while CeC is  
1138 running. This typically only occurs once CeC has reached consistent running. This has not  
1139 yet happened to date, however it is expected that toward the end of Run-21 operations there  
1140 will be several days of stable CeC operations, at which time we are likely to record 26.5 GeV  
1141 fixed-target data.

## 1142 1.5 Physics Opportunity for Run-21

### 1143 Pinning down the precise role of geometry on collectivity with central d+Au 1144 collisions

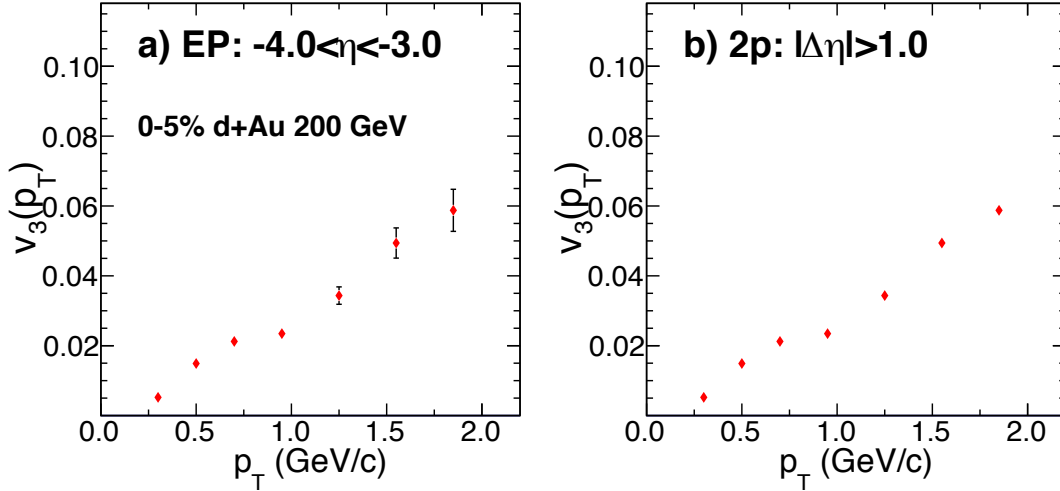


**Figure 37:** Projection for  $v_3$  with forward and midrapidity acceptance in high multiplicity d+Au collisions utilizing the extended pseudorapidity capability of iTPC and EPDs.

1145

1146 The first striking evidence of collective behavior in small collision systems was observed  
1147 in the pattern of anisotropy of particle emissions in rare high activity p+p collisions at  
1148 the LHC [197]. This, followed by measurements in p+Pb collisions [6, 14, 112], started a  
1149 strong debate on whether such correlations originate at a very early stages due to collective  
1150 behavior of gluons inside colliding protons, or whether they originate at a late stage due to  
1151 the formation of a fluid like medium. Measurements of azimuthal anisotropy coefficients ( $v_n$ )  
1152 in most central (0-5%) small collision systems  $^3He + Au$  [61],  $d + Au$  [49, 60] and  $p + Au$  [66]  
1153 with different initial shapes from RHIC have confirmed that even in small collision systems  
1154 fluid-dynamic final state effects are essential to drive collectivity [67]. Such results from the  
1155 PHENIX experiment using the combination of particles from mid-rapidity ( $|\eta| < 0.35$ ) and  
1156 another from forward rapidity ( $1 < \eta < 3$ , Au-going side) indicate a specific ordering of  
1157 triangular harmonic anisotropy  $v_3(^3He + Au) > v_3(d + Au) \sim v_3(p + Au)$ . This hints at  
1158 the possibility that a more triangular initial geometry is produced in  $^3He + Au$  collisions  
1159 (compared to  $d + Au$  and  $p + Au$ ) as expected from a nucleon based initial state model [247].

1160

1161 However, recent STAR preliminary results using two particle correlations with both par-  
1162 ticles at mid-rapidity ( $|\eta| < 1$ ) show  $v_3(^3He + Au) \sim v_3(d + Au) \sim v_3(p + Au)$  [216]  
1163 implying no system dependence of triangularity indicating fluctuations or geometry at the  
1164 sub-nucleonic scale drives anisotropy. This qualitative difference of system dependence of  
1165  $v_3$  measurements between STAR and PHENIX kinematics is very striking. With the antici-  
pated high statistics d+Au run by triggering on central events at RHIC it will be possible to

1166 perform measurements of  $v_n$  using acceptance similar to both previous PHENIX and STAR  
1167 measurements and answer:

- 1168 • How will  $v_3$  measurements in d+Au change from mid-rapidity to forward rapidity?
- 1169 • How will forward  $v_3$  measurements in d+Au from STAR compare to the same from  
1170 PHENIX?

1171 Fig.37 shows a projection plot for  $v_3$  using particles from forward and midrapidity accep-  
1172 tance in high multiplicity d+Au collisions utilizing the extended pseudorapidity capability  
1173 of STAR. The two panels show estimates for  $v_3$  in two-particle correlation approach by using  
1174 : 1) tracks from TPC+iTPC ( $|\eta| < 1.5$ ) and hits from EPDs ( $2.1 < |\eta| < 5.1$ ), 2) pairs  
1175 of tracks from TPC+iTPC ( $|\eta| < 1.5$ ) and using a relative pseudorapidity gap of  $|\Delta\eta| > 1$ .  
1176 To start with we assume STAR will collect data at the rate of 2.2 kHz and a combined  
1177 RHIC×STAR down time of 50% (12 hour/day) for three days of running during Run-21.  
1178 The desired run conditions will be such that the coincidence rate of ZDCs will be about  
1179 10 kHz. The idea is to dedicate the first day entirely on collecting minimum bias events.  
1180 This will lead to the accumulation of about  $1(\text{day}) \times 86400(\text{sec.}) \times 0.5(\text{downtime}) \times 2200(\text{rate})$   
1181  $\times 1.0(\text{bandwidth}) \approx 95$  Million events. On the second and the third day, we plan to split  
1182 the bandwidth equally into collecting min-bias and high multiplicity events with a dedicated  
1183 trigger. Following the same estimates of rate, we can collect 95 million events for the two  
1184 case. Therefore over all three days, we will be able to accumulate 190 Million min-bias events  
1185 and 95 Million high multiplicity events. With such statistics and aforementioned measure-  
1186 ments it will possible to revisit the  $v_n$  measurements in STAR and PHENIX kinematics and  
1187 understand the apparent discrepancy between the previous measurements.

## 2 Cold QCD Physics with $p^\uparrow p^\uparrow$ and $p^\uparrow + A$ Collisions at 510 and 200 GeV

The exploration of the fundamental structure of strongly interacting matter has always thrived on the complementarity of lepton scattering and purely hadronic probes. As the community eagerly anticipates the future Electron Ion Collider (EIC), an outstanding scientific opportunity remains to complete “must-do” measurements in  $pp$  and  $p+A$  physics during the final years of RHIC. These measurements will be essential if we are to fully realize the scientific promise of the EIC, by providing a comprehensive set of measurements in hadronic collisions that, when combined with future data from the EIC, will establish the validity and limits of factorization and universality. Much of the Run-22 and Run-24 physics program outlined here is, on the one hand, unique to proton-proton and proton-nucleus collisions and offers discovery potential on its own. On the other hand, these studies will lay the groundwork for the EIC, both scientifically and in terms of refining the experimental requirements of the physics program, and thus are the natural next steps on the path to the EIC. When combined with data from the EIC these STAR results will provide a broad foundation to a deeper understanding of fundamental QCD.

The separation between the intrinsic properties of hadrons and interaction-dependent dynamics, formalized by the concept of factorization, is a cornerstone of QCD and largely responsible for the predictive power of the theory in many contexts. While this concept and the associated notion of universality of the quantities that describe hadron structure have been successfully tested for unpolarized and, to a lesser extent, longitudinally polarized parton densities, its experimental validation remains an unfinished task for much of what the EIC is designed to study – the three-dimensional structure of the proton and the physics of dense partonic systems in heavy nuclei. To establish the validity and limits of factorization and universality, it is essential to have data from *both* lepton-ion and proton-ion collisions, with experimental accuracy that makes quantitative comparisons meaningful.

Beginning in Run-22, STAR will be in a unique position to provide this essential  $pp$  and  $p+A$  data. A full suite of forward detectors will be installed this year, providing excellent charged-particle tracking at high pseudorapidity ( $2.5 < \eta < 4$ ) for the first time, coupled with both electromagnetic and hadronic calorimetry. This will enable STAR to explore the interesting regimes of high- $x$  (largely valence quark) and low- $x$  (primarily gluon) partonic physics with unparalleled precision. In addition, mid-rapidity detector upgrades motivated primarily by the BES-II program, in particular the iTPC, will substantially extend STAR’s already excellent kinematic reach and particle identification capabilities beyond those that existed during previous  $pp$  and  $p+A$  runs.

For the case of  $pp$  spin physics, it is important to recognize the complementary roles that will be played by Run-22 at 510 GeV and Run-24 at 200 GeV. The combination of 510 GeV  $pp$  collisions and the STAR Forward Upgrade will provide access to forward jet physics at perturbative scales, thereby enabling measurements at the highest and lowest  $x$  values. In parallel, mid-rapidity measurements at 510 and, especially, 200 GeV will interpolate between the high and low  $x$  values, with significant overlaps to probe evolution effects

1229 and provide cross-checks. Together, the two runs will allow STAR to measure fundamental  
1230 proton properties, such as the Sivers and transversity distributions, over nearly the entire  
1231 range  $0.005 < x < 0.5$ .

1232 Run-24 will also provide outstanding opportunities to probe fundamental questions re-  
1233 garding QCD in cold nuclear matter. The STAR Forward Upgrade will enable an extensive  
1234 suite of measurements probing the quark-gluon structure of heavy nuclei and the regime of  
1235 low- $x$  non-linear gluon dynamics, as predicted by saturation models. STAR will also ex-  
1236 plore how a nucleus, serving as a color filter, modifies the propagation, attenuation, and  
1237 hadronization of colored quarks and gluons.

1238 For these reasons, STAR requests at least 16 weeks of polarized  $pp$  data-taking at  $\sqrt{s} =$   
1239 510 GeV in Run-22. All data-taking will involve proton beams polarized transversely relative  
1240 to their momentum direction in order to focus on those observables where factorization,  
1241 universality, and/or evolution remain open questions, with spins aligned vertically at the  
1242 STAR IR. Based on the latest guidance from CAD, and mindful of ‘lessons learned’ in  
1243 previous  $pp$  runs at full energy (see Fig. 38), we will ask for luminosity-leveling of the collision  
1244 rate to maximize the efficiency of our main tracking detectors. Assuming we will have running  
1245 conditions similar to those achieved in Run-17, we expect to sample at least  $400 \text{ pb}^{-1}$  for  
1246 our rare / non-prescaled triggers. Reducing the Run-22 run time from 20 to 18 cryo-weeks  
1247 would have a significant impact on our physics program described in section 2.1.1. Along  
1248 with the luminosity loss associated with fewer running weeks, STAR will be commissioning  
1249 its newly installed, and critical for the proposed program, forward detector suite which will  
1250 result in additional luminosity being subtracted from physics running. In total, this would  
1251 result in at least 15% less sampled luminosity, as the loss will occur near the end of the run  
1252 when the detectors and RHIC will be operating most efficiently.

1253 STAR also requests at least 11 weeks of polarized  $pp$  data-taking at  $\sqrt{s} = 200 \text{ GeV}$   
1254 and 11 weeks of polarized  $p+\text{Au}$  data-taking at  $\sqrt{s_{NN}} = 200 \text{ GeV}$  during Run-24. All of  
1255 the running will involve transversely polarized protons, with the choice between vertical or  
1256 radial polarization to be determined during the coming year. Based on recent CAD guidance,  
1257 we expect to sample at least  $235 \text{ pb}^{-1}$  of  $pp$  collisions and  $1.3 \text{ pb}^{-1}$  of  $p+\text{Au}$  collisions.  
1258 These totals represent 4.5 times the luminosity that STAR sampled during transversely  
1259 polarized  $pp$  collisions in Run-15, and 3 times the luminosity that STAR sampled during  
1260 transversely polarized  $p+\text{Au}$  collisions in Run-15. Effectively, we request approximately  
1261 equal nucleon-nucleon luminosities for  $pp$  and  $p+\text{Au}$  which is essential to optimize several  
1262 critical, and in many cases luminosity-demanding, measurements that require comparisons of  
1263 the same observable in (polarized or unpolarized)  $pp$  and  $p+\text{Au}$  collisions, described further  
1264 in Section 2.2. Any significant reduction of the available running period, e.g. 20 instead of  
1265 28 weeks, would almost certainly result in the impossibility of fulfilling the unique physics  
1266 goals in Run-24.

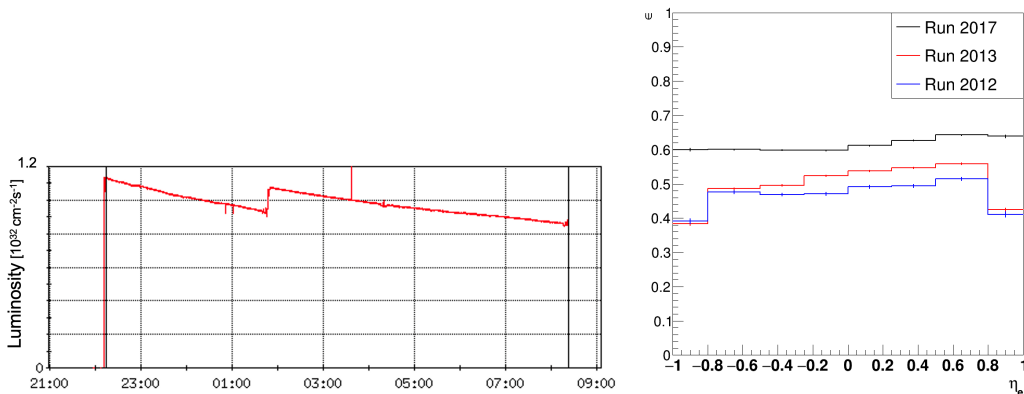


**Figure 38:** Example of the leveled luminosity profile for a fill from Run-17 at 510 GeV (left). The right panel shows the impact of the luminosity leveling on the  $W$  boson reconstruction efficiency. Luminosity leveling was applied during Run-17 but not for Run-12 and Run-13. A higher  $W$  efficiency is clearly seen in Run-17 with the luminosity leveling applied. The more uniform efficiency in Run-17 for two outer lepton- $\eta$  bins is the result of a different cut at  $|\eta| < 0.9$  to remove the detector edge effects.

## 1267 2.1 Run-22 Request for $p^\uparrow p^\uparrow$ Collisions at 510 GeV

### 1268 2.1.1 Inclusive Transverse Spin Asymmetries at Forward Rapidities

1269 The experimental study of spin phenomena in nuclear and particle physics has a long history  
 1270 of producing important, and often surprising, results. Attempts to understand such data  
 1271 have pushed the field forward, forcing the development of both new theoretical frameworks  
 1272 and new experimental techniques. Recent and ongoing detector upgrades at STAR, at mid-  
 1273 and forward-rapidity, coupled with the versatility of RHIC, will allow us to gain new insights  
 1274 into long-standing puzzles, and to probe more deeply the complexities of emergent behavior  
 1275 in QCD.

1276 Results from PHENIX and STAR have shown that large transverse single-spin asymme-  
 1277 tries (TSSA) for inclusive hadron production, first seen in  $pp$  collisions at fixed-target en-  
 1278 ergies and modest  $p_T$ , extend to the highest RHIC center-of-mass energies,  $\sqrt{s} = 510$  GeV,  
 1279 and surprisingly large  $p_T$ . Figure 39 summarizes the world data for the inclusive neutral  
 1280 pion asymmetries  $A_N$  as a function of Feynman- $x$ . The asymmetries are seen to be nearly  
 1281 independent of  $\sqrt{s}$  over the very wide range of roughly 19 to 500 GeV.

1282 To understand the observed TSSAs, one needs to go beyond the conventional leading-  
 1283 twist (twist-2) collinear parton picture for the hard-scattering processes. Two theoretical  
 1284 formalisms have been developed to try to explain these sizable asymmetries in the QCD  
 1285 framework: transverse-momentum-dependent (TMD) parton distribution and fragmentation  
 1286 functions, such as the Sivers and Collins functions; and transverse-momentum-integrated  
 1287 (collinear) quark-gluon-quark correlations, which are twist-3 distributions in the initial state  
 1288 proton or in the fragmentation process. For many of the experimentally accessible spin  
 1289 asymmetries, several of these functions can contribute, and need to be disentangled in order

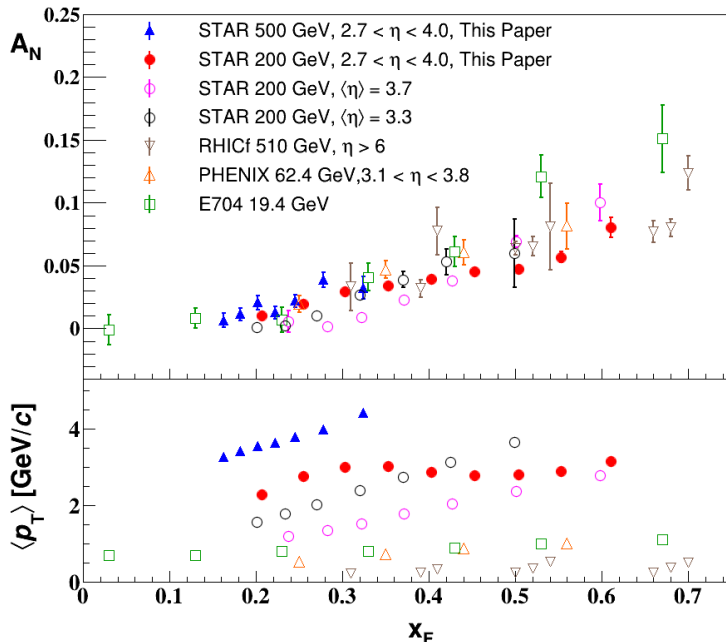


**Figure 39:** Transverse single-spin asymmetry  $A_N$  measurements for neutral pion in  $pp$  collisions at different center-of-mass energies as a function of Feynman- $x$  [36].

1290 to understand the experimental data in detail, in particular the observed  $p_T$  dependence.  
 1291 These functions manifest their spin dependence either in the initial state—for example, the  
 1292 Sivers distribution and its twist-3 analog, the Efremov-Teryaev-Qiu-Sterman (ETQS) func-  
 1293 tion [262]—or in the final state via the fragmentation of polarized quarks, such as in the  
 1294 Collins function and related twist-3 function  $\hat{H}_{FU}(z, z_z)$ .

1295 Incorporating the fragmentation term within the collinear twist-3 approach demonstrated  
 1296 the ability of this formalism to describe the large values of  $A_N$  for  $\pi^0$  production observed at  
 1297 RHIC [187]. In this work, the relevant (non-pole) 3-parton collinear fragmentation function  
 1298  $\hat{H}_{FU}(z, z_z)$  was fit to the RHIC data. The so-called soft-gluon pole term, involving the ETQS  
 1299 function  $T_{q,F}(x_1, x_2)$ , was also included by fixing  $T_{q,F}$  through its well-known relation to the  
 1300 TMD Sivers function  $f_{1T}^\perp$ . The authors obtained a very good description of the data due to  
 1301 the inclusion of the non-pole fragmentation function and based on this work they were able  
 1302 to make predictions for  $\pi^+$  and  $\pi^-$  production asymmetries  $A_N$  at the forward rapidities  
 1303 covered by the STAR upgrades,  $2.5 < \eta < 4$ . The results are shown in Fig. 40 for  $\sqrt{s} = 200$   
 1304 and 500 GeV for two rapidity ranges,  $2 < \eta < 3$  and  $3 < \eta < 4$ .

1305 In Run-22, with the full suite of forward tracking detectors and calorimetry installed,  
 1306 STAR will for the first time be able to map out inclusive charged-hadron asymmetries up to  
 1307 the highest energies achievable at RHIC and at these forward rapidities in the Feynman- $x$   
 1308 region  $0.2 < x_F < 0.7$ . It would be very interesting to confirm that these asymmetries are  
 1309 indeed largely independent of center-of-mass energy. The measurements of  $A_N$  for charged  
 1310 hadrons, together with analogous data (from Run-22 as well as previous STAR runs) on

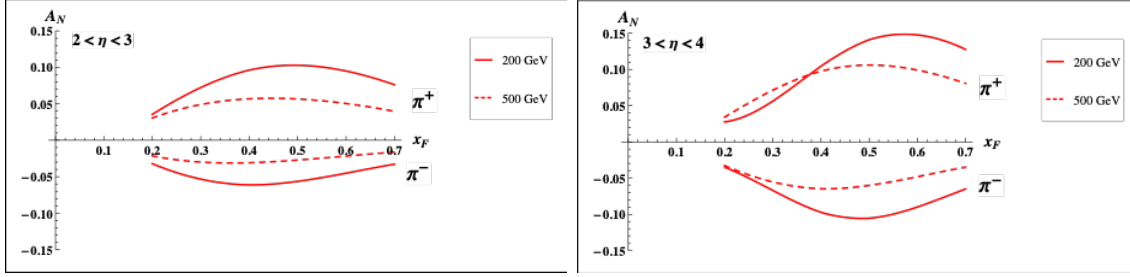


**Figure 40:** Predictions for  $A_N$  for  $\pi^+$  and  $\pi^-$  production over the ranges  $2 < \eta < 3$  (left) and  $3 < \eta < 4$  (right) at  $\sqrt{s} = 200$  GeV (solid lines) and 500 GeV (dashed lines).

1311  $A_N$  for direct photons and neutral pions, should provide the best data set in the world  
 1312 to constrain the evolution and flavor dependence of the twist-3 ETQS distributions and to  
 1313 determine if the 3-parton collinear fragmentation function  $\hat{H}_{FV}$  is the main driver of the  
 1314 large forward inclusive asymmetries. The expected separation power between positively and  
 1315 negatively charged hadrons in the pseudorapidity region  $2.5 < \eta < 4$  with the STAR forward  
 1316 upgrade is presented in Figure 41.

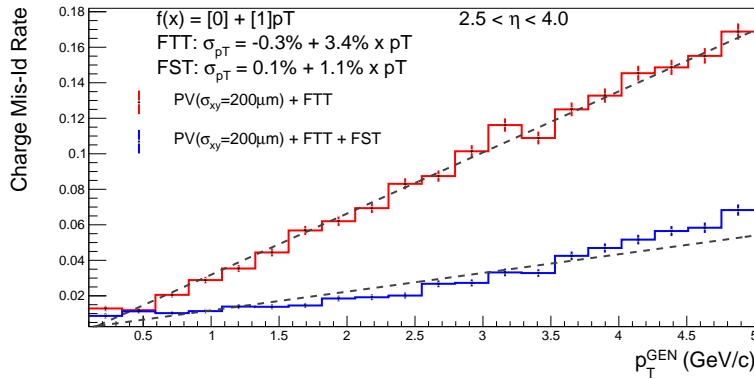


**Figure 41:** The expected charge mis-identification rate as a function of particle  $p_T$  in the pseudo-rapidity region  $2.5 < \eta < 4$  with the STAR forward upgrade. The results in blue correspond to full tracking system including both sTGC and silicon detectors and the red ones include sTGC only.

### 1317 2.1.2 Siverson and Efremov-Teryaev-Qiu-Sterman Functions

1318 There is great theoretical interest in testing the relation between the ETQS correlation  
 1319 functions and the Siverson function. As discussed above, both the Siverson and the ETQS  
 1320 functions encapsulate partonic spin correlations within the proton, but they are formally  
 1321 defined in different frameworks. While the Siverson function is a TMD quantity that depends  
 1322 explicitly on spin-dependent transverse partonic motion  $k_T$ , the ETQS function is a twist-3  
 1323 collinear distribution, in which SSAs are generated through soft collinear gluon radiation.

1324 Measurements of forward jet production from the ANDY collaboration [94] indicated  
 1325 rather small asymmetries. This was argued to be consistent with the idea that the twist-3

1326 parton correlation functions for up and down valence quarks should cancel, because their  
 1327 behavior reflects the Siverson functions extracted from fits to the SIDIS data that demonstrate  
 1328 opposite sign, but equal magnitude, up and down quark Siverson functions. Preliminary STAR  
 1329 results on charge-tagged dijets at mid-rapidity [227] (see Fig. 46) support this interpretation,  
 1330 with the caveat that the measured observable (a spin-dependent  $\langle k_T \rangle$ ) is defined in the TMD,  
 1331 and not the twist-3, framework. Moreover, recently published STAR results for forward  
 1332 inclusive electromagnetic jets [36] also show small TSSA as seen in Fig. 42. The results have  
 1333 been analyzed with the generalized parton model approach [96], and when incorporated  
 1334 in the reweighing procedure of the quark Siverson functions extracted from SIDIS data they  
 1335 significantly improved its uncertainty at larger momentum fraction  $x$  (see Fig. 43).

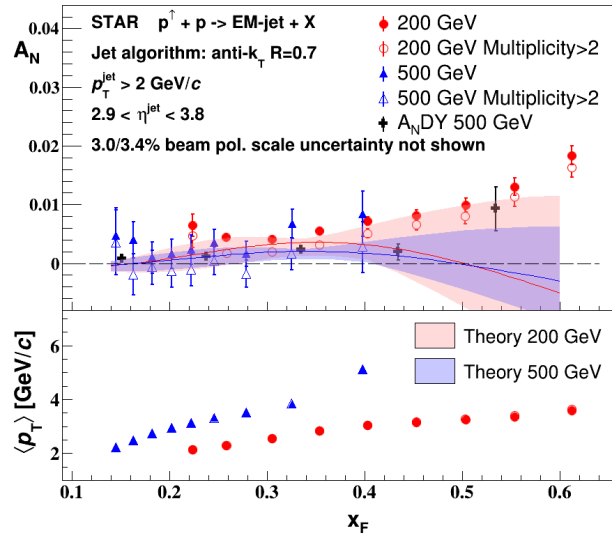


**Figure 42:** New STAR results on inclusive electromagnetic jets TSSA in  $pp$  collisions at both 200 and 500 GeV [36]. The results that require more than two photons observed inside a jet are shown as open symbols. Theory curves [149] for TSSA of full jets at rapidity  $\langle y \rangle = 3.25$  for 200 GeV (red) and  $\langle y \rangle = 3.57$  for 500 GeV (blue) are also shown. The average  $p_T$  of the jet for each  $x_F$  bin is shown in the lower panel.

1336 To better test quantitatively the relation between the twist-3 and TMD regimes, one  
 1337 can measure spin asymmetries for jets which are *intentionally* biased towards up or down  
 1338 quark jets via detection of a high- $z$  charged hadron within the jet. Figure 44 shows the  
 1339 flavor of initial partons for positively and negatively charged leading hadrons in the rapidity  
 1340 range  $2.6 < \eta < 4.1$  for different regions of Feynman- $x$  based on PYTHIA Minimum Bias  
 1341 studies for  $pp$  at 510 GeV. For  $x_F > 0.2$  one can see a significant enhancement of the  $u$ -  
 1342 quark contribution for positively charged leading hadrons, and the  $d$ -quark contribution for  
 1343 negatively charged ones.

1344 Higher-twist calculations of jet asymmetries based on the Siverson function predict sizeable  
 1345 effects for these flavor-enhanced jets. With the suite of new forward detectors installed  
 1346 at STAR, full jet reconstruction, along with identification of a high- $z$  hadron of known

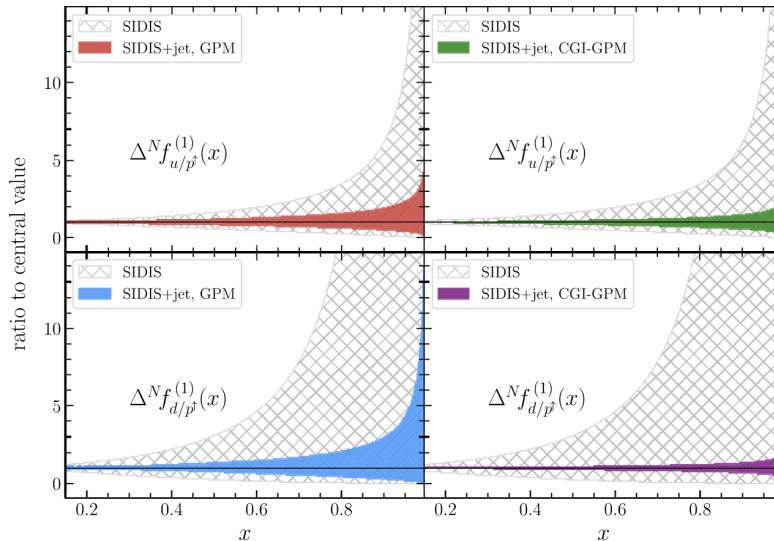


**Figure 43:** Comparison between the Sivers function first moments normalized to the corresponding central value from SIDIS data and their reweighted counterparts that incorporate new STAR results on electromagnetic jets [36] extracted in [96] in the generalized parton model (left panels) and color gauge invariant generalized parton model (right panels) framework. In both plots, results for  $u$  (upper panels) and  $d$  (lower panels) quarks are shown.

1347 charge sign (see Fig. 41), will be possible at high pseudorapidity. Using realistic simulation  
 1348 of the forward calorimeter, and requiring a charged hadron with  $z > 0.5$ , the expected  
 1349 statistical uncertainties of asymmetries has been extracted and are presented in Fig. 45.  
 1350 The simulations have assumed an integrated luminosity of  $350 \text{ pb}^{-1}$  at  $\sqrt{s} = 510 \text{ GeV}$ .  
 1351 No tracking or hadron reconstruction has been included, and the trigger effects have been  
 1352 accounted for by applying jet  $p_T$  thresholds (4, 6, 7.5 GeV/ $c$ ) for jet-patch triggers in two  
 1353 pseudo-rapidity regions spanning  $2.5 < \eta < 3.5$  and  $3 < \eta < 4$  respectively. A similar  
 1354 measurement is also expected at 200 GeV. Figure 45 also compares the Run-22 projections  
 1355 to the single spin asymmetries calculated by the ETQS function, based on the SIDIS Sivers  
 1356 functions.

1357 In a TMD framework, the Sivers effect manifests itself as a correlation (a triple product)  
 1358 between the transverse momentum of a parton ( $\vec{k}_T$ ) with momentum fraction  $x$ , and the  
 1359 transverse spin ( $\vec{S}$ ) of a polarized proton moving in the longitudinal ( $\vec{p}$ ) direction. Thus,  
 1360 for transversely polarized protons, the Sivers effect probes whether the  $k_T$  of the constituent  
 1361 quarks is preferentially oriented in a direction perpendicular to both the proton momentum  
 1362 and its spin. Momentum conservation then implies that the two jets in the final state will  
 1363 not emerge back-to-back on average, but instead will ‘tilt’ in the direction of the summed  
 1364  $k_T$  of the initial state partons. Moreover, the (average) tilt of interest will reverse direction  
 1365 under a ‘flip’ of the proton spin; a spin-dependent  $\langle k_T \rangle$  can then be extracted by associating  
 1366 the azimuthal opening angle of the jet pair with this tilt.

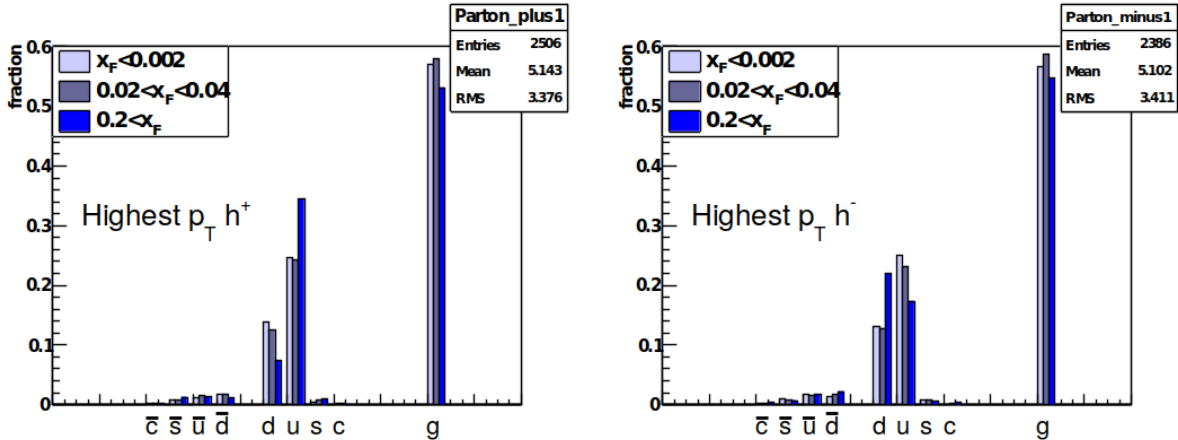


**Figure 44:** Flavor of initial partons for events with positively (left) and negatively (right) charged leading hadrons in the rapidity range  $2.6 < \eta < 4.1$  for different regions of Feynman- $x$  based on PYTHIA Minimum Bias studies for  $pp$  at 510 GeV. For  $x_F > 0.2$  one can see an enhancement of the  $u$ -quark contribution for positively charged leading hadrons, and the  $d$ -quark contribution for negatively charged ones.

1367 STAR carried out an earlier measurement of this transverse single-spin asymmetry using  
 1368 a dijet dataset with  $\sim 1 \text{ pb}^{-1}$  of integrated luminosity [12], and found it to be consistent  
 1369 with zero within  $2\sigma$ . An ongoing and much improved analysis based on Run-12 and Run-15  
 1370 has past STAR paper preview process, and the preliminary results can be found in [227].  
 1371 Perhaps most significantly, the jets were sorted according to their net charge  $Q$ , calculated  
 1372 by summing the signed momentum of all particle tracks with  $p > 0.8 \text{ GeV}$ , to minimize  
 1373 underlying event contributions, yielding jet samples with enhanced contributions from  $u$   
 1374 quarks (positive  $Q$ ) and  $d$  quarks (negative  $Q$ ), with a large set near  $Q = 0$  dominated by  
 1375 gluons. Simple kinematics allow for conversion from the spin-dependent ‘tilt’ of the dijet  
 1376 pair to a value of  $k_T$  on an event-by-event basis; these are then sorted by the  $Q$  of the jet  
 1377 and binned by the summed pseudorapidities of the outgoing jets,  $\eta^{\text{total}} \equiv \eta_3 + \eta_4$ . Because  
 1378 the contributions of different partons ( $u$ ,  $d$ , all else) to  $\langle k_T \rangle$  vary with both  $Q$  and also  $\eta^{\text{total}}$ ,  
 1379 in a way that can be estimated robustly using simulation, the data can be inverted to yield  
 1380 values of  $\langle k_T \rangle$  for the individual partons, though with coarser binning in  $\eta^{\text{total}}$ . Figure 46  
 1381 shows the preliminary results for the spin-dependent  $\langle k_T \rangle$  values for  $u$ ,  $d$  and *gluon + sea*.

1382 With the new forward detectors in place, along with the enhanced reach in  $\eta$  afforded by  
 1383 the iTPC, this technique can be expanded in Run-22 to cover pseudorapidities at STAR from  
 1384 roughly  $-1$  to  $4$ , though with a gap at  $1.5 < \eta < 2.5$ . Despite this gap, values of  $\langle k_T \rangle$  can be  
 1385 extracted for  $u$  and  $d$  quarks for  $\eta^{\text{total}}$  ranging from  $\sim -1.5$  to as high as  $7$  with reasonable  
 1386 statistics. This latter regime will probe  $2 \rightarrow 2$  hard scattering events in which  $x_1 \gg x_2$ ,  
 1387 *i.e.*, a sample enriched in valence quarks interacting with low- $x$  gluons. Such measurements,  
 1388 exploiting the full kinematic reach of STAR, will not only allow precise determinations of  
 1389 the average transverse partonic motion,  $\langle k_T \rangle$ , exhibited by individual partonic species in

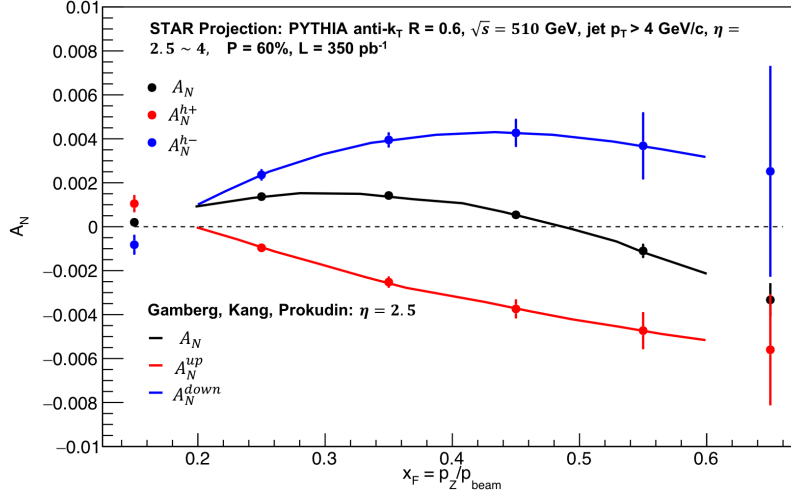


**Figure 45:** Up quark (red line), down quark (blue line) and all jet (black line) single spin asymmetries as a function of  $x_F$  as calculated by the ETQS function, which is based on the SIDIS Sivvers functions, for 200 GeV center-of-mass energy proton collisions – the 510 GeV results are expected to be qualitatively similar. Overlaid on the theory curves are the expected experimental sensitivities for jet asymmetries tagging in addition a positive hadron with  $z$  above 0.5 (red points), a negative hadron with  $z$  above 0.5 (blue points) or all jets (black) as a function of  $x_F$  at 510 GeV.

1390 the initial state, but will provide important information on the  $x$  dependence of the proton  
 1391 Sivvers functions.

1392 Collisions at  $\sqrt{s} = 510$  GeV will also allow STAR to continue our successful program  
 1393 to study the evolution and sign change of the Sivvers function. By focusing on interactions  
 1394 in which the final state involves only weakly interacting particles, and hence the transverse  
 1395 partonic motion (in a TMD framework) or the collinear gluon radiation (in twist-3) must be  
 1396 in the initial state, one can test for the predicted sign change in  $A_N$  relative to interactions  
 1397 in which these terms must appear in the final state, such as SIDIS measurements. Following  
 1398 the low statistics Run-11 proof-of-principle measurement, STAR has measured  $A_N$  in  $W$  and  
 1399  $Z$  in Run-17, which had about 14 times more integrated luminosity than Run-11. Figure 47  
 1400 compares the reconstructed  $Z$  mass between combined Runs-11+12+13 and Run-17. From  
 1401 the comparison one can see a consistent mass spectrum and the clearly visible  $Z$  mass  
 1402 peak. The Run-17 preliminary  $Z$  and  $W^\pm$   $A_N$  results plotted as a function of reconstructed  
 1403 boson rapidity are shown in Figs. 48 and 49, respectively. The systematic uncertainties  
 1404 assigned to the  $W$   $A_N$  preliminary results were estimated by varying the various cut criteria,  
 1405 in particular the lepton  $E_T$  cut, according to the Barlow criteria. A more sophisticated  
 1406 uncertainty estimation is currently underway. With the increased precision provided by  
 1407 Run-17 we find smaller asymmetries than were suggested by Run-11. As a result it is critical  
 1408 that we increase the statistics of our dataset with Run-22 to improve the precision of our  
 1409 asymmetry measurements in order to provide a conclusive test of the Sivvers' function sign  
 1410 change.

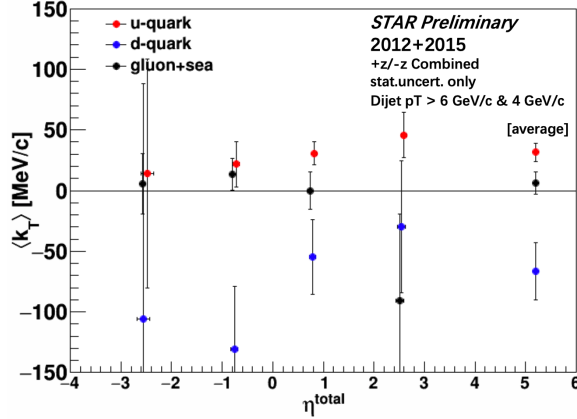


**Figure 46:** Preliminary results for the spin-dependent  $\langle k_T \rangle$  values for  $u$ ,  $d$  and  $gluon+sea$  from the dijet Sivers measurement as a function of the sum of dijet pseudorapidities  $\eta_1 + \eta_2 \sim \ln(\frac{x_1}{x_2})$  [227].

1411 The improved tracking capabilities provided by the iTPC upgrade will allow us to push  
 1412 our mid-rapidity  $W^\pm$  and  $Z$  measurements to larger rapidity  $y_{W/Z}$ , a regime where the  
 1413 asymmetries are expected to increase in magnitude and the anti-quark Sivers' functions  
 1414 remain largely unconstrained. In addition to the noted extension of our kinematic reach, an  
 1415 additional 16 weeks of beam time at  $\sqrt{s} = 510$  GeV in Run-22 would increase our dataset by  
 1416 about a factor of 2. This experimental accuracy would significantly enhance the quantitative  
 1417 reach of testing the limits of factorization and universality in lepton-proton and proton-  
 1418 proton collisions.

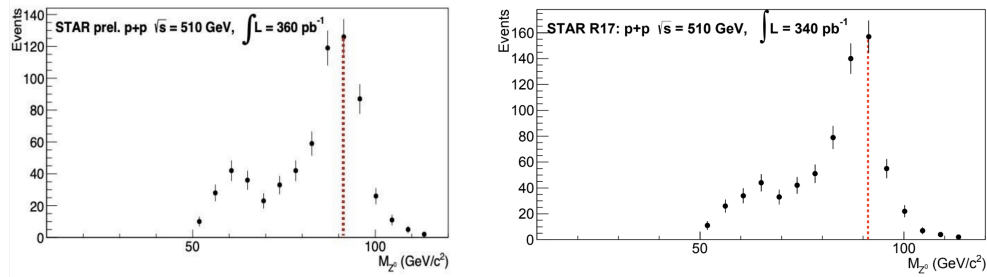


**Figure 47:** [PLACE HOLDER - Put both distributions onto the same canvas] Preliminary results for the reconstructed  $Z$  boson mass for Run-11 + 12 +13 (left) and Run-17 (right).

### 1419 2.1.3 Transversity, Collins Function and Interference Fragmentation Function

1420 A complete picture of nucleon spin structure at leading twist must include contributions  
 1421 from the unpolarized and helicity distributions, as well as those involving transverse polar-  
 1422 ization, such as the transversity distribution [175, 245, 265]. The transversity distribution  
 1423 can be interpreted as the net transverse polarization of quarks within a transversely polar-  
 1424 ized proton. The difference between the helicity and transversity distributions for quarks

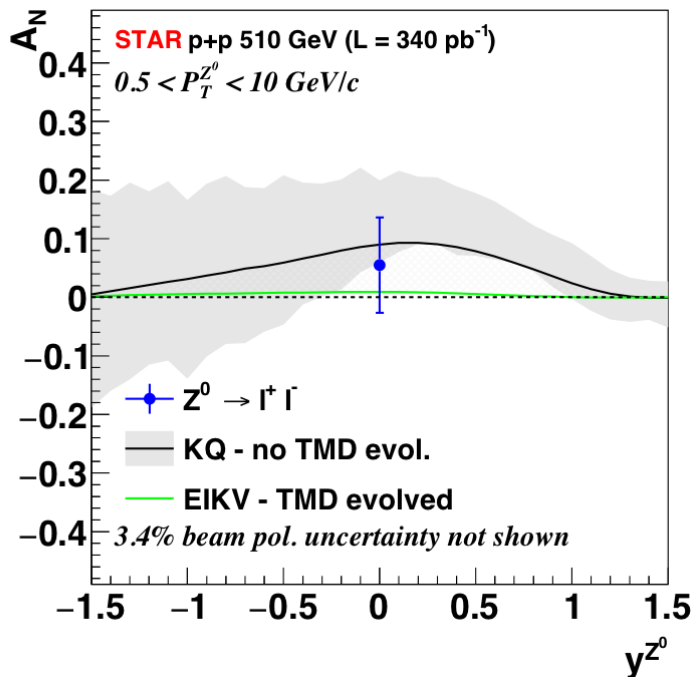


**Figure 48:** [PLACE HOLDER - Update theory curves] Preliminary results for the transverse single-spin asymmetries of  $Z$  boson as a function of rapidity for Run-17. The dark and light green lines are theoretical predictions from the KQ [193] and EIKV [299] groups, respectively, folding in data on the sea-quark Sivers functions.

1425 and antiquarks provides a direct,  $x$ -dependent connection to nonzero orbital angular mo-  
 1426 mentum components in the wave function of the proton [289]. Recently, the first lattice  
 1427 QCD calculation of the transversity distribution has been performed [76]. In addition,  
 1428 the measurement of transversity has received substantial interest as a means to access the  
 1429 tensor charge of the nucleon, defined as the integral over the valence quark transversity:  
 1430  $\delta q^a = \int_0^1 [\delta q^a(x) - \delta \bar{q}^a(x)] dx$  [174, 175]. Measuring the tensor charge is very important for  
 1431 several reasons. First, it is an essential and fundamental quantity to our understanding of  
 1432 the spin structure of the nucleon. Also, the tensor charge can be calculated on the lattice  
 1433 with comparatively high precision, due to the valence nature of transversity, and hence is  
 1434 one of the few quantities that allow us to compare experimental results on the spin structure  
 1435 of the nucleon directly to *ab initio* QCD calculations. Finally, the tensor charge describes  
 1436 the sensitivity of observables in low-energy hadronic reactions to beyond the standard model  
 1437 physics processes with tensor couplings to hadrons. Examples are experiments with ultra-  
 1438 cold neutrons and nuclei.

1439 Transversity is difficult to access due to its chiral-odd nature, requiring the coupling of  
 1440 this distribution to another chiral-odd distribution. Semi-inclusive deep-inelastic scattering  
 1441 (SIDIS) experiments have successfully probed transversity through two channels: asym-  
 1442 metric distributions of single pions, convoluting the TMD transversity distribution with

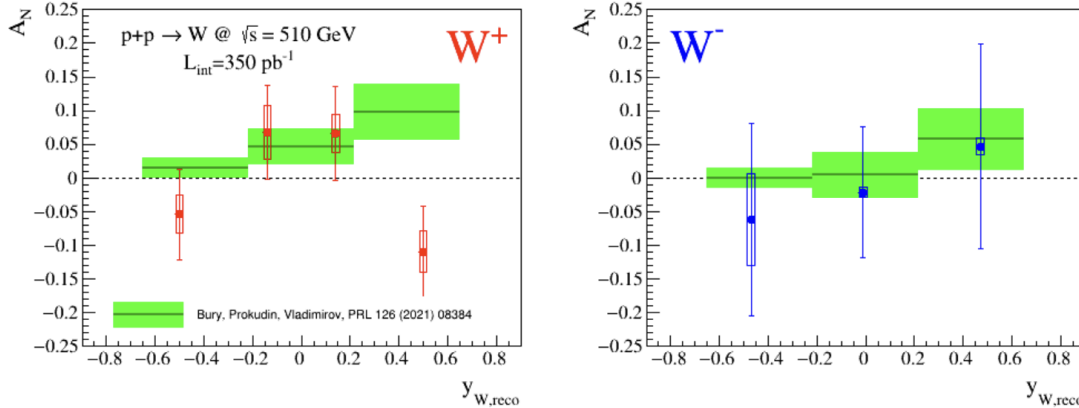


**Figure 49:** [PLACE HOLDER - Update syst. errors] Preliminary results for the transverse single-spin asymmetries of  $W^\pm$  bosons as a function of their rapidity for Run-17. The green lines and boxes are theoretical predictions from [108] using data from SIDIS, pion-induced polarized Drell-Yan, and  $W^{+/-}/Z^0$ -boson  $A_N$  STAR measurements from Run-11.

1443 the TMD Collins fragmentation function, and azimuthally asymmetric distributions of di-  
 1444 hadrons, coupling transversity to the so-called “interference fragmentation function” (IFF)  
 1445 in the framework of collinear factorization. Yet in spite of a wealth of lepton-scattering  
 1446 data, the kinematic reach of existing SIDIS experiments limits the precision with which the  
 1447 proton’s transversity can be extracted, as the range of Bjorken- $x$  values that can be accessed  
 1448 does not extend above  $x \sim 0.3$ .

1449 In hadronic collisions, the  $k_T$  integrated quark transversity distribution may be accessed  
 1450 mainly via two channels. The first is the single spin asymmetry of the azimuthal distribution  
 1451 of hadrons in high energy jets [191]. In the jet+hadron channel, the collinear transversity  
 1452 distribution couples to the TMD Collins function [191, 192]. This makes  $pp$  collisions a more  
 1453 direct probe of the Collins fragmentation function than Collins asymmetries in SIDIS [191],  
 1454 where a convolution with the TMD transversity distribution enters. This also makes the  
 1455 Collins asymmetry in  $pp$  collisions an ideal tool to explore the fundamental QCD questions  
 1456 of TMD factorization, universality, and evolution. The second channel is the single spin  
 1457 asymmetry of pion pairs, where transversity couples to the collinear interference fragmen-  
 1458 tation function [121]. STAR mid-rapidity IFF data [45] have been included in the first  
 1459 extraction of transversity from SIDIS and proton-proton IFF asymmetries [263]. In addi-  
 1460 tion, transverse spin transfer,  $D_{TT}$ , of  $\Lambda$  hyperons in  $pp$  collisions is also expected to be able  
 1461 to provide sensitivity for the strange quark transversity through the polarized fragmenta-  
 1462 tion functions. The strange quark transversity is not constrained at all currently. The first  
 1463  $D_{TT}$  measurement of  $\Lambda$  and  $\bar{\Lambda}$  hyperons at  $\sqrt{s} = 200$  GeV has been performed with the  
 1464 Run-12  $pp$  dataset [28], and current results didn’t indicate a sizable spin transfer yet. The  
 1465 iTPC upgrade will help to reach near-forward pseudo-rapidity  $\eta < 1.5$  for the spin transfer  
 1466 measurements.

1467 The universality of TMD PDFs and fragmentation functions in  $pp$  collisions has been an

1468 open question. General arguments [120, 270] have shown that factorization can be violated  
 1469 in hadron-hadron collisions for TMD PDFs like the Sivers function, though very recent  
 1470 calculations indicate the violations might be quite small [190, 228]. In contrast, while there  
 1471 is no general proof that the Collins effect in  $pp$  collisions is universal to all orders, explicit  
 1472 calculations [191, 192, 324, 325] have shown that diagrams like those that violate factorization  
 1473 of the Sivers function make no contribution to the Collins effect at the one- or two-gluon  
 1474 exchange level, thereby preserving its universality at least to that level.

1475 Comparisons of the transversity distributions extracted from the Collins and IFF channels  
 1476 will allow STAR to study the size and nature of any factorization breaking effects for TMD  
 1477 observables in hadronic collisions. Likewise, comparisons with the transversity, Collins and  
 1478 IFF distributions extracted from SIDIS collisions will shed light on universality and constrain  
 1479 evolution effects. The measurement of evolution effects in TMD distributions is particularly  
 1480 important because, unlike the collinear case, TMD evolution contains a non-perturbative  
 1481 component that cannot be calculated directly. Measurements at  $\sqrt{s}$  of 200 and 510 GeV will  
 1482 provide additional experimental constraints on evolution effects and provide insights into the  
 1483 size and nature of TMD observables at the future Electron-Ion Collider.

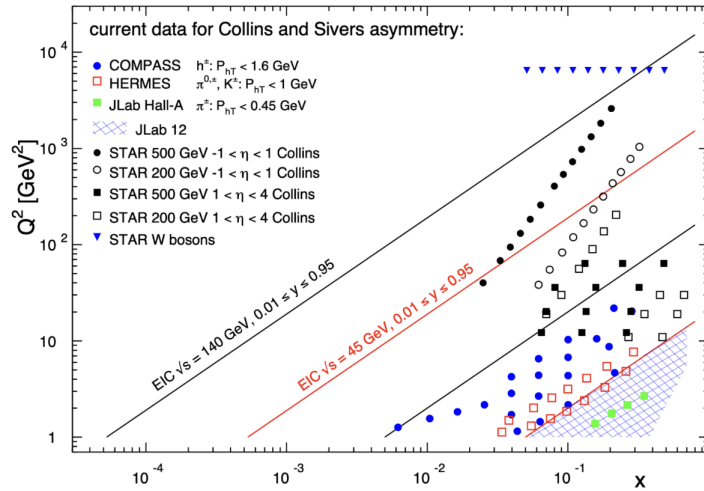


**Figure 50:**  $x - Q^2$  coverage of RHIC measurements compared to existing Collins and Sivers effect measurements in SIDIS and the future coverage of the EIC.

1484 Extending measurements of di-hadron and Collins asymmetries to the forward direction  
 1485 during Run-22 will allow access to transversity in the region  $x > 0.3$ . This valence quark  
 1486 region is not currently probed by any experiments and is essential for the determination of  
 1487 the tensor charge, which receives 70% of its contributions from  $0.1 < x < 1.0$ . In addition,  
 1488 probing transversity in  $pp$  collisions also provides better access to the  $d$ -quark transversity  
 1489 than is available in SIDIS, due to the fact that there is no charge weighting in the hard  
 1490 scattering QCD  $2 \rightarrow 2$  process in  $pp$  collisions. This is a fundamental advantage of  $pp$   
 1491 collisions, as any SIDIS measurement of the  $d$ -quark transversity has to be on a bound  
 1492 system, *e.g.* He-3, which ultimately requires nuclear corrections to extract distributions.

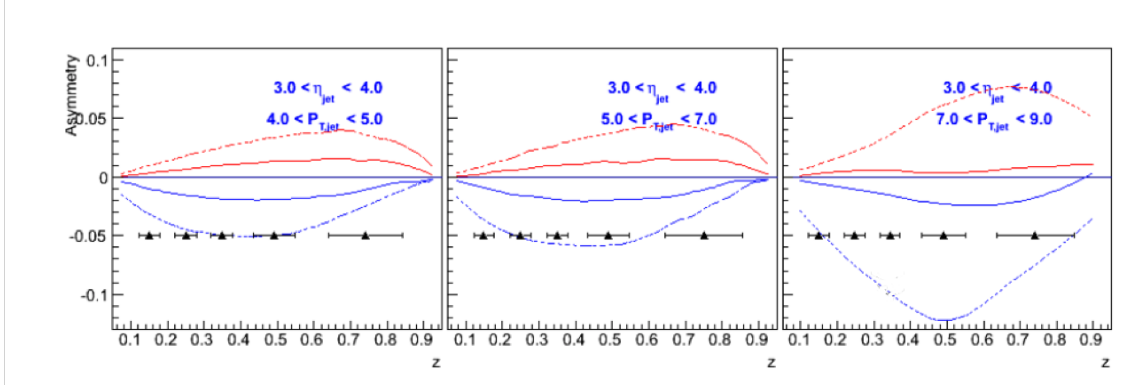


**Figure 51:** Expected  $h^-$  Collins asymmetry uncertainties at  $3 < \eta < 4$  (black points) from a sampled luminosity of  $350 \text{ pb}^{-1}$  at  $\sqrt{s} = 510 \text{ GeV}$ , compared to positive (red) and negative (blue) pion asymmetries based on the Torino extraction (full lines) and the Soffer bound (dashed lines) as a function of hadron  $z$  for bins in jet  $p_T$ . Most uncertainties are smaller than the height of the triangles.

1493 The high scale we can reach in 500 GeV collisions at RHIC has allowed STAR [56] to  
 1494 demonstrate, for the first time, that previous SIDIS measurements at low scales are in fact  
 1495 accessing the nucleon at leading twist. Figure 50 shows the  $x - Q^2$  coverage spanned by  
 1496 the RHIC measurements compared to the future EIC, JLab-12, and the current SIDIS world  
 1497 data.

1498 Another fundamental advantage of  $pp$  collisions is the ability to access gluons directly.  
 1499 While gluons cannot be transversely polarized in a transversely polarized spin 1/2 hadron,  
 1500 they can be linearly polarized. Similarly, there exists an equivalent of the Collins fragmen-  
 1501 tation function for the fragmentation of linearly polarized gluons into unpolarized hadrons [78].  
 1502 The linear polarization of gluons is a largely unexplored phenomenon, but it has been a focus  
 1503 of recent theoretical work, in particular due to the relevance of linearly polarized gluons in  
 1504 unpolarized hadrons for the  $p_T$  spectrum of the Higgs boson measured at the LHC. Polar-  
 1505 ized proton collisions with  $\sqrt{s} = 510 \text{ GeV}$  at RHIC, in particular for asymmetric parton  
 1506 scattering if jets are detected in the backward direction, are an ideal place to study the  
 1507 linearly polarized gluon distribution in polarized protons. (Note that the distributions of  
 1508 linearly polarized gluons inside an unpolarized and a polarized proton provide independent  
 1509 information). A first measurement of the ‘‘Collins-like’’ effect for linearly polarized gluons  
 1510 has been done by STAR with data from Run-11 [56], providing constraints on this function  
 1511 for the first time.

1512 Figure 51 shows projected  $h^-$  Collins asymmetry uncertainties along with  $\pi^+/-$  Collins  
 1513 asymmetries from theory calculations at 510 GeV with the Forward Upgrade during Run-22.  
 1514 Figure 52 shows STAR’s expected  $h^\pm$  Collins asymmetry corresponding to the kinematic  
 1515 regions shown in Fig. 51, but with a zoomed in vertical scale. As indicated on the figure, jets  
 1516 with  $2.5 < \eta < 4$  and  $4 < p_T < 9 \text{ GeV}/c$  will explore transversity in the important region  
 1517  $0.3 < x < 0.5$  that has not yet been probed in SIDIS. A realistic momentum smearing of final  
 1518 state hadrons as well as jets in this rapidity range was assumed and dilutions due to beam

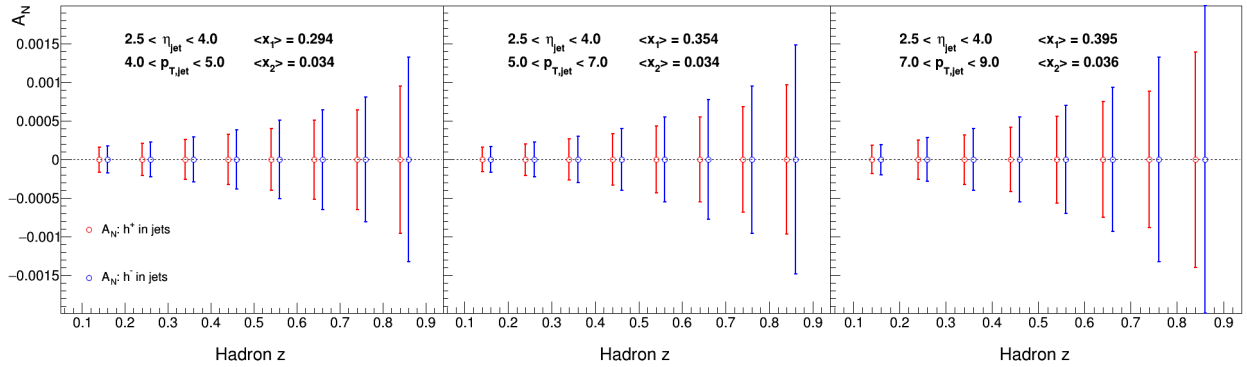


**Figure 52:** Expected  $h^\pm$  Collins asymmetry uncertainties at  $2.5 < \eta < 4$  for the three momentum bins shown in Fig. 51, based on a sampled luminosity of  $350 \text{ pb}^{-1}$  at  $\sqrt{s} = 510 \text{ GeV}$ .

1519 remnants (which become substantial at rapidities close to the beam) and underlying event  
1520 contributions have been taken into account. As no dedicated particle identification at forward  
1521 rapidities will be available for these measurements, only charged hadrons were considered.  
1522 This mostly reduces the expected asymmetries due to dilution by protons (10-14%) and a  
1523 moderate amount of kaons (12-13%). As anti-protons are suppressed compared to protons  
1524 in the beam remnants, especially the negative hadrons can be considered a good proxy for  
1525 negative pions ( $\sim 78\%$  purity according to PYTHIA6). Given their sensitivity to the down  
1526 quark transversity via favored fragmentation, they are particularly important since SIDIS  
1527 measurements, due to their electromagnetic interaction, are naturally dominated by up-  
1528 quarks. We have estimated our statistical uncertainties based on an accumulated luminosity  
1529 of  $350 \text{ pb}^{-1}$ , which leaves nearly invisible uncertainties after smearing. These expected  
1530 uncertainties are compared to the asymmetries obtained from the transversity extractions  
1531 based on SIDIS and Belle data [79] as well as from using the Soffer positivity bound for  
1532 the transversity PDF [294]. More recent global fits have slightly different central up and  
1533 down quark transversity distributions. But due to the lack of any SIDIS data for  $x > 0.3$ ,  
1534 the upper uncertainties are compatible with the Soffer bounds. This high- $x$  coverage will  
1535 give important insights into the tensor charge, which is essential to understand the nucleon  
1536 structure at leading twist.

1537 Although the studies presented here are for the Collins asymmetries, the resulting sta-  
1538 tistical uncertainties will be similar for other measurements using azimuthal correlations of  
1539 hadrons in jets. One important example is the measurement of ‘‘Collins-like’’ asymmetries to  
1540 access the distribution of linearly polarized gluons. As described earlier, the best kinematic  
1541 region to access this distribution is at backward angles with respect to the polarized proton  
1542 and at small jet  $p_T$ . Figure 51 shows that a high precision measurement of the distribution  
1543 of linearly polarized gluons down to  $x \sim 0.005$  will be performed concurrently.

1544 It is also important to recognize that these hadron-in-jet measurements with the STAR  
1545 Forward Upgrade will provide very valuable experience detecting jets close to beam rapidity  
1546 that will inform the planning for future jet measurements in similar kinematics at the EIC.

1547 While the STAR Forward Upgrade will provide sensitivity to transversity to the highest  $x$ ,

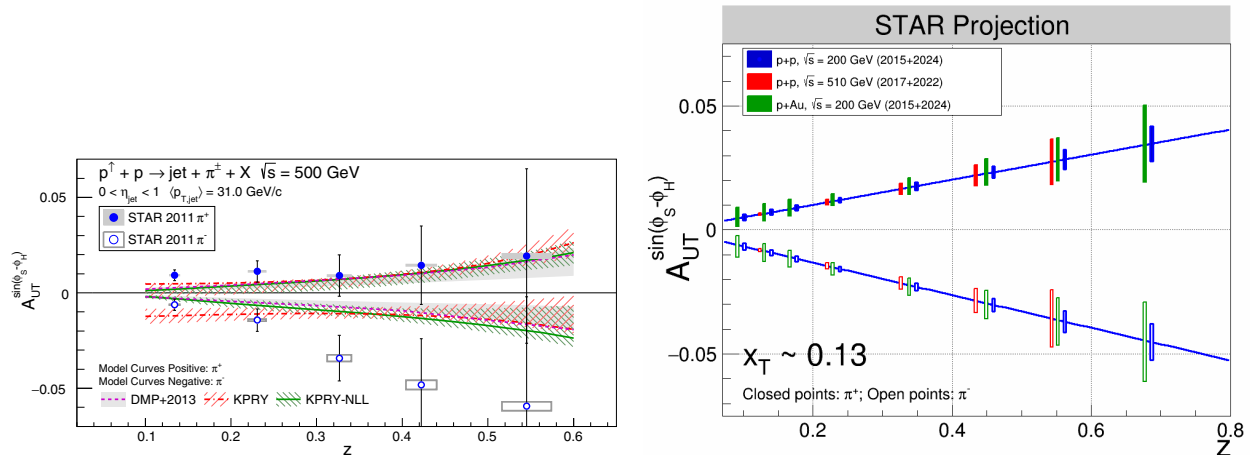


**Figure 53:** The left panel shows STAR measurements of the Collins asymmetry vs. pion  $z$  in 500 GeV  $pp$  collisions from Run-11, compared to several model calculations. See [56] for details. The right panel shows projected statistical uncertainties for STAR Collins asymmetry measurements at  $0 < \eta < 0.9$  in  $pp$  at  $\sqrt{s} = 200$  and 510 GeV and  $p$ -Au at  $\sqrt{s_{NN}} = 200$  GeV. The points have arbitrarily been drawn on the solid lines, which represent simple linear fits to the STAR preliminary 200 GeV  $pp$  Collins asymmetry measurements from 2015. (Note that only one bin is shown spanning  $0.1 < z < 0.2$  for 510 GeV  $pp$  whereas three bins are shown covering the same  $z$  range for the 200 GeV measurements).

1548 concurrent mid-rapidity measurements (see Fig. 50) will provide the most precise information  
 1549 as a function of  $x$ ,  $z$ ,  $j_T$ , and  $Q^2$  to probe questions of TMD factorization, universality, and  
 1550 evolution. The left panel of Fig. 53 shows published STAR measurements of the Collins  
 1551 asymmetry vs. pion  $z$  in 500 GeV Run-11  $pp$  collisions [56]. The results, which represented the  
 1552 first ever observation of the Collins effect in  $pp$  collisions, are consistent at the  $2\sigma$  level with  
 1553 model predictions, with and without TMD evolution, derived from fits to  $e^+e^-$  and SIDIS  
 1554 data [139, 191]. However, greater precision is clearly necessary for a detailed universality  
 1555 test, as well as to set the stage for the EIC.

1556 STAR Run-17 sampled about 14 times the luminosity that we recorded in Run-11. In  
 1557 Run-22, we propose to record another data set equivalent to 16 times the sampled luminos-  
 1558 ity from Run-11. Furthermore, during Run-22 the iTPC will improve the  $dE/dx$  particle  
 1559 identification compared to the previous years. Studies using the  $dE/dx$  distributions seen in  
 1560 our 200 GeV  $pp$  data from Run-15 and the actual  $dE/dx$  resolution improvements that have  
 1561 been achieved during BES-II indicate the iTPC will yield a 20 – 25% increase in the effective  
 1562 figure-of-merit for pions with  $|\eta| < 0.9$ . The right-hand panel of Fig. 53 shows the projected  
 1563 STAR statistical uncertainties for the Collins asymmetry at  $0 < \eta < 0.9$  in 510 GeV  $pp$   
 1564 collisions once the Run-17 and Run-22 data sets are fully analyzed. It’s also important to  
 1565 recognize that the iTPC will also enable STAR to measure the Collins asymmetry over the  
 1566 region  $0.9 < \eta < 1.3$  during Run-22, in addition to the projections that are shown in Fig. 53.

1567 The statistical precision of transversity measured in 510 GeV  $pp$  collisions using IFF  
 1568 asymmetries are expected to be comparable to the statistical improvements from Run-11 [45]

1569 to Run-17 + Run22 shown for the Collins effect data in Fig. 53.

### 1570 2.1.4 Probing Unpolarized Distributions in the Proton

1571 STAR can also provide important information related to unpolarized quark distributions  
 1572 and constrain unpolarized TMD PDFs by measuring the spin integrated  $W$  and  $Z$  cross  
 1573 sections. As discussed in Sec. 1.3, the  $W^+/W^-$  cross-section ratio is sensitive to the  $\bar{d}/\bar{u}$   
 1574 quark distribution, providing complimentary information to Drell-Yan experiments [136,306].  
 1575 Recent results from STAR [42] have been shown to not only have an impact on constraining  
 1576 the  $\bar{d}/\bar{u}$  quark distribution, but other quark distributions as well [255]. Figure 54 shows  
 1577 the uncertainty on PDF distributions where STAR data was included in the global analysis  
 1578 relative to the uncertainties where it was not. This global analysis shows about 30% relative  
 1579 uncertainty reduction in the region  $0.2 < x < 0.3$ . An additional 16 weeks of running during  
 1580 Run-22 would yield similar statistics as was achieved in Run-17. Combining our already  
 1581 measured datasets with what would be collected during Run-22 would provide a precision  
 1582 measurement of  $W^+/W^-$  consisting of about  $1000 \text{ pb}^{-1}$ . Furthermore, STAR's  $Z$  differential  
 1583 cross section as a function of the boson  $p_T$  can serve as input to constrain unpolarized TMD  
 1584 PDFs. Figure 55 shows preliminary results for the Run-11, 12, 13, and 17 combined datasets.

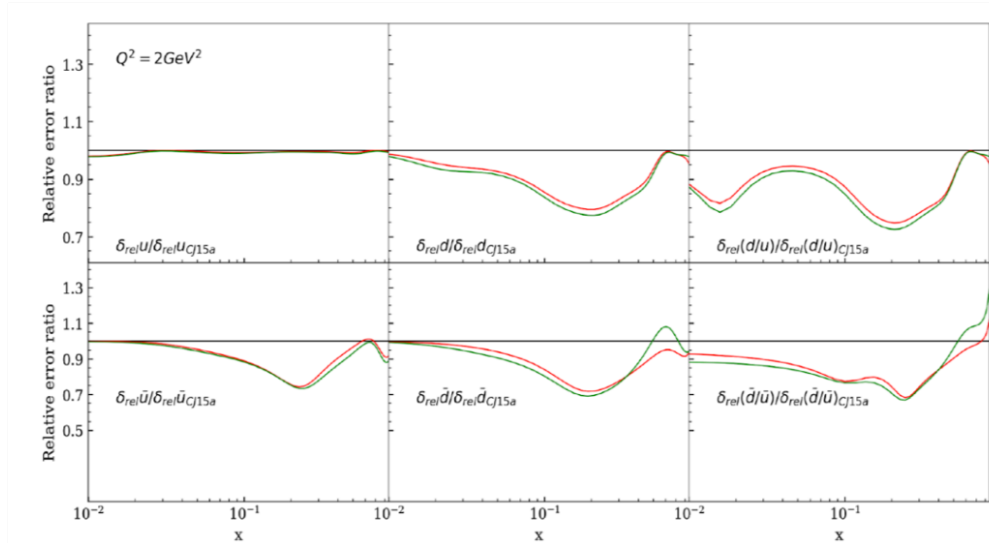


**Figure 54:** CJ collaboration global analysis comparing the uncertainties on unpolarized PDF distributions where STAR data was included in the analysis relative to the uncertainties where it was not [255].

### 1585 2.1.5 Spatial Imaging of the Nucleon

1586 Diffractive and Ultra Peripheral processes at RHIC are an essential tool that can elucidate  
 1587 the origin of single-spin asymmetries in polarized  $pp$  collisions and access the orbital motion

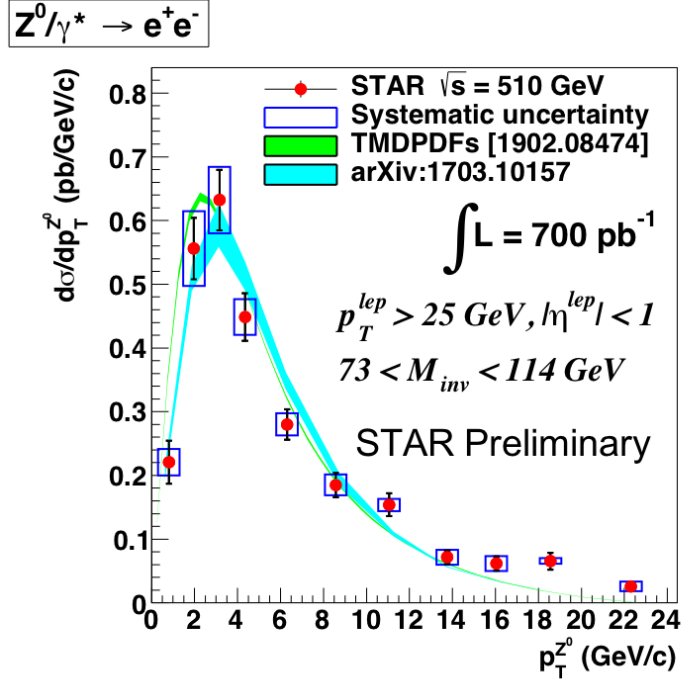


**Figure 55:**  $Z$  differential cross section as a function of boson  $p_T$  for combined Run-11,12, 13, and 17 datasets.

1588 of partons inside the proton. Also at the EIC diffractive processes have been identified as  
 1589 the golden tool to study several key physics programs

- 1590
- What is the spatial distribution of quarks and gluons inside the nucleon?
- 1591
- What is the role of orbital motion of sea quarks and gluons in building the nucleon  
 1592 spin?
- 1593
- Saturation in nuclei.

1594 **Diffraction:** The essential characteristics of diffraction in QCD are summarized by two  
 1595 facts:

- 1596
- The event is still called diffractive if there is a rapidity gap. Due to the presence  
 1597 of a rapidity gap, the diffractive cross-section can be thought of as arising from an  
 1598 exchange of several partons with zero net color between the target and the projectile.  
 1599 In high-energy scattering, which is dominated by gluons, this color neutral exchange  
 1600 (at the lowest order) consists of at least two exchanged gluons. This color singlet  
 1601 exchange has historically been called the pomeron, which had a specific interpretation  
 1602 in Regge theory. A crucial question in diffraction is the nature of the color neutral  
 1603 exchange between the protons. This interaction probes, in a novel fashion, the nature  
 1604 of confining interactions within hadrons.

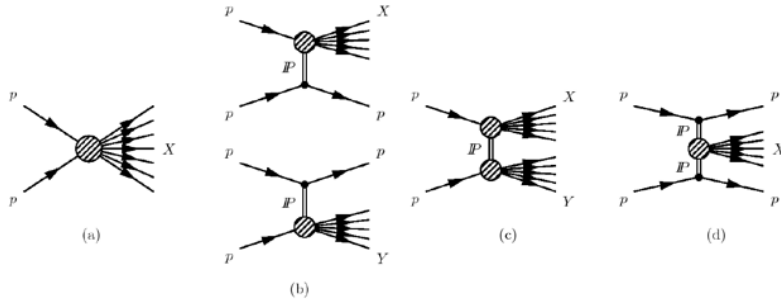


**Figure 56:** Schematic diagrams of (a) nondiffractive,  $pp \rightarrow X$ , (b) singly diffractive,  $pp \rightarrow Xp$  or  $pp \rightarrow pY$ , (c) doubly diffractive,  $pp \rightarrow XY$ , and (d) centrally diffracted,  $pp \rightarrow pXp$ , events.

- The proton/nuclear target is not always an opaque “black disk” obstacle of geometric optics. A projectile that interacts more weakly due to color-screening and asymptotic freedom is likely to produce a different diffractive pattern from a larger, more strongly interacting, projectile.

HERA discovered that 15% of the total  $ep$  cross-section is given by diffractive events (for details see [8] and references therein), basically independent of kinematics. At RHIC center-of-mass energies diffractive scattering events constitute  $\sim 25\%$  of the total inelastic  $pp$  cross-section [199]. As described above diffraction is defined as an interaction that is mediated by the exchange of the quantum numbers of the vacuum, as shown in Fig. 56. Experimentally these events can be characterized by the detection of a very forward scattered proton and jet (singly diffractive) or two jets (doubly diffractive) separated by a large rapidity gap. Central diffraction, where two protons, separated by rapidity gaps, are reconstructed along with a jet at mid-rapidity, is also present, but suppressed compared to singly and doubly diffractive events. To date, there have been no data in  $pp$  collisions studying spin effects in diffractive events at high  $\sqrt{s}$  apart from measuring single spin asymmetries in elastic  $pp$  scattering [46, 104–106].

A discovery of large transverse single spin asymmetries in diffractive processes would open a new avenue to study the properties and understand the nature of the diffractive exchange in  $pp$  collisions. One of the primary observables of STAR to access transverse spin phenomena has been forward neutral pion production in transversely polarized  $pp$  collisions at both  $\sqrt{s} = 200$  and 500 GeV. Figure 32 shows the isolated and non-isolated transverse single spin asymmetries  $A_N$  for  $\pi^0$  detected in the STAR FMS at  $2.5 < \eta < 4.0$  as a function of  $x_F$ , where the neutral pion  $A_N$  is larger for isolated pion than when it is accompanied by additional nearby photons [36]. A similar observation was seen in STAR’s 200 GeV  $p+A$  results [40].

All these observations might indicate that the underlying subprocess causing a significant fraction of the large transverse single spin asymmetries in the forward direction are not of  $2 \rightarrow 2$  parton scattering processes but of diffractive nature. PYTHIA-8 [291] was used to evaluate the fraction of hard diffractive events [166] contributing to the inclusive  $\pi^0$  cross-section at forward rapidities. Figure 57 shows the hard diffractive cross-section for  $\pi^0$  production at  $\sqrt{s} = 200$  GeV and 500 GeV for a rapidity range of  $2.5 < \eta < 4.0$  with and without applying several experimental cuts, i.e. the proton in the STAR Roman Pot acceptance. The prediction from this PYTHIA-8 simulation is that 20% of the total inclusive

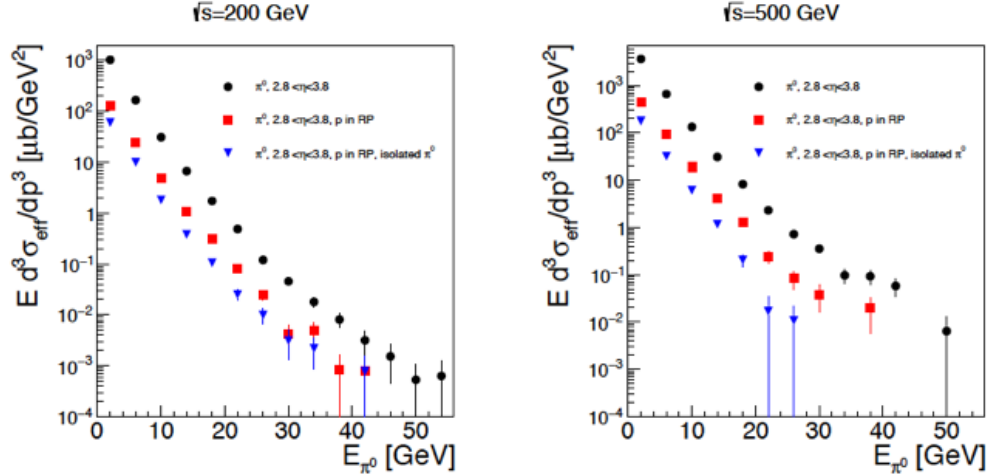


**Figure 57:** Estimate of the cross-section for hard diffractive processes at  $\sqrt{s} = 200$  GeV and 500 GeV using PYTHIA 8. The different points reflect different analysis cuts applied:  $\pi^0$  in rapidity  $2.8 < \eta < 3.8$  (black), one proton is required to be detected in the STAR Roman Pot acceptance (red) and an isolation cut of 35 mrad around the  $\pi^0$  (blue).

1638 cross-section at forward rapidities is of diffractive nature. This result is in agreement with  
 1639 measurements done over a wide range of  $\sqrt{s}$  (see Fig. 12 in Ref. [8]).

1640 In 2015 STAR collected data in  $\sqrt{s} = 200$  GeV transversely polarized  $pp$  collisions,  
 1641 where an isolated  $\pi^0$  is detected in the forward pseudorapidity range along with the forward-  
 1642 going proton, which scatters with a near-beam forward pseudorapidity into Roman Pot  
 1643 detectors. The sum of the  $\pi^0$  and the scattered proton energies is consistent with the  
 1644 incident proton energy of 100 GeV, indicating that no further particles are produced in this  
 1645 direction. Correlations between the  $\pi^0$  and scattered proton have been presented [135], along  
 1646 with single-spin asymmetries which depend on the azimuthal angles of both the pion and  
 1647 the proton. This is the first time that spin asymmetries have been explored for this process,  
 1648 and a model to explain their azimuthal dependence is needed.

1649 The STAR Forward Upgrade will be a game changer for diffractive measurements at  
 1650 RHIC. It will allow the reconstruction of full jets both at  $\sqrt{s} = 200$  GeV and 510 GeV.  
 1651 As at HERA we will be able to reconstruct jets produced with the scattered proton tagged  
 1652 in Roman Pots and/or requiring rapidity gaps. Measuring spin asymmetries for diffractive  
 1653 events as function of  $\sqrt{s}$  might reveal surprises, which will inspire new physics opportunities  
 1654 for EIC, i.e SSA in polarized e+A collisions.

## 1655 2.2 Run-24 Request for Polarized $pp$ and $p+A$ Collisions at 200 GeV

1656 Run-24, with polarized  $pp$  and  $p+Au$  collisions at  $\sqrt{s_{NN}} = 200$  GeV, will likely be the last  
 1657 RHIC spin/cold QCD run. This run will provide STAR with the unique opportunity to in-  
 1658 vestigate these 200 GeV collision systems with the Forward Upgrade providing full tracking  
 1659 and calorimetry coverage over the region  $2.5 < \eta < 4$  and the iTPC providing enhanced

1660 particle identification and expanded pseudorapidity coverage at mid-rapidity. These power-  
 1661 ful detection capabilities, when combined with substantially increased sampled luminosity  
 1662 compared to Run-15, will enable critical measurements to probe universality and factoriza-  
 1663 tion in transverse spin phenomena and nuclear PDFs and fragmentation functions, as well as  
 1664 low- $x$  non-linear gluon dynamics characteristic of the onset of saturation. This will provide  
 1665 unique insights into fundamental QCD questions in the near term, and essential baseline  
 1666 information for precision universality tests when combined with measurements from the EIC  
 1667 in the future.

1668 We therefore request at least 11 weeks of polarized  $pp$  data-taking at  $\sqrt{s} = 200$  GeV and  
 1669 11 weeks of polarized  $p$ +Au data-taking at  $\sqrt{s_{NN}} = 200$  GeV during Run-24. Effectively,  
 1670 we request approximately equal nucleon-nucleon luminosities for  $pp$  and  $p$ +Au which is  
 1671 essential to optimize several critical measurements that require comparisons of the same  
 1672 observable in (polarized or unpolarized)  $pp$  and  $p$ +Au collisions described in the following  
 1673 sections. All of the running will involve transversely polarized protons, with the choice  
 1674 between vertical or radial polarization to be determined during the coming year. Based on  
 1675 recent C-AD guidance, we expect to sample at least  $235 \text{ pb}^{-1}$  of  $pp$  collisions and  $1.3 \text{ pb}^{-1}$  of  
 1676  $p$ +Au collisions. These totals represent 4.5 times the luminosity that STAR sampled during  
 1677 transversely polarized  $pp$  collisions in Run-15 and 3 times the luminosity that STAR sampled  
 1678 during transversely polarized  $p$ +Au collisions in Run-15.

### 1679 **2.2.1 Spin Physics with Polarized $pp$ and $p$ +A Collisions at 200 GeV**

1680 Section 1.3 described several very mature STAR analyses and recent publications that are  
 1681 based on the transversely polarized  $pp$  and  $p$ +Au data sets that we recorded during 2015.  
 1682 Run-24 will enable STAR to probe these questions with a far more capable detector and  
 1683 much larger data sets than were available during Run-15, thereby allowing us to set the  
 1684 stage for related future measurements at the EIC. Here we give brief descriptions of several  
 1685 of the opportunities presented by Run-24.

### 1686 **Forward Transverse Spin Asymmetries**

1687  
 1688 Section 1.3.3 presents some results that STAR recently published in a pair of papers  
 1689 discussing forward transverse spin asymmetries in  $pp$   $p$ +Al and  $p$ +Au collisions measured  
 1690 with the Forward Meson Spectrometer (FMS). One paper focuses on the dynamics that  
 1691 underlie the large asymmetries that have been seen to date. Figure 32 shows that  $A_N$  for  
 1692 forward  $\pi^0$  production in  $pp$  collisions at 200 and 500 GeV is substantially larger when the  
 1693  $\pi^0$  is isolated than when it is accompanied by additional nearby photons. The same analysis  
 1694 also shows that  $A_N$  for inclusive electromagnetic jets (EM-jets) in 200 and 500 GeV collisions  
 1695 is substantially larger than that for EM-jets that contain three or more photons and that the  
 1696 Collins asymmetry for  $\pi^0$  in EM-jets is very small. The other paper focuses on the nuclear  
 1697 dependence of  $A_N$  for  $\pi^0$  in  $\sqrt{s_{NN}} = 200$  GeV collisions. It presents a detailed mapping of  
 1698  $A_N$  as functions of  $x_F$  and  $p_T$  for all three collision systems. Figure 31 shows the observed

1699 nuclear dependence is very weak. The same analysis shows that isolated *vs.* non-isolated  $\pi^0$   
1700 behave similarly in  $p+Al$  and  $p+Au$  collisions as they do in  $pp$  collisions.

1701 These two papers provide a wealth of new data to inform the ongoing discussion regard-  
1702 ing the origin of the large inclusive hadron transverse spin asymmetries that have been seen  
1703 in  $pp$  collisions at forward rapidity over a very broad range of collision energies. Nonetheless,  
1704 the STAR Forward Upgrade will be a game changer for such investigations. It will enable  
1705 measurements of  $A_N$  for  $h^{+/-}$ , in addition to  $\pi^0$ . It will enable isolation criteria to be applied  
1706 to the  $h^{+/-}$  and  $\pi^0$  that account for nearby charged, as well as neutral, fragments. It will  
1707 enable full jet asymmetry and Collins effect measurements, again for  $h^{+/-}$  in addition to  
1708  $\pi^0$ , rather than just EM-jet measurements. It will permit all of these measurements to be  
1709 performed at both 510 GeV, as discussed in Sects. 2.1.1 and 2.1.2, and at 200 GeV. In addi-  
1710 tion, all of these observables can be tagged by forward protons detected in the STAR Roman  
1711 pots to identify the diffractive component of the observed transverse spin asymmetries. For  
1712  $pp$  there will be considerable overlap between the kinematics at the two energies, but the  
1713 510 GeV measurements will access higher  $p_T$ , while the 200 GeV measurements will access  
1714 higher  $x_F$ . Moreover, at 200 GeV we will also perform the full suite of measurements in  
1715  $p+Au$  to identify any nuclear effects. Figure 40 shows one set of predictions for the inclusive  
1716  $\pi^{+/-}$   $A_N$  in 200 and 500 GeV  $pp$  collisions, while Fig. 45 shows the predictions for the one  
1717 hadron-in-jet measurement that will help to isolate the Siverts effect contribution at 200 GeV.

### 1718 Siverts Effect

1719 Section 2.1.2 describe the first ever observation of the Siverts effect in dijet production. Such  
1720 measurements are crucial to explore questions regarding factorization of the Siverts function in  
1721 dijet hadroproduction [120,190,228,270]. Those results were derived from 200 GeV transverse  
1722 spin data that STAR recorded in Run-12 and Run-15 (total sampled luminosity  $\sim 75 \text{ pb}^{-1}$   
1723 for the two years combined). Nonetheless, the uncertainties remain large, as can be seen in  
1724 Fig. 46. Run-24 data will reduce the uncertainties for  $|\eta_3 + \eta_4| < 1$  by a factor of two. The  
1725 increased acceptance from the iTPC will reduce the uncertainties at  $|\eta_3 + \eta_4| \approx 2.5$  by a  
1726 much larger factor, while the Forward Upgrade will enable the measurements to be extended  
1727 to even larger values of  $|\eta_3 + \eta_4|$ . When combined with the 510 GeV data from Run-17 and  
1728 Run-22 (see Sect. 2.1.2), the results will provide a detailed mapping *vs.*  $x$  for comparison to  
1729 results for Siverts functions extracted from SIDIS, Drell-Yan, and vector boson production.

### 1730 Transversity and Related Quantities

1731  
1732 As described in Sect. 2.1.3, measurements of the Collins asymmetry and IFF in  $pp$  colli-  
1733 sions at RHIC probe fundamental questions regarding TMD factorization, universality, and  
1734 evolution. Data from 200 GeV  $pp$  collisions will play an essential role toward answering these  
1735 questions. Figure 50 shows that 200 GeV  $pp$  collisions interpolate between the coverage that  
1736 we will achieve during Run-22 at high- $x$  with the Forward Upgrade and at low- $x$  with the  
1737 STAR mid-rapidity detectors. They will also provide a significant overlapping region of  $x$   
1738 coverage, but at  $Q^2$  values that differ by a factor of 6. This will provide valuable information

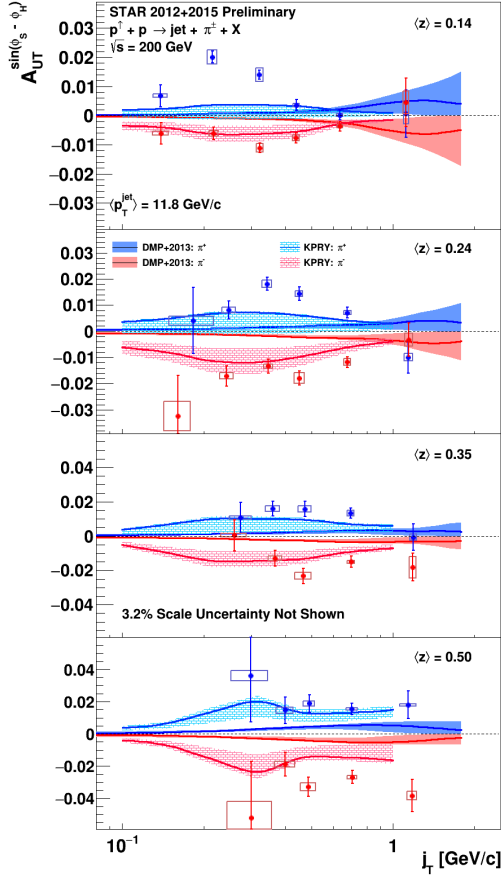


**Figure 58:** Preliminary Run-12 and Run-15 results for the Collins asymmetry for charged pions in 200 GeV  $pp$  collisions as a function of  $z$  and  $j_T$ , integrated over  $9.9 < p_T < 31.6$  GeV/ $c$  and  $0 < \eta < 0.9$ . Theoretical evaluations from [123] with their uncertainties are presented for  $\pi^+$  (blue) and  $\pi^-$  (red).

1739 about evolution effects, as well as cross-checks between the two measurements. Furthermore,  
 1740 for most of the overlapping  $x$  region, 200 GeV  $pp$  collisions will also provide the greatest sta-  
 1741 tistical precision (see for example Fig. 53), thereby establishing the most precise benchmark  
 1742 for future comparisons to  $ep$  data from the EIC.

1743 The high statistical precision of the Run-24 data will enable detailed multi-dimensional  
 1744 binning for the Collins asymmetry results. This is particularly valuable because, as empha-  
 1745 sized in [191, 192], hadron-in-jet measurements in  $pp$  collisions provide a direct probe of the  
 1746 Collins fragmentation function since they combine it with the *collinear* transversity distri-  
 1747 bution. In general, the observed asymmetries are functions of jet ( $p_T, \eta$ ), hadron ( $z, j_T$ ), and  
 1748  $Q^2$ . However, the physics interpretations associated with these variables separate, with  $p_T$   
 1749 and  $\eta$  primarily coupling to the incident quark  $x$  and the polarization transfer in the hard  
 1750 scattering, while  $z$  and  $j_T$  characterize the fragmentation kinematics. Thus,  $A_{UT}$  vs.  $p_T$ ,  
 1751 as shown in Fig. 28 for the preliminary Run-12 and Run-15 analysis, provides information  
 1752 about the transversity distribution. In parallel, the  $(z, j_T)$  dependence, integrated over a  
 1753 wide range of jet  $p_T$ , as shown in Fig. 58 for the preliminary Run-12 and Run-15 results,  
 1754 provides a detailed look at the Collins fragmentation function. Note that STAR finds the  
 1755 maximum value of  $A_{UT}$  shift to higher  $j_T$  as  $z$  increases which is not seen in the current  
 1756 theory evaluations [123]. The statistical uncertainties in Figs. 28 and 58 will be reduced by

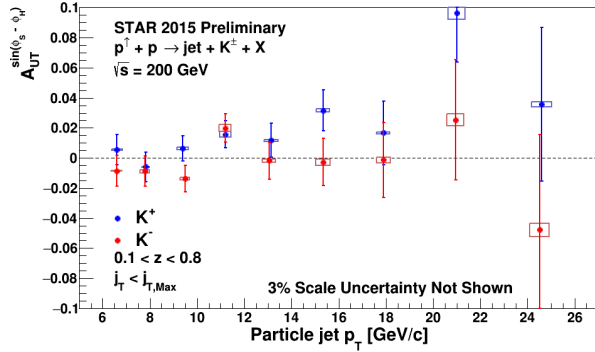


**Figure 59:** Preliminary Run-15 results for the  $K^{+/-}$  Collins asymmetries *vs.* jet  $p_T$  for  $0 < \eta < 0.9$  in 200 GeV  $pp$  collisions.

1757 a factor of about 2.5 when Run-12, Run-15 and Run-24 data are combined together.

1758 The Run-15 Collins analysis has also, for the first time, measured the Collins effect for  
 1759 charged kaons in  $pp$  collisions, as shown in Fig. 59. The asymmetries for  $K^+$ , which like  
 1760  $\pi^+$  have a contribution from favored fragmentation of  $u$  quarks, are about 1.5-sigma larger  
 1761 than those for  $\pi^+$  in Fig. 28, while those for  $K^-$ , which can only come from unfavored  
 1762 fragmentation, are consistent with zero at the 1-sigma level. These trends are similar to  
 1763 those found in SIDIS by HERMES [68] and COMPASS [63], and provide additional insight  
 1764 into the Collins fragmentation function. This same analysis with Run-24 data will yield  
 1765 statistical uncertainties a factor of 3 smaller than those in Fig. 59. This is a much greater  
 1766 improvement than would be expected from the increase in sampled luminosity thanks to  
 1767 the improved  $dE/dx$  resolution provided by the iTPC. In addition, the iTPC will enable  
 1768 the measurements in Figs. 28, 58, and 59 to be extended to an additional higher  $\eta$  bin  
 1769 ( $0.9 < \eta < 1.3$ ).

1770 RHIC has the unique opportunity to extend the Collins effect measurements to nuclei.  
 1771 This will provide an alternative look at the universality of the Collins effect in hadron-  
 1772 production by dramatically increasing the color flow options of the sort that have been  
 1773 predicted to break factorization for TMD PDFs like the Sivers effect [120, 270]. This will  
 1774 also explore the spin dependence of the hadronization process in cold nuclear matter. STAR  
 1775 collected a proof-of-principle data set during the 2015  $p$ +Au run that is currently under  
 1776 analysis. Those data will provide a first estimate of medium-induced effects. However, the  
 1777 small nuclear effects seen by STAR for forward inclusive  $\pi^0$   $A_N$  (see Fig. 31) indicate that  
 1778 greater precision will likely be needed. Figure 53 shows the projected Run-15 and Run-24  
 1779 statistical uncertainties for the  $p$ +Au Collins asymmetry measurement at  $\sqrt{s_{NN}} = 200$  GeV,  
 1780 compared to those for the  $pp$  at the same energy.

## 1781 Ultra-peripheral Collisions

1782

1783 The formalism of generalized parton distributions (GPDs) provides a theoretical frame-  
 1784 work which addresses some of the above questions [107, 181, 246, 264]. Constraints on GPDs  
 1785 have mainly been provided by exclusive reactions in DIS, e.g. deeply virtual Compton  
 1786 scattering. RHIC, with its unique capability to collide transversely polarized protons at

1787 high energies, has the opportunity to measure  $A_N$  for exclusive  $J/\Psi$  production in ultra-  
 1788 peripheral collisions (UPCs) [203]. In such a UPC process, a photon emitted by the opposing  
 1789 beam particle (p or A) collides with the polarized proton. The measurement is at a fixed  
 1790  $Q^2 \sim M_{J/\psi}^2 \approx 10 \text{ GeV}^2$  and  $10^{-4} < x < 10^{-1}$ . A nonzero asymmetry would be the first  
 1791 signature of a nonzero GPD  $E_g$  for gluons, which is sensitive to spin-orbit correlations and is  
 1792 intimately connected with the orbital angular momentum carried by partons in the nucleon  
 1793 and thus with the proton spin puzzle.

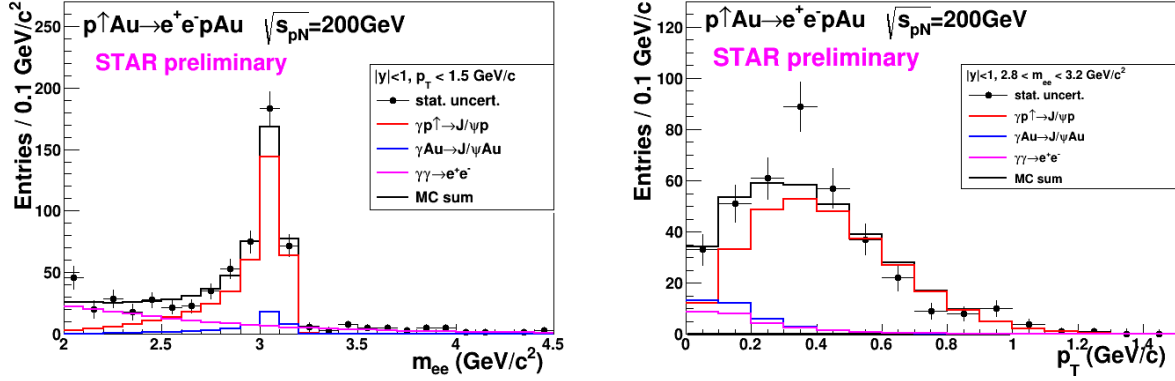


**Figure 60:** Mass distribution of selected  $e^+e^-$  pairs (left), and  $p_T$  distribution of the  $J/\psi$  mass peak (right). The colored histograms are the indicated processes modelled by STARlight and the sum fit to the data.

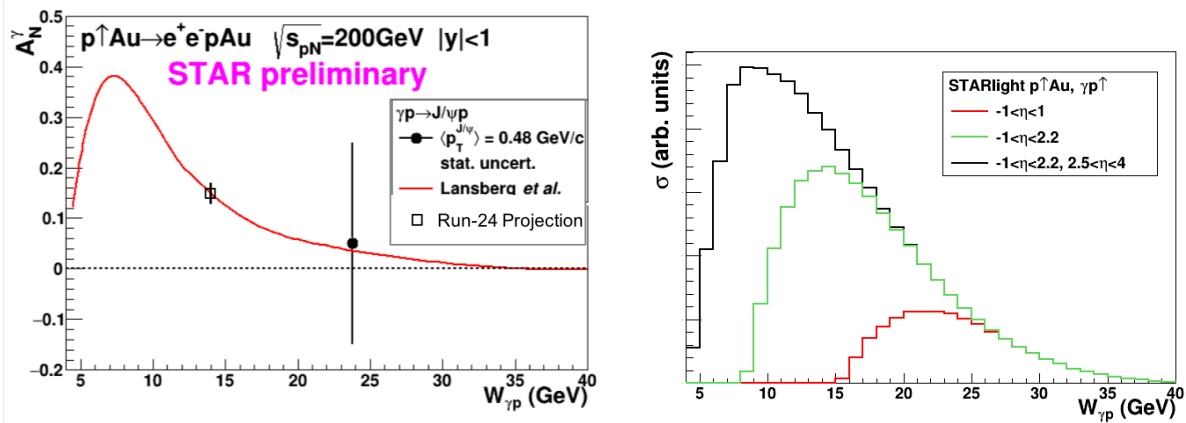


**Figure 61:** Left: The measured  $J/\psi$  transverse asymmetry  $A_N^\gamma$  and a prediction based on a parameterization of  $E_g$ . Right: The accepted cross section for  $\gamma+p\uparrow \rightarrow J/\psi$  for various detector pseudorapidity  $\eta$  ranges; the black curve shows the result for the full STAR detector with the Forward Upgrade and the iTPC.

1794 The Run-15  $p\uparrow$ -Au data allowed a proof-of-principle of such a measurement. A trigger  
 1795 requiring back-to-back energy deposits in the Barrel Electromagnetic Calorimeter selected

1796  $J/\Psi$  candidates. The  $e^+e^-$  mass distribution after selection cuts is shown in the left of Fig. 60,  
 1797 and the pair  $p_T$  distribution of the  $J/\psi$  mass peak is shown on the right of that figure. The  
 1798 data are well described by the STARlight model [204] (colored histograms in the figure),  
 1799 including the dominant  $\gamma+p\uparrow\rightarrow J/\psi$  signal process and the  $\gamma+\text{Au}\rightarrow J/\psi$  and  $\gamma+\gamma\rightarrow e^+e^-$   
 1800 background processes. The left of Fig. 61 shows the STAR preliminary measurement (solid  
 1801 circle marker) of the transverse asymmetry  $A_N^\gamma$  for the  $J/\psi$  signal, which have a mean  
 1802 photon-proton center-of-mass energy  $W_{\gamma p} \approx 24$  GeV. The result is consistent with zero. Also  
 1803 shown is a prediction based on a parameterization of  $E_g$  [217]; the present data provide no  
 1804 discrimination of this prediction.

1805 This measurement can be greatly improved with a high statistics transversely polarized  
 1806  $p\uparrow$ -Au Run-24. The integrated luminosity for the Run-15 measurement was  $140 \text{ nb}^{-1}$ ; the  
 1807 Run-24 will provide  $1.3 \text{ pb}^{-1}$ , allowing a sizeable reduction of statistical uncertainty in the  
 1808 same  $W_{\gamma p}$  range. However, the Forward Upgrade and iTPC will also provide a significant  
 1809 extension of the  $W_{\gamma p}$  range of the measurement. The right panel of Fig. 61 shows the  
 1810 accepted cross section for  $\gamma+p\uparrow \rightarrow J/\psi$  for various detector pseudorapidity ranges. With the  
 1811 full detector, the sensitive cross section is a factor of five times the central barrel alone and  
 1812 the expected asymmetry is substantially larger. The projected statistical uncertainty on  $A_N^\gamma$   
 1813 as shown in the left of Fig. 61 (open square marker) will be  $\approx 0.02$ , offering a powerful test of  
 1814 a non-vanishing  $E_g$ . Also, the accepted region has a lower mean  $W_{\gamma p} \approx 14$  GeV. Predictions  
 1815 based on  $E_g$  parameterizations such as shown in the figure have a larger asymmetry at lower  
 1816  $W_{\gamma p}$ , with increased possibility of a nonzero result. Alternatively, the increased statistics  
 1817 will allow a measurement of  $A_N^\gamma$  in bins of  $W_{\gamma p}$ .

1818 The UPC cross section scales with  $Z^2$  of the the nucleus emitting the photon; for protons  
 1819 this is  $1/79^2$  relative to Au nuclei, which makes analogous measurements in  $pp$  collisions  
 1820 extremely luminosity-hungry. Therefore, the  $p$ +Au run is critical for this measurement.

## 1821 2.2.2 Physics Opportunities with Unpolarized proton-Nucleus Collisions

1822 Our quest to understand QCD processes in Cold Nuclear Matter (CNM) centers on the  
 1823 following fundamental questions:

- 1824 • Can we experimentally find evidence of a novel universal regime of non-linear QCD  
 1825 dynamics in nuclei?
- 1826 • What is the role of saturated strong gluon fields, and what are the degrees of freedom  
 1827 in this high gluon density regime?
- 1828 • What is the fundamental quark-gluon structure of light and heavy nuclei?
- 1829 • Can a nucleus, serving as a color filter, provide novel insight into the propagation,  
 1830 attenuation and hadronization of colored quarks and gluons?

1831 Various aspects of these questions have been addressed by numerous experiments and  
 1832 facilities around the world, most of them at significantly lower center-of-mass energies and  
 1833 kinematic reach than RHIC. Deep inelastic scattering on nuclei addresses some of these

1834 questions with results from, for instance, HERMES at DESY [69–71], CLAS at JLab [103],  
 1835 and in the future from the JLab 12 GeV. This program is complemented by hadron-nucleus  
 1836 reactions in fixed target  $p+A$  at Fermilab (E772, E886, and E906) [309] and at the CERN-  
 1837 SPS.

1838 In the following we propose a measurement program unique to RHIC to constrain the  
 1839 initial state effects in strong interactions in the nuclear environment. We also highlight the  
 1840 complementarity to the LHC  $p$ -Pb program and stress why RHIC data are essential and  
 1841 unique in the quest to further our understanding of nuclei. The uniqueness of the RHIC  
 1842 program is based on the flexibility of the RHIC accelerator to run collisions of different  
 1843 particle species at very different center-of-mass energies. This in combination with the  
 1844 enhanced STAR detector capabilities in Run-24 allows to disentangle nuclear effects in the  
 1845 initial and final state as well as leading twist shadowing from saturation effects in a kinematic  
 1846 regime where all these effects are predicted to be large. Most of the discussed measurements  
 1847 critically rely on the Forward Upgrade.

## 1848 The Initial State of Nuclear Collisions

1849

1850 **Nuclear parton distribution functions:** A main emphasis of the Run-15 and later  
 1851  $p+A$  runs is to determine the initial conditions of the heavy ion nucleus before the collision  
 1852 to support the theoretical understanding of the A–A program both at RHIC and the LHC.  
 1853 In the following, the current status of nPDFs will be discussed, including where the unique  
 1854 contributions of RHIC lie, in comparison to the LHC and the future EIC.

1855 Our current understanding of nuclear parton distribution functions (nPDFs) is still very  
 1856 limited, in particular, when compared with the rather precise knowledge of PDFs for free  
 1857 protons collected over the past 30 years. Figure 62 shows an extraction of nPDFs from  
 1858 available data, along with estimates of uncertainties. All results are shown in terms of  
 1859 the nuclear modification ratios, i.e., scaled by the respective PDF of the free proton. The  
 1860 yellow bands indicate regions in  $x$  where the fits are not constrained by data [256] and  
 1861 merely reflect the freedom in the functional form *assumed* in the different fits. Clearly, high  
 1862 precision data at small  $x$  and for various different values of  $Q^2$  are urgently needed to better  
 1863 constrain the magnitude of suppression in the  $x$  region where non-linear effects in the scale  
 1864 evolution are expected. In addition, such data are needed for several different nuclei, as  
 1865 the A-dependence of nPDFs cannot be predicted from first principles in pQCD and, again,  
 1866 currently relies on assumptions. Note that the difference between DSSZ [130] and EPS09  
 1867 for the gluon modification arise from the different treatment of the PHENIX midrapidity  
 1868  $\pi^0 R_{dAu}$  data [62], which in the EPS09 [140] fit are included with an extra weight of 20. The  
 1869  $\pi^0 R_{dAu}$  data are the only data, which can probe the gluon in the nucleus directly, but these  
 1870 data also suffer from unknown nuclear effects in the final state (see [272]). Therefore, it is  
 1871 absolutely critical to have high precision data only sensitive to nuclear modification in the  
 1872 initial state over a wide range in  $x$  and intermediate values of  $Q^2$  (away from the saturation  
 1873 regime) to establish the nuclear modification of gluons in this kinematic range.

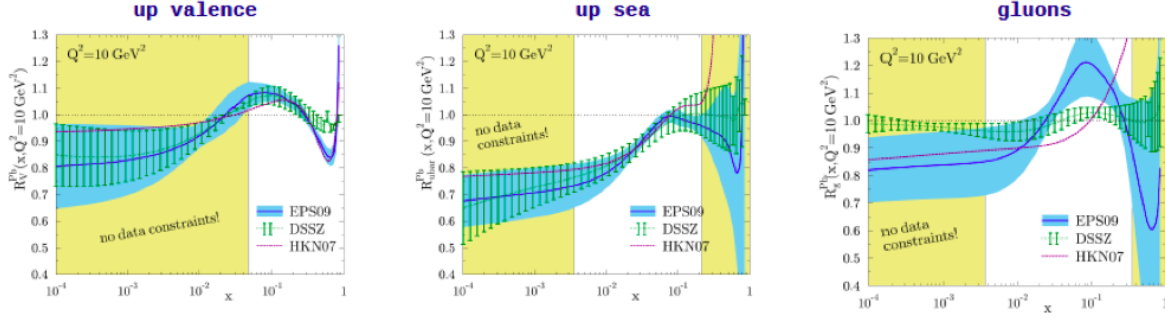


**Figure 62:** Summary of the most recent sets of nPDFs. The central values and their uncertainty estimates are given for the up valence quark, up sea quark, and the gluon. The yellow bands indicate regions in  $x$  where the fits are not constrained by any data (taken from Ref. [256]).

1874 It is important to realize that the measurements from RHIC are compelling and essential  
 1875 even when compared to what can be achieved in  $p$ -Pb collisions at the LHC. Due to the  
 1876 higher center-of-mass system energy most of the LHC data have very high  $Q^2$ , where the  
 1877 nuclear effects are already reduced significantly by evolution and are therefore very difficult  
 1878 to constrain. Two recent articles [82, 141] assessed the impact of the available LHC Run-  
 1879 I  $p$ +Pb data on determinations of nPDFs. The rather moderate impact of these data is  
 1880 illustrated in Fig. 63. Note that the extra weight factor of 20 for the PHENIX midrapidity  
 1881  $\pi^0 R_{dAu}$  data [62] in the original EPS09 [140] fit was removed in all of the new fits, leading  
 1882 to a much smaller nuclear modification factor for gluons, especially at medium to high  $x$ .

1883 RHIC has the *unique* capability to provide data in a kinematic regime (moderate  $Q^2$  and  
 1884 medium-to-low  $x$ ) where the nuclear modification of the sea quark and the gluon is expected  
 1885 to be sizable and currently completely unconstrained. In addition, and unlike the LHC,  
 1886 RHIC has the potential to vary the nucleus in  $p$ +A collisions and as such also constrain the  
 1887  $A$ -dependence of nPDFs.

1888 Extraction of this information is less ambiguous if one uses processes in which strong  
 1889 (QCD) final-state interactions can be neglected or reduced. Such golden channels would  
 1890 include: a measurement of  $R_{pA}$  for Drell-Yan production at forward pseudo-rapidities with  
 1891 respect to the proton direction ( $2.5 < \eta < 4$ ) to constrain the nuclear modifications of sea-  
 1892 quarks; and of  $R_{pA}$  for direct photon production in the same kinematic regime to constrain  
 1893 the nuclear gluon distribution. Data for the first measurement of  $R_{pA}$  for direct photon  
 1894 production have already been taken during the  $p$ +Au and  $p$ +Al Run-15, with recorded  
 1895 luminosities by STAR of  $L_{pAu} = 0.45 \text{ pb}^{-1}$  and  $L_{pAl} = 1 \text{ pb}^{-1}$ , respectively. The anticipated  
 1896 statistical precision for  $p$ +Au runs in Run-15 and projections for the Run-24 are shown  
 1897 in Fig. 64. The Forward Upgrade with its tracking at forward rapidities will also provide  
 1898 the possibility to measure  $R_{pA}$  for positive and negatively charged hadrons. Approximately  
 1899 equal nucleon-nucleon luminosities for  $pp$  and  $p$ +Au are important for the optimization of  
 1900  $R_{pA}$  measurements as they directly compare the same observable—yields—in both collision  
 1901 systems.

1902 Figure 65 (left) shows the significant impact of the Run-15 and Run-24  $R_{pA}$  for direct

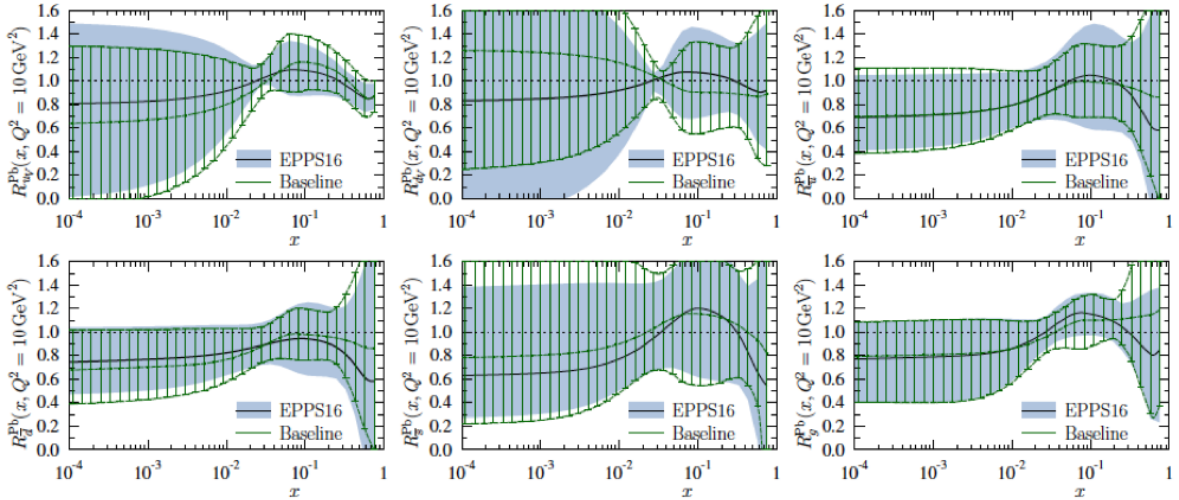


**Figure 63:** The nuclear modifications at  $Q^2 = 10 \text{ GeV}^2$  from the EPPS-16 fit (black central line and light-blue bands) compared with the Baseline fit (green curves with hatching) which uses only the data included in the EPS09 fit.

1903 photon production on the corresponding theoretical expectations and their uncertainties  
 1904 obtained with the EPPS-16 set of nPDFs. The uncertainty bands are obtained through a  
 1905 re-weighting procedure [258] by using the projected data shown in Fig. 64 and randomizing  
 1906 them according to their expected statistical uncertainties around the central values obtained  
 1907 with the current set of EPPS-16 nPDFs. Figure 65 (right) shows how these measurements  
 1908 will help significantly in further constraining the nuclear gluon distribution in a broad range  
 1909 of  $x$  that is roughly correlated with accessible transverse momenta of the photon, i.e., few  
 1910 times  $10^{-3} < x < \text{few times } 10^{-2}$ . The relevant scale  $Q^2$  is set be  $\sim p_T^2$  and ranges from 6  
 1911  $\text{GeV}^2$  to about  $40 \text{ GeV}^2$ . Like all other inclusive probes in  $pp$  and  $p+A$  collisions, e.g., jets,  
 1912 no access to the exact parton kinematics can be provided event-by-event but global QCD  
 1913 analyses easily account for that. After the  $p+\text{Au}$  Run-24, the statistical precision of the  
 1914 prompt photon data will be sufficient to contribute to a stringent test of the universality  
 1915 of nuclear PDFs when combined with the expected data from the EIC (see Figure 2.22 and  
 1916 2.23 in Ref [83]).

1917 Figure 66 shows the kinematic coverage in  $x-Q^2$  of past, present, and future experiments  
 1918 capable of constraining nuclear parton distribution functions. The shown experiments pro-  
 1919 vide measurements that access the initial state parton kinematics on an event-by event basis  
 1920 (in a leading order approximation) while remaining insensitive to any nuclear effects in the  
 1921 final state. Some of the LHC experiments cover the same  $x$ -range as DY at forward pseudo-  
 1922 rapidities at RHIC but at a much higher scale  $Q^2$ , where nuclear modifications are already  
 1923 significantly reduced [82, 143, 257]. At intermediate  $Q^2$ , DY at STAR will extend the low- $x$   
 1924 reach by nearly one decade compared to EIC.

1925 The biggest challenge of a DY measurement is to suppress the overwhelming hadronic  
 1926 background: the total DY cross-section is about  $10^{-5}$  to  $10^{-6}$  smaller than the corresponding

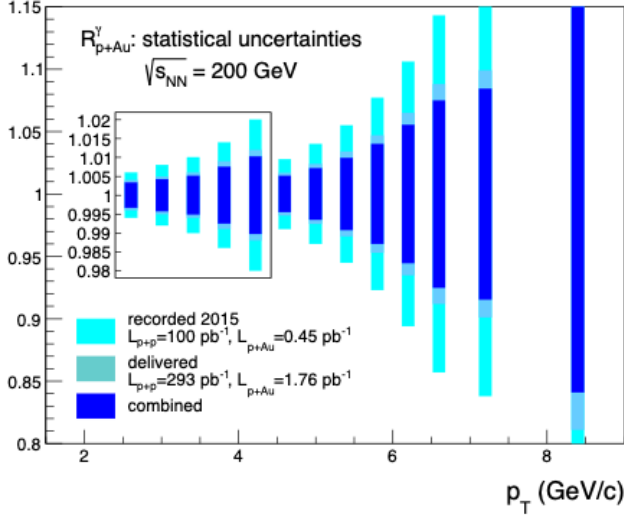


**Figure 64:** Projected statistical uncertainties for  $R_{pA}$  for direct photons in Run-15 (light blue) and Run-24 (blue) and the sum of both (dark blue). The recorded luminosity for Run-15 was  $L_{pAu} = 450 \text{ nb}^{-1}$  and  $L_{pp} = 100 \text{ pb}^{-1}$ . The delivered luminosity for Run-24 is assumed to be  $L_{pAu} = 1.8 \text{ pb}^{-1}$  and  $L_{pp} = 300 \text{ pb}^{-1}$ .

1927 hadron production cross-sections. Therefore, the probability of misidentifying a hadron  
 1928 track as a lepton has to be suppressed to the order of 0.1% while maintaining reasonable  
 1929 electron detection efficiencies. To that end, we have studied the combined electron/hadron  
 1930 discriminating power of the Forward Upgrade. It was found that by applying multivariate  
 1931 analysis techniques to the features of EM/hadronic shower development and momentum  
 1932 measurements we can achieve hadron rejection powers of 200 to 2000 for hadrons of 15 GeV  
 1933 to 50 GeV with 80% electron detection efficiency.

1934 The same procedure as for the direct photon  $R_{pA}$  was used to study the potential impact  
 1935 of the DY  $R_{pA}$  data for the EPPS-19 sets of nPDFs. We expect again a significant impact  
 1936 on the uncertainties of  $R_{pA}$  DY upon including the projected and properly randomized data.  
 1937 Clearly, the DY data from RHIC will be instrumental in reducing present uncertainties in  
 1938 nuclear modifications of sea quarks. Again, these data will prove to be essential in testing the  
 1939 fundamental universality property of nPDFs in the future when EIC data become available.

1940 STAR's unique detector capabilities will provide the first data on  $J/\Psi$ -production in  
 1941 ultra-peripheral collisions. This measurement provides access to the spatial gluon distri-  
 1942 bution by measuring the  $t$ -dependence of  $d\sigma/dt$ . As follows from the optical analogy, the  
 1943 Fourier-transform of the square root of this distribution yields the source distribution of the  
 1944 object probed. To study the gluon distribution in the gold nucleus, events need to be tagged  
 1945 where the photon is emitted from the proton. For both observables a measurement with  
 1946 different nuclei is required to pin down the A-dependence of nPDFs. The  $J/\Psi$ -production  
 1947 in ultra-peripheral collisions requires significantly more statistics than accumulated to date.

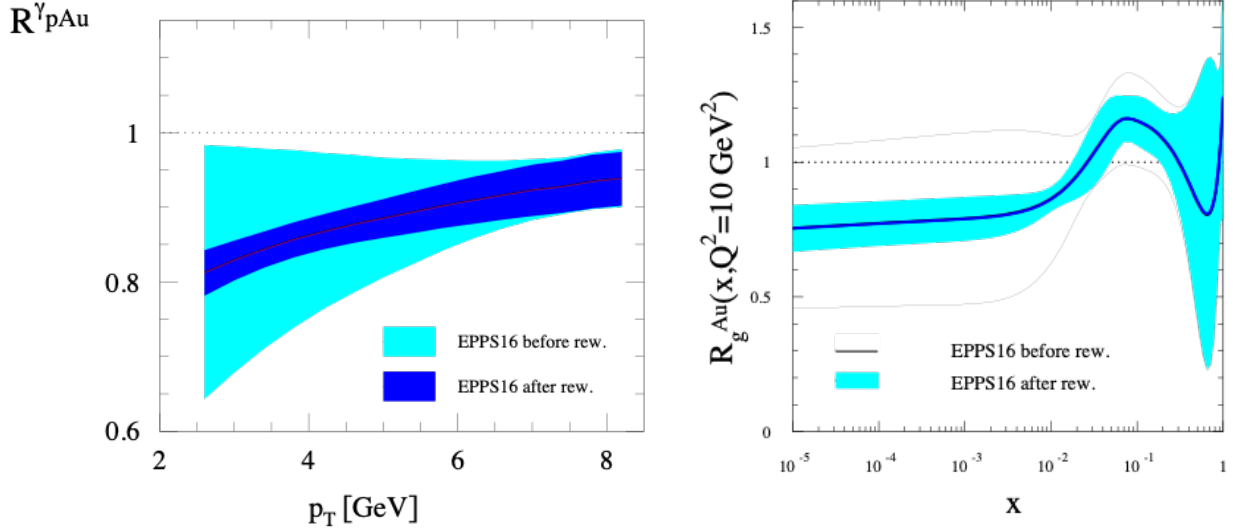


**Figure 65:** (left) The impact of the direct photon  $R_{pA}$  data measured in Run-15 (blue band) and for the anticipated statistics for the future  $p+Au$  Run-24 (dark blue band) compared with the current uncertainties (cyan band) from EPPS-16. (right) The impact of the direct photon  $R_{pA}$  data measured in Run-15 and for the anticipated statistics for the future Run-24  $p+Au$  run on EPPS-16. The impact is shown on the nuclear suppression factor  $R_g$  of nPDF to the proton PDF, the grey bands represent the uncertainties before including the RHIC pseudo data.

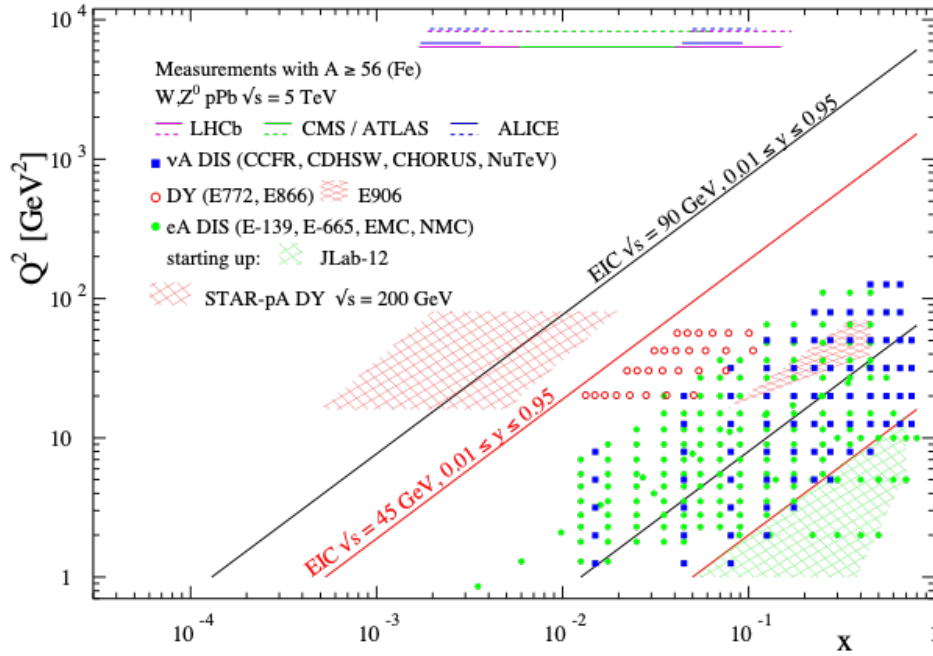


**Figure 66:** The kinematic coverage in  $x - Q^2$  of past, present and future experiments constraining nPDFs with access to the exact parton kinematics event-by-event and no fragmentation in the final state.

## Gluon Saturation

1948  
1949  
1950  
1951  
1952  
1953  
1954  
1955  
1956

Our understanding of the proton structure and of the nuclear interactions at high energy would be advanced significantly with the definitive discovery of the saturation regime [150, 160, 161, 171, 176, 210, 316]. Saturation physics would provide an infrared cutoff for perturbative calculations, the saturation scale  $Q_s$ , which grows with the atomic number of the nucleus  $A$  and with decreasing value of  $x$ . If  $Q_s$  is large it makes the strong coupling constant small,  $\alpha_s(Q_s^2) \ll 1$  allowing for perturbative QCD calculations to be under theoretical control.

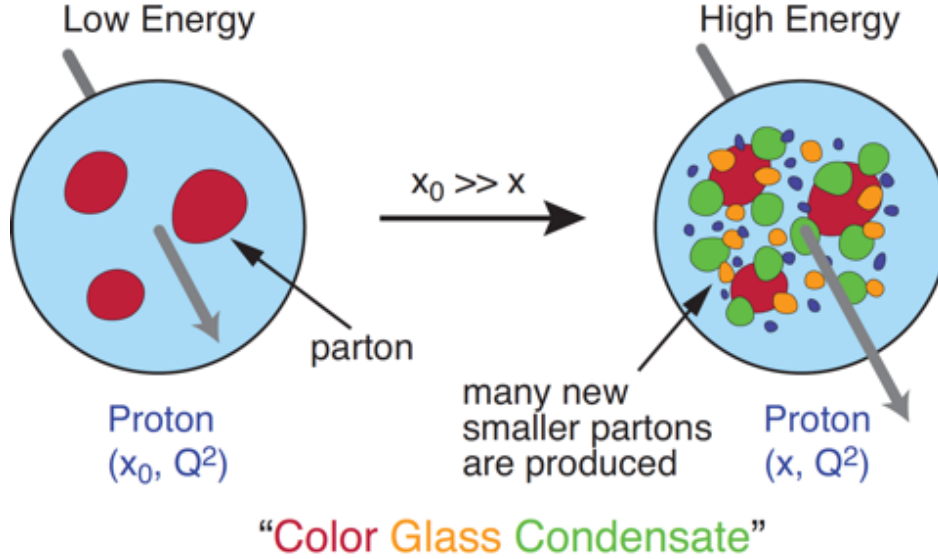


**Figure 67:** Proton wave function evolution towards small- $x$ .

1957  
1958  
1959  
1960  
1961  
1962  
1963  
1964  
1965  
1966  
1967  
1968  
1969  
1970  
1971  
1972

It is well known that PDFs grow at small- $x$ . If one imagines how such a high number of small- $x$  partons would fit in the (almost) unchanged proton radius, one arrives at the picture presented in Fig. 67: the gluons and quarks are packed very tightly in the transverse plane. The typical distance between the partons decreases as the number of partons increases, and can get small at low- $x$  (or for a large nucleus instead of the proton). One can define the saturation scale as the inverse of this typical transverse inter-parton distance. Hence  $Q_s$  indeed grows with  $A$  and decreasing  $x$ .

The actual calculations in saturation physics start with the classical gluon fields (as gluons dominate quarks at small- $x$ ) [178, 206, 207, 234–236, 243], which are then evolved using the nonlinear small- $x$  BK/JIMWLK evolution equations [87, 88, 169, 170, 177, 179, 208, 209, 241, 242, 242]. The saturation region can be well-approximated by the following formula:  $Q_s^2 \sim (A/x)^{1/3}$ . Note again that at small enough  $x$  the saturation scale provides an IR cutoff, justifying the use of perturbative calculations. This is important beyond saturation physics, and may help us better understand small- $x$  evolution of the TMDs.

While the evidence in favor of saturation physics has been gleaned from the data collected at HERA, RHIC and the LHC, the case for saturation is not sealed and alternative

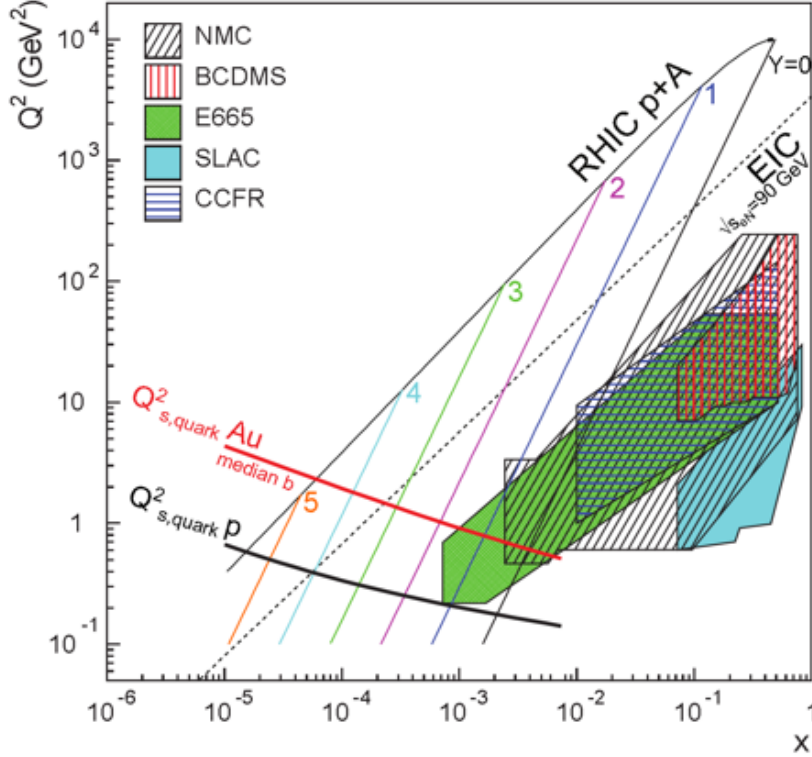


**Figure 68:** Kinematic coverage in the  $x - Q^2$  plane for  $p+A$  collisions at RHIC, along with previous  $e-A$  measurements, the kinematic reach of an electron-ion collider, and estimates for the saturation scale  $Q_s$  in Au nuclei and protons. Lines are illustrative of the range in  $x$  and  $Q^2$  covered with hadrons at various rapidities.

1973 explanations of these data exist. The EIC is slated to provide more definitive evidence for  
 1974 saturation physics [19]. To help the EIC complete the case for saturation, it is mandatory to  
 1975 generate higher-precision measurements in  $p+Au$  collisions at RHIC. These higher-precision  
 1976 measurements would significantly enhance the discovery potential of the EIC as they would  
 1977 enable a stringent test of universality of the CGC. We stress again that a lot of theoretical  
 1978 predictions and results in the earlier Sections of this document would greatly benefit from  
 1979 saturation physics: the small- $x$  evolution of TMDs in a longitudinally or transversely polarized  
 1980 proton, or in an unpolarized proton, can all be derived in the saturation framework [211]  
 1981 in a theoretically better-controlled way due to the presence of  $Q_s$ . Hence saturation physics  
 1982 may help us understand both the quark and gluon helicity PDFs as well as the Sivers and  
 1983 Boer-Mulders functions.

1984 The saturation momentum is predicted to grow approximately like a power of energy,  
 1985  $Q_s^2 \sim E^{\lambda/2}$  with  $\lambda \sim 0.2 - 0.3$ , as phase space for small- $x$  (quantum) evolution opens up.  
 1986 The saturation scale is also expected to grow in proportion to the valence charge density at  
 1987 the onset of small- $x$  quantum evolution. Hence, the saturation scale of a large nucleus should  
 1988 exceed that of a nucleon by a factor of  $A^{1/3} \sim 5$  (on average over impact parameters). RHIC  
 1989 is capable of running  $p+A$  collisions for different nuclei to check this dependence on the mass  
 1990 number. This avoids potential issues with dividing say  $p-Pb$  collisions in  $N_{part}$  classes [113].  
 1991 Figure 68 shows the kinematic coverage in the  $x - Q^2$  plane for  $p+A$  collisions at RHIC, along  
 1992 with previous  $e-A$  measurements and the kinematic reach of an EIC. The saturation scale for  
 1993 a Au nucleus and the proton is also shown. To access at RHIC a kinematic regime sensitive

1994 to saturation with  $Q^2 > 1 \text{ GeV}^2$  requires measurements at forward rapidities. For these  
1995 kinematics the saturation scale is moderate, on the order of a few  $\text{GeV}^2$ , so measurements  
1996 sensitive to the saturation scale are by necessity limited to semi-hard processes.

1997 Until today the golden channel at RHIC to observe strong hints of saturation has been  
1998 the angular dependence of two-particle correlations, because it is an essential tool for testing  
1999 the underlying QCD dynamics [113]. In forward-forward correlations facing the  $p(d)$  beam  
2000 direction one selects a large- $x$  parton in the  $p(d)$  interacting with a low- $x$  parton in the  
2001 nucleus. For  $x < 0.01$  the low- $x$  parton will be back-scattered in the direction of the large-  
2002  $x$  parton. Due to the abundance of gluons at small  $x$ , the backwards-scattered partons  
2003 are dominantly gluons, while the large- $x$  partons from the  $p(d)$  are dominantly quarks. The  
2004 measurements of di-hadron correlations by STAR and PHENIX [58, 102], have been compared  
2005 with theoretical expectations using the CGC framework based on a fixed saturation scale  $Q_s$   
2006 and considering valence quarks in the deuteron scattering off low- $x$  gluons in the nucleus with  
2007 impact parameter  $b = 0$  [74, 232]. Alternative calculations [194] based on both initial and  
2008 final state multiple scattering, which determine the strength of this transverse momentum  
2009 imbalance, in which the suppression of the cross-section in d+Au collisions arises from cold  
2010 nuclear matter energy loss and coherent power corrections have also been very successful to  
2011 describe the data.

2012 The  $p$ +Au Run-15 at RHIC has provided unique opportunities to study this channel in  
2013 more detail at STAR. The high delivered integrated luminosities allow one to vary the trigger  
2014 and associated particle  $p_T$  from low to high values and thus crossing the saturation boundary  
2015 as shown in Fig. 68 and reinstate the correlations for central  $p$ +A collisions for forward-  
2016 forward  $\pi^0$ 's. Studying di-hadron correlations in  $p$ +A collisions instead of d+Au collisions has  
2017 a further advantage. In reference [298], the authors point out that the contributions from  
2018 double-parton interactions to the cross-sections for  $dA \rightarrow \pi^0 \pi^0 X$  are not negligible. They  
2019 find that such contributions become important at large forward rapidities, and especially in  
2020 the case of d+Au scattering. Figure 36 shows the results for the di-hadron correlations for  $\pi^0$   
2021 from the 2015  $pp$  and  $p$ +Au run. Shown is the ratio of the area, the width and the level of  
2022 pedestal of the backward peak for  $p$ +Au and  $pp$  as function of the  $p_T$  of the trigger and the  
2023 associated  $\pi^0$  and the activity in the collision as measured by the BBC.

2024 The results show basically no change in the width of the backward peak and the back-  
2025 ground/pedestal the peak is sitting on shows only up to a 20% increase in  $p$ +Au to  $pp$ .  
2026 However, the area of the backward peak shows a large suppression with increasing activity  
2027 in the collision. For fixed activity the biggest suppression is observed for the smallest trigger  
2028  $p_T$  in combination with the smallest  $p_T$  for the associated  $\pi^0$ . This behaviour is consistent  
2029 with different calculations based on the CGC formalism. This result is the first clean ob-  
2030 servable, which cannot yet be explained in a different framework than CGC and as such a  
2031 clear hint for non-linear effects.

2032 It is important to note that for the measurements to date in  $p(d)$ -A collisions both initial  
2033 and final states interact strongly, leading to severe complications in the theoretical treatment  
2034 (see [75, 142], and references therein). As described in detail in the Section above in  $p$ +A  
2035 collisions, these complications can be ameliorated by removing the strong interaction from

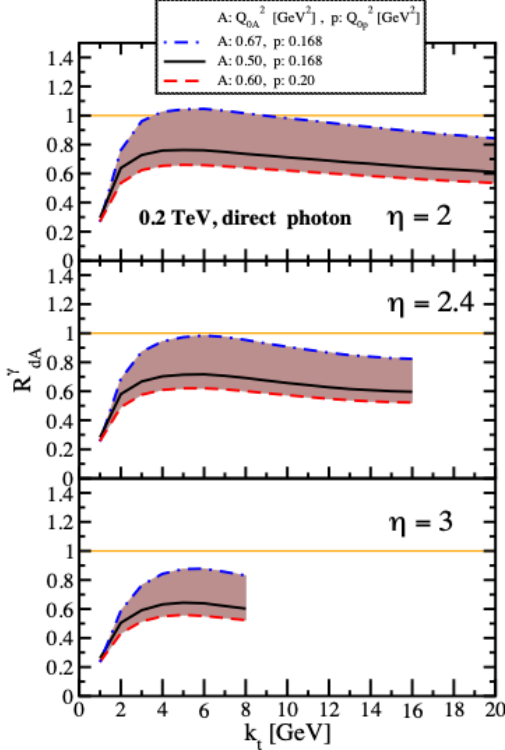


**Figure 69:** Nuclear modification factor for direct photon production in  $p(d)$ - $A$  collisions at various rapidities at RHIC  $\sqrt{s} = 200$  GeV. The curves are the results obtained from Eq. (12) in Ref. [180] and the solution to rcBK equation using different initial saturation scales for a proton  $Q_{op}$  and a nucleus  $Q_{oA}$ . The band shows our theoretical uncertainties arising from allowing a variation of the initial saturation scale of the nucleus in a range consistent with previous studies of DIS structure functions as well as particle production in minimum-bias  $pp$ ,  $p+A$  and  $A-A$  collisions in the CGC formalism, see Ref. [180] for details.

2036 the final state, by using photons and Drell-Yan electrons. The Run-15  $p+A$  run will for the  
 2037 first time provide data on  $R_{pA}$  for direct photons and therefore allow one to test CGC based  
 2038 predictions on this observable as depicted in Fig. 69 (taken from Ref. [180]). The higher  
 2039 delivered integrated luminosity for the upcoming  $p+Au$  Run-24 together with the Forward  
 2040 Upgrade will enable one to study more luminosity hungry processes and/or complementary  
 2041 probes to the di- $\pi^0$  correlations, i.e. di-hadron correlations for charged hadrons, photon-jet,  
 2042 photon-hadron and di-jet correlations, which will allow a rigorous test of the calculation  
 2043 in the CGC formalism. It is important to stress that the comparison of these correlation  
 2044 probes in  $pp$  and  $p+Au$  requires approximately equal nucleon-nucleon luminosities for these  
 2045 two collision systems for optimal measurements. It is noted that these results are crucial for  
 2046 the equivalent measurements at an EIC, which are planned at close to identical kinematics,  
 2047 because only if non-linear effects are seen with different complementary probes, i.e.,  $ep$  and  
 2048  $p+A$  one can claim a discovery of saturation effects and their universality.

2049 We use direct photon plus jet (direct  $\gamma$ +jet) events as an example channel to indicate what  
 2050 can be done in Run-24. These events are dominantly produced through the gluon Compton  
 2051 scattering process,  $g+q \rightarrow \gamma+q$ , and are sensitive to the gluon densities of the nucleon and  
 2052 nuclei in  $pp$  and  $p+A$  collisions. Through measurements of the azimuthal correlations in  
 2053  $p+A$  collisions for direct  $\gamma$ +jet production, one can study gluon saturation phenomena at  
 2054 small- $x$ . Unlike di-jet production that is governed by both the Weizsäcker-Williams and  
 2055 dipole gluon densities, direct  $\gamma$ +jet production only accesses the dipole gluon density, which  
 2056 is better understood theoretically [180, 267]. On the other hand, direct  $\gamma$ +jet production  
 2057 is experimentally more challenging due to its small cross-section and large background con-

2058 tribution from di-jet events in which photons from fragmentation or hadron decay could be  
 2059 misidentified as direct photons. The feasibility to perform direct  $\gamma$ +jet measurements with  
 2060 the Forward Upgrade in unpolarized  $pp$  and  $p$ +Au collisions at  $\sqrt{s_{\text{NN}}} = 200$  GeV has been  
 2061 studied. PYTHIA-8.189 [290] was used to produce direct  $\gamma$ +jet and di-jet events. In order  
 2062 to suppress the di-jet background, the leading photon and jet are required to be balanced  
 2063 in transverse momentum,  $|\phi^\gamma - \phi^{\text{jet}}| > 2\pi/3$  and  $0.5 < p_T^\gamma/p_T^{\text{jet}} < 2$ . Both the photon and  
 2064 jet have to be in the forward acceptance  $1.3 < \eta < 4.0$  with  $p_T > 3.2$  GeV/ $c$  in 200 GeV  
 2065  $pp$  collisions. The photon needs to be isolated from other particle activities by requiring the  
 2066 fraction of electromagnetic energy deposition in the cone of  $\Delta R = 0.1$  around the photon  
 2067 is more than 95% of that in the cone of  $\Delta R = 0.5$ . Jets are reconstructed by an anti- $k_T$   
 2068 algorithm with  $\Delta R = 0.5$ . After applying these selection cuts, the signal-to-background  
 2069 ratio is around 3:1 [261]. The expected number of selected direct  $\gamma$ +jet events is around  
 2070 1.0M/0.9M at  $\sqrt{s_{\text{NN}}} = 200$  GeV in  $p$ +Au collisions for the proposed Run-24. We conclude  
 2071 that a measurement of direct photon-jet correlation from  $p$ +Au collisions is feasible, which is  
 2072 sensitive to the gluon density in  $0.001 < x < 0.005$  in the Au nucleus where parton saturation  
 2073 is expected.

## 2074 The Final State

2075

2076 **Nuclear fragmentation functions:** In spite of the remarkable phenomenological suc-  
 2077 cesses of QCD, a quantitative understanding of the hadronization process is still one of the  
 2078 great challenges for the theory. Hadronization describes the transition of a quark or gluon  
 2079 into a final state hadron. It is a poorly understood process even in elementary collisions.  
 2080 RHIC's unique versatility will make it possible to study hadronization in vacuum and in the  
 2081 nuclear medium, and additionally with polarized beams (see Sect. 2.2.1 for the latter).

2082 It has long been recognized that the hadron distributions within jets produced in  $pp$   
 2083 collisions are closely related to the fragmentation functions that have typically been measured  
 2084 in  $e^+e^-$  collisions and SIDIS. The key feature of this type of observable is the possibility to  
 2085 determine the relevant momentum fraction  $z$  experimentally as the ratio of the hadron to  
 2086 the jet transverse momentum. Recently [195] a quantitative relationship has been derived in  
 2087 a form that enables measurements of identified hadrons in jets in  $pp$  collisions to be included  
 2088 in fragmentation function fits on an equal footing with  $e^+e^-$  and SIDIS data. Furthermore,  
 2089 hadrons in  $pp$  jets provide unique access to the gluon fragmentation function, which is poorly  
 2090 determined in current fits [126], in part due to some tension found in the inclusive high  
 2091  $p_T$  pion yields measured by the PHENIX and ALICE collaborations. Here, the proposed  
 2092 measurements can provide valuable new insight into the nature of this discrepancy.

2093 This development motivated STAR to initiate a program of identified particle fragmen-  
 2094 tation function measurements using  $pp$  jet data at 200 and 500 GeV from Run-11, Run-12,  
 2095 and Run-15. Figure 70 shows the precision that is anticipated for identified  $\pi^+$  and  $\pi^-$  in  
 2096 200 GeV  $pp$  collisions for three representative jet  $p_T$  bins after the existing data from Run-12  
 2097 and Run-15 are combined with future 200 GeV  $pp$  data from Run-24. Identified kaon and

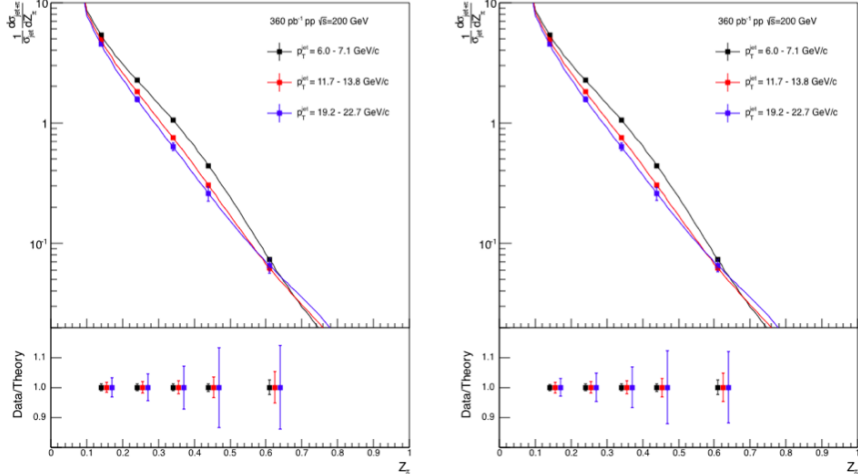


**Figure 70:** Anticipated precision for identified  $\pi^+$  (left) and  $\pi^-$  (right) within jets at  $|\eta| < 0.4$  in 200 GeV  $pp$  collisions for three representative jet  $p_T$  bins. The data points are plotted on theoretical predictions based on the DSSV14 pion fragmentation functions [126, 195]. Kaons and (anti)protons will also be measured, over the range from  $z < 0.5$  at low jet  $p_T$  to  $z < 0.2$  at high jet  $p_T$ , with uncertainties a factor of  $\sim 3$  larger than those for pions.

2098 (anti)proton yields will also be obtained, with somewhat less precision, over a more limited  
 2099 range of hadron  $z$ . Once the Run-17 data are fully analyzed, the uncertainties for 510 GeV  
 2100  $pp$  collisions will be comparable to that shown in Fig. 70 at high jet  $p_T$ , and a factor of  $\sim$   
 2101 2 larger than shown in Fig. 70 at low jet  $p_T$ . Identified hadron yields will also be measured  
 2102 multi-dimensionally vs.  $j_T$ ,  $z$ , and jet  $p_T$ , which will provide important input for unpolarized  
 2103 TMD fits.

2104 Data from the HERMES experiment [69, 71, 202] have shown that production rates of  
 2105 identified hadrons in semi-inclusive deep inelastic  $e$ -A scattering differ from those in  $ep$   
 2106 scattering. These differences cannot be explained by nuclear PDFs, as nuclear effects of  
 2107 strong interactions in the initial state should cancel in this observable. Only the inclusion of  
 2108 nuclear effects in the hadronization process allows theory to reproduce all of the dependencies  
 2109 ( $z$ ,  $x$ , and  $Q^2$ ) of  $R_{eA}$  seen in SIDIS, as shown in Fig. 71.

2110 It is critical to see if these hadronization effects in cold nuclear matter persist at the higher  
 2111  $\sqrt{s}$  and  $Q^2$  accessed at RHIC and EIC – both to probe the underlying mechanism, which is  
 2112 not understood currently, and to explore its possible universality. The combination of  $pp$  jet  
 2113 data from RHIC and future SIDIS data from EIC will also provide a much clearer picture of  
 2114 modified gluon hadronization than will be possible with EIC data alone. Using the Run-15  
 2115 200 GeV  $p$ +Au data, STAR will be able to make a first opportunistic measurement of these  
 2116 hadron-jet fragmentation functions in nuclei, but the precision will be limited. Additional  $pp$   
 2117 and  $p$ +Au data will be needed in Run-24 in order to provide a sensitive test for universality,  
 2118 as shown in Fig. 72.

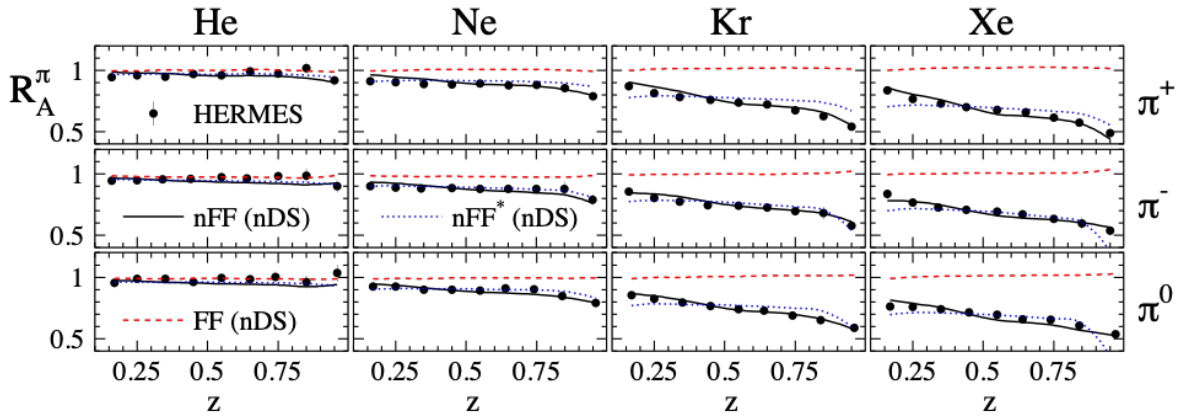


**Figure 71:**  $R_{eA}$  in SIDIS for different nuclei in bins of  $z$  as measured by HERMES [69,71,202]. The solid lines correspond to the results using effective nuclear FF [272] and the nDS medium modified parton densities [125]. The red dashed lines are estimates assuming the nDS medium modified PDFs but standard DSS vacuum FFs [127,128] and indicate that nPDFs are insufficient to explain the data

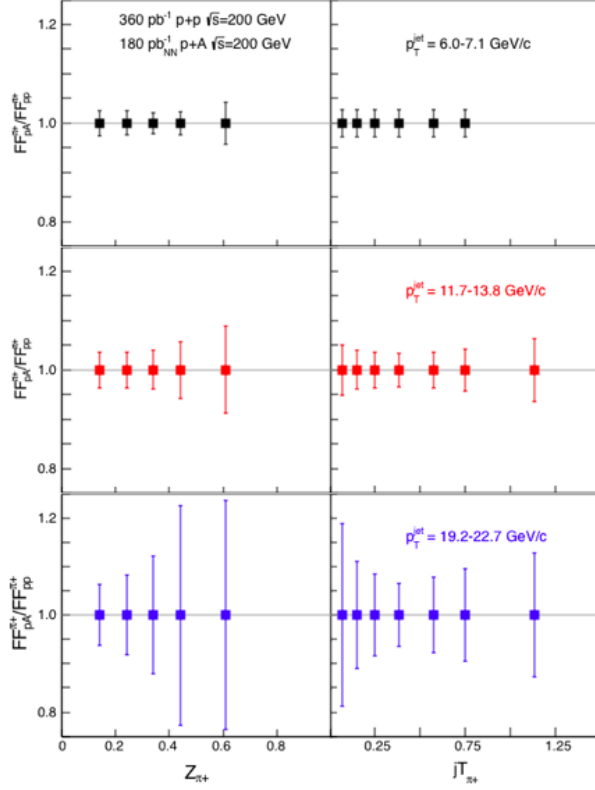


**Figure 72:** Anticipated precision for measurements of  $\pi^+$  fragmentation functions in  $p+App$  at  $|\eta| < 0.4$  vs.  $z$  and  $j_T$  in Run-24 for three representative jet  $p_T$  bins. Uncertainties for  $\pi^-$  will be similar to those shown here for  $\pi^+$ , while those for kaons and (anti)protons will be a factor of  $\sim 3$  larger. Note that, to be species independent, the nucleon-nucleon equivalent luminosity is specified for  $p+Au$ .

### 2119 3 Exploring the Microstructure of the QGP (Run-23 and 2120 Run-25 Au+Au)

2121 The completion of RHIC’s scientific mission involves the two central goals of (i) mapping out  
2122 the phase diagram of the QCD, and (ii) probing the inner workings of the QGP by resolving  
2123 its properties at short length scales [81]. The complementarity of the RHIC and LHC  
2124 facilities to study the latter is scientifically as essential as having more than one experiment  
2125 independently study the microstructure of the QGP. With several years of operating the  
2126 iTPC upgrade and the soon-to-be installation and operation of the forward detectors, the  
2127 STAR collaboration will be in an excellent position to take advantage of its vastly improved  
2128 detection capabilities. Combine this with the prospect of a substantial increase in beam  
2129 luminosities and RHIC will be uniquely positioned to fully engage in a detailed exploration  
2130 of the QGP’s microstructure. Through careful discussions in its physics working groups,  
2131 the STAR collaboration has identified a number of topics that together make a compelling  
2132 case to take data during Runs 23-25 alongside sPHENIX, and successfully complete RHIC’s  
2133 scientific mission. In this section, we present a selection of those topics that will take full  
2134 advantage of both STAR and RHIC’s unique capabilities and address the following important  
2135 questions about the inner workings of the QGP.

- 2136 • What is the precise temperature dependence of the shear  $\eta/s$ , and bulk  $\zeta/s$  viscosity?
- 2137 • What is the nature of the 3-dimensional initial state at RHIC energies? How does  
2138 a twist of the event shape break longitudinal boost invariance and decorrelate the  
2139 direction of an event plane?
- 2140 • How is global vorticity transferred to the spin angular momentum of particles on such  
2141 short time scales? And, how can the global polarization of hyperons be reconciled with  
2142 the spin alignment of vector mesons?
- 2143 • What is the precise nature of the transition near  $\mu_B = 0$ , and where does the sign-  
2144 change of the susceptibility ratio  $\chi_6^B/\chi_2^B$  take place?
- 2145 • What is the electrical conductivity, and what are the chiral properties of the medium?
- 2146 • What can we learn about confinement and thermalization in a QGP from charmonium  
2147 measurements?
- 2148 • What are the underlying mechanisms of jet quenching at RHIC energies? What do jet  
2149 probes tell us about the microscopic structure of the QGP as a function of resolution  
2150 scale?

2151 The event statistics projections that are used in this section will rely on the CAD’s  
2152 recently update 2023E and 2025E Au+Au luminosities [268] and are listed in Table 9. For  
2153 each year we presume 24 weeks of RHIC operations, and based on past run operations  
2154 an overall average of  $85\% \times 60\%$  (STAR×RHIC) uptime, respectively. The minimum-bias

2155 rates assume a conservative 1.5 kHz DAQ rates which will allow sufficient bandwidth for  
 2156 specialized triggers which are listed as integral luminosities. In order to achieve the projected  
 2157 luminosities, the collaboration will look into optimizing the interaction rates at STAR by  
 2158 allocating low and high luminosity periods within fills. Such periods, in which low interaction  
 2159 rates are sampled in the early part of a fill and high interaction rates typically in the later  
 2160 part, will allow us to collect clean, low pile-up, minimum bias events, while at the same  
 2161 time not burn beam luminosities that could affect interaction rates for sPHENIX. Clean  
 2162 minimum bias events will improve tracking efficiencies which in turn are expected to benefit  
 2163 many of the proposed correlation analyses. Optimization of the available bandwidth for  
 2164 high- $p_T$  triggers would allow us to push for lower  $p_T$  thresholds, thus further reducing biases.  
 2165 The impact of such an optimization will lead to some reduction in the projected rates, while  
 2166 still enabling a significant improvement in the precision and kinematic reach of current STAR  
 2167 measurements, and making important measurements that are yet more differential possible.

year	minimum bias [ $\times 10^9$ events]	high- $p_T$ int. luminosity [ $\text{nb}^{-1}$ ]		
		all vz	$ \text{vz}  < 70\text{cm}$	$ \text{vz}  < 30\text{cm}$
2014	2	27	19	16
2016				
2023	20	63	56	38
2025				

**Table 9:** STAR minimum bias event statistics and high- $p_T$  luminosity projections for the 2023 and 2025 Au+Au runs. For comparison the 2014/2016 event statistics and luminosities are listed as well.

2168 At RHIC it is possible to build detectors that can span from mid-rapidity to beam  
 2169 rapidity – with the two recent upgrades STAR is able to achieve this unique capability.  
 2170 STAR’s BES-II upgrade sub-systems comprised of the inner Time Projection Chamber  
 2171 (iTPC,  $1.0 < |\eta| < 1.5$ ), endcap Time Of Flight (eTOF,  $1 < \eta < 1.5$ ) and Event Plane  
 2172 Detector (EPDs,  $2.1 < |\eta| < 5.1$ ), that are all commissioned and fully operational since the  
 2173 beginning of 2019 [57, 293, 304]. As will be discussed in Section 4, the STAR collaboration  
 2174 is constructing a forward rapidity ( $2.5 < \eta < 4$ ) upgrade that will include charged particle  
 2175 tracking and electromagnetic/hadronic calorimetry [297]. For charge particle tracking the  
 2176 aim is to construct a combination of silicon detectors and small strip thin gap chamber de-  
 2177 tectors. The combination of these two tracking detectors will be referred to as the forward  
 2178 tracking system (FTS). The FTS will be capable of discriminating the hadron charge sign.  
 2179 It should be able to measure transverse momentum of charged particles in the range of  $0.2 <$   
 2180  $p_T < 2$  GeV/ $c$  with 20 – 30% momentum resolution. In what follows, we will refer to the  
 2181 combination of the existing TPC ( $|\eta| < 1$ ) and the iTPC upgrade as iTPC ( $|\eta| < 1.5$ ) for  
 2182 simplicity.

2183 The impetus for running STAR during the year of 2023-2025 in terms of bulk correlation  
 2184 measurements in Au+Au 200 GeV collisions comes from gains via: i) extended acceptance  
 2185 and ii) enhanced statistics. In the first subsections, we briefly describe how these two op-

2186 opportunities can be exploited to perform correlations measurements that are unique to the  
 2187 physics goals of the RHIC heavy-ion program.

2188 Next, thanks to a reduced material budget between the beam and the iTPC, STAR will  
 2189 be uniquely positioned to perform dielectron measurements with which we propose to probe  
 2190 degrees of freedom of the medium and its transport properties. For that we will use the  
 2191 high precision dilepton excess yield, i.e.  $l^+l^-$  invariant mass distribution after subtraction  
 2192 of dilepton sources produced after freeze-out, and contributions from the initial collisions  
 2193 such as Drell-Yan and correlated charm-anticharm pairs. Furthermore, we propose to study  
 2194 the virtuality, Wigner function and final-state magnetic field in the QGP. For the latter  
 2195 photon-photon collisions in ultra-peripheral, peripheral, and midcentral reactions and  $p+A$   
 2196 (all centralities) in both channels  $e^+e^-$ ,  $\mu^+\mu^-$  will be measured with high accuracy.

2197 In the last subsections, we address our proposed charmonium measurements and motivate  
 2198 the importance of STAR's proposed program of precise jet measurements to explore the  
 2199 micro-structure of the QGP.

2200 Figure 82 shows the kinematic projection plot for the STAR past (until 2015), current,  
 2201 and with Run23+25 hard probes measurements. The corresponding STAR measurements  
 2202 are compared with the LHC (published) measurements.

### 2203 3.1 Correlation Measurements Utilizing Extended Acceptance

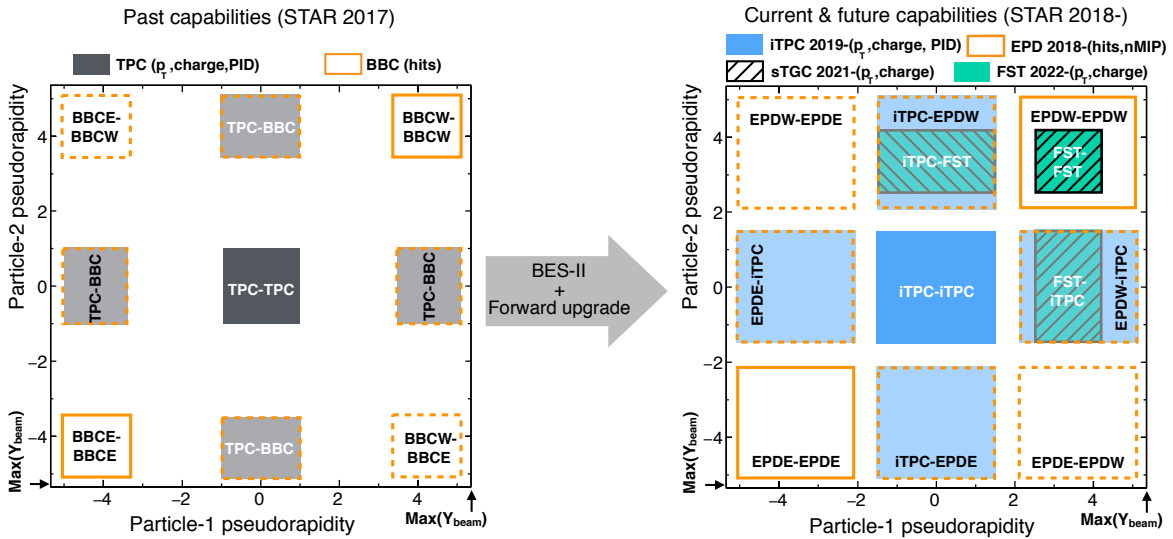


**Figure 73:** A visual representation of two-particle phase space in pseudorapidity covered by STAR detectors with respect to the region allowed by maximum beam rapidity ( $Y_{beam}=5.36$  at 200 GeV Au+Au collisions) of RHIC. Left and right panels show the capabilities before and after BES-II and forward upgrades of the STAR detector, respectively. Note that in addition to a larger pair acceptance, the EPD granularity is over an order of magnitude larger than that of the BBC, and individual EPD tiles are shown to be separable into 1, 2, 3 MIP responses.

2204 Figure 73 demonstrates how STAR, with the BES-II and forward upgrades, will extend  
 2205 the two-particle phase-space (in terms of  $\eta_1$  and  $\eta_2$  with respect to beam rapidity) many  
 2206 times enabling us to perform correlation measurements over a wide window of relative pseu-  
 2207 dorapidity. Since many of the important correlation measures are based on two-particle  
 2208 correlations, this enhanced phase-space will provide STAR with many advantages: 1) an in-  
 2209 crease in the number of pairs resulting in better precision, 2) a reduction in different sources of  
 2210 the non-flow backgrounds by increasing the pseudorapidity separation. Many multi-particle  
 2211 correlations will also benefit from the increase in triplets, quadruplets and so on due to the  
 2212 overall increased acceptance. With this unique extended pseudorapidity reach our goal is  
 2213 to perform correlation measurements to enable a deeper understanding of the largely unex-  
 2214 plored three-dimensional structure of the initial state, and further improve the extraction of  
 2215 temperature dependent transport properties of the subsequent fluid-like medium produced  
 2216 in heavy ion and small system collisions at RHIC through data-model comparison such as  
 2217 the Bayesian analysis performed in Ref [144].

2218 Two key sets of measurements are of interests: 1) the pseudorapidity dependence of  
 2219 azimuthal correlations, 2) the pseudorapidity dependence of global hyperon polarization.

### 2220 **Pseudorapidity-dependent Azimuthal Correlations to Tightly Constrain the Tem-** 2221 **perature Dependence of Viscosity**

2222 The idea of tightly constraining the temperature dependent viscosity of the QGP was envi-  
 2223 sioned in the 2015 Long Range Plan for Nuclear Science [81]. The QCD matter formed at  
 2224 RHIC shows nearly perfect fluidity characterized by the smallest viscosity to entropy ratio  
 2225  $\eta/s$  known in nature. One major aim is to perform precision measurements to constrain the  
 2226 temperature dependence of the shear  $\eta/s$  (T) and bulk  $\zeta/s$  (T) viscosities. Recent state-  
 2227 of-the-art Bayesian analyses of flow and spectra data within sophisticated event-by-event  
 2228 hydrodynamics models has show strong evidence for temperature dependence of  $\eta/s$  and  
 2229  $\zeta/s$  [93, 144, 251], but the uncertainties are still quite large. On the other hand, hydrody-  
 2230 namic simulations have demonstrated that since the temperature of the produced fireball in  
 2231 HICs vary with the rapidity, the measurement of the rapidity dependence of flow harmonics  
 2232 can provide additional constraint on the  $\eta/s$  (T) and  $\zeta/s$  (T) [133]. For this, RHIC measure-  
 2233 ments have an advantage over the LHC since the smaller beam rapidity at RHIC provides  
 2234 stronger variations of the temperature with rapidity. The beam energy scan at RHIC pro-  
 2235 vides an additional handle on temperature to map  $\eta/s$  (T), and  $\zeta/s$  (T) over a wide range of  
 2236 temperatures. Indeed, the hydrodynamic simulation of Ref. [133] indicates that  $\eta/s$  (T) at  
 2237 lower temperatures, near its possible minimum ( $T = T_c$ ), can be better constrained by RHIC  
 2238 measurements. Results from such simulations are shown in Fig. 74. In this simulation, a  
 2239 number of QCD-motivated parameterizations of the temperature dependence of the shear  
 2240 viscosity were assumed, as shown in Fig. 74 (left).

2241 Existing data from the PHOBOS collaboration suffer from large uncertainties, therefore  
 2242 only limited constraints on the temperature dependence of the transport parameters can  
 2243 be achieved. The BES-II upgrade (with iTPC) and the forward upgrade (FTS) of STAR  
 2244 will provide precise estimations of different azimuthal correlation observables:  $v_n(\eta)$  and

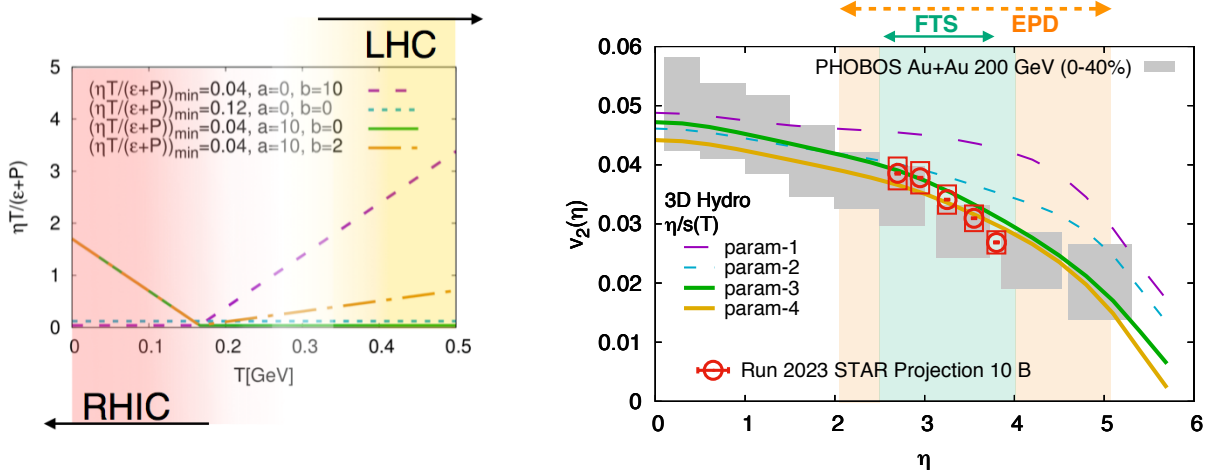


**Figure 74:** (Left) Different parameterizations of the temperature dependence of the shear viscosity to entropy  $\eta/s$  ( $T$ ) (at zero chemical potential) used in the hydrodynamical simulation of Ref. [133]. Interestingly, it has been demonstrated in Ref. [250] that the region of lowest  $\eta/s$  is the one that can be probed at RHIC. (Right) Effects on the elliptic flow co-efficient  $v_2$  due to different parameterizations of the viscosity parameter, indicating better constraints on  $\eta/s$  ( $T$ ) can only be performed by measurements at forward rapidities at RHIC. The interpretation of the existing PHOBOS data is limited by the large uncertainties. Projections for STAR measurements are shown on the same plot.

2245 other higher-order ( $n > 2$ ) flow coefficients  $v_n(\eta)$ , its fluctuations  $\sigma(v_n)/v_n$  that have never  
 2246 been measured at forward rapidity, are essential in terms of constraining  $\eta/s$  ( $T$ ) near its  
 2247 possible minimum. These quantities previously measured at mid-rapidity with previous  
 2248 data are not enough for discriminating different parameterization of  $\eta/s$  ( $T$ ) as shown in the  
 2249 hydrodynamic simulation of Ref. [133]. While transverse momentum integrated quantities  
 2250 at forward rapidity can constrain the shear viscosity, measurement of the  $p_T$  of particles at  
 2251 forward rapidity (i.e. forward tracking) is essential to constrain the bulk viscosity  $\zeta/s$  – in  
 2252 particular the information of  $\langle p_T \rangle$  is needed to constrain  $\zeta/s(T)$ . With the forward tracking  
 2253 systems it will be possible to measure the  $p_T$  dependence of  $v_n$  in Au–Au collisions in 2023.

## 2254 Pseudorapidity-dependent Azimuthal Correlations to Constrain the Longitudi- 2255 nal Structure of the Initial State

2256

2257 Initial-state longitudinal fluctuations and the fluid dynamical response of the medium  
 2258 formed in heavy ion collisions can lead to de-correlations of the direction of the reaction  
 2259 planes  $\Psi_n$  (which determines the orientation of the harmonic anisotropies) with pseudora-  
 2260 pidity (see Fig. 75). Such effects are often referred to as a torque or twist of the event  
 2261 shape [100, 183, 254] that eventually leads to a breaking of longitudinal/boost/rapidity in-  
 2262 variance. The magnitude of the de-correlation is determined by the details of the dynam-  
 2263 ics of initial state, and the distribution of nucleons and partons inside the colliding nu-

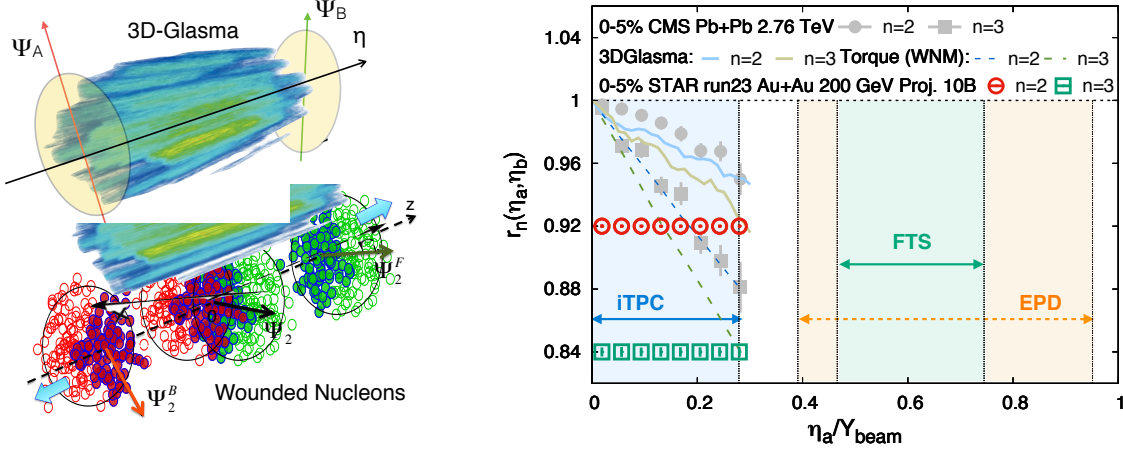


**Figure 75:** (Left) Cartoon to demonstrate the de-correlation of event planes in the longitudinal direction of a collision from a gluon saturation based 3D-Glasma model [273] and a wounded nucleon model (WNM) [100, 221]. (Right) The longitudinal de-correlation of the elliptic anisotropy plane as a function of pseudorapidity in units of beam rapidity. CMS results are compared to predictions from two models in the left with STAR projection for Run-23 (using preliminary Run-19 results) from an anticipated 10 B min-bias events. The colored regions show that the current and future capabilities at STAR (with iTPC+EPD+FTS) can extend such measurements with good precision by covering a large fraction of the beam rapidity at 200 GeV – this demonstrates the unique strength to STAR to study the physics of 3D initial state.

2264 clei. Several promising observables have been proposed to study this effect, Fig. 75 shows  
 2265 one which can be expressed as  $r_n(\eta_a, \eta_b) = V_{n\Delta}(-\eta_a, \eta_b)/V_{n\Delta}(\eta_a, \eta_b)$ , where  $V_{n\Delta}(\eta_a, \eta_b)$  is  
 2266 the Fourier coefficient calculated with pairs of particles taken from three different pseu-  
 2267 dorapidity regions  $-\eta_a$ ,  $\eta_a$  and  $\eta_b$ . The observable  $r_n(\eta_a, \eta_b)$  was originally introduced  
 2268 and measured by CMS collaboration in Ref. [198] and also been measured by the AT-  
 2269 LAS collaboration in [3]. An observable using three-particle correlations that is sensi-  
 2270 tive to this effect is the relative pseudorapidity dependence of the three-particle correlator  
 2271  $C_{m,n,m+n}(\eta_a, \eta_b, \eta_c) = \langle \cos(m\phi_1(\eta_a) + n\phi_2(\eta_b) - (m+n)\phi_3(\eta_c)) \rangle$  [51]. Another, very similar  
 2272 to  $r_n$  in terms of design but involving four-particle correlations, is:  $R_{n,n|n,n}(\eta_a, \eta_b)$  [92]. As  
 2273 shown in Fig. 75, CMS measurements of  $r_n$  show strong de-correlation ( $\sim 16\%$  for  $n=3$ ,  
 2274  $\sim 8\%$  for  $n=2$ ) in central events within the range of their acceptance. In the 3D-Glasma  
 2275 model of initial state, the breaking of boost invariance is determined by the QCD equations  
 2276 which predict the evolution of gluons in the saturation regime with Bjorken-x. At the LHC  
 2277 such models predict weaker de-correlation as compared to when the initial state is described  
 2278 by wounded nucleon models. The 3D-Glasma model does a good job in explaining the  $r_2$   
 2279 data from CMS [273] but over-predicts the  $r_3$  results. One expects the nature of the ini-  
 2280 tial state to change from LHC to RHIC, in particular the region of Bjorken-x probed is  
 2281 very different. It is therefore extremely important to utilize the enhanced acceptance of  
 2282 the STAR detector with a Au+Au 200 GeV run to study this effect. In Fig. 75 STAR's  
 2283 projections using preliminary Run-19 results to estimate the uncertainties for 10 B events

2284 are shown for the measurement of  $r_n$  within the acceptance  $|\eta| < 1.5$ . The colored regions  
 2285 show that the current and future capabilities at STAR (with iTPC+EPD+FTS) can extend  
 2286 such measurements using observables  $r_n, C_{m,n,m+n}, R_{n,n|n,n}$  with good precision by covering  
 2287 either an equal (iTPC only) or larger (iTPC+FTS+EPDs) fraction of the beam rapidity  
 2288 at 200 GeV compared to the LHC measurements. This unique measurement capability will  
 2289 help pin down the nature of the 3-D initial state of heavy ion collisions. It will also help  
 2290 constrain different models of QCD that predict the rapidity (or Bjorken-x) dependence of  
 2291 valance quark and gluon distributions inside colliding nuclei as has been demonstrated by  
 2292 theoretical calculations in Ref. [273, 278].

2293 **Search for Collectivity in Photo-nuclear ( $\gamma + Au$ ) Processes**

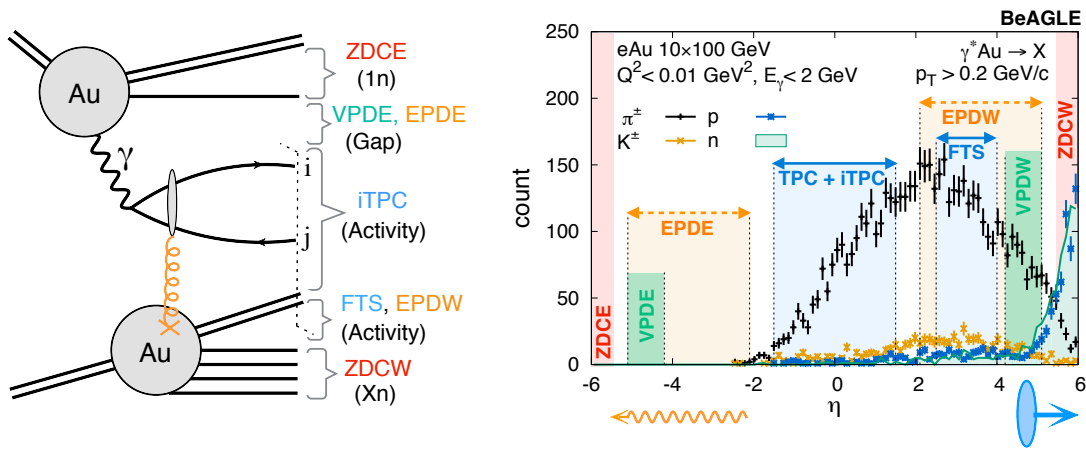


**Figure 76:** (Left)  $\gamma + Au$  process in ultra-peripheral heavy ion collisions associated with a large rapidity asymmetry; the large acceptance of the STAR detector can be used to trigger these events to study bulk observables and search for collectivity, the same can be done in low virtuality  $e+Au$  collisions to search for collectivity at the EIC. (Right) Pseudorapidity distribution of different particles using the state-of-the-art BeAGLE [1, 308] event generator for EIC in  $e+Au$  events. By restricting virtuality and energy of the photon ( $\gamma^*$ ) we try to mimic the kinematics of a  $\gamma + Au$  ( $Au+Au$  UPC) event. The purpose of this plot is to demonstrate how different STAR detectors will be used to identify such UPC processes at the kinematics similar to that at EIC.

2294

2295 Until the EIC at BNL is built, high-energy photoproduction processes (low virtuality limit  
 2296 of deep inelastic scattering) as shown in Fig.76, can be studied using ultra-peripheral ion  
 2297 collisions (UPCs) that occur when two heavy ion interact at large impact parameters. Such  
 2298 collisions can be considered as  $\gamma+A$  collisions but unlike at the EIC, the photons involved  
 2299 in UPCs are quasi-real. Do we expect to see collectivity in such collisions? If observed,  
 2300 this will address an important question. Origin of collectivity in small collision systems  
 2301 has been argued to be driven by the formation of a medium that evolves hydrodynamically.  
 2302 However, due to the phenomenon of saturation, intrinsic correlations for gluons in the  
 2303 colliding hadrons/nuclei have been shown by theoretical models such as color glass conden-

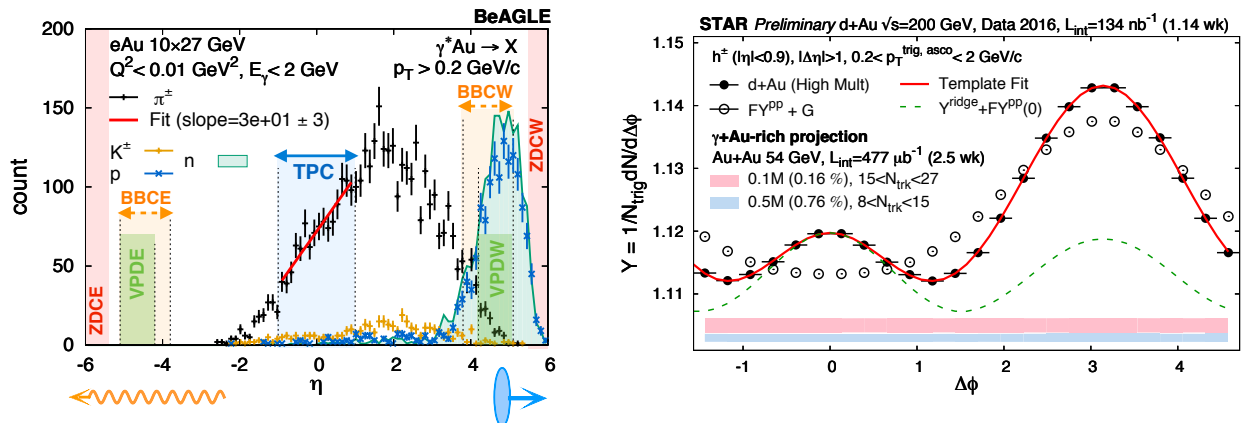


**Figure 77:** (Left)  $\gamma + Au$  processes simulated using BeAGLE event generator in the low virtuality limits ( $Q^2 < 0.01 \text{ GeV}^2$ ) of DIS by restricting the energy of photons to be  $E_\gamma < 2 \text{ GeV}$  and ion energy to be 27 GeV. The pseudorapidity distributions thus produced is used to apply cuts on detectors in STAR to identify  $\gamma + Au$  candidates in 54 GeV Au+Au collisions. (Right) STAR preliminary data on per-trigger yield estimated using di-hadron correlations in d–Au (hadronic) 200 GeV collisions. The correlation function in pp collisions (open circle) is used as a template to fit the same in relatively higher multiplicity d–Au collisions (solid circle) and to extract the long-range ridge-like component. The red and blue band show projections for  $\gamma + Au$  enriched events for two different multiplicity bins. The aim is to use the correlation function from the low multiplicity  $\gamma + Au$  to perform template fit in the high multiplicity bin. With the anticipated Au+Au 200 GeV data collected in Run-23, about 170 more  $\gamma + Au$  candidates can be collected, implying a reduction of the red and blue bands by a factor of 13.

2304 sate (CGC) to contribute to collectivity – experimentally such contributions have not been  
 2305 decisively established. The general consensus is that correlations predicted by both hydro-  
 2306 dynamics and CGC contribute to collectivity – although no experimental measurement has  
 2307 been proposed that can disentangle the contribution from the two effects. No studies have  
 2308 convincingly demonstrated that in  $\gamma + A$  collisions a hydrodynamic medium can be formed.  
 2309 Observation of collectivity in  $\gamma + Au$  (or future e+A), therefore, may very well be the first  
 2310 evidence of purely initial-state gluon driven contribution to such phenomenon as argued in  
 2311 the theoretical work of ref [284]. This will be an important step to understanding the role  
 2312 of gluon saturation or color coherence in driving collectivity, and also pioneer several new  
 2313 measurements in this direction at the BNL EIC.

2314 The search for collectivity in ultra-peripheral (UPC) 5.02 TeV Pb+Pb collisions, by  
 2315 triggering  $\gamma + A$  events, has recently been initiated by the ATLAS collaboration at the LHC  
 2316 where interesting hints of long-range ridge like correlations have been observed [7]. However,  
 2317 RHIC has similar ion energies when compared to the future EIC. This gives STAR the  
 2318 necessary motivation to propose a program to search for the collectivity in  $\gamma + A$  events at  
 2319 RHIC. This is interesting as  $\gamma + A$  UPC events have much synergy with low virtuality events  
 2320 in e+A collisions at the EIC and in many ways this provides a chance to better understand  
 2321 the origin of collectivity. It must be noted the proposed program with STAR will have

2322 several unique strengths to both complement and extend such a search for collectivity at  
 2323 lower collision energies due to: a wider acceptance compared to beam rapidity ( $Y_{\text{beam}}$ ),  
 2324 better momentum resolution to measure the soft part of the spectrum, and better particle  
 2325 identification capabilities. As shown in Fig.76, our goal is to trigger on the  $\gamma + Au$  process in  
 2326 ultra-peripheral heavy ion collisions associated with a large rapidity asymmetry. The figure  
 2327 also demonstrates how the combination of the inner Time Projection Chamber (iTTPC), the  
 2328 new highly granular Event-Plane Detectors (EPD) and the forward tracking system (FTS)  
 2329 and Zero-Degree Calorimeters (ZDC) can be used isolate  $\gamma + Au$  events from peripheral  
 2330 Au+Au events (symmetric in  $\eta$  with no gaps). By triggering on these events our aim will  
 2331 be to study bulk observables ( $dN/dydp_T(\pi^\pm, K^\pm, p/\bar{p})$ ) and long range ridge-like azimuthal  
 2332 correlations to search for collectivity.

2333 A handful of datasets exist on the disk with the appropriate event trigger selection for  
 2334 such a process. For example, Fig.77 show a feasibility study using the dataset of Au+Au  
 2335 collisions at 54 GeV (year 2017) and 200 GeV (year 2019). In order to mimic the kinematics  
 2336 of Fig.77(left) we apply asymmetric cuts on the energy deposition of neutrons in ZDCs  
 2337 (1nXn). For example, if the ZDC east is restricted to have a single neutron hit, while no  
 2338 restriction is placed on the ZDC west we trigger on  $\gamma + Au$  candidates with east going  
 2339 photons, and vice versa. We also apply similar asymmetric cuts in the BBCs to get purer  
 2340 samples. After collecting  $\gamma + Au$ -rich candidates we study di-hadron correlations in such  
 2341 events and compare with the same from hadronic events with same activities. We select two  
 2342 such windows of event activity based on cuts on numbers of tracks in TPC ( $15 < N_{trk}^{|\eta| < 0.5} < 27$   
 2343 and  $1 < N_{trk}^{|\eta| < 0.5} < 8$ ). According to our estimates the percentage of possible  $\gamma + Au$  candidates  
 2344 are about 0.17% and 0.83% of min-bias events in those two windows of multiplicity. Fig.77  
 2345 shows STAR preliminary data on the per-trigger yield in di-hadron correlations in d–Au  
 2346 events where a clear ridge can be seen after template fitting. On the same plot we show  
 2347 projections of uncertainties for the di-hadron correlations in possible  $\gamma + Au$ -rich events  
 2348 using Au+Au 54 GeV data. With the new forward detector capability and new datasets in  
 2349 the future Au+Au 200 GeV (year 2023) run of RHIC with a dedicated trigger selection, we  
 2350 should be able to make measurements at the kinematics similar to that at EIC as shown in  
 2351 Fig.77. Based on the feasibility studies with 54 GeV data, we estimate about 17 – 83 Million  
 2352  $\gamma + Au$  candidates can be obtained with 10 Billion Au+Au events which is about 170 times  
 2353 the statistics shown in Fig.77.

## 2354 Pseudorapidity Dependence of Global Hyperon polarization

2355  
 2356 The global polarization of hyperons produced in Au+Au collisions has been observed by  
 2357 STAR [53]. The origin of such a phenomenon has hitherto been not fully understood. Several  
 2358 outstanding questions remain. How exactly is the global vorticity dynamically transferred  
 2359 to the fluid-like medium on the rapid time scales of a collision? Then, how does the local  
 2360 thermal vorticity of the fluid gets transferred to the spin angular momentum of the produced  
 2361 particles during the process of hadronization and decay? In order to address these questions  
 2362 one may consider measurement of the polarization of different particles that are produced

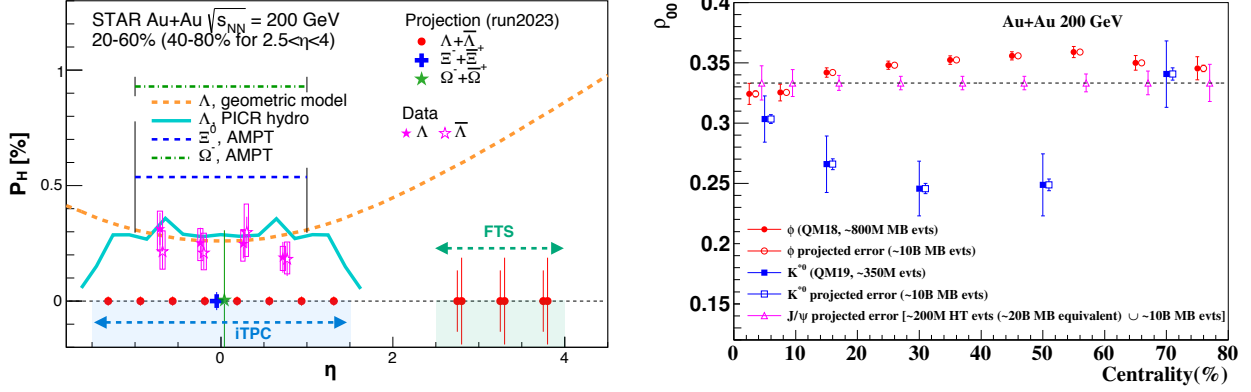


**Figure 78:** (Left) Projections (along with preliminary data) for differential measurements of  $\Lambda$  ( $\bar{\Lambda}$ ) polarization over the extend range of pseudorapidity with the iTPC and FTS detectors of STAR that will help resolve tension between different theoretical model predictions (shown by curves) of polarization with  $\eta$ . In addition, projections for the measurements of spin-1/2  $\Xi$  and spin-3/2  $\Omega$  particles are also shown. (Right) Spin alignment co-efficient  $\rho_{00}$  as a function of centrality, with projected errors based on  $\sim 10$  billion minimum bias events. The enhanced statistics Run-23, combined with the excellent dilepton capabilities of STAR, will enable us to measure  $J/\psi$  alignment along with increasing the significance of the  $\phi$  and  $K^{*0}$  measurements.

2363 in different spatial parts of the system, or at different times. A concrete proposal is to:  
 2364 1) measure the  $\Lambda$  ( $\bar{\Lambda}$ ) polarization as a function of pseudorapidity and 2) measure it for  
 2365 different particles such as  $\Omega$  and  $\Xi$ . Both are limited by the current acceptance and statistics  
 2366 available as recently published by STAR [41]. However, as shown in Fig. 78 with the addition  
 2367 of the iTPC and FTS, and with high statistics data from Run-23 it will be possible to  
 2368 perform such measurements with a reasonable significance. iTPC (+TPC) has excellent  
 2369 PID capability to measure all these hyperons. Although the FTS has no PID capability  
 2370 we can do combinatorial reconstruction of  $\Lambda$  ( $\bar{\Lambda}$ ) candidates via displaced vertices. A similar  
 2371 analysis was performed and published by STAR using the previous FTPC [11]. In order to  
 2372 make a conservative projection we assume similar momentum resolution of 10–20% for single  
 2373 charged tracks, similar overall tracking efficiency, charge state identification capability for  
 2374 the FTS and FTPC (see the forward upgrade section for exact numbers). We also assume the  
 2375 FTS, with it's novel-tracking framework, will be able to measure a minimum separation of 20  
 2376 cm between the all pairs of one positive and one negative track (a possible decay vertex) from  
 2377 the main vertex of the event. This will give rise to about 5% efficiency of  $\Lambda$  ( $\bar{\Lambda}$ ) reconstruction  
 2378 with about 15 – 20% background contribution from  $K_S^0 \rightarrow \pi^+ + \pi^-$  [11]. With this we can  
 2379 make projections for a polarization measurement in Au+Au 200 GeV 40 – 80% assuming 10  
 2380 Billion minimum-bias events as shown in Fig. 78. The two different error bars correspond to  
 2381 lower and upper limits considering current uncertainties on the efficiency of charged track  
 2382 reconstruction and the final efficiency of  $\Lambda$  reconstruction. Currently theoretical models  
 2383 predict contradictory trends for the pseudorapidity dependence of  $\Lambda$  polarization. If the  
 2384 initial local orbital angular momentum driven by collision geometry [222] plays a dominant  
 2385 role it will lead to increases of polarization with pseudorapidity. On the other hand if

2386 the local thermal vorticity and hydrodynamic evolution [318] play a dominant role it will  
 2387 predict decreasing trend or weak dependence with pseudorapidity. Such tensions can be  
 2388 easily resolved with the future proposed measurement during Run-23.

### 2389 3.2 Correlation Measurements Utilizing the Enhanced Statistics

2390 Over the past years the STAR collaboration has pursued dedicated measurements of Au+Au  
 2391 collisions at  $\sqrt{s_{\text{NN}}} = 200$  GeV that have major discovery potential but are intrinsically  
 2392 statistics hungry. Attempts have been made to combine datasets from several years to  
 2393 increase the significance of such measurements. This can result in run-to-run variations and  
 2394 systematics in detector responses that sometimes are tedious to correct. A single stable long  
 2395 run with similar detector conditions, as anticipated during Run-23, can avoid such issues.  
 2396 In the following section, and also in section 1.2.7, we propose correlation measurements that  
 2397 will utilize the enhanced statistics from Run-23 and can lead to high-impact results. To  
 2398 start we assume STAR will collect data at the rate of 1.5 kHz and a combined RHIC×STAR  
 2399 uptime of 50% (12 hour/day) for 24 weeks of running during Run-23. This will lead to the  
 2400 accumulation of about  $24 \times 7 \times 86400 \times 0.5 \times 1500 \approx 10$  billion events.

#### 2401 Global Spin Alignment of $J/\psi$

2402 Surprisingly large signals of global spin alignment of vector mesons such as  $\phi(1020)$  and  
 2403  $K^{*0}(892)$  have been measured via the angular distribution of one of their decay products.  
 2404 These experimental observations of vector meson spin alignment have yet to be interpreted  
 2405 satisfactorily by theory calculations. It has been realized that the mechanism driving the  
 2406 global polarization of hyperons can have its imprint on vector meson spin alignments albeit  
 2407 the observed strength of signals for the two measurements cannot be reconciled. In fact  
 2408 the large quantitative difference between the measurements of  $\phi(1020)$  and  $K^{*0}(892)$  spin  
 2409 alignment as shown in Fig. 78 (right) cannot be simultaneously explained by conventional  
 2410 mechanisms of spin-orbit coupling, driven by angular momentum, without invoking strong  
 2411 force fields. It is argued that the strong force field makes a dominant contribution to the  
 2412 spin-alignment coefficient  $\rho_{00}$  of  $\phi$ , while for  $K^{*0}$ , the contribution is diminished due to the  
 2413 mixing of quark flavors (averaging-out of different meson fields) [279, 280]. Therefore, the  
 2414 current preliminary experimental data from STAR (Fig. 78, showing  $\rho_{00}(\phi) > \rho_{00}(K^{*0})$ )  
 2415 support the role of strong force field as a key mechanism that leads to global spin alignment.  
 2416 However, a stringent test of such a prediction can be performed by measuring the spin  
 2417 alignment of  $J/\psi$ . This is because similar arguments apply for both  $\phi$  and  $J/\psi$ , i.e. like  $s$   
 2418 and  $\bar{s}$ , the strong field component also couples to  $c$  and  $\bar{c}$  quarks leading to larger  $\rho_{00}$  for  $J/\psi$ .  
 2419 In Fig. 78(right) we present the projected uncertainties for  $\rho_{00}$  of  $J/\psi$  estimated for various  
 2420 centralities assuming: 1) 10 billion min-bias events for low  $p_T$   $J/\psi$  measurements and, 2)  
 2421 200 million events implementing High Tower (HT) triggers with the Barrel Electromagnetic  
 2422 Calorimeter for the high  $p_T$   $J/\psi$ . Both assume 24 weeks running anticipated in Run-23.  
 2423 It is worth to mention that apart from  $J/\psi$  spin alignment, such a large statistics dataset  
 2424 will also allow addition differential study of global spin alignment of  $\phi$  and  $K^{*0}$  and help to  
 2425 further elucidate the mechanism behind vector meson spin alignment.

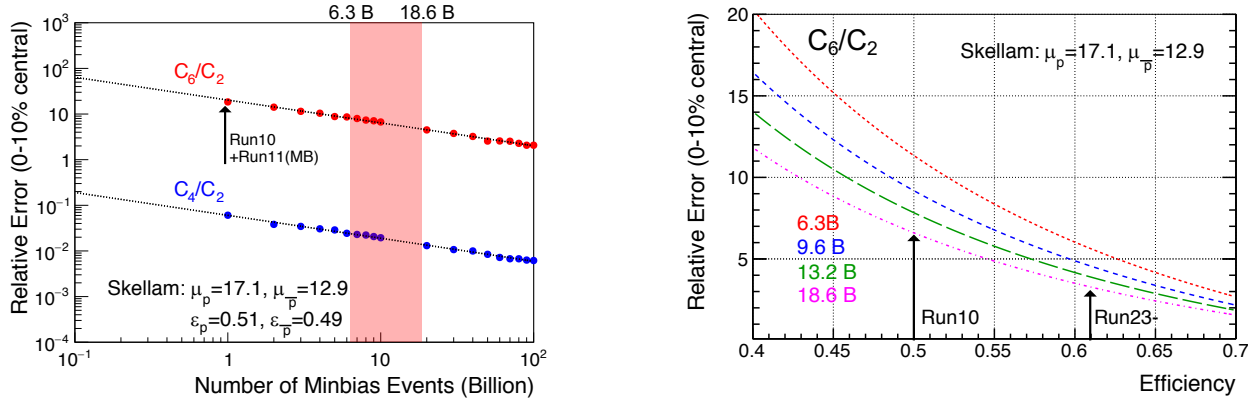


**Figure 79:** Projection for measurement of ratio of sixth order over second order cumulants of net-proton distribution.

### 2426 Sixth Order Cumulant of Net-proton Distributions

2427 LQCD calculations [90, 97] predict a sign change of the susceptibility ratio  $\chi_6^B/\chi_2^B$  with  
 2428 temperature ( $T$  at  $\mu_B = 0$ ) taking place in the range of 145-165 MeV. The observation of  
 2429 this ratio going from positive to negative values is considered to be a signature of a crossover  
 2430 transition. Interestingly, as shown in Section 1.1.1, values of net-proton  $C_6/C_2$  are found  
 2431 to be negative systematically from peripheral to central Au+Au 200 GeV collisions within  
 2432 large statistical uncertainties. The observation of negative  $C_6/C_2$  is intriguing and so far  
 2433 only hinted at in the 200 GeV data, the current result has less than  $2.3\sigma$  significance for 30-  
 2434 40% centrality in terms of statistical uncertainties. The current systematic uncertainty is of  
 2435 similar order as the statistical uncertainty and if based off of combining datasets from Run-10  
 2436 and Run-11. As shown in the projection plot of Fig. 79 it is possible to establish definitive  
 2437 observation of negative  $C_6/C_2$  at 200 GeV with nearly 10 billion minimum-bias events to be  
 2438 collected during the Run-23 with 15% increase in the reconstruction efficiency and enhanced  
 2439 acceptance of the iTPC detector upgrade. A similar measurement can be performed at the  
 2440 LHC for vanishing baryon chemical potential, while only STAR measurements can explore  
 2441 the finite  $\mu_B$  region. Our measurement at  $\sqrt{s_{NN}}=200$  GeV has the potential to establish the  
 2442 first experimental observation of QCD chiral crossover transition at  $\mu_B \approx 20$  MeV.

### 2443 Strong Interaction Measurements

2444 The strong interaction between baryons leads to a residual force; the most common example  
 2445 is  $NY$ . The same force is responsible for binding  $n - p$  into  $d$ . So far, understanding the  
 2446 strong interaction has been limited to the effective theories related to nucleons and the  
 2447 scattering experiments, which are very challenging due to the short lifetime of resonances  
 2448 (a few cm decay length). One of the current challenges is to evaluate the strong interaction  
 2449 between hyperons, as experimentally still very little is known about  $NY$  and  $YY$  interactions.  
 2450 Hypernuclei (a hyperon bound inside an atomic nucleus) are proof of a positive, attractive  
 2451 interaction of  $NY$ . Measurements of  $NN$  and  $NY$  interactions have crucial implications for  
 2452 the possible formations of bound states. Studies of the strong interaction potential via two-

2453 particle correlations in momentum space measured in relativistic heavy-ion and elementary  
 2454 collisions have proven to be useful to gain access to the interactions between exotic and rare  
 2455 particles. Possible combinations can be:  $p\Lambda$ ,  $p\Sigma$ ,  $p\Omega$ ,  $p\Xi$ ,  $\Lambda\Lambda$ ,  $\Xi\Xi$ . In contrast to  $p\Lambda$ , the  
 2456 nature of  $p\Sigma$ ,  $p\Omega$ ,  $\Lambda\Lambda$  still need experimental verification. Even if scattering experiments are  
 2457 available, they are not very conclusive.

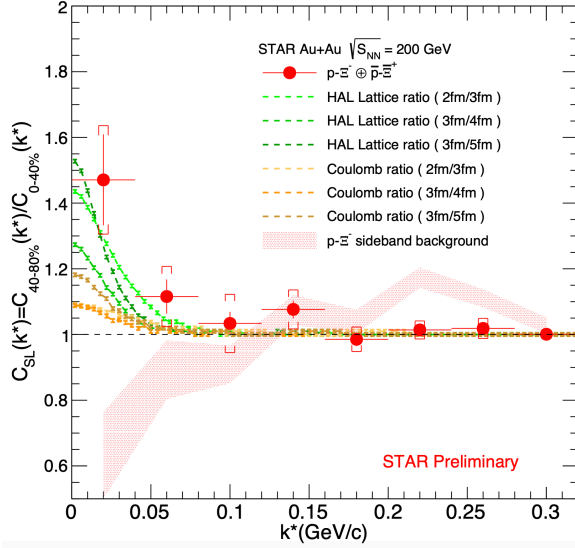


**Figure 80:** Solid circles represent the ratio ( $R$ ) of the small system (40-80% collisions) to the large system (0-40% collisions) for proton- $\Xi$  and  $\bar{p}$ - $\Xi$  correlations. The bars correspond to the statistical uncertainties. The shaded area represents  $R$  for background candidates from the side-band of the  $\Xi$  invariant mass. Coulomb-induced  $R$  are shown in yellow and orange colors. HAL Lattice predictions of  $R$  are shown in green.

2458 Figure 80 shows the preliminary  $p\Xi$  correlations function. All available statistics, 3 billion  
 2459 events accumulated over all previous runs, were used for the  $p\Xi$  and  $p\Omega$  cases. Combining  
 2460 such datasets leads to the run-to-run variations resulting in larger total systematic uncertain-  
 2461 ties in the detector responses. A single stable long run with similar detector settings during  
 2462 the Run-23 will avoid such issues. Statistical uncertainties of the current measurements re-  
 2463 main high, and the number of points that build the correlation function is minimal. This  
 2464 means that the current results are not conclusive enough to study in detail the parameters  
 2465 of the strong interaction. Since the effect of the Coulomb interaction, seen via two-particle  
 2466 correlation, is expected to cancel in the ratio of two correlation functions, the extraction  
 2467 of the strong interaction parameters can be performed with larger datasets by measuring  
 2468 the correlation signal for central and mid-central+peripheral collisions. The collection of  
 2469 10 billion events from Run-23 will make possible the construction of correlation functions  
 2470 of the  $p\Xi$  case with double the number of points and smaller statistical uncertainties than  
 2471 the current measurement. The  $p\Omega$  system is more statistics hungry, and we expect that we  
 2472 will require 20 billion events, from combining Run-23 and Run-25, before we can double of

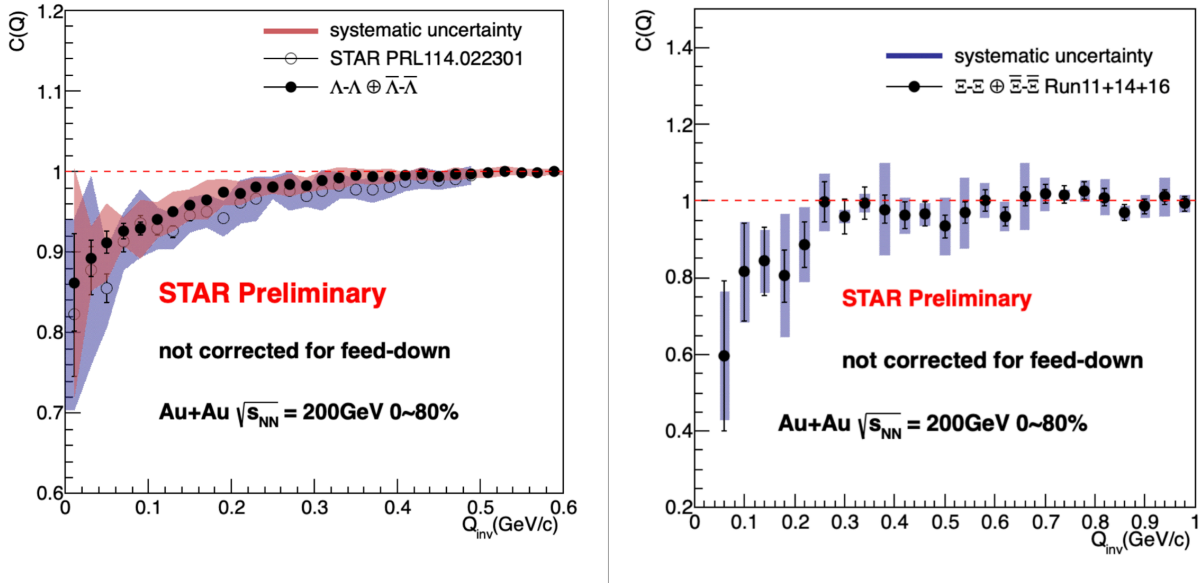


**Figure 81:** Left: combined  $\Lambda\Lambda$  and  $\bar{\Lambda}\bar{\Lambda}$  preliminary correlation functions with systematic uncertainties compared with already published previous STAR results. Right: combined  $\Xi\Xi$  and  $\bar{\Xi}\bar{\Xi}$  correlation functions with systematic uncertainties.

2473 the number of points that build the correlation signal. Previous STAR measurements of  
 2474  $p\Omega$  correlations show that the parameters of the strong interaction can be studied. How-  
 2475 ever, with higher data collections, more precise and detailed studies would be possible. The  
 2476 description of the  $\Lambda\Lambda$  interaction is still an open issue. Such a description is fundamental  
 2477 since it plays a decisive role in understanding the nature of hyperons that appear in neutron  
 2478 stars. If many hyperons appear close to each other and their fraction becomes significant,  
 2479 the  $YY$  interactions are expected to play an essential role in describing the equation of state  
 2480 of the dense system. An alternative way to study hypernuclei is two-particle momentum  
 2481 correlations of  $\Lambda\Lambda$  pairs produced in hadron-hadron collisions thanks to femtoscopy. Figure  
 2482 81 shows primary  $\Lambda\Lambda$  (left) and  $\Xi\Xi$  (right) correlation functions. For current  $\Lambda\Lambda$  and  $\Xi\Xi$   
 2483 systems also data from all previous runs were combined. Due to differences between indi-  
 2484 vidual runs, a significant source of systematic uncertainties exist now, and it will disappear  
 2485 with all 10 billion events collected during the Run-23 for the  $\Lambda\Lambda$  case. More critical seems  
 2486 to be the increased statistics for the  $\Xi\Xi$  case, and having 20 billion events from Run-23 and  
 2487 Run-25 enables the reduction of statistical uncertainties significantly and makes it possible  
 2488 to determine parameters of the strong interaction with higher precision. Having combined  
 2489 data from the Run-23 and Run-25 will also allow the hypotheses about possible bound states  
 2490 to be verified.

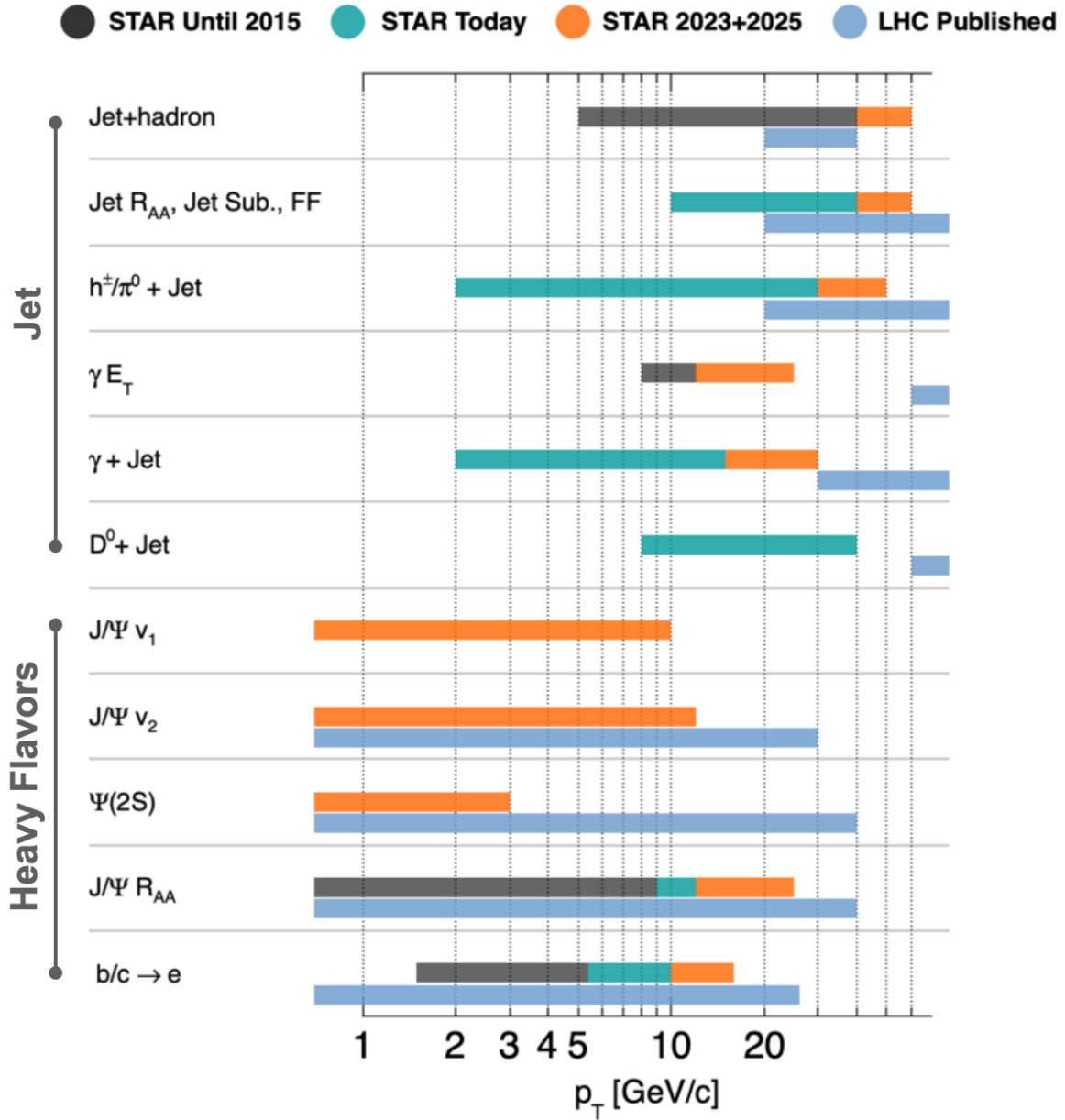


**Figure 82:** The kinematic coverage of the STAR Hard Probes measurements (past, current, and future projection) are shown with the corresponding comparison to the LHC (published) measurements. The details on the projection for precision measurements can be found in section. 3.3.

### 2491 3.3 Hard Probes: Jets and Heavy Flavor

2492 Measurements of fully reconstructed jets and heavy flavor particles over a broad kinematic  
2493 range at RHIC are essential to meet the goal outlined in the NSAC 2015 Long Range Plan  
2494 (LRP), to “probe the inner workings of the QGP” [81].

2495 A diagrammatic representation of STAR’s kinematic coverage for various measurements  
2496 related to hard probes is shown in Figure 82. The different colored horizontal bars show-  
2497 case STAR measurements that were available at the time of the 2015 NSAC-LRP (black),  
2498 ongoing measurements and recently released results (green) and projections for future data-  
2499 taking in years 2023 and 2025 (orange). The current high statistics STAR Au+Au collision  
2500 datasets available were recorded in 2014 and 2016, the integrated luminosities sampled by  
2501 STAR’s BEMC triggers are shown in Table 9. STAR’s capabilities are compared with the  
2502 corresponding LHC (light blue) published measurements. This overview reveals our ability  
2503 to investigate the QGP over a wide range of temperatures and medium properties produced  
2504 in heavy-ion collisions. Some of the flagship measurements are listed along the different rows  
2505 grouped into two topics related to ‘Jets’ and ‘Heavy Flavors’, where the x-axis represents a  
2506  $p_T$  scale. The Run-23+25 RHIC heavy-ion runs will enable an expanded kinematic range of  
2507 fully reconstructed jets and open heavy flavor measurements through the semi-leptonic decay  
2508 channel, providing an overlap with the LHC data. They will also facilitate measurements  
2509 of low transverse momentum  $J/\psi$  elliptic flow ( $v_2$ ) to study the recombination mechanism  
2510 in more detail,  $J/\psi$  directed flow ( $v_1$ ) that will allow us to study the initial tilt of the bulk  
2511 medium and suppression of the loosely bounded  $\psi(2S)$  state to explore the temperature  
2512 profile of the medium.

2513 The dependence of jet energy loss on the jet  $p_T$  and/or resolution or angular scale tagged  
2514 by jet substructure observables, are key tools in discriminating various jet quenching mech-  
2515 anisms [111, 214, 237, 238]. In addition, the measurement of jet acoplanarity is a sensitive  
2516 probe of transverse momentum broadening and medium-induced radiative effects [326], par-  
2517 ticularly for jets at low  $p_T$  which are accessible at STAR by selecting a given momentum  
2518 transfer via a photon trigger. Such a measurement is also minimally affected by background  
2519 arising from vacuum Sudakov radiation at RHIC energies [117, 244], potentially enabling a  
2520 precise extraction of in-medium jet scattering.

2521 Measurements of open heavy flavor and quarkonium production in heavy-ion collisions  
2522 provide important information about the properties of the created medium. Production of  
2523 open heavy flavor hadrons,  $J/\psi$  and  $\Upsilon$  mesons in Au+Au collisions at RHIC was found to be  
2524 suppressed compared to the production in  $pp$  collisions. The suppression of open heavy flavor  
2525 production at high  $p_T$  is due to energy loss of heavy quarks in the QGP, while the suppression  
2526 of quarkonium states is due to a screening of the  $Q\bar{Q}$  potential by the medium color charges.  
2527 In addition,  $J/\psi$  production can be affected by recombination of charm quarks in a later  
2528 stage of the collision evolution. The regeneration mechanism is expected to contribute mostly  
2529 at the low  $J/\psi$  transverse momentum range. Furthermore, recent theoretical calculations  
2530 suggest that measurements of the directed flow of heavy flavors particles can be used to shed  
2531 light on the initial geometry and the magnetic field information created during heavy-ion  
2532 collisions [114, 124].

2533 STAR’s unique geometry allows collection of events over a wide range of vertex positions  
 2534 along the beam direction ( $vz$ ) for jet and heavy flavor analyses, thereby efficiently sampling  
 2535 the provided RHIC luminosity. Optimization of the  $vz$  range used in the various analyses  
 2536 involves a balance between statistical precision and complexity of corrections, with the latter  
 2537 predominantly contributing to the systematic uncertainties of the measurement. Recent  
 2538 STAR jet measurements in Au+Au collisions have employed two classes of  $z$ -vertex cuts: the  
 2539 inclusive charged-particle jet analysis [34] utilizes  $|vz| < 30$  cm, whereas the  $\gamma_{\text{dir}} + \text{jet}$  analysis  
 2540 utilizes  $|vz| < 70$  cm. With the  $\gamma_{\text{dir}} + \text{jet}$  measurement successfully utilizing the broad  $vz$  range  
 2541 with controlled systematic precision, we are exploring similar event selections maximizing  
 2542 the available statistics for future jet measurements, including the inclusive/differential jet  
 2543 analyses. In Section 3 we present the sampled integrated luminosity in 2023 and 2025 for  
 2544 both the 30 cm and 70 cm  $vz$  cuts. The following physics performance projections are based  
 2545 on the 70 cm cut, using the cumulative sampled integrated luminosity for Run-14, Run-16,  
 2546 and 2023 and 2025 together. For  $|vz| < 70$  cm, this total is  $53.3 \text{ nb}^{-1}$ , which is roughly a  
 2547 factor 7 increase in trigger statistics relative to the current analyses based on Run-14 data.

2548 The following paragraphs in this section will highlight some of these measurements in  
 2549 greater detail.

### 2550 3.3.1 Precision Jet Measurements to Study the QGP Micro-Structure

2551 To quantify the effect of the marked increase in integrated luminosity, we utilize two mature  
 2552 jet measurements currently in progress and discuss their expected improvement with en-  
 2553 hanced integrated luminosity. These analyses are the semi-inclusive distribution of charged-  
 2554 particle jets recoiling from a high- $E_T$  direct-photon trigger ( $\gamma_{\text{dir}} + \text{jet}$ ); and the differential  
 2555 measurement of energy loss for jet populations selected by varying a substructure metric.  
 2556 Since these analyses are mature, their analysis methodologies and correction schemes are  
 2557 optimized, so that their projections based on increased statistics are meaningful. We do  
 2558 not imply that these will be the only flagship measurements that STAR will make with  
 2559 the 2023/2025 datasets; we will additionally continue to focus, for instance, on fully re-  
 2560 constructed jets and utilizing substructure observables, including those not yet developed.  
 2561 However, these analyses are most mature at present, and therefore provide the most accurate  
 2562 projections of gain in precision.

#### 2563 Semi-inclusive $\gamma_{\text{dir}} + \text{jet}$ Measurements

2564  
 2565 Figure 83 shows  $I_{AA}$  for fully-corrected semi-inclusive distributions of charged-particle  
 2566 jets (anti- $k_T$ ,  $R = 0.5$ ) recoiling from a direct-photon trigger with  $15 < E_T < 20$  GeV in  
 2567 central Au+Au collisions at  $\sqrt{s_{NN}} = 200$  GeV, for the current analysis based on  $10 \text{ nb}^{-1}$  [271]  
 2568 within  $|vz| < 70$  cm. The projected uncertainties for Run-23 and Run-25 ( $75 \text{ nb}^{-1}$  including  
 2569 the previous years and Run-23 and Run-25) are shown in the yellow and green colored  
 2570 bands respectively. Significant reduction in the uncertainty band is seen to result from the  
 2571 increase in integrated luminosity, together with a significant increase in kinematic reach.

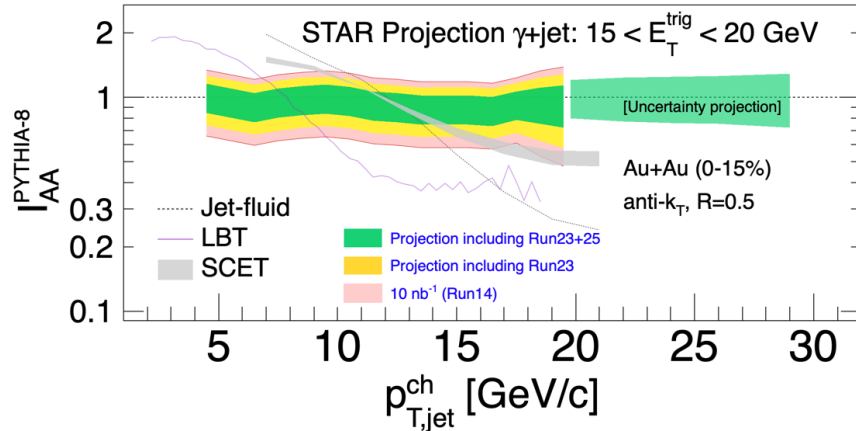


**Figure 83:** Projections for the  $I_{AA}$  for semi-inclusive anti- $k_T$ ,  $R = 0.5$  jets recoiling from a direct-photon trigger with  $15 < E_T < 20$  GeV for central (0-15%) Au+Au collisions at  $\sqrt{s_{NN}} = 200$  GeV. The colored bands show the cumulative uncertainty for the current analysis and projections for future analysis with the higher statistics datasets.

2572 An additional Run-25 not only reduces the uncertainty but also improves the precision  
 2573 measurement of high jet  $p_{T,jet}$  as evident by the extended green band along the x-axis.

2574 The revised luminosity projection of  $75 \text{ nb}^{-1}$  reduces the systematic uncertainty band  
 2575 by a factor of  $1/\sqrt{7.5}$  from the current measurement since systematic uncertainty of this  
 2576 measurement, dominated by the unfolding procedure, is correlated with the statistical pre-  
 2577 cision. Due to this correlation, the improvement shown in Fig. 83 should be regarded as a  
 2578 conservative estimate of the improvement in precision of this measurement channel with the  
 2579 projected integrated luminosity increase.

2580 The  $p_T$  broadening due to medium effects not only modifies the shape but also introduces  
 2581 a decorrelation between the di-jet angular distributions. The vacuum QCD process (Sudakov  
 2582 radiation) makes such measurements challenging in heavy-ion collisions, although at RHIC  
 2583 the Sudakov effect is smaller than at the LHC as it depends on the virtuality  $Q^2$  [117,  
 2584 244]. A detailed study is needed to understand both these effects (medium-induced and  
 2585 vacuum radiation) at a wide range of jet  $p_{T,jet}$  both at RHIC and the LHC energies. Such  
 2586 measurements are crucial to probe  $\hat{q}$  and/or quest for the predicted large-angle jet scattering  
 2587 off of quasi-particles in the QGP [134].

2588 In this direction, STAR is undertaking a preliminary study using  $\gamma_{dir} + \text{jet}$  and  $\pi^0 + \text{jet}$  with  
 2589  $11 < E_T < 15$  GeV and a charged-particle jet (anti- $k_T$ ,  $R = 0.2$  and  $0.5$ ) with  $10 <$   
 2590  $p_{T,jet}^{ch} < 15$  GeV/ $c$ . The analysis techniques pertaining to this measurement are being studied  
 2591 extensively to achieve precision on systematic uncertainty. Such measurements with higher  
 2592 energy triggers ( $\gamma_{dir}$  and  $\pi^0$ )  $E_T^{trig}$  and  $p_{T,jet}$  are crucial to study the inner working of the  
 2593 QGP. This is limited by the current statistics, particularly to study recoil jets at a large  $\Delta\phi$   
 2594 angle. A similar study at the LHC is also ongoing using h+jet measurements [253].

2595 The left plot of Fig. 84 shows the semi-inclusive distribution of the azimuthal separation  
 2596 between a direct-photon trigger with  $15 < E_T < 20$  GeV and a charged-particle jet (anti- $k_T$ ,

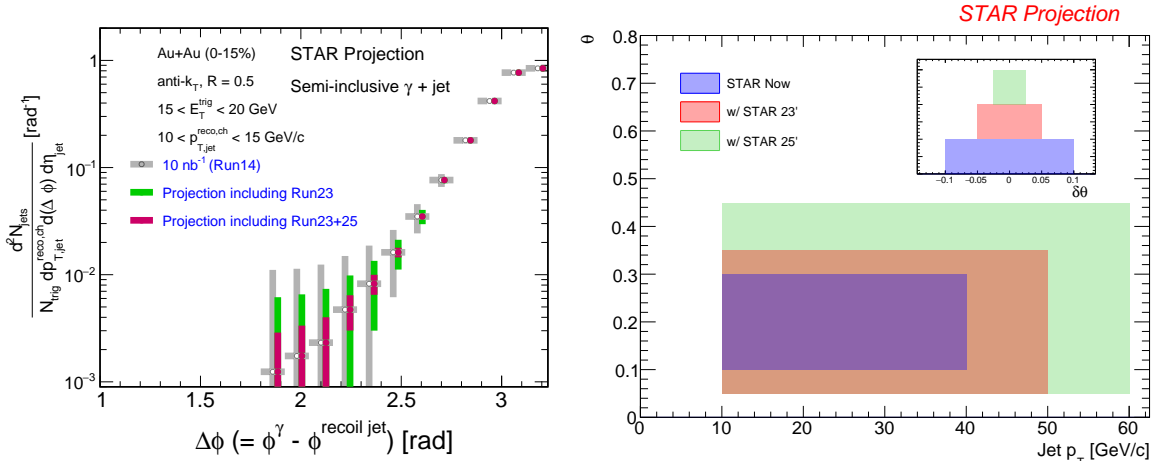


**Figure 84:** Left: Projections for the acoplanarity for semi-inclusive anti- $k_T$ ,  $R = 0.5$  jets recoiling from a direct-photon trigger with  $15 < E_T < 20$  GeV for central (0-15%) Au+Au collisions at  $\sqrt{s_{NN}} = 200$  GeV. The colored bands show the cumulative uncertainty for the current analysis and projections for future analysis with the higher statistics datasets. Right: The subjet opening angle as a function of jet  $p_{T,jet}$  in 0-20% central Au+Au collisions for various scenarios of data-taking. The inset is the corresponding resolution of  $\theta$ . Blue, red, and green represent current ( $10\text{nb}^{-1}$ ), with Run-23, and with Run-23+Run-25, respectively.

2597  $R = 0.5$ ) with  $10 < p_{T,jet}^{ch} < 15$  GeV/ $c$ , in central Au+Au collisions at  $\sqrt{s_{NN}} = 200$  GeV with  
 2598 only statistical uncertainties. The azimuthal smearing of this observable due to uncorrelated  
 2599 background is small, and such acoplanarity measurements are therefore strongly statistics-  
 2600 dominated [22, 55]. The grey points are from the current preliminary measurement based  
 2601 on  $10 \text{ nb}^{-1}$ , whereas the green and red points correspond to including Run-23 and Run-  
 2602 23+25 ( $75 \text{ nb}^{-1}$ ), respectively. A marked increase in measurement precision is projected,  
 2603 with corresponding qualitative increase in physics impact.

## 2604 Differential Measurements of Energy Loss Tagged with a Substructure Metric

2605

2606 Systematic exploration of parton energy loss controlled for variations in the jet shower  
 2607 forms an integral part of the jet program at STAR. Since parton showers are inherently  
 2608 probabilistic, a jet population contains patterns of radiation varying in both angle and mo-  
 2609 mentum fraction which can be extracted via jet substructure measurements designed with  
 2610 jet constituents' angle and/or momentum via algorithms or correlations. By selecting jets  
 2611 based on their substructure, STAR can differentially measure jet-medium interactions for  
 2612 various types of energy loss e.g. color coherence, dead cone, etc. In other words, the STAR  
 2613 jet program for Run-23+Run-25 will focus on jet substructure as a jet-tagger.

2614 Theory calculations show significant differences between energy loss signatures for jets  
 2615 perceived by the medium as a single or multiple color charges [238]. The integrated luminosity  
 2616 from the Run-23+Run-25 datasets not only provide a substantial increase in statistics in the

2617 current measurements of jet substructure, they also increase the available phase space for  
2618 rare processes such as wide angle emissions from high- $p_T$  jets. This enables STAR to extend  
2619 our current measurements of differential energy loss, with a resolution of  $\delta\theta = 0.1$  to finer  
2620 resolution  $\delta\theta \approx 0.025$  in the jet opening angle, measured via reconstructed subjects as shown  
2621 in Fig. 84 (right) and also extend to jets of higher momenta. By extending to high energy  
2622 splittings within jets, at varied opening angles, we can probe earlier formation times whereby  
2623 vacuum-like emissions and medium induced radiations are expected to occur.

2624 Given the unique nature of jet-medium interactions at RHIC, with the jet and sub-jet  
2625 scales sufficiently closer to the medium scale, the aforementioned measurements bolster the  
2626 importance of the STAR jet program with the goal of extracting the microscopic properties  
2627 of the QGP as outlined in the 2015 LRP.

### 2628 3.3.2 Deconfinement and Thermalization With Charmonia Measurements

2629 An important observable for studying the properties of the deconfined medium is the second  
2630 order flow harmonic of the Fourier expansion of the azimuthal distribution of the produced  
2631 hadrons, the elliptic flow coefficient  $v_2$ . As in the case of light hadrons, a positive  $v_2$  of  
2632  $D$ -mesons and electrons from heavy-flavor hadron decays was observed at RHIC energies  
2633 of 54.4 and 200 GeV. Which suggests that charm quarks may (partially) thermalize and  
2634 participate in the bulk medium collective evolution. On the other hand, the  $v_2$  of heavier  
2635  $J/\psi$  reported by STAR based on the 2010 Au+Au 200 GeV data sample was found to be  
2636 consistent with zero, albeit within large statistical uncertainties and systematic uncertainties  
2637 due to non-flow effects. The precision of the measurement was also not enough to distinguish  
2638 between theoretical model calculations that assume only primordial  $J/\psi$  production and ones  
2639 that include additional  $J/\psi$  production via recombination. This calls for a larger sample of  
2640 heavy-ion data at 200 GeV, as will be provided by RHIC in 2023 and 2025, in order to  
2641 observe a possible non-zero  $J/\psi$   $v_2$  at RHIC energies and put more constraints on the  $J/\psi$   
2642 production models especially regarding its regeneration. Particularly important for these  
2643 studies is STAR's potential to measure low transverse momentum  $J/\psi$  with a very good  
2644 precision. This excellent low- $p_T$  performance at STAR can be achieved thanks to its low  
2645 material budget and great particle identification capabilities.

2646 Moreover, the second order Event Plane (EP) can be reconstructed using the new Event  
2647 Plane Detectors (EPD) installed before Run-18. It is expected that using the forward EPD  
2648 will significantly decrease the contribution from the non-flow effects and consequently the  
2649 measurement's systematic uncertainties. Also, an inverse of the EP resolution enters di-  
2650 rectly the  $J/\psi$   $v_2$  uncertainty calculation. Thanks to the EPD, the resolution of the EP  
2651 reconstruction at forward rapidity for the  $J/\psi$   $v_2$  measurement at STAR will improve. Fig-  
2652 ure 85 presents statistical projections for the  $J/\psi$   $v_2$  measurement in 0-80% central Au+Au  
2653 collisions assuming 20 B MB events and HT triggered events corresponding to an integrated  
2654 luminosity of  $63 \text{ nb}^{-1}$ . Both cases of the second order EP reconstruction, using the for-  
2655 ward EPD and mid-rapidity TPC detectors, are considered and shown. A clear significant  
2656 improvement in the precision of the  $J/\psi$   $v_2$  can be seen across the whole experimentally  
2657 accessible  $J/\psi$   $p_T$  coverage of the previous measurement. In addition, the new larger dataset

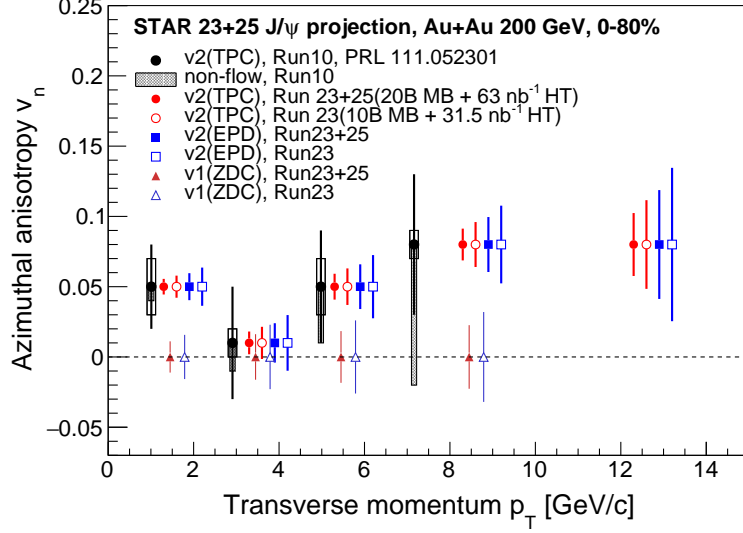


**Figure 85:** Projections for the  $J/\psi$  ( $J/\psi \rightarrow e^+e^-$ ) directed ( $v_1$ ) and elliptic ( $v_2$ ) flow vs  $J/\psi$   $p_T$  in 0-80% Au+Au collisions at 200 GeV, assuming 20 B MB events and HT triggered events corresponding to an integrated luminosity of  $63 \text{ nb}^{-1}$  with  $|V_Z| < 30 \text{ cm}$ .

2658 would allow to extend the measured  $p_T$  range beyond 10 GeV/ $c$ .

2659 Studies of the directed flow,  $v_1$ , as a function of rapidity provide crucial information to  
 2660 understand the initial tilt of the medium produced in heavy-ion collision [114, 124]. Heavy  
 2661 quarks are produced in the early stage of a heavy-ion collision and thus are of particu-  
 2662 lar interest for the medium initial asymmetry studies. STAR recently reported the first  
 2663 measurement of D-meson  $v_1$  in Au+Au collisions at 200 GeV where the magnitude of the  
 2664 heavy-flavor meson  $v_1$  is about 25 times larger than the  $v_1$  for charged kaons. With the  
 2665 2023-2025 data, STAR would have a unique opportunity to also study the  $v_1$  of a bound  
 2666  $c\bar{c}$  state, the  $J/\psi$  mesons, for which even larger directed flow can be expected [116]. In  
 2667 addition to STAR's excellent capability to reconstruct low- $p_T$   $J/\psi$ , as discussed above, the  
 2668 iTPC detector completed in 2018 will improve the momentum resolution and extend the  
 2669 pseudorapidity coverage. This will provide better precision for the slope extraction of the  $v_1$   
 2670 vs  $y$  measurement, that quantifies the strength of directed flow. The expected precision of a  
 2671  $J/\psi$   $v_1$  measurement vs  $p_T$  at STAR in 2023-2025, assuming 20 B MB events and HT trig-  
 2672 gered events corresponding to an integrated luminosity of  $63 \text{ nb}^{-1}$ , in 0-80% central Au+Au  
 2673 collisions at 200 GeV is shown in Fig. 85. Together with the  $J/\psi$   $v_2$  measurements,  $v_1$  would  
 2674 provide a more complete picture of the  $J/\psi$  production mechanism as well as the medium  
 2675 properties in heavy-ion collisions at RHIC.

2676  $\psi(2S)$  is the most loosely bounded quarkonium state currently accessible to heavy-ion  
 2677 collision experiments. Its dissociation temperature is predicted to be around, or below, the  
 2678 critical temperature, and is much less than that of  $J/\psi$  and  $\Upsilon$  states. It is therefore more  
 2679 likely to be dissociated in the early stage and in the core of the fireball, and those  $\psi(2S)$   
 2680 that are measured may have significant contributions from regeneration at a later stage in

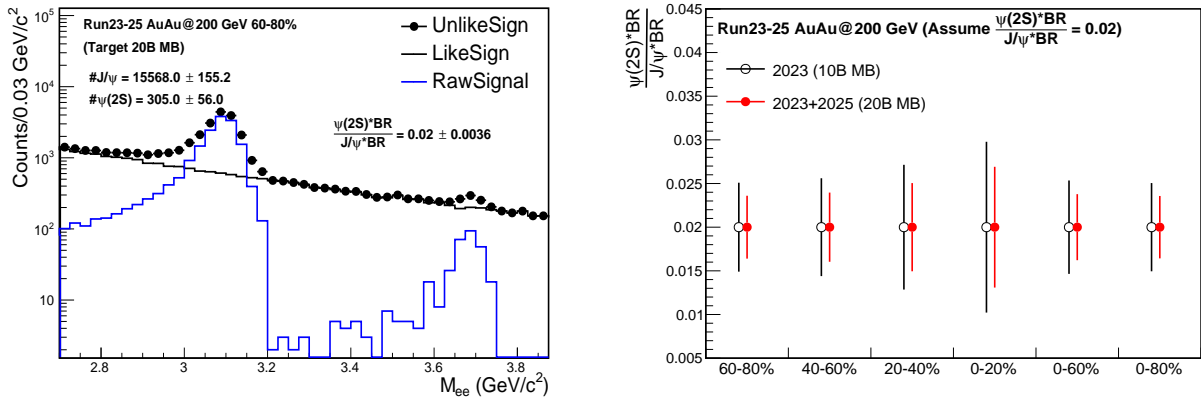


**Figure 86:** Projections for the  $J/\psi$  and  $\psi(2S)$  signals in 60-80% Au+Au collisions at 200 GeV and the yield ratio in various centrality bins. The improvement of momentum and  $dE/dx$  resolution thanks to the iTPC upgrade have not been taken into account.

2681 the evolution of the fireball. The relative suppression of  $\psi(2S)$  and  $J/\psi$  is sensitive to the  
2682 temperature profile of the fireball produced in heavy-ion collisions and its space-time evolu-  
2683 tion. It is also argued that the charmonium formation process from a  $c\bar{c}$  pair may be affected  
2684 by both the QGP and the initial strong external magnetic field, altering the relative yields  
2685 among different charmonium states [115, 162]. The measurement of  $\psi(2S)$  is much more  
2686 difficult than that of  $J/\psi$  due to a much smaller production cross-section and dilepton decay  
2687 branching ratio, resulting in a very low signal-to-background ratio. The ALICE Collabora-  
2688 tion successfully measured the relative suppression of  $\psi(2S)$  and  $J/\psi$  in Pb+Pb collisions  
2689 at forward rapidity [23], and the ATLAS and CMS Collaborations published the relative  
2690 suppression in Pb+Pb collisions at mid-rapidity and high  $p_T$  [5, 286]. Attempts to measure  
2691  $\psi(2S)$  suppression in heavy-ion collisions at RHIC have not been successful to date. The low  
2692 material budget and excellent particle identification capability of STAR together with the  
2693 combined large data sample in 2023 and 2025 will provide a unique opportunity to measure  
2694 the suppression of  $\psi(2S)$  at low  $p_T$  and mid-rapidity in heavy-ion collisions. Figure 86 shows  
2695 the projections of  $\psi(2S)$  signal and the yield ratio of  $\psi(2S)$  and  $J/\psi$  from 20 B MB events  
2696 in Au+Au collisions. Here the  $\psi(2S)/J/\psi$  ratio is assumed to be 0.02, and the performance  
2697 of detectors from existing data before STAR iTPC upgrade is used for the projection. As  
2698 shown in the figure, the  $\psi(2S)$  signal significance will be around  $3\sigma$  level in the 0-20% cen-  
2699 trality bin. This significance could become even smaller depending on the level of further  
2700 suppression for  $\psi(2S)$  compared to  $J/\psi$ . Despite the improvement of momentum and  $dE/dx$   
2701 resolution thanks to the STAR iTPC upgrade, it is crucial to have both the 2023 and 2025  
2702 data for a significant  $\psi(2S)$  measurement.

### 2703 3.4 Electromagnetic Probes and Ultra-peripheral collisions

#### 2704 3.4.1 Probing the degrees of freedom of the medium and its transport properties: 2705

2706 At  $\mu_B \sim 0$  Lattice QCD works and can be directly tested against experimental results.  
 2707 This will help to disentangle  $\rho$  melting from other explanations such as collision broadening.  
 2708 In case the measured in-medium spectral function merges into the QGP description this  
 2709 would indicate a transition from hadrons into a structure-less quark-antiquark continuum,  
 2710 thus providing the manifestation of chiral symmetry restoration. We will continue to search  
 2711 for a direct signature of chiral symmetry restoration via chiral  $\rho$ - $a_1$  mixing. The signal is  
 2712 predicted to be detectable in the dilepton intermediate mass range. Difficulties are related  
 2713 to the fact that correlated charm-anticharm and QGP saturate the invariant mass region  
 2714 of 1.1 — 1.3  $\text{GeV}/c^2$ . Therefore an accurate measurement of the excess dilepton yield, i.e.  
 2715 dilepton yield after subtraction of the cocktail of contributions from final-state decays, Drell-  
 2716 Yan and those from correlated heavy-flavor decays, up to invariant mass of 2.5  $\text{GeV}/c^2$  is  
 2717 required. The challenging analysis on charmed-decayed dielectron is ongoing from the data  
 2718 sets taken with the Heavy Flavor Tracker at STAR [276]. Thus deeper understanding of  
 2719 origin of thermal radiation in Au+Au collisions at  $\sqrt{s_{\text{NN}}} = 200$  GeV from  $\sim$ zero mass up  
 2720 to 2.5  $\text{GeV}/c^2$  will become possible with rigorous theoretical efforts and improved dielectron  
 2721 measurements. Figure 87 shows the expected statistical and systematic uncertainties of the  
 2722 dielectron excess mass spectrum with all the detector upgrades and for the anticipated total  
 2723 Run-23/Run-25 statistics of  $20 \times 10^9$  events.

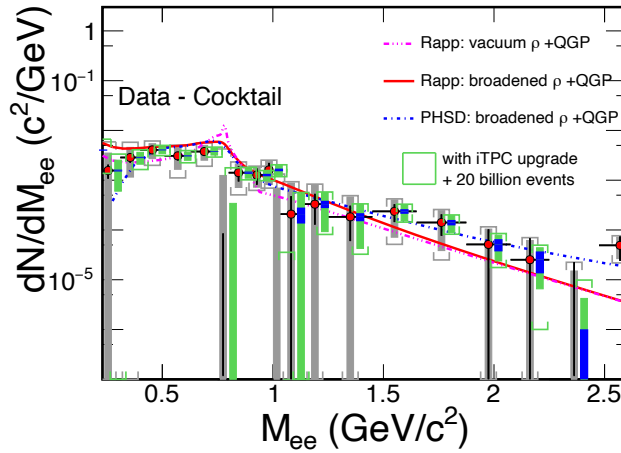


**Figure 87:** The expected statistical and systematic uncertainties on the dielectron excess mass spectrum with the iTPC upgrade compared to the current TPC case. The data are from our measurements in  $\sqrt{s_{\text{NN}}} = 200$  GeV Au+Au collisions [47]. Model comparisons are also shown. The boxes represent systematic uncertainties from data and the brackets represent the total systematic uncertainties including those from cocktails. The grey ones are for the current case while the green ones are for the Run-23+Run-25 case. The blue bands represent statistical uncertainties from 20 billion minimum-bias events with the iTPC upgrade.

2724 Another application of dileptons is to use them to measure transport coefficients. The  
 2725 electrical conductivity can be directly obtained as the low-energy limit of the EM spectral  
 2726 function. We aim to extract such information by studying excess dielectron yields at the low-  
 2727 energy regime of the dilepton spectra and the conductivity peak at small invariant masses,  
 2728 i.e. at low invariant mass and low  $p_T^{ee}$ . Low field run could be profitable, however already  
 2729 now dileptons with pair  $p_T^{ee}$  down to 60 MeV/ $c$  could be measured. Measurement of Drell-Yan  
 2730 in  $p$ +A collisions at low  $p_T$  would provide an important reference to constrain the dilepton  
 2731 cocktail.

2732 To gain a deeper understanding of the microscopic origin of the excess radiation, we will

- 2733 • separate early from later time radiation by measuring dilepton elliptic flow ( $v_2$ ) as a  
 2734 function of dilepton mass;
- 2735 • identify the source of dilepton radiation by studying dilepton polarization versus in-  
 2736 variant mass (helicity angle);
- 2737 • measure precisely the lifetime of the interacting fireball. As an observable we will use  
 2738 integrated low-mass yield but also compare explicit model calculations with various  
 2739  $\tau_{fireball}$ ;
- 2740 • extract an average radiating source temperature from the fit of a Boltzmann distrib-  
 2741 ution to the invariant mass slope in the range 1.1 - 2.5 GeV/ $c^2$  spectrum. The higher  
 2742 the invariant mass, the stronger the QGP contribution to the spectrum, the higher the  
 2743 chance to measure temperature of the QGP.

2744 Last, but not least, concerning direct-photon emission, the existing difference, on the  
 2745 order of a factor of two, between the low momentum spectra from PHENIX and STAR in  
 2746 200 GeV Au+Au collisions, has to be resolved. In order to clarify the direct photon puzzle  
 2747 we will measure the direct virtual photon yield as well as its elliptic flow coefficient. We will  
 2748 particularly focus on low  $p_T$   $\eta$  measurement which might be instrumental in clarifying this  
 2749 long standing question.

### 2750 3.4.2 Studying the Photon Wigner Function and Final-state Magnetic Fields 2751 in the QGP

2752

2753  
 2754 The unsuccessful description of STAR data by the STARLight model led to the attri-  
 2755 bution of the broadening to the possible residual magnetic field trapped in an electrically  
 2756 conducting QGP [27]; which is key information to the study of the chiral magnetic effect.

2757 Similarly, ATLAS quantified the effect via the acoplanarity of lepton pairs in contrast  
 2758 to the measurements in UPC and explained the additional broadening by multiple electro-  
 2759 magnetic scatterings in the hot and dense medium [4], which is analogous to the medium  
 2760  $P_{\perp}$ -broadening effects for jet quenching.

2761 These descriptions of the broadening in hadronic collisions are based on the assumption  
 2762 that there is no impact parameter dependence of the transverse momentum distribution for  
 2763 the electromagnetic production. Recent lowest-order QED calculations, in which the impact  
 2764 parameter dependence is recovered, could reasonably describe the broadening observed by  
 2765 STAR and ATLAS without any in-medium effect. To solve the puzzle, we propose to precisely  
 2766 study the initial  $P_{\perp}$ -broadening for the dilepton pair in ultra-peripheral collisions. Different  
 2767 neutron emission tags serve as the centrality definition, and will allow us to explore the  
 2768 broadening baseline variation with impact parameter. Furthermore, the differential spectrum  
 2769 as a function of pair  $P_{\perp}$ , rapidity, and mass enable us to study the Wigner function of the  
 2770 initial electromagnetic field, which provide the information to extract the momentum and  
 2771 space correlation of EM field.

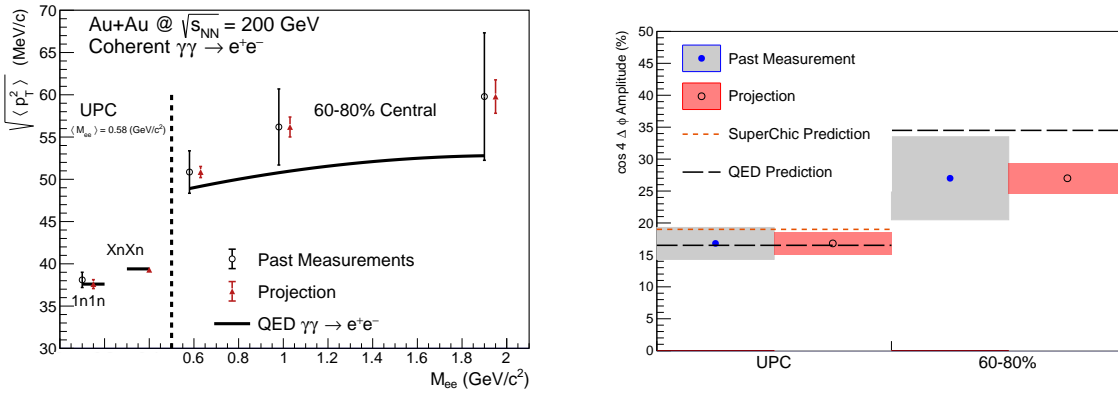


**Figure 88:** (Color online) Projections for measurements of the  $\gamma\gamma \rightarrow e^+e^-$  process in peripheral and ultra-peripheral collisions. Left: The  $\sqrt{\langle p_T^2 \rangle}$  of di-electron pairs within the fiducial acceptance as a function of pair mass,  $M_{ee}$ , for 60–80% central and ultra-peripheral Au+Au collisions at  $\sqrt{s_{NN}} = 200$  GeV. Right: The projection of the  $\cos 4\Delta\phi$  measurement for both peripheral (60–80%) and ultra-peripheral collisions.

2772 As shown in Fig. 88, comparing with the latest QED calculation, there still exists addi-  
 2773 tional broadening in peripheral collisions, although the significance is only about  $1\sigma$ , which  
 2774 still leave room for the medium effect. In Run-23 and Run-25, as projected in the figure, we  
 2775 could judge the existence of additional broadening with much higher precision and further  
 2776 constrain the strength of final-state magnetic field in the QGP.

2777 Precision measurement of the amplitude of the recently observed  $\cos 4\Delta\phi$  modulation of  
 2778 the  $\gamma\gamma \rightarrow e^+e^-$  process will allow precision mapping of the photon Wigner function and  
 2779 provide additional constraints on possible final-state effects, thereby complementing the  $P_{\perp}$   
 2780 broadening measurement. Figure 88 right panel shows the projected precision for a mea-  
 2781 surement of the  $\cos 4\Delta\phi$  modulation in Run-23+25. The modulation is a direct result of  
 2782 the mismatch in initial and final spin configuration of the  $\gamma\gamma \rightarrow e^+e^-$  process. Any final-  
 2783 state effect that modifies the  $P_{\perp}$  will necessarily reduce the amplitude of the modulation.  
 2784 Assuming the same central value as previously measured, evidence for suppression of the

2785  $\cos 4\Delta\phi$  modulation will be visible at the  $> 3\sigma$  level (stat. & syst. uncertainty). Preci-  
 2786 sion measurement of the  $\cos 4\Delta\phi$  modulation in Run-23+25 may also allow a first direct  
 2787 experimental measurement of the impact parameter dependence of this new observable (by  
 2788 comparing UPC and 60 – 80%). Assuming the same central values as previously measured,  
 2789 the improved precision will provide evidence for impact parameter dependence at the  $> 3\sigma$   
 2790 level (stat. & syst. uncertainty). Assuming the central value predicted by QED would lead  
 2791 to a  $> 5\sigma$  difference between the UPC case and the 60 – 80% case.

### 2792 **3.4.3 Ultra-peripheral Au+Au Collisions: Probe Gluon Distribution Inside the** 2793 **Nucleus**

2794  
 2795 STAR recently observed a significant  $\cos 2\Delta\phi$  azimuthal modulation in  $\pi^+\pi^-$  pairs from  
 2796 photonuclear  $\rho^0$  and continuum production. The structure of the observed modulation as  
 2797 a function of the  $\pi^+\pi^-$  pair transverse momentum,  $P_\perp$ , appears related to the diffractive  
 2798 pattern. Recent theoretical calculations [319], which implemented linearly polarized pho-  
 2799 tons interacting with the saturated gluons inside a nucleus, have successfully described the  
 2800 qualitative features of the observed modulation (see Fig. 89), and indicate that the detailed  
 2801 structure of the  $\cos 2\Delta\phi$  modulation vs.  $P_\perp$  is sensitive to the nuclear geometry and gluon  
 2802 distribution. Data from Run-23+25 would allow the additional statistical reach needed to  
 2803 perform multi-differential analysis, providing stronger theoretical constraints. Specifically,  
 2804 multi-differential analysis of the  $\cos 2\Delta\phi$  modulation with respect to pair rapidity and pair  
 2805 mass are needed. Multi-differential analysis with respect to pair mass is needed to separate  
 2806 the  $\rho^0$  production from the continuum Drell-Soding production. Multi-differential analysis  
 2807 with respect to the pair rapidity is needed to quantitatively investigate how the double-slit  
 2808 interference mechanism effects the structure of the observed azimuthal modulation. Addi-  
 2809 tional statistical precision is also needed for measurement of the higher harmonics. Similar  
 2810 measurements with  $J/\Psi \rightarrow e^+e^-$  can be performed and such measurements at higher mass  
 2811 provide better comparison with more reliable QCD calculation.

2812 Ultraperipheral Å collisions, where photons generated by the Lorentz-boosted electro-  
 2813 magnetic field of one nucleus interact with the gluons inside the other nucleus, can provide  
 2814 certain 3D gluonic tomography measurements of heavy ions, even before the operation of  
 2815 the future EIC. STAR has performed experimental measurements of the photoproduction  
 2816 of  $J/\psi$  at low transverse momentum in non-UPC heavy-ion collisions [305], accompanying  
 2817 the violent hadronic collisions. A detailed study with  $p_T$  distributions has shown that the  
 2818  $|t|$  distribution in peripheral collisions is more consistent with the coherent diffractive pro-  
 2819 cess than the incoherent process. Although models [138, 327] incorporating different partial  
 2820 coherent photon and nuclear interactions could explain the yields, it remains unclear how  
 2821 the coherent process happens and whether final-state effects play any role [283]. Resolving  
 2822 this puzzle with high statistical data and detailed  $|t|$  distributions at different centralities  
 2823 at RHIC as projected for Run-23+25 in Fig. 89 may be important for understanding what  
 2824 defines the coherentness of the photoproduction, how vector mesons are formed in the pro-  
 2825 cess and how exclusive the similar process has to be in future EIC experiments with forward

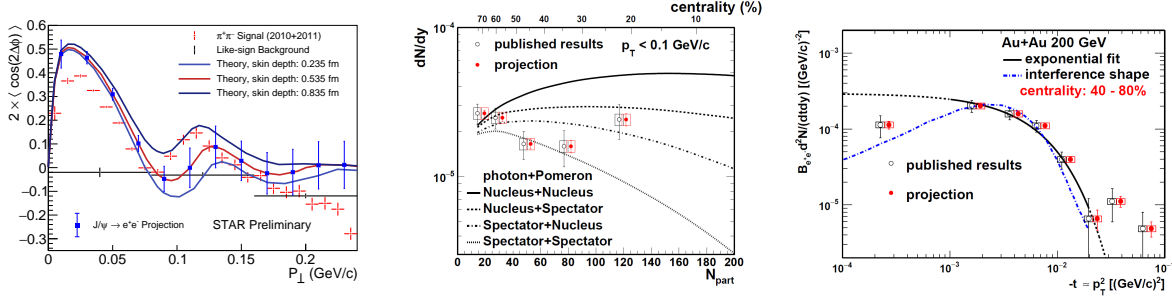


**Figure 89:** Left: Measurement of the  $\cos 2\Delta\phi$  modulation of  $\pi^+\pi^-$  pairs from photonuclear  $\rho^0$  and continuum production compared to theoretical predictions [319]. Projections are shown for a similar measurement of the azimuthal modulation of  $e^+e^-$  pairs from photonuclear production of the  $J/\psi$ . Center: Projection of the  $dN/dy$  of photoproduced  $J/\psi$  in non-UPC events vs. the event centrality ( $N_{\text{part}}$ ) compared to various theoretical production scenarios. Right: Projection of the  $t$  spectra of photoproduced  $J/\psi$  in 40 – 80% central collisions.

2826 neutron veto/tagging.

## 4 Forward Upgrade

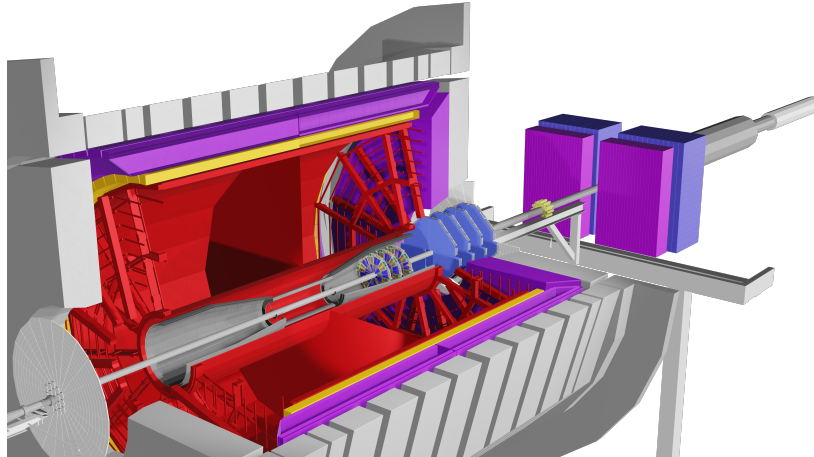


**Figure 90:** A view of the detectors comprising the STAR forward upgrade, rendered by simulation.

2828

2829

2830

2831

2832

2833

2834

2835

2836

2837

2838

2839

2840

2841

2842

2843

2844

2845

2846

2847

2848

2849

2850

2851

2852

STAR is finalizing construction of the forward detector system, realized by combining tracking with electromagnetic and hadronic calorimeters, in preparation for first data taking in Run-22. It will have superior detection capability for neutral pions, photons, electrons, jets, and leading hadrons within the pseudorapidity range  $2.5 < \eta < 4$ .

The design of the Forward Calorimeter System (FCS) was driven by consideration of detector performance, integration into STAR, and cost optimization. For the electromagnetic calorimeter, components of the refurbished PHENIX sampling EMCAL were used, while the hadronic calorimeter has been newly constructed as a sandwich iron/scintillator plate sampling type, based on extensive STAR Forward Upgrade and EIC Calorimeter Consortium R&D. The existing Event Plane Detector (EPD) will be used as a trigger detector, especially for di-electron triggers. Both calorimeters share the same cost-effective readout electronics, with SiPMs as photo-sensors. The FCS system will have very good electromagnetic ( $\sim 10\%/\sqrt{E}$ ) and hadronic ( $\sim 50\%/\sqrt{E} + 10\%$ ) energy resolution.

In addition, a Forward Tracking System (FTS) is being constructed. The FTS will be capable of discriminating hadron charge sign for transverse spin asymmetry and Drell-Yan measurements in  $pp$  and  $p+A$  collisions. In heavy ion collisions, measurements of charged-particle transverse momenta over the range  $0.2 < p_T < 2$  GeV/ $c$  with 20-30% momentum resolution are required. To keep multiple scattering and photon conversion backgrounds under control, the material budget of the FTS must be small. Hence, the FTS design is based on three Silicon mini-strip detectors that consist of disks with a wedge-shaped design to cover the full azimuth and  $2.5 < \eta < 4.0$ ; they are read out radially from the outside to minimize the material. The Si-disks are combined with four small-strip Thin Gap Chamber (sTGC) wheels following the ATLAS design [18, 292]. The three Si mini-strip disks will be located in the region  $z = 146.6 - 173.7$  cm, while the four sTGC wheels will be placed 30 cm apart starting from  $z = 273$  cm. The Si-Disks readout is based on APV chips and will reuse

2853 the readout chain of the IST, which was part of the STAR HFT. For the sTGC the readout  
2854 will be based on the ATLAS VMM3 chip [168].

## 2855 4.1 Status

2856 Following a successful Director’s Review in November 2018, the FCS consortium submitted  
2857 an NSF Major Research Instrumentation (MRI) proposal for construction of the EMCAL  
2858 and HCAL and associated electronics. The MRI was approved in Summer 2019 and work  
2859 began in earnest on all aspects of the upgrade. In August 2020, another successful Director’s  
2860 Review was conducted on the status of the upgrades. No serious issues were found. By the  
2861 end of 2020, construction of both the EMCAL and HCAL had been successfully completed;  
2862 they are now being commissioned as part of the ongoing Run-21. The Silicon Tracker and  
2863 sTGC Tracker systems are expected to finish construction in June 2021, and will be installed  
2864 in STAR prior to the start of Run-22.

## 2865 4.2 Forward Calorimeter System

2866 The platform that supports the HCAL and EMCAL was installed in 2019, followed by  
2867 installation and stacking of the refurbished PHENIX EMCAL blocks.

2868 Production of the HCAL absorber blocks at Chapman Lake Instrumentation and Gatto  
2869 Industrial Plating was completed in late summer 2020, with all parts delivered to BNL. All of  
2870 the 18,200 scintillating tiles have been produced and polished at ACU, Valparaiso, UCLA and  
2871 OSU. Front-end electronics boards were designed and tested at Indiana University, sent out  
2872 for commercial production, then QA’ed at IU and UKY. Other parts have been fabricated,  
2873 tested, and calibrated at Rutgers, Temple, BNL and UCLA. HCAL construction started on  
2874 the platform in Fall 2020, and successfully finished by the end of 2020 on schedule despite  
2875 following COVID19 restrictions, as seen in Fig. 91.

2876 For both the EMCAL and HCAL, front-end electronics cards with SiPM sensors were  
2877 installed, calibrated, and commissioned with very few failures, and are now fully working.  
2878 Seventy-eight DEP/ADC readout boards and three DEP/IO boards for trigger processing  
2879 have been produced and installed in five crates at STAR. They are connected to DAQ PCs  
2880 and are currently being used to take data during Run-21. About 0.5% of channels were  
2881 found to have issues, and will be fixed during the upcoming shutdown.

2882 LED systems were also installed for both the EMCAL and HCAL. They are being used  
2883 for mapping verification, as shown in Fig. 92, and for short- and long-term gain stability  
2884 monitoring, as well as determining temperature compensation for the SiPM voltages. Ra-  
2885 diation damage monitoring has started and small increases in the dark current have been  
2886 observed, which fall well within the expected range.

2887 A signal splitter for the west EPD has been designed, and two prototype boards were  
2888 produced. These will be installed in late May 2021 for testing and for timing adjustments  
2889 during the remaining weeks of Run-21. A total of 24 boards (plus spares) will be produced  
2890 and installed prior to Run-22.

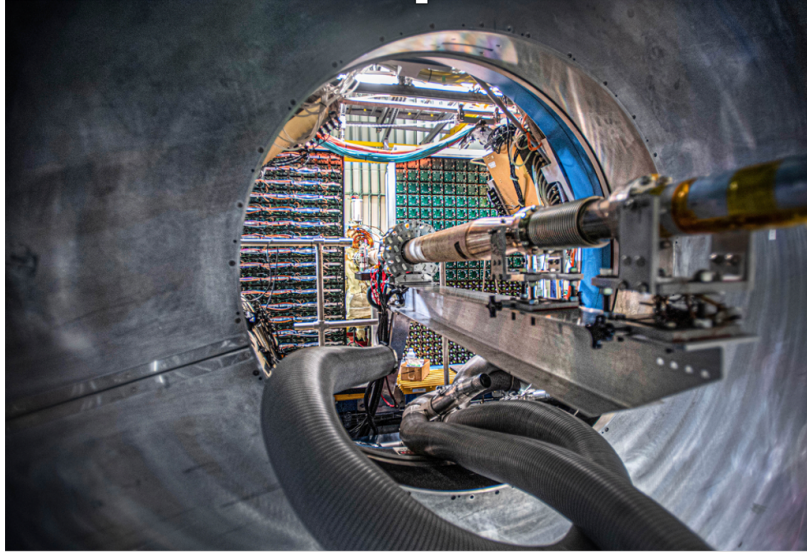


**Figure 91:** A view of the installed forward EMCAL, with the HCAL behind, left and right of the beam pipe.

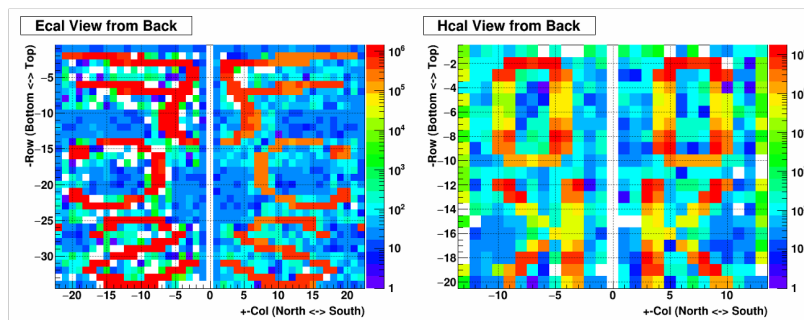


**Figure 92:** An event display of FCS EMCAL and HCal with voltage patterns loaded for mapping checks.

### 2891 4.3 Forward Silicon Tracker

2892 The Forward Silicon Tracker (FST) consists of three disks, each with 12 wedge-shaped de-  
 2893 tector modules. Each module is separated into two sections along the radial direction, with  
 2894 Silicon mini-strip sensors mounted on different sides of the module respectively. These mod-  
 2895 ules will be mounted on an aluminum support structure and inserted into the inner cone  
 2896 of the STAR TPC. Two prototype detector modules were assembled and their efficiency  
 2897 and resolution were verified with cosmic ray (see Figure 93). Mass production of detector  
 2898 modules started after a FST production readiness review in Aug. 2020. As of May 2021,  
 2899 about 40 detector modules have been fully assembled and tested successfully at Fermilab  
 2900 and at the University of Illinois at Chicago. Six of these have arrived at BNL for initial  
 2901 installation tests; the rest will be shipped in the first week of June. The support structure  
 2902 and its associated installation tooling have been fabricated and assembled in the STAR clean

2903 room. Mounting detector modules onto the support structure has started, together with the  
 2904 full set of cabling and cooling tube connections. The cooling and DAQ systems, which were  
 2905 used previously for the HFT-IST sub-system, have been incorporated into the FST and their  
 2906 performance has been verified. The operation of the entire detector will be verified by run-  
 2907 ning the cooling and DAQ systems with the fully assembled detector in the clean room in  
 2908 June-July before installation into STAR in August, 2021. Despite all the complications and  
 2909 challenges imposed by COVID19, the Forward Silicon Tracker upgrade project has stayed  
 2910 on schedule and the detector is expected to be ready for physics data taking in Run-22.

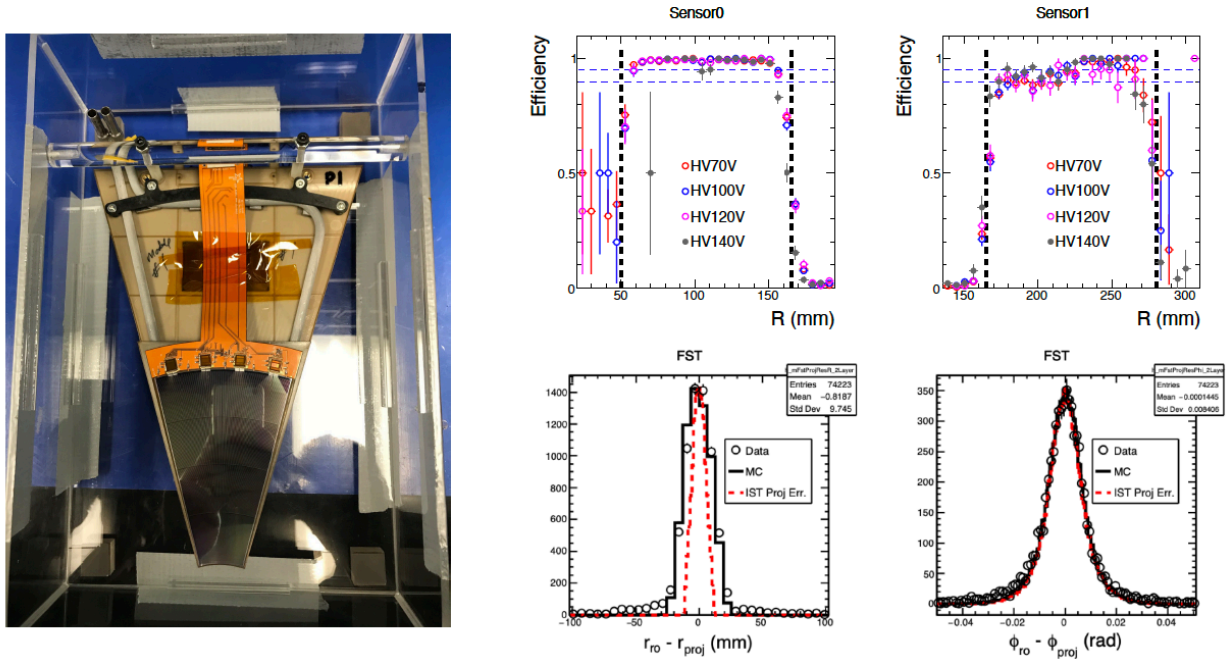


**Figure 93:** Left: a photograph of a FST detector module in the storage box with the Silicon sensor in the inner section facing up. Right: measured FST detector module performance from cosmic ray testing. Shown on the top are the efficiencies for the inner (left) and outer sensor (right) respectively. Shown in the bottom are the residual distributions between the measured and projected positions in the radial and azimuthal directions, respectively.

#### 2911 4.4 Forward sTGC Tracker

2912 The sTGC system for the forward upgrade has been designed by collaborators from Shandong  
 2913 University, who also oversee the mass production and testing of the sTGC modules. A  $60 \times 60$   
 2914  $\text{cm}^2$  sTGC module was produced, and was found to have a position resolution of 140 microns  
 2915 and a detector efficiency of 97.3%. This module was shipped to BNL and installed at STAR  
 2916 for data taking this year. Due to space constraints around the beam pipe, the final sTGC  
 2917 modules have been designed to have a pentagon shape (see Figure 94). Four pentagon  
 2918 pre-production modules were assembled in August 2020. Following an sTGC production  
 2919 readiness review in Nov. 2020, comments and suggestions received from the review committee

2920 were addressed. Mass production of pentagon modules started in March 2021; 20 pentagon  
 2921 sTGC stations have been produced as of mid-May this year.

2922 High detector efficiencies and low leakage currents have been demonstrated for the pro-  
 2923 duced stations. Final position resolutions will be measured using the new read-out electron-  
 2924 ics, which is based on the ATLAS VMM3a chip developed for a similar detector. The strips  
 2925 of each sTGC layer will be read out by 24 Front-End Boards (FEBs), so a total of 96 FEBs  
 2926 are needed for the four sTGC layers. The signals are sent to a Readout Board Driver (ROD)  
 2927 and interfaced to STAR DAQ. The electronics design and fabrication was carried out by  
 2928 USTC. The FEB design is complete and final production is ongoing. RDO construction is  
 2929 finished, as is design of the installation and mounting frames. The required n-pentane gas  
 2930 system and interlocks have been designed and approved at BNL. The full sTGC system will  
 2931 be installed at STAR during the shutdown this summer.

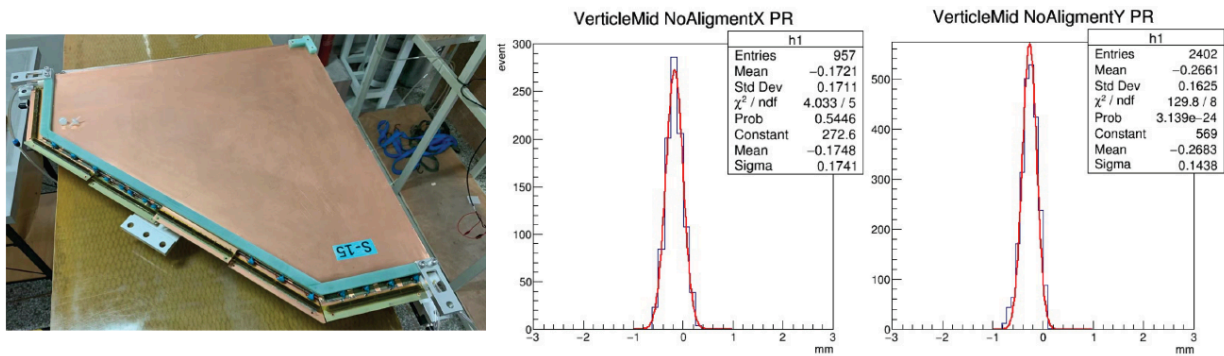


**Figure 94:** Left: a photograph of a pentagon-shaped sTGC module. Middle and right: residual distributions between the measured and projected positions of the  $60 \times 60 \text{ cm}^2$  sTGC prototype in the x and y directions, respectively, from cosmic ray testing.

2932 In order to mitigate the effect of COVID19 and stay on schedule, more engineers for  
 2933 module production were hired at Shandong University. However, the delay in procurement  
 2934 of necessary materials to build up sTGC mechanical supporting structures and unpredicted  
 2935 damages to our first 4 pentagon-shaped sTGC modules in the shipping process make our  
 2936 schedule very tight even though we think we can still make our trackers ready for Run-22.

## 2937 4.5 Software

2938 Much of the software needed for the Forward Calorimeter System has already been developed,  
 2939 including DAQ, online monitoring, trigger algorithm simulation and verification, slow control  
 2940 and alarming, and recording the detector status to the STAR database. Offline codes for  
 2941 fitting pulse shapes, cluster finding, and cluster analysis are working. From test data taken  
 2942 with 200 GeV Au+Au collisions during Run-19,  $\pi^0$  and MIP peaks in the EMCAL were  
 2943 successfully reconstructed and identified, as shown in Fig. 95 and Fig. 96. Data have also  
 2944 been collected from 200 GeV O+O collisions during the ongoing Run-21 using the fully  
 2945 assembled FCS, and are being analyzed to set final calibrations.

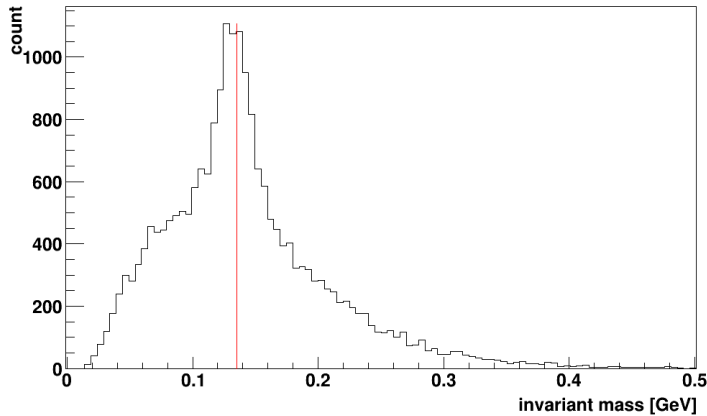


**Figure 95:** Reconstructed  $\pi^0$  peak from 200 GeV Au+Au collisions taken during Run-19.

2946 Sets of trigger algorithms for the FCS have been developed, based on simulations per-  
 2947 formed by Texas A&M. FPGA codes have been written, loaded to the DEP/IO boards,  
 2948 their timing adjusted and verified, and are currently being used for data taking during the  
 2949 ongoing Run-21. We will continue to work on refining the algorithms, as it was found that  
 2950 more powerful logic is available on the FPGAs than is used in current algorithms.

2951 Preliminary versions of slow control, DAQ, and online monitoring software for the track-  
 2952 ing detectors have also been developed and tested. Track reconstruction algorithms utilizing  
 2953 hits from the four sTGC planes and the three Si layers have been developed, and good per-  
 2954 formance has been demonstrated. The tracking algorithm is based on modern techniques:  
 2955 it depends on GENFIT, a general purpose tracking toolkit, and on the iLCSoft KiTrack, a  
 2956 Cellular Automata library, which is used to seed track finding. Other components of the  
 2957 offline software needed for the tracking detectors are being developed and tested.

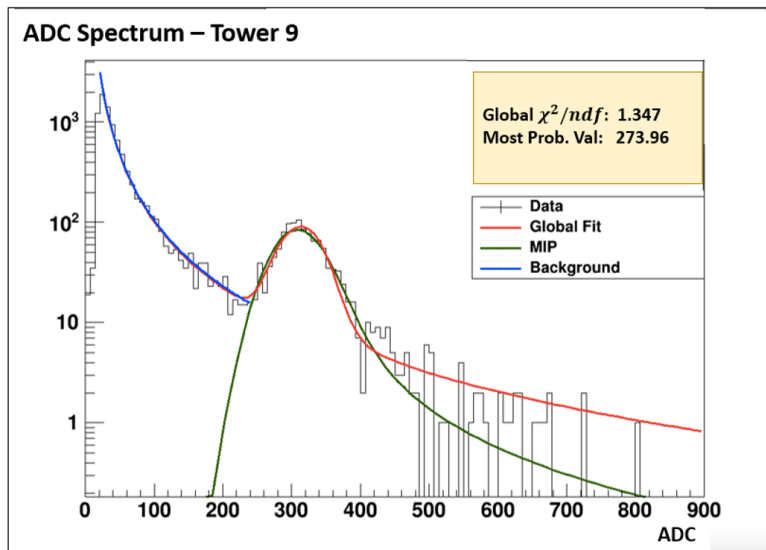


**Figure 96:** Reconstructed MIP peak from 200 GeV Au+Au collisions taken during Run-19.

## 2958 5 Future Opportunities

2959 Experience from the BES-II has taught us that the excellent performance from RHIC may  
 2960 enable us to take short opportunistic datasets that enable unique physics programs with  
 2961 minimal extra running time. With this in mind we outlined in Section 1.5 a request for a  
 2962 short d+Au run in Run-21 if time permits. If this is not possible, STAR remains interested  
 2963 in taking this data if the opportunity arrives in 2023-2025. Below we outline two other  
 2964 opportunistic programs, both are of great interest to STAR and the larger nuclear physics  
 2965 community.

### 2966 5.1 Shape Tomography of Atomic Nuclei Using Collective Flow 2967 Measurements

2968 The success of the hydrodynamic framework of heavy-ion collisions permits us today to  
 2969 perform quantitative extractions of the transport properties of the QGP via the state-of-the-  
 2970 art multi-system Bayesian analysis approaches [93,144,251]. Such extractions rely largely on  
 2971 a correct description of the initial condition of the QGP prior to the hydrodynamic expansion.  
 2972 Recent experimental data in  $^{238}\text{U}+^{238}\text{U}$  [48] (see also Figs. 3) and  $^{129}\text{Xe}+^{129}\text{Xe}$  [77, 84, 288]  
 2973 collisions, as well as dedicated theoretical studies [151, 158, 165, 285], have indicated the  
 2974 importance of nuclear deformation on the measured anisotropic flow. However, the effects  
 2975 of nuclear deformation are not yet considered in these Bayesian approaches. For a reliable  
 2976 extraction of transport properties and initial-state from the flow data, it is pressing to ensure  
 2977 the uncertainty associated with the structure of the colliding ions is under control, especially  
 2978 since all species for which high statistics of events have been collected at RHIC and the LHC  
 2979 are expected to present some deformation in the ground state, as indicated in Table 10).

	$\beta_2$	$\beta_3$	$\beta_4$
$^{238}\text{U}$	0.286 [266]	0.078 [65]	0.094 [65]
$^{208}\text{Pb}$	0.05 [266]	0.04 [269]	?
$^{197}\text{Au}$	-(0.13-0.16) [167, 239]	?	-0.03 [239]
$^{129}\text{Xe}$	0.16 [239]	?	?
$^{96}\text{Ru}$	0.05-0.16 [131]	?	?
$^{96}\text{Zr}$	0.08-0.22 [131]	?	0.06 [239]

**Table 10:** Some estimates of the deformation values  $\beta_2, \beta_3$ , and  $\beta_4$  for the large nuclei collided at RHIC and the LHC with references given, mostly based on global analysis of the  $B(E_n)$  transition data.

2980 It is straightforward to see why the geometry of heavy-ion collisions is sensitive to nuclear  
 2981 deformation. We refer to the cartoon in Figure 97. A nucleus can be conveniently modeled  
 2982 through a nucleon density of Woods-Saxon form:

$$\rho(r, \theta, \phi) = \frac{\rho_0}{1 + e^{[r-R(\theta, \phi)]/a}}, \quad R(\theta, \phi) = R_0 (1 + \beta_2[\cos \gamma Y_{2,0} + \sin \gamma Y_{2,2}] + \beta_3 Y_{3,0} + \beta_4 Y_{4,0}), \quad (3)$$

2983 where the nuclear surface  $R(\theta, \phi)$  includes only the most relevant deformation components,  
 2984  $Y_{n,m}(\theta, \phi) = \sqrt{2}(-1)^m \text{Re}[Y_n^m]$ , from nuclear structure physics, quadrupole  $n = 2$ , octupole  
 2985  $n = 3$  and hexadecapole  $n = 4$ . The angle  $0 \leq \gamma \leq \pi/3$  controls the triaxiality of the  
 2986 quadrupole deformation or the three radii  $a, b, c$  of the ellipsoid, with  $\gamma = 0$  corresponds to  
 2987 prolate ( $a = b < c$ ), and  $\gamma = \pi/3$  corresponds to oblate ( $a < b = c$ ). In central heavy-  
 2988 ion collisions, the shape of the deformed ions determines the geometry of overlap. The  
 2989 entire mass distribution is probed simultaneously, and one can use multi-particle correlation  
 2990 observables to probe it. This way of probing nuclear densities is very different from the  
 2991 standard techniques of low-energy physics, namely  $e+A$  collisions which access only the  
 2992 shape averaged over orientations, and low energy experiments from which one can infer  
 2993  $\beta_n$  from multipole transition probabilities,  $B(E_n)$ , between low-lying rotational states. The  
 2994  $B(E_n)$  method is also sensitive to whether the rotor undergoes rigid or wavelike (irrotational)  
 2995 rotations, while heavy ion collisions only care about the spatial distribution of nucleons.  
 2996 Furthermore, the time scales involved in heavy ion collisions are much shorter ( $10^{-24}$ s), than  
 2997 the typical lifetime of isomers involved in the rotational bands (typically on the order of  
 2998  $10^{-12}$ s). As we shall also argue below, a remarkable question is indeed whether the nuclear  
 2999 deformation– manifestation of the collective features of the nuclear many-body system—is  
 3000 the same across energy scales.

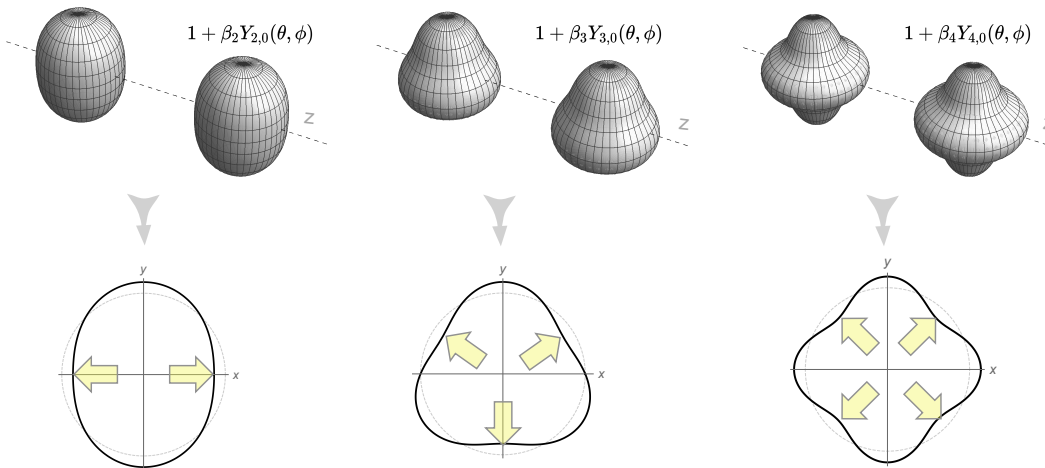


**Figure 97:** A cartoon of a collision of nuclei with quadrupole (left), octupole (middle) and hexadecapole (right) deformations including only the  $Y_{n,0}$  mode and with  $\beta_n = 0.25$  (we ignore the large Lorentz contraction in the  $z$ -direction). The bottom row shows how the initial condition of the medium formed after the collision looks like in the transverse plane. The yellow arrows indicate the direction of maximum pressure gradients along which the medium expands with the largest velocity, leading to final state harmonic flow  $v_n$  with  $n$ -fold symmetry.

3001 The presence of multipoles,  $\beta_n$ , in the colliding ions modifies nontrivially the corre-  
 3002 sponding spatial anisotropy,  $\varepsilon_n$ , of the produced QGP, and consequently the final-state flow  
 3003 harmonic,  $v_n$ . For  $n = 2$  both the mean-squared eccentricity and the mean-squared elliptic

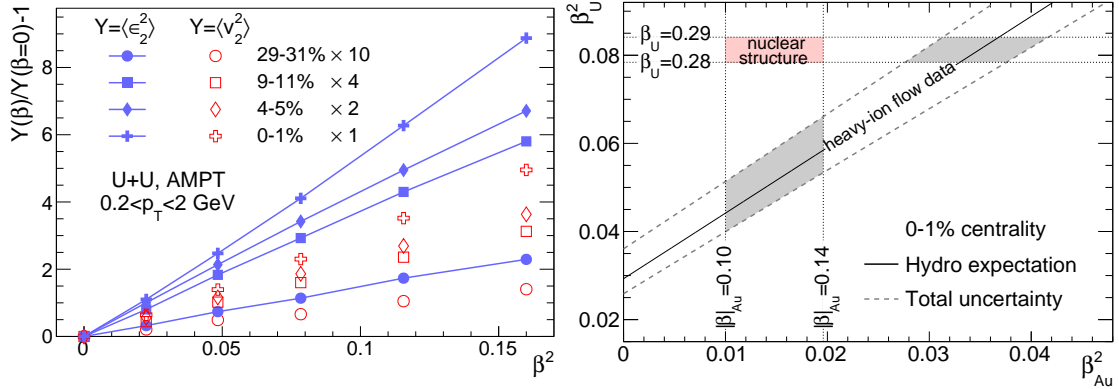


**Figure 98:** Left panel:  $\langle v_2^2(\beta) \rangle / \langle v_2^2(0) \rangle - 1 = b/a \beta_2^2$  (empty symbols) and  $\langle \epsilon_2^2(\beta_2) \rangle / \langle \epsilon_2^2(0) \rangle - 1 = b'/a' \beta_2^2$  (full symbols) as a function of  $\beta_2^2$  in U+U collisions from the AMPT model. Different symbols correspond to different centrality classes. Right panel:  $\beta_{2,U}^2$  as a function of  $\beta_{2,Au}^2$ . The region between the dashed lines is consistent with the hydrodynamic expectation based on Eq. (5) and STAR  $v_2$  data in 0–1% centrality. Figures taken from Ref. [157].

3004 flow are simple functions of the quadrupole deformation parameter [151, 182] (see Fig. 98)

$$\langle \epsilon_2^2 \rangle = a' + b' \beta_2^2, \quad \langle v_2^2 \rangle = a + b \beta_2^2, \quad (4)$$

3005 where the  $a'$  and  $a$  are mean-squared eccentricity and elliptic flow without deformation,  
 3006  $a' = \langle \epsilon_2^2 \rangle|_{\beta_2=0}$  and  $a = \langle v_2^2 \rangle|_{\beta_2=0}$ , while the  $b'$  and  $b$  describe the parametric dependence of  
 3007 the deformation-enhanced component of eccentricity and elliptic flow, respectively. Interest-  
 3008 ingly, the response coefficients for the deformation-independent and deformation-dependent  
 3009 components are not the same, i.e.  $k_a \equiv a/a' \neq b/b' \equiv k_b$ , which opens up the possibility to  
 3010 test hydrodynamics using  $\beta_2$  as a new control variable. The value  $b' \approx 0.2$  reflects a simple  
 3011 phase space factor accounting for the average over all random orientations, and is found to  
 3012 be nearly independent of the colliding systems. The strict quadratic dependence of Eq. 4  
 3013 leads to a very robust equation relating the  $\beta_2$  between any pair of collision systems, X+X  
 3014 and Y+Y, that are close in mass number [182]:

$$\beta_{2,Y}^2 = \left( \frac{r_{v_2^2} r_a - 1}{r_Y} \right) + \left( r_{v_2^2} \right) \beta_{2,X}^2, \quad r_{v_2^2} = \langle v_2^2 \rangle_Y / \langle v_2^2 \rangle_X, \quad (5)$$

3015 The ratios  $r_a$  and  $r_Y$  reflect properties of the initial state geometry and are robust against  
 3016 details of final-state effects. This provides a data-driven way to constrain the  $\beta_2$ . Applied to  
 3017 RHIC data, it allows one to derive a constraint on the  $\beta_{2,U}$  and  $\beta_{2,Au}$ , as shown in the right  
 3018 panel of Fig. 98. This highlights how, at present, the low-energy nuclear structure model  
 3019 calculation and the flow data from high-energy nuclear collisions are fairly inconsistent.  
 3020 Relations similar to Eq. 4 can also be written down for  $v_3$  and  $v_4$ , which can be used to  
 3021 potentially constrain octupole and hexadecapole deformations.

3022 An additional observable presenting a dramatic sensitivity to the nuclear quadrupole de-  
 3023 formation is the Pearson correlation coefficient,  $\rho(v_2^2, [p_T])$ , between  $v_2$  and the mean trans-  
 3024 verse momentum,  $[p_T]$ , in central collisions. This observable probes in particular the full

3025 quadrupole structure of the colliding ions [182], i.e., both  $\beta_{20}$  and its triaxiality  $\gamma$  in Eq. 3.  
 3026 This observable has been measured by the STAR collaboration in U+U and Au+Au collisions  
 3027 (Fig. 3 in Section 1.1.1). These measurements establish unambiguously the large and domi-  
 3028 nating influence of the nuclear quadrupole deformation. The large  $\beta_2$  of  $^{238}\text{U}$  yields a strong  
 3029 negative contribution to the  $v_2-[p_T]$  correlation, enough to make it change sign. Similar effect  
 3030 have further been observed in the fluctuations of  $[p_T]$  (Fig. 4 in Section 1.1.1). Hydrodynamic  
 3031 models based on state-of-the-art initial conditions with deformation values from Table 10  
 3032 struggle to describe quantitatively all these experimental measurements [152, 155, 274]. This  
 3033 suggests that the response of the radial flow of the system to the fluctuations induced by  
 3034 the deformation of the colliding ions is poorly captured by the existing models. Collisions  
 3035 of well-deformed ions, and their comparisons with the collisions of more spherical species,  
 3036 provide us with a new way to test the hydrodynamic description.

3037 We propose thus to collide more species to extract their value of  $\beta_2$ , and other deformation  
 3038 parameters  $\gamma$ ,  $\beta_3$  and  $\beta_4$ , from flow measurements, with a twofold purpose: 1) provide a new  
 3039 handle on the initial state and hydrodynamic response of the QGP, 2) perform studies of  
 3040 nuclear structure physics at high energy to complement the information coming from lower  
 3041 energies, and so assess the consistency of nuclear phenomena across energy scales. The  
 3042 ground state of almost all stable nuclei is deformed (see for example the interactive chart in  
 3043 Ref. [2]). RHIC, with its flexibility to collide almost any nuclei from  $p+p$  to U+U, is a unique  
 3044 facility to perform such studies in the foreseeable future. The best example to showcase this  
 3045 capability is the run of isobars performed in 2018, where the two systems, Zr+Zr and Ru+Ru,  
 3046 were alternated on a fill-by-fill basis, leading to extremely small systematic uncertainties on  
 3047 the final observables [30] (also Section 1.2). This allows one to detect minute differences  
 3048 in the physics observables such as multiplicity,  $[p_T]$  and  $v_n$  in the comparison of the two  
 3049 systems. Consequently, even small differences in the values of  $\beta_n$  of the colliding systems can  
 3050 be precisely mapped [156]. For each species, we need roughly 100 million minimum bias and  
 3051 50 million 0-5% central events. Assuming the standard 50% RHIC+STAR up time and 1.5  
 3052 KHz DAQ rate, same as Au+Au running, we will be able to collect 130M minbias events and  
 3053 64M central events in three days of physics running. This is slightly less than the existing  
 3054 U+U dataset taken in 2011, but with comparable statistical precision due to the increased  
 3055 acceptance from the iTPC. Adding two days of setup time, this leads to about five days of  
 3056 total time for each species.

3057 The system scan we propose can be divided into two steps. Given the tight schedule for  
 3058 the next few years, instead of making an explicit proposal on how much running time are  
 3059 needed to fully explore these topics, we discuss what can be achieved if we are given certain  
 3060 number of days.

- 3061 •  **$\approx 10$  days:** In the first step, we would like to scan a few nuclei in the vicinity of  
 3062 the most studied species at RHIC,  $^{197}\text{Au}$ , to assess whether the modeling of Au+Au  
 3063 collisions is under control, an information which is in fact crucial for the future precision  
 3064 interpretation of high-statistics data expected during the operation of sPHENIX. To  
 3065 achieve this, ideal candidates are  $^{208}\text{Pb}$  and  $^{196}\text{Hg}$  (or  $^{198}\text{Hg}$  could be a substitute  
 3066 depending on availability). Having  $^{208}\text{Pb}$  at  $\sqrt{s_{\text{NN}}} = 200$  GeV will provide a crucial

3067 bridge with Au+Au at the same energy, as well as with the  $^{208}\text{Pb}$  at LHC energies.  
 3068 Comparison between  $^{208}\text{Pb}$  measurements at RHIC and the LHC will constrain any  
 3069 possible energy dependence of the initial state effects and pre-equilibrium dynamics.  
 3070 Additionally,  $^{208}\text{Pb}$  is nearly spherical, so that Pb+Pb collisions will effectively allow  
 3071 us to better understand the impact of the moderate deformation of  $^{197}\text{Au}$  in Au+Au  
 3072 collisions. The run of Hg+Hg collisions would then permit us to understand more  
 3073 deeply the nature of the deformation of  $^{197}\text{Au}$ , which, being an odd-mass nucleus, has  
 3074 never been determined in low-energy experiments.  $^{196}\text{Hg}$  is an oblate nucleus with  
 3075  $|\beta_2| \approx 0.1$ . Thanks to the observable  $\rho(v_2^2, [p_T])$ , it will be possible to quantify whether  
 3076  $^{197}\text{Au}$  is more or less oblate than  $^{196}\text{Hg}$ , an information which will allow us gauge even  
 3077 more tightly the initial geometry of Au+Au collisions.

- 3078 • **Additional time:** In the second step, our proposal is to use RHIC to perform precision  
 3079 tests of the predictions of low-energy nuclear physics by studying the evolution of the  
 3080 quadrupole deformation along the chain of stable samarium isotopes. It would be  
 3081 useful in particular to collide three isotopes:  $^{144}\text{Sm}$ , which is essentially as spherical  
 3082 as  $^{208}\text{Pb}$ ,  $^{148}\text{Sm}$ , mildly deformed and triaxial much as  $^{129}\text{Xe}$  and  $^{197}\text{Au}$ , and  $^{154}\text{Sm}$   
 3083 ( $\beta_2 = 0.34$ ), which is a well-deformed nucleus like  $^{238}\text{U}$ . The evolution of the quadrupole  
 3084 structure of these ions can be mapped precisely at RHIC, thus offering a precision test  
 3085 of nuclear structure knowledge. If data on  $^{154}\text{Sm}+^{154}\text{Sm}$  collisions is available, it would  
 3086 be valuable to also collect data on  $^{154}\text{Gd}+^{154}\text{Gd}$  ( $\beta_2 = 0.31$ ) collisions. The comparison  
 3087 between the two well-deformed isobaric systems could potentially yield the most precise  
 3088 information about the relative deformation of two ground states. Theoretical studies  
 3089 further suggest that ground states in the region  $Z \sim 56/N \sim 88$  [109] (including the  
 3090 samarium isotopes) may display enhanced octupole correlations, i.e.,  $\beta_3$  values. These  
 3091 would manifest in high-energy collisions as enhanced triangular flow coefficients, as well  
 3092 as in the correlators  $\rho(v_3^2, [p_T])$ . Evidence of static octupole moments at low energies is  
 3093 rather sparse, and heavy ion collisions might be a more sensitive approach. The study  
 3094 of octupole deformation is also fundamentally interesting because nuclei with large  $\beta_3$   
 3095 provides a stringent test of the electric-dipole moment (EDM) [226]. The exact choice  
 3096 of species is still under refinement, presently we have a preference for  $^{154}\text{Sm}$  and  $^{148}\text{Sm}$ ,  
 3097 followed by  $^{154}\text{Gd}$  and  $^{144}\text{Sm}$ .

3098 Finally, one should note that the STAR DAQ rate for these moderate-sized systems  
 3099 could be significantly larger, possibly reaching 2KHz. This enhanced DAQ rate will  
 3100 compensate partially the smaller number of charged particles expected in these systems  
 3101 compared to larger systems.

## 3102 5.2 Fixed-target Measurements Using Light Beam and Target Com- 3103 binations

3104 Although the proposed fixed-target Au+Au energy scan has been completed, if the oppor-  
 3105 tunity exists for further measurements, light beam and target combinations could help to

3106 clarify the role and mechanisms of nucleon stopping. Indeed, STAR was recommended to  
3107 consider installing a beryllium target, that being the lowest  $Z$  feasible solid target which  
3108 could work with the target apparatus. This was not done previously because changing the  
3109 target requires opening the STAR beampipe and removing the existing target, and that  
3110 could not be done until the Au+Au energy scan had been completed. Both the collider and  
3111 STAR have demonstrated that fixed-target runs can be quickly tuned, as the demands on  
3112 collider operations are modest, and efficiently run, as the collider can control and deliver  
3113 sufficient intensity to fill the STAR DAQ bandwidth and the experiment can cleanly trigger  
3114 on these events.

3115 It is possible that fixed-target collisions using light beam and target combinations could  
3116 also benefit the Space Radiation Protection community. Cosmic rays are a serious concern  
3117 to astronauts, electronics, and spacecraft. Although 90% of the cosmic ray flux is comprised  
3118 of energetic protons and another 9% is Helium nuclei, the remaining 1%, which is made  
3119 up of nuclei from Li to Fe, is not negligible both because the energy loss is proportional  
3120 to  $Z^2$  and because additional damage is done by the energetic light nuclei (p, d, t,  $^3He$ ,  
3121 and  $^4He$ ) produced through the fragmentation of the target and projectile nuclei. Light ion  
3122 cross section measurements represent the largest uncertainty in space radiation estimates.  
3123 The energy spectrum of cosmic rays in the solar system is concentrated at energies below  
3124 1 GeV/n. Extensive measurements have been made using the dedicated NSRL facility at  
3125 the booster, and at other lower energy facilities. However, the Space Radiation Community  
3126 has recently identified higher energy systems, using beams from 3 to 50 GeV/n on C, Al,  
3127 and Fe targets as one of the next areas of need. The requirements would be to measure the  
3128 cross section for light nucleus (p, d, t,  $^3He$ , and  $^4He$ ) production through fragmentation  
3129 of the target and projectile. STAR has very good particle identification for all of these  
3130 particle species using both  $dE/dx$  and time-of-flight, however the acceptance is only in the  
3131 target-side of the rapidity distribution. For symmetric systems this is not a problem. For  
3132 asymmetric systems this would require both light-on-heavy and heavy-on-light combinations.  
3133 Efforts are underway to determine if the STAR detector has sufficient acceptance in  $p_T$  and  
3134  $y$  to meet the needs of the Space Radiation Protection community. If it is determined that  
3135 the measurements that could be made at RHIC using the STAR detector would meet those  
3136 needs, STAR is likely to propose brief energy scans using He, Si, and Fe beams on light  
3137 targets in years 23, 24, and 25. Such measurements could not be made in 2022 because the  
3138 timeline to prepare for the Run-22 is very brief and there is not be adequate time to open  
3139 the STAR beampipe and replace the targets.

## 3142 **6 Charge for 2021 NPP PAC**

- 3143 • STAR: Beam Use Requests for Runs 22-25
- 3144 • sPHENIX: Beam Use Requests for Runs 23-25
- 3145 • CeC: Beam Use Requests

3146 The Beam Use Requests should be submitted in written form to PAC by May 14, 2021. The  
3147 BURs should be based on the following number of expected cryo-weeks. First number is  
3148 minimal expected RHIC run duration and second number is optimal duration:

- 3149 2022: 18 (20)
- 3150 2023: 20 (28)
- 3151 2024: 20 (28)
- 3152 2025: 20 (28)

## References

- 3153
- 3154 [1] BeAGLE: a Tool to Refine Detector Requirements for eA Collisions EIC R&D; Project  
3155 eRD17 E. Aschenauer, M. Baker, W. Chang, J. Lee, Z. Tu et al. [https://wiki.bnl.](https://wiki.bnl.gov/eic/index.php/BeAGLE)  
3156 [gov/eic/index.php/BeAGLE](https://wiki.bnl.gov/eic/index.php/BeAGLE).
- 3157 [2] Chart of Nuclear Quadrupole Deformations, <https://www.nndc.bnl.gov/nudat2/>.
- 3158 [3] M. Aaboud et al. Measurement of longitudinal flow decorrelations in Pb+Pb collisions  
3159 at  $\sqrt{s_{NN}} = 2.76$  and 5.02 TeV with the ATLAS detector. *Eur. Phys. J. C*, 78(2):142,  
3160 2018.
- 3161 [4] M. Aaboud et al. Observation of centrality-dependent acoplanarity for muon pairs  
3162 produced via two-photon scattering in Pb + Pb collisions at  $\sqrt{s_{NN}} = 5.02$  TeV with  
3163 the atlas detector. *Phys. Rev. Lett.*, 121:212301, Nov 2018.
- 3164 [5] M. Aaboud et al. Prompt and non-prompt  $J/\psi$  and  $\psi(2S)$  suppression at high trans-  
3165 verse momentum in 5.02 TeV Pb+Pb collisions with the ATLAS experiment. *Eur.*  
3166 *Phys. J. C*, 78(9):762, 2018.
- 3167 [6] G. Aad et al. Observation of Associated Near-Side and Away-Side Long-Range Corre-  
3168 lations in  $\sqrt{s_{NN}}=5.02$  TeV Proton-Lead Collisions with the ATLAS Detector. *Phys.*  
3169 *Rev. Lett.*, 110(18):182302, 2013.
- 3170 [7] G. Aad et al. Two-particle azimuthal correlations in photonuclear ultraperipheral  
3171 Pb+Pb collisions at 5.02 TeV with ATLAS. 1 2021.
- 3172 [8] F. Aaron et al. Combined inclusive diffractive cross sections measured with forward  
3173 proton spectrometers in deep inelastic  $ep$  scattering at HERA. *Eur. Phys. J. C*, 72:2175,  
3174 2012.
- 3175 [9] M. Abdallah et al. Invariant Jet Mass Measurements in  $pp$  Collisions at  $\sqrt{s} = 200$   
3176 GeV at RHIC. 3 2021.
- 3177 [10] M. Abdallah et al. Longitudinal double-spin asymmetry for inclusive jet and dijet  
3178 production in polarized proton collisions at  $\sqrt{s} = 200$  GeV. 3 2021.
- 3179 [11] B. Abelev et al. Forward Lambda production and nuclear stopping power in d + Au  
3180 collisions at  $s(NN)^{1/2} = 200$ -GeV. *Phys. Rev. C*, 76:064904, 2007.
- 3181 [12] B. Abelev et al. Measurement of transverse single-spin asymmetries for di-jet pro-  
3182 duction in proton-proton collisions at  $\sqrt{s} = 200$  GeV. *Phys. Rev. Lett.*, 99:142003,  
3183 2007.
- 3184 [13] B. Abelev et al. Observation of an Antimatter Hypernucleus. *Science*, 328(5974):58,  
3185 2010.

- 3186 [14] B. Abelev et al. Long-range angular correlations on the near and away side in  $p$ -Pb  
3187 collisions at  $\sqrt{s_{NN}} = 5.02$  TeV. *Phys. Lett. B*, 719:29–41, 2013.
- 3188 [15] B. B. Abelev et al. Centrality, rapidity and transverse momentum dependence of  $J/\psi$   
3189 suppression in Pb-Pb collisions at  $\sqrt{s_{NN}}=2.76$  TeV. *Phys. Lett. B*, 734:314–327, 2014.
- 3190 [16] B. I. Abelev et al. Global polarization measurement in Au+Au collisions. *Phys. Rev.*  
3191 *C*, 76:024915, 2007. [Erratum: *Phys.Rev.C* 95, 039906 (2017)].
- 3192 [17] M. C. Abreu et al. Evidence for deconfinement of quarks and gluons from the  $J/\psi$   
3193 suppression pattern measured in Pb + Pb collisions at the CERN SPS. *Phys. Lett. B*,  
3194 477:28–36, 2000.
- 3195 [18] A. Abusleme et al. Performance of a Full-Size Small-Strip Thin Gap Chamber Proto-  
3196 type for the ATLAS New Small Wheel Muon Upgrade. *Nucl. Instrum. Meth.*, A817:85–  
3197 92, 2016.
- 3198 [19] A. Accardi et al. Electron Ion Collider: The Next QCD Frontier: Understanding the  
3199 glue that binds us all. *Eur. Phys. J. A*, 52(9):268, 2016.
- 3200 [20] S. Acharya et al. Global polarization of  $\Lambda\bar{\Lambda}$  hyperons in Pb-Pb collisions at  $\sqrt{s_{NN}} =$   
3201 2.76 and 5.02 TeV. *Phys. Rev. C*, 101(4):044611, 2020.
- 3202 [21] S. Acharya et al. Unveiling the strong interaction among hadrons at the LHC. *Nature*,  
3203 588:232, 2020.
- 3204 [22] J. Adam et al. Measurement of jet quenching with semi-inclusive hadron-jet distribu-  
3205 tions in central Pb-Pb collisions at  $\sqrt{s_{NN}} = 2.76$  TeV. *JHEP*, 09:170, 2015.
- 3206 [23] J. Adam et al. Differential studies of inclusive  $J/\psi$  and  $\psi(2S)$  production at forward  
3207 rapidity in Pb-Pb collisions at  $\sqrt{s_{NN}} = 2.76$  TeV. *JHEP*, 05:179, 2016.
- 3208 [24] J. Adam et al. Global polarization of  $\Lambda$  hyperons in Au+Au collisions at  $\sqrt{s_{NN}} = 200$   
3209 GeV. *Phys. Rev. C*, 98:014910, 2018.
- 3210 [25] J. Adam et al. Improved measurement of the longitudinal spin transfer to  $\Lambda$  and  
3211  $\bar{\Lambda}$  hyperons in polarized proton-proton collisions at  $\sqrt{s} = 200$  GeV. *Phys. Rev. D*,  
3212 98(11):112009, Dec 2018.
- 3213 [26] J. Adam et al. Longitudinal Double-Spin Asymmetries for Dijet Production at Inter-  
3214 mediate Pseudorapidity in Polarized  $pp$  Collisions at  $\sqrt{s} = 200$  GeV. *Phys. Rev. D.*,  
3215 98:032011, 2018.
- 3216 [27] J. Adam et al. Low- $p_T$   $e^+e^-$  pair production in Au+Au collisions at  $\sqrt{s_{NN}} = 200$  GeV  
3217 and U + U collisions at  $\sqrt{s_{NN}} = 193$  GeV at star. *Phys. Rev. Lett.*, 121:132301, Sep  
3218 2018.

- 3219 [28] J. Adam et al. Transverse spin transfer to  $\Lambda$  and  $\bar{\Lambda}$  hyperons in polarized proton-proton  
3220 collisions at  $\sqrt{s} = 200$  GeV. *Phys. Rev. D*, 98:091103(R), 2018.
- 3221 [29] J. Adam et al. Measurement of inclusive  $J/\psi$  suppression in Au+Au collisions at  $\sqrt{s_{NN}}$   
3222  $= 200$  GeV through the dimuon channel at STAR. *Phys. Lett. B*, 797:134917, 2019.
- 3223 [30] J. Adam et al. Methods for a blind analysis of isobar data collected by the STAR  
3224 collaboration. 2019.
- 3225 [31] J. Adam et al. The Proton-Omega correlation function in Au+Au collisions at 200  
3226 GeV. *Phys. Lett. B*, 790:490, 2019.
- 3227 [32] J. Adam et al. Charge separation measurements in p(d)+Au and Au+Au collisions  
3228 implications for the chiral magnetic effect. 2020.
- 3229 [33] J. Adam et al. Measurement of groomed jet substructure observables in p+p collisions  
3230 at  $\sqrt{s} = 200$  GeV with STAR. *Phys. Lett. B*, 811:135846, 2020.
- 3231 [34] J. Adam et al. Measurement of inclusive charged-particle jet production in Au+Au  
3232 collisions at  $\sqrt{s_{NN}} = 200$  GeV. 5 2020.
- 3233 [35] J. Adam et al. Measurement of inclusive  $J/\psi$  polarization in  $p + p$  collisions at  $\sqrt{s}$   
3234  $= 200$  GeV by the STAR experiment. *Phys. Rev. D*, 102(9):092009, 2020.
- 3235 [36] J. Adam et al. Measurement of transverse single-spin asymmetries of  $\pi^0$  and electro-  
3236 magnetic jets at forward rapidity in 200 and 500 GeV transversely polarized proton-  
3237 proton collisions. *accepted by Phys. Rev. D*, 12 2020.
- 3238 [37] J. Adam et al. Pair invariant mass to isolate background in the search for the chiral  
3239 magnetic effect in Au+Au collisions at  $s_{NN} = 200$  GeV. 2020.
- 3240 [38] J. Adam et al. Results on total and elastic cross sections in proton-proton collisions  
3241 at  $\sqrt{s} = 200$  GeV. *Phys. Lett. B*, 808:135663, 2020.
- 3242 [39] J. Adam et al. Underlying event measurements in  $p + p$  collisions at  $\sqrt{s} = 200$  GeV at  
3243 RHIC. *Phys. Rev. D*, 101(5):052004, 2020.
- 3244 [40] J. Adam et al. Comparison of transverse single-spin asymmetries for forward  $\pi^0$  pro-  
3245 duction in polarized  $pp$ ,  $pA$  and  $pAu$  collisions at nucleon pair c.m. energy  $\sqrt{s_{NN}} = 200$   
3246 GeV. *Phys. Rev. D*, 103:072005, 2021.
- 3247 [41] J. Adam et al. Global Polarization of  $\Xi$  and  $\Omega$  Hyperons in Au+Au Collisions at  $\sqrt{s_{NN}}$   
3248  $= 200$  GeV. *Phys. Rev. Lett.*, 126(16):162301, 2021.
- 3249 [42] J. Adam et al. Measurements of  $W$  and  $Z/\gamma^*$  cross sections and their ratios in p+p  
3250 collisions at RHIC. *Phys. Rev. D*, 103(1):012001, 2021.

- 3251 [43] J. Adam et al. Nonmonotonic Energy Dependence of Net-Proton Number Fluctuations.  
3252 *Phys. Rev. Lett.*, 126(9):092301, 2021.
- 3253 [44] J. Adam et al. Observation of  $D_s^\pm/D^0$  enhancement in Au+Au collisions at  $\sqrt{s_{NN}} =$   
3254 200 GeV. 1 2021.
- 3255 [45] L. Adamczyk, J. Adams, J. Adkins, G. Agakishiev, M. Aggarwal, Z. Ahammed, N. Aji-  
3256 tanand, I. Alekseev, D. Anderson, R. Aoyama, and et al. Transverse spin-dependent  
3257 azimuthal correlations of charged pion pairs measured in  $p\uparrow + p$  collisions at  $\sqrt{s} =$   
3258 500 gev. *Phys. Lett. B*, 780:332–339, 2018.
- 3259 [46] L. Adamczyk et al. Single Spin Asymmetry  $A_N$  in Polarized Proton-Proton Elastic  
3260 Scattering at  $\sqrt{s} = 200$  GeV. *Phys. Lett. B*, 719:62–69, 2013.
- 3261 [47] L. Adamczyk et al. Dielectron Mass Spectra from Au+Au Collisions at  $\sqrt{s_{NN}} = 200$   
3262 GeV. *Phys. Rev. Lett.*, 113(2):022301, 2014. [Addendum: *Phys.Rev.Lett.* 113, 049903  
3263 (2014)].
- 3264 [48] L. Adamczyk et al. Azimuthal anisotropy in U+U and Au+Au collisions at RHIC.  
3265 *Phys. Rev. Lett.*, 115(22):222301, 2015.
- 3266 [49] L. Adamczyk et al. Long-range pseudorapidity dihadron correlations in  $d$ +Au collisions  
3267 at  $\sqrt{s_{NN}} = 200$  GeV. *Phys. Lett. B*, 747:265–271, 2015.
- 3268 [50] L. Adamczyk et al. Measurement of Interaction between Antiprotons. *Nature*, 527:345,  
3269 2015.
- 3270 [51] L. Adamczyk et al. Harmonic decomposition of three-particle azimuthal correlations  
3271 at RHIC. *Manuscript under preparation*, 2016.
- 3272 [52] L. Adamczyk et al. Energy dependence of  $J/\psi$  production in Au+Au collisions at  
3273  $\sqrt{s_{NN}} = 39, 62.4$  and 200 GeV. *Phys. Lett. B*, 771:13–20, 2017.
- 3274 [53] L. Adamczyk et al. Global  $\Lambda$  hyperon polarization in nuclear collisions: evidence for  
3275 the most vortical fluid. *Nature*, 548:62–65, 2017.
- 3276 [54] L. Adamczyk et al. Measurement of the cross section and longitudinal double-spin  
3277 asymmetry for di-jet production in polarized  $pp$  collisions at  $\sqrt{s} = 200$  GeV. *Phys.*  
3278 *Rev. D*, 95(7):071103, 2017.
- 3279 [55] L. Adamczyk et al. Measurements of jet quenching with semi-inclusive hadron+jet  
3280 distributions in Au+Au collisions at  $\sqrt{s_{NN}} = 200$  GeV. *Phys. Rev. C*, 96(2):024905,  
3281 2017.
- 3282 [56] L. Adamczyk et al. Azimuthal transverse single-spin asymmetries of inclusive jets and  
3283 charged pions within jets from polarized-proton collisions at  $\sqrt{s} = 500$  GeV. *Phys.*  
3284 *Rev. D*, 97(3):032004, 2018.

- 3285 [57] J. Adams et al. The STAR Event Plane Detector. *Nucl. Instrum. Meth. A*, 968:163970,  
3286 2020.
- 3287 [58] A. Adare et al. Suppression of back-to-back hadron pairs at forward rapidity in  $d+Au$   
3288 Collisions at  $\sqrt{s_{NN}} = 200$  GeV. *Phys. Rev. Lett.*, 107:172301, 2011.
- 3289 [59] A. Adare et al. Transverse-Momentum Dependence of the  $J/\psi$  Nuclear Modification  
3290 in  $d+Au$  Collisions at  $\sqrt{s_{NN}} = 200$  GeV. *Phys. Rev. C*, 87(3):034904, 2013.
- 3291 [60] A. Adare et al. Measurement of long-range angular correlation and quadrupole  
3292 anisotropy of pions and (anti)protons in central  $d+Au$  collisions at  $\sqrt{s_{NN}}=200$  GeV.  
3293 *Phys. Rev. Lett.*, 114(19):192301, 2015.
- 3294 [61] A. Adare et al. Measurements of elliptic and triangular flow in high-multiplicity  
3295  $^3He+Au$  collisions at  $\sqrt{s_{NN}} = 200$  GeV. *Phys. Rev. Lett.*, 115(14):142301, 2015.
- 3296 [62] S. Adler et al. Centrality dependence of  $\pi^0$  and  $\eta$  production at large transverse  
3297 momentum in  $s(NN)^{1/2} = 200$ -GeV  $d+Au$  collisions. *Phys. Rev. Lett.*, 98:172302,  
3298 2007.
- 3299 [63] C. Adolph, R. Akhunzyanov, M. Alexeev, G. Alexeev, A. Amoroso, V. Andrieux,  
3300 V. Anosov, A. Austregesilo, B. Badełek, F. Balestra, and et al. Collins and sivers  
3301 asymmetries in muonproduction of pions and kaons off transversely polarised protons.  
3302 *Phys. Lett. B*, 744:250–259, 2015.
- 3303 [64] T. Auye. Unfolding algorithms and tests using RooUnfold. In *PHYSTAT 2011*, Geneva,  
3304 5 2011. CERN.
- 3305 [65] S. E. Agbemava, A. V. Afanasjev, and P. Ring. Octupole deformation in the ground  
3306 states of even-even nuclei: a global analysis within the covariant density functional  
3307 theory. *Phys. Rev. C*, 93(4):044304, 2016.
- 3308 [66] C. Aidala et al. Measurement of long-range angular correlations and azimuthal  
3309 anisotropies in high-multiplicity  $p+Au$  collisions at  $\sqrt{s_{NN}} = 200$  GeV. *Phys. Rev.*  
3310 *C*, 95(3):034910, 2017.
- 3311 [67] C. Aidala et al. Creation of quark–gluon plasma droplets with three distinct geometries.  
3312 *Nature Phys.*, 15(3):214–220, 2019.
- 3313 [68] A. Airapetian, N. Akopov, Z. Akopov, E. Aschenauer, W. Augustyniak, R. Avakian,  
3314 A. Avetissian, E. Avetisyan, A. Bacchetta, S. Belostotski, and et al. Effects of transver-  
3315 sity in deep-inelastic scattering by polarized protons. *Phys. Lett. B*, 693:11–16, 2010.
- 3316 [69] A. Airapetian et al. Quark fragmentation to  $\pi^{+-}$ ,  $\pi^0$ ,  $K^{+-}$ ,  $p$  and anti- $p$  in the nuclear  
3317 environment. *Phys. Lett. B*, 577:37–46, 2003.

- 3318 [70] A. Airapetian et al. Hadronization in semi-inclusive deep-inelastic scattering on nuclei.  
3319 *Nucl. Phys. B*, 780:1–27, 2007.
- 3320 [71] A. Airapetian et al. Transverse momentum broadening of hadrons produced in semi-  
3321 inclusive deep-inelastic scattering on nuclei. *Phys. Lett. B*, 684:114–118, 2010.
- 3322 [72] N. N. Ajitanand, R. A. Lacey, A. Taranenko, and J. M. Alexander. A New method for  
3323 the experimental study of topological effects in the quark-gluon plasma. *Phys. Rev.*,  
3324 C83:011901, 2011.
- 3325 [73] J. L. Albacete, G. Giacalone, C. Marquet, and M. Matas. Forward dihadron back-to-  
3326 back correlations in  $pA$  collisions. *Phys. Rev. D*, 99(1):014002, 2019.
- 3327 [74] J. L. Albacete and C. Marquet. Azimuthal correlations of forward di-hadrons in d+Au  
3328 collisions at RHIC in the Color Glass Condensate. *Phys. Rev. Lett.*, 105:162301, 2010.
- 3329 [75] J. L. Albacete and C. Marquet. Single and double inclusive particle production in  
3330 d+Au collisions at RHIC, leading twist and beyond. *Nucl. Phys. A*, 854:154–167,  
3331 2011.
- 3332 [76] C. Alexandrou, K. Cichy, M. Constantinou, K. Jansen, A. Scapellato, and F. Steffens.  
3333 Transversity parton distribution functions from lattice qcd. *Phys. Rev. D*, 98:091503,  
3334 2018.
- 3335 [77] ALICE Collaboration. Anisotropic flow in Xe-Xe collisions at  $\sqrt{s_{\text{NN}}} = 5.44$  TeV. *Phys.*  
3336 *Lett. B*, 784:82–95, 2018.
- 3337 [78] M. Anselmino, M. Boglione, U. D’Alesio, E. Leader, S. Melis, and F. Murgia. The  
3338 general partonic structure for hadronic spin asymmetries. *Phys. Rev. D*, 73:014020,  
3339 2006.
- 3340 [79] M. Anselmino, M. Boglione, U. D’Alesio, A. Kotzinian, F. Murgia, A. Prokudin, and  
3341 C. Türk. Transversity and collins functions from sidis and  $e+e-$  data. *Phys. Rev. D*,  
3342 75:054032, 2007.
- 3343 [80] Y. Aoki, G. Endrodi, Z. Fodor, S. D. Katz, and K. K. Szabo. The Order of the quan-  
3344 tum chromodynamics transition predicted by the standard model of particle physics.  
3345 *Nature*, 443:675–678, 2006.
- 3346 [81] A. Arahamian et al. Reaching for the horizon: The 2015 long range plan for  
3347 nuclear science, 2015. The 2015 Long Range Plan for Nuclear Science “Reach-  
3348 ing for the Horizon” [http://science.energy.gov/~media/np/nsac/pdf/2015LRP/  
3349 2015\\_LRPNS\\_091815.pdf](http://science.energy.gov/~media/np/nsac/pdf/2015LRP/2015_LRPNS_091815.pdf).
- 3350 [82] N. Armesto, H. Paukkunen, J. M. Penín, C. A. Salgado, and P. Zurita. An analysis of  
3351 the impact of LHC Run I proton–lead data on nuclear parton densities. *Eur. Phys. J.*  
3352 *C*, 76(4):218, 2016.

- 3353 [83] E. Aschenauer et al. eRHIC Design Study: An Electron-Ion Collider at BNL. 9 2014.
- 3354 [84] ATLAS Collaboration. Measurement of the azimuthal anisotropy of charged-particle  
3355 production in Xe+Xe collisions at  $\sqrt{s_{NN}} = 5.44$  TeV with the ATLAS detector. 2019.
- 3356 [85] X. Bai. Quarkonium measurements in nucleus-nucleus collisions with ALICE. *Nucl.*  
3357 *Phys. A*, 1005:121769, 2021.
- 3358 [86] V. Bairathi, M. R. Haque, and B. Mohanty. Selecting specific initial configurations  
3359 using spectator neutrons in U + U collisions. *Phys. Rev. C*, 91(5):054903, 2015.
- 3360 [87] I. Balitsky. Operator expansion for high-energy scattering. *Nucl. Phys.*, B463:99–160,  
3361 1996.
- 3362 [88] I. Balitsky. Factorization and high-energy effective action. *Phys. Rev. D*, 60:014020,  
3363 1999.
- 3364 [89] S. A. Bass et al. Microscopic models for ultrarelativistic heavy ion collisions. *Prog.*  
3365 *Part. Nucl. Phys.*, 41:255–369, 1998. [Prog. Part. Nucl. Phys.41,225(1998)].
- 3366 [90] A. Bazavov et al. The QCD Equation of State to  $\mathcal{O}(\mu_B^6)$  from Lattice QCD. *Phys.*  
3367 *Rev. D*, 95(5):054504, 2017.
- 3368 [91] A. Bazavov et al. Skewness, kurtosis and the 5th and 6th order cumulants of net  
3369 baryon-number distributions from lattice QCD confront high-statistics STAR data.  
3370 2020.
- 3371 [92] A. Behera, M. Nie, and J. Jia. Longitudinal eccentricity decorrelations in heavy ion  
3372 collisions. *Phys. Rev. Res.*, 2(2):023362, 2020.
- 3373 [93] J. E. Bernhard, J. S. Moreland, S. A. Bass, J. Liu, and U. Heinz. Applying Bayesian  
3374 parameter estimation to relativistic heavy-ion collisions: simultaneous characterization  
3375 of the initial state and quark-gluon plasma medium. *Phys. Rev. C*, 94(2):024907, 2016.
- 3376 [94] L. Bland, E. Brash, H. Crawford, A. Derevschikov, K. Drees, J. Engelage, C. Folz,  
3377 M. Jones, E. Judd, X. Li, N. Liyanage, Y. Makdisi, N. Minaev, R. Munroe, L. Nogach,  
3378 A. Ogawa, C. Perdrisat, C. Perkins, M. Planinic, V. Punjabi, G. Schnell, G. Simatovic,  
3379 T. Throwe, C. Van Hulse, and A. Vasiliev. Cross sections and transverse single-spin  
3380 asymmetries in forward jet production from proton collisions at s=500 gev. *Physics*  
3381 *Letters B*, 750:660 – 665, 2015.
- 3382 [95] M. Bleicher et al. Relativistic hadron hadron collisions in the ultrarelativistic quantum  
3383 molecular dynamics model. *J. Phys. G*, 25:1859–1896, 1999.
- 3384 [96] M. Boglione, U. D’Alesio, C. Flore, J. O. Gonzalez-Hernandez, F. Murgia, and  
3385 A. Prokudin. Reweighting the Sivers function with jet data from STAR. *Phys. Lett.*  
3386 *B*, 815:136135, 2021.

- 3387 [97] S. Borsanyi, Z. Fodor, J. N. Guenther, S. K. Katz, K. K. Szabo, A. Pasztor, I. Portillo,  
3388 and C. Ratti. Higher order fluctuations and correlations of conserved charges from  
3389 lattice QCD. *JHEP*, 10:205, 2018.
- 3390 [98] P. Bozek. Transverse-momentum–flow correlations in relativistic heavy-ion collisions.  
3391 *Phys. Rev. C*, 93(4):044908, 2016.
- 3392 [99] P. Bozek and W. Broniowski. Transverse-momentum fluctuations in relativistic heavy-  
3393 ion collisions from event-by-event viscous hydrodynamics. *Phys. Rev. C*, 85:044910,  
3394 2012.
- 3395 [100] P. Bozek, W. Broniowski, and J. Moreira. Torqued fireballs in relativistic heavy-ion  
3396 collisions. *Phys. Rev.*, C83:034911, 2011.
- 3397 [101] P. Bozek and H. Mehrabpour. Correlation coefficient between harmonic flow and  
3398 transverse momentum in heavy-ion collisions. *Phys. Rev. C*, 101(6):064902, 2020.
- 3399 [102] E. Braidot. Two Particle Correlations at Forward Rapidity in STAR. *Nucl. Phys. A*,  
3400 854:168–174, 2011.
- 3401 [103] W. Brooks and H. Hakobyan. Experimental Studies of Hadronization and Parton  
3402 Propagation in the Space-Time Domain. *Nucl. Phys. A*, 830:361C–368C, 2009.
- 3403 [104] S. L. Bultmann et al. First measurement of proton proton elastic scattering at RHIC.  
3404 *Phys. Lett. B*, 579:245–250, 2004.
- 3405 [105] S. Bultmann et al. First measurement of  $A(N)$  at  $s^{**}(1/2) = 200$ -GeV in polarized  
3406 proton-proton elastic scattering at RHIC. *Phys. Lett. B*, 632:167–172, 2006.
- 3407 [106] S. Bultmann et al. Double Spin Asymmetries  $A(NN)$  and  $A(SS)$  at  $s^{**}(1/2) = 200$ -  
3408 GeV in Polarized Proton-Proton Elastic Scattering at RHIC. *Phys. Lett. B*, 647:98–103,  
3409 2007.
- 3410 [107] M. Burkardt. Impact parameter dependent parton distributions and off forward parton  
3411 distributions for  $\zeta \rightarrow 0$ . *Phys. Rev. D*, 62:071503, 2000. [Erratum: *Phys.Rev.D*  
3412 66, 119903 (2002)].
- 3413 [108] M. Bury, A. Prokudin, and A. Vladimirov. Extraction of the Sivers Function from  
3414 SIDIS, Drell-Yan, and  $W^\pm/Z$  Data at Next-to-Next-to-Next-to Leading Order. *Phys.*  
3415 *Rev. Lett.*, 126(11):112002, 2021.
- 3416 [109] P. A. Butler. Octupole collectivity in nuclei. *J. Phys. G*, 43(7):073002, 2016.
- 3417 [110] J. Cammarota, L. Gamberg, Z.-B. Kang, J. A. Miller, D. Pitonyak, A. Prokudin,  
3418 T. C. Rogers, and N. Sato. Origin of single transverse-spin asymmetries in high-energy  
3419 collisions. *Phys. Rev. D*, 102(5):054002, 2020.

- 3420 [111] S. Cao, G.-Y. Qin, and S. A. Bass. Energy loss, hadronization, and hadronic interac-  
3421 tions of heavy flavors in relativistic heavy-ion collisions. *Phys. Rev. C*, 92:024907, Aug  
3422 2015.
- 3423 [112] S. Chatrchyan et al. Observation of Long-Range Near-Side Angular Correlations in  
3424 Proton-Lead Collisions at the LHC. *Phys. Lett. B*, 718:795–814, 2013.
- 3425 [113] S. Chatrchyan et al. Studies of dijet transverse momentum balance and pseudorapidity  
3426 distributions in pPb collisions at  $\sqrt{s_{NN}} = 5.02$  TeV. *Eur. Phys. J. C*, 74(7):2951, 2014.
- 3427 [114] S. Chatterjee and P. Bozek. Large directed flow of open charm mesons probes the  
3428 three dimensional distribution of matter in heavy ion collisions. *Phys. Rev. Lett.*,  
3429 120(19):192301, 2018.
- 3430 [115] B. Chen, X. Du, and R. Rapp. Internal Charmonium Evolution in the Quark–Gluon  
3431 Plasma. *Nucl. Part. Phys. Proc.*, 289-290:475–478, 2017.
- 3432 [116] B. Chen, M. Hu, H. Zhang, and J. Zhao. Probe the tilted Quark-Gluon Plasma with  
3433 charmonium directed flow. *Phys. Lett. B*, 802:135271, 2020.
- 3434 [117] L. Chen, G.-Y. Qin, S.-Y. Wei, B.-W. Xiao, and H.-Z. Zhang. Probing Transverse Mo-  
3435 mentum Broadening via Dihadron and Hadron-jet Angular Correlations in Relativistic  
3436 Heavy-ion Collisions. *Phys. Lett. B*, 773:672–676, 2017.
- 3437 [118] S. Choudhury et al. Investigation of Experimental Observables in Search of the Chiral  
3438 Magnetic Effect in Heavy-ion Collisions in the STAR experiment. 5 2021.
- 3439 [119] X. Chu. Di-hadron correlations in p+p, p+Au and p+Al collisions at STAR.  
3440 In *2020 Fall Meeting of the APS Division of Nuclear Physics, online*, 2020.  
3441 [https://meetings.aps.org/Meeting/DNP20/APS\\_epitome](https://meetings.aps.org/Meeting/DNP20/APS_epitome).
- 3442 [120] J. Collins and J.-W. Qiu.  $k_t$  factorization is violated in production of high-transverse-  
3443 momentum particles in hadron-hadron collisions. *Phys. Rev. D*, 75:114014, 2007.
- 3444 [121] J. C. Collins, S. F. Heppelmann, and G. A. Ladinsky. Measuring transversity densities  
3445 in singly polarized hadron hadron and lepton - hadron collisions. *Nucl. Phys. B*,  
3446 420:565–582, 1994.
- 3447 [122] U. D’Alesio, F. Murgia, and C. Pisano. Azimuthal asymmetries for hadron distributions  
3448 inside a jet in hadronic collisions. *Phys. Rev. D*, 83:034021, 2011.
- 3449 [123] U. D’Alesio, F. Murgia, and C. Pisano. Testing the universality of the Collins function  
3450 in pion-jet production at RHIC. *Phys. Lett. B*, 773:300–306, 2017.
- 3451 [124] S. K. Das, S. Plumari, S. Chatterjee, J. Alam, F. Scardina, and V. Greco. Directed  
3452 Flow of Charm Quarks as a Witness of the Initial Strong Magnetic Field in Ultra-  
3453 Relativistic Heavy Ion Collisions. *Phys. Lett. B*, 768:260–264, 2017.

- 3454 [125] D. de Florian and R. Sassot. Nuclear parton distributions at next-to-leading order.  
3455 *Phys. Rev. D*, 69:074028, 2004.
- 3456 [126] D. de Florian, R. Sassot, M. Epele, R. J. Hernández-Pinto, and M. Stratmann. Parton-  
3457 to-Pion Fragmentation Reloaded. *Phys. Rev. D*, 91(1):014035, 2015.
- 3458 [127] D. de Florian, R. Sassot, and M. Stratmann. Global analysis of fragmentation functions  
3459 for pions and kaons and their uncertainties. *Phys. Rev. D*, 75:114010, 2007.
- 3460 [128] D. de Florian, R. Sassot, and M. Stratmann. Global analysis of fragmentation functions  
3461 for protons and charged hadrons. *Phys. Rev. D*, 76:074033, 2007.
- 3462 [129] D. de Florian, R. Sassot, M. Stratmann, and W. Vogelsang. Evidence for polarization  
3463 of gluons in the proton. *Phys. Rev. Lett.*, 113(1):012001, 2014.
- 3464 [130] D. de Florian, R. Sassot, P. Zurita, and M. Stratmann. Global Analysis of Nuclear  
3465 Parton Distributions. *Phys. Rev. D*, 85:074028, 2012.
- 3466 [131] W.-T. Deng, X.-G. Huang, G.-L. Ma, and G. Wang. Test the chiral magnetic effect  
3467 with isobaric collisions. *Phys. Rev. C*, 94:041901, 2016.
- 3468 [132] W.-T. Deng, X.-G. Huang, G.-L. Ma, and G. Wang. Predictions for isobaric collisions  
3469 at  $\sqrt{s_{\text{NN}}} = 200$  GeV from a multiphase transport model. *Phys. Rev. C*, 97(4):044901,  
3470 2018.
- 3471 [133] G. Denicol, A. Monnai, and B. Schenke. Moving forward to constrain the shear viscosity  
3472 of QCD matter. *Phys. Rev. Lett.*, 116(21):212301, 2016.
- 3473 [134] F. D’Eramo, K. Rajagopal, and Y. Yin. Molière scattering in quark-gluon plasma:  
3474 finding point-like scatterers in a liquid. *JHEP*, 01:172, 2019.
- 3475 [135] C. Dilks. Measurement of Transverse Single Spin Asymmetries in  $\pi^0$  Production from  
3476  $p^\uparrow + p$  and  $p^\uparrow + A$  Collisions at STAR. *PoS*, DIS2016:212, 2016.
- 3477 [136] J. Dove et al. The asymmetry of antimatter in the proton. *Nature*, 590(7847):561–565,  
3478 2021.
- 3479 [137] F. A. Dreyer, L. Necib, G. Soyez, and J. Thaler. Recursive Soft Drop. *JHEP*, 06:093,  
3480 2018.
- 3481 [138] M. B. G. Ducati and S. Martins. Heavy meson photoproduction in peripheral  $aa$   
3482 collisions. *Phys. Rev. D*, 97:116013, Jun 2018.
- 3483 [139] U. D’Alesio, F. Murgia, and C. Pisano. Testing the universality of the collins function  
3484 in pion-jet production at rhic. *Phys. Lett. B*, 773:300–306, 2017.
- 3485 [140] K. Eskola, H. Paukkunen, and C. Salgado. Nuclear PDFs at NLO - status report and  
3486 review of the EPS09 results. *Nucl. Phys. A*, 855:150–157, 2011.

- 3487 [141] K. J. Eskola, P. Paakkinen, H. Paukkunen, and C. A. Salgado. EPPS16: Nuclear  
3488 parton distributions with LHC data. *Eur. Phys. J. C*, 77(3):163, 2017.
- 3489 [142] K. J. Eskola, H. Paukkunen, and C. A. Salgado. An Improved global analysis of nuclear  
3490 parton distribution functions including RHIC data. *JHEP*, 07:102, 2008.
- 3491 [143] K. J. Eskola, H. Paukkunen, and C. A. Salgado. A perturbative QCD study of dijets  
3492 in p+Pb collisions at the LHC. *JHEP*, 10:213, 2013.
- 3493 [144] D. Everett et al. Multi-system Bayesian constraints on the transport coefficients of  
3494 QCD matter. *Phys. Rev. C*, 103(5):054904, 2021.
- 3495 [145] E. G. Ferreira, F. Fleuret, J. P. Lansberg, N. Matagne, and A. Rakotozafindrabe.  
3496 Centrality, Rapidity, and Transverse-Momentum Dependence of Gluon Shadowing and  
3497 Antishadowing on  $J/\psi$  Production in  $dAu$  Collisions at  $\sqrt{s}=200$  GeV. *Few Body Syst.*,  
3498 53:27–36, 2012.
- 3499 [146] L. Finch and S. Murray. Investigating local parity violation in heavy-ion collisions  
3500 using  $\Lambda$  helicity. *Phys. Rev. C*, 96(4):044911, 2017.
- 3501 [147] R. J. Fries, B. Muller, C. Nonaka, and S. A. Bass. Hadronization in heavy ion collisions:  
3502 Recombination and fragmentation of partons. *Phys. Rev. Lett.*, 90:202303, 2003.
- 3503 [148] B. Friman, F. Karsch, K. Redlich, and V. Skokov. Fluctuations as probe of the QCD  
3504 phase transition and freeze-out in heavy ion collisions at LHC and RHIC. *Eur. Phys.*  
3505 *J. C*, 71:1694, 2011.
- 3506 [149] L. Gamberg, Z.-B. Kang, and A. Prokudin. Indication on the process-dependence of  
3507 the Sivers effect. *Phys. Rev. Lett.*, 110(23):232301, 2013.
- 3508 [150] F. Gelis, E. Iancu, J. Jalilian-Marian, and R. Venugopalan. The Color Glass Conden-  
3509 sate. *Ann. Rev. Nucl. Part. Sci.*, 60:463–489, 2010.
- 3510 [151] G. Giacalone. Elliptic flow fluctuations in central collisions of spherical and deformed  
3511 nuclei. *Phys. Rev. C*, 99(2):024910, 2019.
- 3512 [152] G. Giacalone. Constraining the quadrupole deformation of atomic nuclei with rela-  
3513 tivistic nuclear collisions. *Phys. Rev. C*, 102(2):024901, 2020.
- 3514 [153] G. Giacalone. Observing the deformation of nuclei with relativistic nuclear collisions.  
3515 *Phys. Rev. Lett.*, 124(20):202301, 2020.
- 3516 [154] G. Giacalone, F. G. Gardim, J. Noronha-Hostler, and J.-Y. Ollitrault. Correlation  
3517 between mean transverse momentum and anisotropic flow in heavy-ion collisions. *Phys.*  
3518 *Rev. C*, 103(2):024909, 2021.

- 3519 [155] G. Giacalone, F. G. Gardim, J. Noronha-Hostler, and J.-Y. Ollitrault. Skewness  
3520 of mean transverse momentum fluctuations in heavy-ion collisions. *Phys. Rev. C*,  
3521 103(2):024910, 2021.
- 3522 [156] G. Giacalone, J. Jia, and V. Somà. Accessing the shape of atomic nuclei with relativistic  
3523 collisions of isobars. 2 2021.
- 3524 [157] G. Giacalone, J. Jia, and C. Zhang. The impact of nuclear deformation on relativistic  
3525 heavy-ion collisions: assessing consistency in nuclear physics across energy scales. 5  
3526 2021.
- 3527 [158] G. Giacalone, J. Noronha-Hostler, M. Luzum, and J.-Y. Ollitrault. Hydrodynamic  
3528 predictions for 5.44 TeV Xe+Xe collisions. *Phys. Rev. C*, 97(3):034904, 2018.
- 3529 [159] G. Giacalone, B. Schenke, and C. Shen. Observable signatures of initial state momen-  
3530 tum anisotropies in nuclear collisions. *Phys. Rev. Lett.*, 125(19):192301, 2020.
- 3531 [160] G. Giuliani, H. Zheng, and A. Bonasera. The many facets of the (non relativistic)  
3532 Nuclear Equation of State. *Prog. Part. Nucl. Phys.*, 76:116–164, 2014.
- 3533 [161] L. Gribov, E. Levin, and M. Ryskin. Semihard Processes in QCD. *Phys. Rept.*, 100:1–  
3534 150, 1983.
- 3535 [162] X. Guo, S. Shi, N. Xu, Z. Xu, and P. Zhuang. Magnetic Field Effect on Charmonium  
3536 Production in High Energy Nuclear Collisions. *Phys. Lett. B*, 751:215–219, 2015.
- 3537 [163] J. Hammelmann, A. Soto-Ontoso, M. Alvioli, H. Elfner, and M. Strikman. Influence  
3538 of the neutron-skin effect on nuclear isobar collisions at RHIC. 8 2019.
- 3539 [164] M. R. Haque, Z.-W. Lin, and B. Mohanty. Multiplicity, average transverse momentum  
3540 and azimuthal anisotropy in U+U collisions at  $\sqrt{s_{NN}} = 200$  GeV using AMPT model.  
3541 *Phys.Rev.*, C85:034905, 2012.
- 3542 [165] U. W. Heinz and A. Kuhlman. Anisotropic flow and jet quenching in ultrarelativistic  
3543 U + U collisions. *Phys.Rev.Lett.*, 94:132301, 2005.
- 3544 [166] I. Helenius. Recent pythia 8 developments: Hard diffraction, colour reconnection and  
3545  $\gamma\gamma$  collisions. In *7th International Workshop on Multiple Partonic Interactions at the*  
3546 *LHC*, 2015. <http://indico.ictp.it/event/a14280/session/266/contribution/1042/>.
- 3547 [167] S. Hilaire and M. Girod. Large-scale mean-field calculations from proton to neutron  
3548 drip lines using the D1S Gogny force. *Eur. Phys. J. A*, 33(2):237–241, 2007.
- 3549 [168] Iakovidis, George. Vmm - an asic for micropattern detectors. *EPJ Web Conf.*,  
3550 174:07001, 2018.
- 3551 [169] E. Iancu, A. Leonidov, and L. D. McLerran. Nonlinear gluon evolution in the color  
3552 glass condensate. I. *Nucl. Phys.*, A692:583–645, 2001.

- 3553 [170] E. Iancu, A. Leonidov, and L. D. McLerran. The Renormalization group equation for  
3554 the color glass condensate. *Phys. Lett. B*, 510:133–144, 2001.
- 3555 [171] E. Iancu and R. Venugopalan. The Color glass condensate and high-energy scattering  
3556 in QCD. In *In \*Hwa, R.C. (ed.) et al.: Quark gluon plasma\* 249-3363*, 2003.
- 3557 [172] Y. B. Ivanov, V. D. Toneev, and A. A. Soldatov. Estimates of hyperon polariza-  
3558 tion in heavy-ion collisions at collision energies  $\sqrt{s_{NN}} = 4\text{--}40$  GeV. *Phys. Rev. C*,  
3559 100(1):014908, 2019.
- 3560 [173] R. Jaffe. Perhaps a Stable Dihyperon. *Phys. Rev. Lett.*, 38:617, 1977.
- 3561 [174] R. Jaffe and X.-D. Ji. Chiral odd parton distributions and polarized Drell-Yan. *Phys.*  
3562 *Rev. Lett.*, 67:552–555, 1991.
- 3563 [175] R. Jaffe and X.-D. Ji. Chiral odd parton distributions and Drell-Yan processes. *Nucl.*  
3564 *Phys. B*, 375:527–560, 1992.
- 3565 [176] J. Jalilian-Marian and Y. V. Kovchegov. Saturation physics and deuteron-Gold colli-  
3566 sions at RHIC. *Prog. Part. Nucl. Phys.*, 56:104–231, 2006.
- 3567 [177] J. Jalilian-Marian, A. Kovner, A. Leonidov, and H. Weigert. The Wilson renormal-  
3568 ization group for low  $x$  physics: Towards the high density regime. *Phys. Rev. D*,  
3569 59:014014, 1998.
- 3570 [178] J. Jalilian-Marian, A. Kovner, L. McLerran, and H. Weigert. Intrinsic glue distribution  
3571 at very small  $x$ . *Phys. Rev. D*, 55:5414–5428, May 1997.
- 3572 [179] J. Jalilian-Marian, A. Kovner, and H. Weigert. The Wilson renormalization group for  
3573 low  $x$  physics: Gluon evolution at finite parton density. *Phys. Rev. D*, 59:014015, 1998.
- 3574 [180] J. Jalilian-Marian and A. H. Rezaeian. Prompt photon production and photon-hadron  
3575 correlations at RHIC and the LHC from the Color Glass Condensate. *Phys. Rev. D*,  
3576 86:034016, 2012.
- 3577 [181] X.-D. Ji. Gauge-Invariant Decomposition of Nucleon Spin. *Phys. Rev. Lett.*, 78:610–  
3578 613, 1997.
- 3579 [182] J. Jia, S. Huang, and C. Zhang. Constraining nuclear quadrupole deformation from  
3580 correlation of elliptic flow and transverse momentum in nuclear collisions. 5 2021.
- 3581 [183] J. Jia and P. Huo. Forward-backward eccentricity and participant-plane angle fluc-  
3582 tuations and their influences on longitudinal dynamics of collective flow. *Phys. Rev.*,  
3583 C90(3):034915, 2014.
- 3584 [184] Y. Jiang, S. Shi, Y. Yin, and J. Liao. Quantifying the chiral magnetic effect from  
3585 anomalous-viscous fluid dynamics. *Chin. Phys. C*, 42(1):011001, 2018.

- 3586 [185] D. Kalinkin. Measurement of Mid-rapidity Inclusive Jet Cross Section in pp Collisions  
3587 at  $\sqrt{s} = 200$  GeV. In *APS Division of Nuclear Physics Meeting*, 2020.
- 3588 [186] D. Kalinkin. Measurement of Mid-rapidity Inclusive Jet Cross Section in *pp* Collisions  
3589 at  $\sqrt{s} = 200$  GeV. In *XXVIII International Workshop on Deep-Inelastic Scattering*  
3590 *and Related Subjects*, 2021.
- 3591 [187] K. Kanazawa, Y. Koike, A. Metz, and D. Pitonyak. Towards an explanation of trans-  
3592 verse single-spin asymmetries in proton-proton collisions: The role of fragmentation in  
3593 collinear factorization. *Phys. Rev. D*, 89:111501, Jun 2014.
- 3594 [188] Z.-B. Kang, K. Lee, X. Liu, and F. Ringer. Soft drop groomed jet angularities at the  
3595 LHC. *Phys. Lett. B*, 793:41–47, 2019.
- 3596 [189] Z.-B. Kang, K. Lee, and F. Ringer. Jet angularity measurements for single inclusive  
3597 jet production. *JHEP*, 04:110, 2018.
- 3598 [190] Z.-B. Kang, K. Lee, D. Y. Shao, and J. Terry. The sivers asymmetry in hadronic dijet  
3599 production, 2020.
- 3600 [191] Z.-B. Kang, X. Liu, F. Ringer, and H. Xing. The transverse momentum distribution  
3601 of hadrons within jets. *JHEP*, 11:068, 2017.
- 3602 [192] Z.-B. Kang, A. Prokudin, F. Ringer, and F. Yuan. Collins azimuthal asymmetries of  
3603 hadron production inside jets. *Phys. Lett. B*, 774:635–642, 2017.
- 3604 [193] Z.-B. Kang and J.-W. Qiu. Testing the time-reversal modified universality of the sivers  
3605 function. *Phys. Rev. Lett.*, 103:172001, Oct 2009.
- 3606 [194] Z.-B. Kang, I. Vitev, and H. Xing. Dihadron momentum imbalance and correlations  
3607 in d+Au collisions. *Phys. Rev. D*, 85:054024, 2012.
- 3608 [195] T. Kaufmann, A. Mukherjee, and W. Vogelsang. Hadron Fragmentation Inside Jets  
3609 in Hadronic Collisions. *Phys. Rev. D*, 92(5):054015, 2015. [Erratum: *Phys.Rev.D* 101,  
3610 079901 (2020)].
- 3611 [196] M. Kenji, O. Akira, E. Faisal, and H. Tetsuo. Probing Multi-Strange Dibaryon  
3612 with Proton-Omega Correlation in High-energy Heavy Ion Collisions. *Phys. Rev. C*,  
3613 94(031901), 2016.
- 3614 [197] V. Khachatryan et al. Observation of Long-Range Near-Side Angular Correlations in  
3615 Proton-Proton Collisions at the LHC. *JHEP*, 09:091, 2010.
- 3616 [198] V. Khachatryan et al. Evidence for transverse momentum and pseudorapidity depen-  
3617 dent event plane fluctuations in PbPb and pPb collisions. *Phys. Rev. C*, 92(3):034911,  
3618 2015.

- 3619 [199] V. Khachatryan et al. Measurement of diffraction dissociation cross sections in pp  
3620 collisions at  $\sqrt{s} = 7$  TeV. *Phys. Rev. D*, 92(1):012003, 2015.
- 3621 [200] D. Kharzeev. Parity violation in hot QCD: Why it can happen, and how to look for  
3622 it. *Phys.Lett.*, B633:260–264, 2006.
- 3623 [201] D. Kharzeev and R. D. Pisarski. Pionic measures of parity and CP violation in high-  
3624 energy nuclear collisions. *Phys.Rev.*, D61:111901, 2000.
- 3625 [202] A. Khouaja et al. Reaction cross-section and reduced strong absorption radius mea-  
3626 surements of neutron-rich nuclei in the vicinity of closed shells N=20 and N=28. *Nucl.*  
3627 *Phys. A*, 780:1–12, 2006.
- 3628 [203] S. Klein and J. Nystrand. Photoproduction of J / psi and Upsilon in pp and anti-p p  
3629 collisions. In *5th Workshop on Small x and Diffractive Physics*, 10 2003.
- 3630 [204] S. R. Klein, J. Nystrand, J. Seger, Y. Gorbunov, and J. Butterworth. STARlight:  
3631 A Monte Carlo simulation program for ultra-peripheral collisions of relativistic ions.  
3632 *Comput. Phys. Commun.*, 212:258–268, 2017.
- 3633 [205] L. Kluberger. 20 years of J/psi suppression at the CERN SPS: Results from experiments  
3634 NA38, NA51 and NA50. *Eur. Phys. J. C*, 43:145–156, 2005.
- 3635 [206] Y. V. Kovchegov. Non-abelian weizsäcker-williams field and a two-dimensional effective  
3636 color charge density for a very large nucleus. *Phys. Rev. D*, 54:5463–5469, Nov 1996.
- 3637 [207] Y. V. Kovchegov. Quantum structure of the non-abelian weizsäcker-williams field for  
3638 a very large nucleus. *Phys. Rev. D*, 55:5445–5455, May 1997.
- 3639 [208] Y. V. Kovchegov. Small x F(2) structure function of a nucleus including multiple  
3640 pomeron exchanges. *Phys. Rev.*, D60:034008, 1999.
- 3641 [209] Y. V. Kovchegov. Unitarization of the BFKL pomeron on a nucleus. *Phys. Rev. D*,  
3642 61:074018, 2000.
- 3643 [210] Y. V. Kovchegov and E. Levin. *Quantum chromodynamics at high energy*, volume 33.  
3644 Cambridge University Press, 8 2012.
- 3645 [211] Y. V. Kovchegov and M. D. Sievert. Calculating TMDs of a Large Nucleus: Quasi-  
3646 Classical Approximation and Quantum Evolution. *Nucl. Phys. B*, 903:164–203, 2016.
- 3647 [212] A. Kuhlman, U. W. Heinz, and Y. V. Kovchegov. Gluon saturation effects in relativistic  
3648 U+U collisions. *Phys. Lett. B*, 638:171–177, 2006.
- 3649 [213] A. J. Kuhlman and U. W. Heinz. Multiplicity distribution and source deformation in  
3650 full-overlap U+U collisions. *Phys. Rev. C*, 72:037901, 2005.

- 3651 [214] A. Kumar et al. Jet quenching in a multi-stage Monte Carlo approach. *Nucl. Phys. A*,  
3652 1005:122009, 2021.
- 3653 [215] J. Kwasizur. Longitudinal Double-Spin Asymmetries for Dijet Production at Interme-  
3654 diate Pseudorapidity in Polarized Proton-Proton Collisions at  $\sqrt{s} = 510$  GeV. In *APS*  
3655 *Division of Nuclear Physics Meeting*, 2020.
- 3656 [216] R. A. Lacey. Long-range collectivity in small collision-systems with two- and four-  
3657 particle correlations @ STAR. *Nucl. Phys. A*, 1005:122041, 2021.
- 3658 [217] J. Lansberg, L. Massacrier, L. Szymanowski, and J. Wagner. Single-Transverse-Spin  
3659 Asymmetries in Exclusive Photo-production of  $J/\psi$  in Ultra-Peripheral Collisions in  
3660 the Fixed-Target Mode at the LHC and in the Collider Mode at RHIC. *Phys. Lett. B*,  
3661 793:33–40, 2019.
- 3662 [218] J.-P. Lansberg and H.-S. Shao. Towards an automated tool to evaluate the impact of  
3663 the nuclear modification of the gluon density on quarkonium, D and B meson produc-  
3664 tion in proton–nucleus collisions. *Eur. Phys. J. C*, 77(1):1, 2017.
- 3665 [219] A. J. Larkoski, S. Marzani, G. Soyez, and J. Thaler. Soft Drop. *JHEP*, 05:146, 2014.
- 3666 [220] A. J. Larkoski, S. Marzani, and J. Thaler. Sudakov Safety in Perturbative QCD. *Phys.*  
3667 *Rev. D*, 91(11):111501, 2015.
- 3668 [221] W. Li. Collective flow from AA, pA to pp collisions – Toward a unified paradigm.  
3669 *Nucl. Phys. A*, 967:59–66, 2017.
- 3670 [222] Z.-T. Liang, J. Song, I. Upsal, Q. Wang, and Z.-B. Xu. Rapidity dependence of global  
3671 polarization in heavy ion collisions. 12 2019.
- 3672 [223] Z.-T. Liang and X.-N. Wang. Globally polarized quark-gluon plasma in non-central  
3673 A+A collisions. *Phys. Rev. Lett.*, 94:102301, 2005. [Erratum: *Phys.Rev.Lett.* 96,  
3674 039901 (2006)].
- 3675 [224] S. H. Lim and J. L. Nagle. Exploring Origins for Correlations between Flow Harmonics  
3676 and Transverse Momentum in Small Collision Systems (Unambiguous Ambiguity). 3  
3677 2021.
- 3678 [225] Y. Lin. Measurement of the charge separation along the magnetic field with Signed  
3679 Balance Function in 200 GeV Au + Au collisions at STAR. *Nucl. Phys. A*, 1005:121828,  
3680 2021.
- 3681 [226] C. J. Lister and J. Butterworth. Exotic pear-shaped nuclei. *Nature*, 497:190–191, 2013.
- 3682 [227] H. Liu. Measurement of transverse single-spin asymmetries for dijet production in  
3683 polarized p+p collisions at  $\sqrt{s} = 200$  GeV at STAR. In *Nuclear Physics Seminar*,  
3684 *Brookhaven National Laboratory*, 2020. <https://indico.bnl.gov/event/8633/>.

- 3685 [228] X. Liu, F. Ringer, W. Vogelsang, and F. Yuan. Factorization and its breaking in dijet  
3686 single transverse spin asymmetries in  $pp$  collisions, 2020.
- 3687 [229] Y. Ma and R. Vogt. Private Communications.
- 3688 [230] N. Magdy, S. Shi, J. Liao, N. Ajitanand, and R. A. Lacey. New correlator to detect  
3689 and characterize the chiral magnetic effect. *Phys. Rev. C*, 97(6):061901, 2018.
- 3690 [231] A. Majumder and J. Putschke. Mass depletion: a new parameter for quantitative jet  
3691 modification. *Phys. Rev. C*, 93(5):054909, 2016.
- 3692 [232] C. Marquet. Forward inclusive dijet production and azimuthal correlations in p(A)  
3693 collisions. *Nucl. Phys. A*, 796:41–60, 2007.
- 3694 [233] S. Marzani, G. Soyez, and M. Spannowsky. *Looking inside jets: an introduction to jet*  
3695 *substructure and boosted-object phenomenology*, volume 958. Springer, 2019.
- 3696 [234] L. McLerran and R. Venugopalan. Computing quark and gluon distribution functions  
3697 for very large nuclei. *Phys. Rev. D*, 49:2233–2241, Mar 1994.
- 3698 [235] L. McLerran and R. Venugopalan. Gluon distribution functions for very large nuclei  
3699 at small transverse momentum. *Phys. Rev. D*, 49:3352–3355, Apr 1994.
- 3700 [236] L. McLerran and R. Venugopalan. Green’s function in the color field of a large nucleus.  
3701 *Phys. Rev. D*, 50:2225–2233, Aug 1994.
- 3702 [237] Y. Mehtar-Tani and K. Tywoniuk. Radiative energy loss of neighboring subjects. *Nucl.*  
3703 *Phys. A*, 979:165–203, 2018.
- 3704 [238] Y. Mehtar-Tani and K. Tywoniuk. Sudakov suppression of jets in QCD media. *Phys.*  
3705 *Rev. D*, 98(5):051501, 2018.
- 3706 [239] P. Möller, A. J. Sierk, T. Ichikawa, and H. Sagawa. Nuclear ground-state masses and  
3707 deformations: FRDM(2012). *Atom. Data Nucl. Data Tabl.*, 109-110:1–204, 2016.
- 3708 [240] D. Molnar and S. A. Voloshin. Elliptic flow at large transverse momenta from quark  
3709 coalescence. *Phys. Rev. Lett.*, 91:092301, 2003.
- 3710 [241] A. H. Mueller. Soft gluons in the infinite momentum wave function and the BFKL  
3711 pomeron. *Nucl. Phys.*, B415:373–385, 1994.
- 3712 [242] A. H. Mueller and B. Patel. Single and double BFKL pomeron exchange and a dipole  
3713 picture of high-energy hard processes. *Nucl. Phys. B*, 425:471–488, 1994.
- 3714 [243] A. H. Mueller and J.-w. Qiu. Gluon Recombination and Shadowing at Small Values  
3715 of  $x$ . *Nucl. Phys. B*, 268:427–452, 1986.

- 3716 [244] A. H. Mueller, B. Wu, B.-W. Xiao, and F. Yuan. Probing Transverse Momentum  
3717 Broadening in Heavy Ion Collisions. *Phys. Lett. B*, 763:208–212, 2016.
- 3718 [245] P. Mulders and R. Tangerman. The Complete tree level result up to order  $1/Q$  for  
3719 polarized deep inelastic lepton production. *Nucl. Phys. B*, 461:197–237, 1996. [Erratum:  
3720 *Nucl.Phys.B* 484, 538–540 (1997)].
- 3721 [246] D. Müller, D. Robaschik, B. Geyer, F.-M. Dittes, and J. Hořejší. Wave functions,  
3722 evolution equations and evolution kernels from light ray operators of QCD. *Fortsch.*  
3723 *Phys.*, 42:101–141, 1994.
- 3724 [247] J. L. Nagle et al. Exploiting Intrinsic Triangular Geometry in Relativistic He3+Au  
3725 Collisions to Disentangle Medium Properties. *Phys. Rev. Lett.*, 113(11):112301, 2014.
- 3726 [248] J. Nam. Measurements of  $W$  and  $Z/\gamma^*$  cross sections and their ra-  
3727 tios in  $pp$  collisions at STAR. In *XXVIII International Workshop on*  
3728 *Deep-Inelastic Scattering and Related Subjects, Stony Brook University*, 2021.  
3729 <https://indico.bnl.gov/event/9726/contributions/46577/>.
- 3730 [249] C. Nepali, G. Fai, and D. Keane. Advantage of U+U over Au+Au collisions at constant  
3731 beam energy. *Phys. Rev. C*, 73:034911, 2006.
- 3732 [250] H. Niemi, G. S. Denicol, P. Huovinen, E. Molnar, and D. H. Rischke. Influence of  
3733 a temperature-dependent shear viscosity on the azimuthal asymmetries of transverse  
3734 momentum spectra in ultrarelativistic heavy-ion collisions. *Phys. Rev.*, C86:014909,  
3735 2012.
- 3736 [251] G. Nijs, W. van der Schee, U. Gürsoy, and R. Snellings. A transverse momentum  
3737 differential global analysis of Heavy Ion Collisions. 10 2020.
- 3738 [252] E. R. Nocera, R. D. Ball, S. Forte, G. Ridolfi, and J. Rojo. A first unbiased global  
3739 determination of polarized PDFs and their uncertainties. *Nucl. Phys.*, B887:276–308,  
3740 2014.
- 3741 [253] J. Norman. Jet acoplanarity via hadron+jet measurements in Pb-Pb collisions at  
3742  $\sqrt{s_{NN}} = 5.02$  TeV with ALICE. In *10th International Conference on Hard and Elec-*  
3743 *tromagnetic Probes of High-Energy Nuclear Collisions: Hard Probes 2020*, 9 2020.
- 3744 [254] L.-G. Pang, H. Petersen, G.-Y. Qin, V. Roy, and X.-N. Wang. Decorrelation of  
3745 anisotropic flow along the longitudinal direction. *Eur. Phys. J.*, A52(4):97, 2016.
- 3746 [255] S. Park. CJ15 global PDF analysis with new electroweak data. In *XXVIII International*  
3747 *Workshop on Deep-Inelastic Scattering and Related Subjects, Stony Brook University*,  
3748 2021. <https://indico.bnl.gov/event/9726/contributions/46569/>.

- 3749 [256] H. Paukkunen. The LHC p+Pb run from the nuclear PDF perspective. In *XXII*  
3750 *International Workshop on Deep-Inelastic Scattering and Related Subjects*, 2014.  
3751 <https://indico.cern.ch/event/258017/contributions/1588381>.
- 3752 [257] H. Paukkunen, K. J. Eskola, and C. Salgado. Dijets in p + Pb collisions and their  
3753 quantitative constraints for nuclear PDFs. *Nucl. Phys. A*, 931:331–336, 2014.
- 3754 [258] H. Paukkunen and P. Zurita. PDF reweighting in the Hessian matrix approach. *JHEP*,  
3755 12:100, 2014.
- 3756 [259] B. Pokhrel. Transverse Spin Dependent Azimuthal Correlations of Charged hadrons  
3757 in Collisions at  $\sqrt{s} = 200$  GeV. In *XXVIII International Workshop on Deep-Inelastic*  
3758 *Scattering and Related Subjects*, 2021.
- 3759 [260] B. Pokhrel. Transverse Spin Dependent Azimuthal Correlations of Charged hadrons(s)  
3760 in  $p \uparrow p$  Collisions at  $\sqrt{s} = 200$  GeV. In *XXVIII International Workshop*  
3761 *on Deep-Inelastic Scattering and Related Subjects, Stony Brook University*, 2021.  
3762 <https://indico.bnl.gov/event/9726/contributions/46262/>.
- 3763 [261] Di-jet production from pythia8.189 is scaled down due to its overestimation of inclusive  
3764  $\pi_0$  yields compared to those reported by BRAHMS in *phys. rev. lett.* 98 (2007) 252001  
3765 and STAR in *phys. rev. lett.* 97 (2006) 152302.
- 3766 [262] J.-w. Qiu and G. F. Sterman. Single transverse spin asymmetries in hadronic pion  
3767 production. *Phys. Rev. D*, 59:014004, 1999.
- 3768 [263] M. Radici and A. Bacchetta. First Extraction of Transversity from a Global Analysis  
3769 of Electron-Proton and Proton-Proton Data. *Phys. Rev. Lett.*, 120(19):192001, 2018.
- 3770 [264] A. Radyushkin. Scaling limit of deeply virtual Compton scattering. *Phys. Lett. B*,  
3771 380:417–425, 1996.
- 3772 [265] J. P. Ralston and D. E. Soper. Production of dimuons from high-energy polarized  
3773 proton-proton collisions. *Nuclear Physics B*, 152(1):109 – 124, 1979.
- 3774 [266] S. Raman, C. W. G. Nestor, Jr, and P. Tikkanen. Transition probability from the  
3775 ground to the first-excited 2+ state of even-even nuclides. *Atom. Data Nucl. Data*  
3776 *Tabl.*, 78:1–128, 2001.
- 3777 [267] A. H. Rezaeian. Semi-inclusive photon-hadron production in pp and pA collisions at  
3778 RHIC and LHC. *Phys. Rev. D*, 86:094016, 2012.
- 3779 [268] RHIC luminosity projection [https://www.rhichome.bnl.gov//RHIC/Runs/  
3780 \[RhicProjections.pdf\]\(https://www.rhichome.bnl.gov//RHIC/Runs/RhicProjections.pdf\)](https://www.rhichome.bnl.gov//RHIC/Runs/RhicProjections.pdf).
- 3781 [269] L. M. Robledo and G. F. Bertsch. Global systematics of octupole excitations in even-  
3782 even nuclei. *Phys. Rev. C*, 84:054302, 2011.

- 3783 [270] T. C. Rogers and P. J. Mulders. No generalized transverse momentum dependent  
3784 factorization in the hadroproduction of high transverse momentum hadrons. *Phys.*  
3785 *Rev. D*, 81:094006, 2010.
- 3786 [271] N. R. Sahoo. Measurement of  $\gamma$ +jet and  $\pi^0$ +jet in central Au+Au collisions at  $\sqrt{s_{NN}}$   
3787 = 200 GeV with the STAR experiment, 8 2020.
- 3788 [272] R. Sassot, M. Stratmann, and P. Zurita. Fragmentations Functions in Nuclear Media.  
3789 *Phys. Rev. D*, 81:054001, 2010.
- 3790 [273] B. Schenke and S. Schlichting. 3D glasma initial state for relativistic heavy ion colli-  
3791 sions. *Phys. Rev.*, C94(4):044907, 2016.
- 3792 [274] B. Schenke, C. Shen, and D. Teaney. Transverse momentum fluctuations and their  
3793 correlation with elliptic flow in nuclear collision. *Phys. Rev. C*, 102(3):034905, 2020.
- 3794 [275] B. Schenke, C. Shen, and P. Tribedy. Multi-particle and charge-dependent azimuthal  
3795 correlations in heavy-ion collisions at the Relativistic Heavy-Ion Collider. *Phys. Rev.*,  
3796 C99(4):044908, 2019.
- 3797 [276] F. Seck. Measurements of dielectron production in Au+Au collisions at  $\sqrt{s_{NN}} = 27$ ,  
3798 54.4 and 200 GeV with the STAR experiment. In *28th International Conference on*  
3799 *Ultrarelativistic Nucleus-Nucleus Collisions (Quark Matter 2019)*, 2019.
- 3800 [277] N. Shah, Y. Ma, J. Chen, and S. Zhang. Production of multistrange hadrons, light  
3801 nuclei and hypertriton in central Au+Au collisions at 11.5 and 200 GeV. *Phys. Lett.*  
3802 *B*, 754:6, 2016.
- 3803 [278] C. Shen and B. Schenke. Dynamical initial state model for relativistic heavy-ion colli-  
3804 sions. *Phys. Rev.*, C97(2):024907, 2018.
- 3805 [279] X.-L. Sheng, L. Oliva, and Q. Wang. What can we learn from the global spin alignment  
3806 of  $\phi$  mesons in heavy-ion collisions? *Phys. Rev. D*, 101(9):096005, 2020.
- 3807 [280] X.-L. Sheng, Q. Wang, and X.-N. Wang. Improved quark coalescence model for spin  
3808 alignment and polarization of hadrons. 7 2020.
- 3809 [281] S. Shi, Y. Jiang, E. Lilleskov, and J. Liao. Anomalous Chiral Transport in Heavy Ion  
3810 Collisions from Anomalous-Viscous Fluid Dynamics. *Annals Phys.*, 394:50–72, 2018.
- 3811 [282] S. Shi, H. Zhang, D. Hou, and J. Liao. Signatures of Chiral Magnetic Effect in the  
3812 Collisions of Isobars. *Phys. Rev. Lett.*, 125:242301, 2020.
- 3813 [283] W. Shi, W. Zha, and B. Chen. Charmonium Coherent Photoproduction and Hadropro-  
3814 duction with Effects of Quark Gluon Plasma. *Phys. Lett. B*, 777:399–405, 2018.
- 3815 [284] Y. Shi, L. Wang, S.-Y. Wei, B.-W. Xiao, and L. Zheng. Exploring collective phenomena  
3816 at the electron-ion collider. *Phys. Rev. D*, 103(5):054017, 2021.

- 3817 [285] Q. Y. Shou, Y. G. Ma, P. Sorensen, A. H. Tang, F. Videbæk, and H. Wang. Parameter-  
3818 ization of Deformed Nuclei for Glauber Modeling in Relativistic Heavy Ion Collisions.  
3819 *Phys. Lett. B*, 749:215–220, 2015.
- 3820 [286] A. M. Sirunyan et al. Relative Modification of Prompt  $\psi(2S)$  and  $J/\psi$  Yields from pp  
3821 to PbPb Collisions at  $\sqrt{s_{NN}} = 5.02$  TeV. *Phys. Rev. Lett.*, 118(16):162301, 2017.
- 3822 [287] A. M. Sirunyan et al. Constraints on the chiral magnetic effect using charge-dependent  
3823 azimuthal correlations in  $p$ Pb and PbPb collisions at the CERN Large Hadron Collider.  
3824 *Phys. Rev.*, C97(4):044912, 2018.
- 3825 [288] A. M. Sirunyan et al. Charged-particle angular correlations in XeXe collisions at  
3826  $\sqrt{s_{NN}} = 5.44$  TeV. *Phys. Rev. C*, 100(4):044902, 2019.
- 3827 [289] D. Sivers. The Adventure and the Prize. *Nuovo Cim. C*, 035N2:171–186, 2012.
- 3828 [290] T. Sjostrand, S. Mrenna, and P. Z. Skands. A Brief Introduction to PYTHIA 8.1.  
3829 *Comput. Phys. Commun.*, 178:852–867, 2008.
- 3830 [291] T. Sjöstrand, S. Ask, J. R. Christiansen, R. Corke, N. Desai, P. Ilten, S. Mrenna,  
3831 S. Prestel, C. O. Rasmussen, and P. Z. Skands. An introduction to PYTHIA 8.2.  
3832 *Comput. Phys. Commun.*, 191:159–177, 2015.
- 3833 [292] V. Smakhtin, G. Mikenberg, A. Klier, Y. Rozen, E. Duchovni, E. Kajamovitz, and  
3834 A. Hershenhorn. Thin Gap Chamber upgrade for SLHC: Position resolution in a test  
3835 beam. *Nucl. Instrum. Meth.*, A598:196–200, 2009.
- 3836 [293] SN0619 : A Proposal for STAR Inner TPC Sector Upgrade (iTTPC) [https://drupal.  
3837 star.bnl.gov/STAR/starnotes/public/sn0619](https://drupal.star.bnl.gov/STAR/starnotes/public/sn0619).
- 3838 [294] J. Soffer. *Phys. Rev. Lett.*, 74:1292, 1995.
- 3839 [295] H. Song, S. A. Bass, U. Heinz, T. Hirano, and C. Shen. 200 A GeV Au+Au collisions  
3840 serve a nearly perfect quark-gluon liquid. *Phys. Rev. Lett.*, 106:192301, 2011. [Erratum:  
3841 *Phys.Rev.Lett.* 109, 139904 (2012)].
- 3842 [296] STAR 2017 BUR [https://drupal.star.bnl.gov/STAR/system/files/STAR\\_BUR\\_  
3843 Run1718\\_v22\\_0.pdf](https://drupal.star.bnl.gov/STAR/system/files/STAR_BUR_Run1718_v22_0.pdf).
- 3844 [297] The STAR Forward Calorimeter System and Forward Tracking System beyond  
3845 BES-II [https://drupal.star.bnl.gov/STAR/files/Proposal.ForwardUpgrade.  
3846 Nov\\_.2018.Review.pdf](https://drupal.star.bnl.gov/STAR/files/Proposal.ForwardUpgrade.Nov_.2018.Review.pdf).
- 3847 [298] M. Strikman and W. Vogelsang. Multiple parton interactions and forward double pion  
3848 production in pp and dA scattering. *Phys. Rev. D*, 83:034029, 2011.
- 3849 [299] P. Sun, J. Isaacson, C. P. Yuan, and F. Yuan. Universal non-perturbative functions  
3850 for sidis and drell-yan processes, 2014.

- 3851 [300] Y. Sun and C. M. Ko. A hyperon polarization in relativistic heavy ion collisions from  
3852 a chiral kinetic approach. *Phys. Rev. C*, 96(2):024906, 2017.
- 3853 [301] I. Takashi, I. G. Noriyoshi, A. Sinya, and D. Takumi. Baryon-Baryon Interactions in  
3854 the Flavor SU(3) Limit from Full QCD Simulations on the Lattice. *Prog. Theor. Phys.*,  
3855 124:591, 2010.
- 3856 [302] I. Takashi, I. G. Noriyoshi, A. Sinya, and D. Takumi. Two-baryon potentials and  
3857 H-dibaryon from 3-flavor lattice QCD simulations. *Nucl. Phys. A*, 881:28, 2012.
- 3858 [303] A. H. Tang. Probe chiral magnetic effect with signed balance function. *Chin. Phys.*  
3859 *C*, 44(5):054101, 2020.
- 3860 [304] The CBM Collaboration eTOF Group. Physics Program for the STAR/CBM eTOF  
3861 Upgrade. 2016.
- 3862 [305] J. the STAR Collaboration, Adam et al. Observation of excess  $J/\psi$  yield at very low  
3863 transverse momenta in Au+Au collisions at  $\sqrt{s_{NN}} = 200$  GeV and U+U collisions at  
3864  $\sqrt{s_{NN}} = 193$  GeV. *Phys. Rev. Lett.*, 123(13):132302, 2019.
- 3865 [306] R. S. Towell et al. Improved measurement of the anti-d / anti-u asymmetry in the  
3866 nucleon sea. *Phys. Rev.*, D64:052002, 2001.
- 3867 [307] P. Tribedy. Disentangling flow and signals of Chiral Magnetic Effect in U+U, Au+Au  
3868 and p+Au collisions. *Nucl. Phys. A*, 967:740–743, 2017.
- 3869 [308] Z. Tu, A. Jentsch, M. Baker, L. Zheng, J.-H. Lee, R. Venugopalan, O. Hen, D. Hig-  
3870 inbotham, E.-C. Aschenauer, and T. Ullrich. Probing short-range correlations in the  
3871 deuteron via incoherent diffractive  $J/\psi$  production with spectator tagging at the EIC.  
3872 *Phys. Lett. B*, 811:135877, 2020.
- 3873 [309] M. Vasilev et al. Parton energy loss limits and shadowing in Drell-Yan dimuon pro-  
3874 duction. *Phys. Rev. Lett.*, 83:2304–2307, 1999.
- 3875 [310] O. Vitiuk, L. V. Bravina, and E. E. Zabrodin. Is different  $\Lambda$  and  $\bar{\Lambda}$  polarization caused  
3876 by different spatio-temporal freeze-out picture? *Phys. Lett. B*, 803:135298, 2020.
- 3877 [311] S. A. Voloshin. Parity violation in hot QCD: How to detect it. *Phys. Rev.*, C70:057901,  
3878 2004.
- 3879 [312] S. A. Voloshin. Polarized secondary particles in unpolarized high energy hadron-hadron  
3880 collisions? 10 2004.
- 3881 [313] S. A. Voloshin. Testing the Chiral Magnetic Effect with Central U+U collisions. *Phys.*  
3882 *Rev. Lett.*, 105:172301, 2010.

- 3883 [314] S. A. Voloshin. Estimate of the signal from the chiral magnetic effect in heavy-ion  
3884 collisions from measurements relative to the participant and spectator flow planes.  
3885 *Phys. Rev.*, C98(5):054911, 2018.
- 3886 [315] D.-X. Wei, W.-T. Deng, and X.-G. Huang. Thermal vorticity and spin polarization in  
3887 heavy-ion collisions. *Phys. Rev. C*, 99(1):014905, 2019.
- 3888 [316] H. Weigert. Evolution at small  $x(bj)$ : The Color glass condensate. *Prog. Part. Nucl.*  
3889 *Phys.*, 55:461–565, 2005.
- 3890 [317] Y. Xie, D. Wang, and L. P. Csernai. Global  $\Lambda$  polarization in high energy collisions.  
3891 *Phys. Rev. C*, 95(3):031901, 2017.
- 3892 [318] Y. Xie, D. Wang, and L. P. Csernai. Fluid dynamics study of the  $\Lambda$  polarization for  
3893 Au + Au collisions at  $\sqrt{s_{NN}} = 200$  GeV. *Eur. Phys. J. C*, 80(1):39, 2020.
- 3894 [319] H. Xing, C. Zhang, J. Zhou, and Y.-J. Zhou. The  $\cos 2\phi$  azimuthal asymmetry in  $\rho^0$   
3895 meson production in ultraperipheral heavy ion collisions, 2020.
- 3896 [320] H.-J. Xu, X. Wang, H. Li, J. Zhao, Z.-W. Lin, C. Shen, and F. Wang. Importance  
3897 of isobar density distributions on the chiral magnetic effect search. *Phys. Rev. Lett.*,  
3898 121(2):022301, 2018.
- 3899 [321] H.-j. Xu, J. Zhao, X. Wang, H. Li, Z.-W. Lin, C. Shen, and F. Wang. Varying the  
3900 chiral magnetic effect relative to flow in a single nucleus-nucleus collision. *Chin. Phys.*,  
3901 C42(8):084103, 2018.
- 3902 [322] Q. Xu, Z. Liang, and E. Sichtermann. Anti-Lambda polarization in high energy  $pp$   
3903 collisions with polarized beams. *Phys. Rev. D*, 73:077503, 2006.
- 3904 [323] Y. Xu. Longitudinal and Transverse Spin Transfer of  $\Lambda$  and  $\bar{\Lambda}$  Hyperons in Polarized  
3905  $p+p$  Collisions at  $\sqrt{s} = 200$  GeV at RHIC-STAR. In *XXVIII International Work-*  
3906 *shop on Deep-Inelastic Scattering and Related Subjects, Stony Brook University*, 2021.  
3907 <https://indico.bnl.gov/event/9726/contributions/46261/>.
- 3908 [324] F. Yuan. Asymmetric azimuthal distribution of hadrons inside a jet from hadron-  
3909 hadron collisions. *Phys. Rev. Lett.*, 100:032003, 2008.
- 3910 [325] F. Yuan. Collins asymmetry at hadron colliders. *Phys. Rev. D*, 77:074019, 2008.
- 3911 [326] B. G. Zakharov. Radiative  $p_{\perp}$ -broadening of fast partons in an expanding quark-gluon  
3912 plasma. *Eur. Phys. J. C*, 81(1):57, 2021.
- 3913 [327] W. Zha, S. R. Klein, R. Ma, L. Ruan, T. Todoroki, Z. Tang, Z. Xu, C. Yang, Q. Yang,  
3914 and S. Yang. Coherent  $j/\psi$  photoproduction in hadronic heavy-ion collisions. *Phys.*  
3915 *Rev. C*, 97:044910, Apr 2018.

- 3916 [328] J. Zhao. Search for CME in U+U and Au+Au collisions in STAR with different  
3917 approaches of handling backgrounds. 2 2020.
- 3918 [329] J. Zhao, H. Li, and F. Wang. Isolating the chiral magnetic effect from backgrounds by  
3919 pair invariant mass. *Eur. Phys. J. C*, 79(2):168, 2019.
- 3920 [330] X. Zhao and R. Rapp. Charmonium in medium: From correlators to experiment. *Phys.*  
3921 *Rev. C*, 82:064905, Dec 2010.
- 3922 [331] K. Zhou, N. Xu, Z. Xu, and P. Zhuang. Medium effects on charmonium production  
3923 at ultrarelativistic energies available at the cern large hadron collider. *Phys. Rev. C*,  
3924 89:054911, May 2014.